OPTICAL PROPERTIES OF APERIODIC METALLIC PHOTONIC CRYSTAL STRUCTURES

Von der Fakultät für Mathematik und Physik der Universität Stuttgart zur Erlangung der Würde eines Doktors der Naturwissenschaften (Dr. rer. nat.) genehmigte Abhandlung

vorgelegt von

Christina Bauer

aus Stuttgart

Hauptberichter:	Prof. Dr. Harald Gießen
Mitberichter:	Prof. Dr. Clemens Bechinger
Tag der Einreichung:	21.05.2013
Tag der mündlichen Prüfung:	18.07.2013

4. Physikalisches Institut der Universität Stuttgart

2013

Zusammenfassung

In dieser Arbeit werden die linearen optischen Eigenschaften von aperiodischen metallischen photonischen Kristallen untersucht. Alle Strukturen bestehen aus einem Metallgitter, das sich auf einem Wellenleiter befindet. Das einfallende Licht kann plasmonische Moden im Metall sowie photonische Moden im darunter liegenden Wellenleiter anregen. Diese Resonanzen sind aneinander gekoppelt.

Im ersten Teil dieser Arbeit werden die Proben untersucht, die ein eindimensionales Metallgitter besitzen. Die Anordnung dieser Metalldrähte auf der dielektrischen Wellenleiterschicht ist ungeordnet, quasikristallin oder fraktal. Für die Unordnungsproben zeigt die experimentell bestimmte Kopplungskonstante reduzierte Werte bei größerer Unordnung. Zusätzlich werden die berechneten Kopplungskonstanten mit den experimentell bestimmten Urbach-Energien verglichen. Es zeigt sich, dass der Zusammenhang zwischen diesen beiden Parametern vom Unordnungsmodell sowie von der mittleren Gitterperiode abhängt. Die optischen Eigenschaften der Proben mit der quasikristallinen und der fraktalen Anordnung der Metalldrähte werden in Bezug auf ihre lange, kurze und mittlere Drahtabstände analysiert.

Der nächste Teil dieser Arbeit beschäftigt sich mit den zweidimensionalen Metallgittern. Die Metallpartikel sind quasikristallin angeordnet. Die Partikel sind elliptisch und in Bezug auf die x-Achse der Probe rotiert. Es zeigt sich, dass die optischen Eigenschaften solcher Strukturen von der Exzentrizität der Metallpartikel sowie vom Rotationswinkel zwischen der kleinen Hauptachse und der x-Achse der Probe abhängen. Anschließend wird ein theoretisches Modell entwickelt, um die optischen Eigenschaften solcher Strukturen zu beschreiben. Mit diesem theoretischen Verfahren ist es möglich, die Spektren für senkrechten Lichteinfall sowie für winkelabhängigen Lichteinfall zu berechnen. Dieses Modell wird dazu benutzt, um die erhöhte Absorption von plasmonischen Solarzellen vorherzusagen.

Abstract

In this thesis the linear optical properties of aperiodic metallic photonic crystals are studied. All structures consist of a metal grating on top of a waveguide material. The incident light can excite plasmonic modes in the metal as well as photonic modes in the waveguide underneath. These resonances are coupled to each other.

In the first part of the thesis, the samples with a one-dimensional metal grating are studied. The structural arrangement of the metal wires on top of the dielectric waveguide layer is disordered, quasicrystalline, or fractal. For the disorder samples, the experimentally obtained coupling constant shows reduced values for larger disorder amounts. Additionally, the calculated coupling constants are compared to the experimentally obtained Urbach energies. It is found that the relation between these two parameters is dependent on the disorder model as well as on the average grating period. The optical properties of the samples with the quasicrystalline and fractal metal wire arrangement are analyzed with respect to their long, short, and average wire distances.

The next part of the thesis deals with two-dimensional metal gratings. The metal disks are arranged in a quasicrystalline fashion with the disks being elliptically shaped and rotated with respect to the sample x axis. It is found that the optical properties of such structures are dependent on the eccentricity of the metal disks as well as on the rotation angle between the short main axis and the sample x axis. Afterwards, a theoretical model is developed in order to describe the optical properties of such structures. With the theoretical approach it is possible to calculate the normal incidence spectra as well as the oblique light incidence spectra. This model is used to predict the absorption enhancement of plasmonic solar cells.

Publications

Parts of this thesis have already been published:

In scientific journals:

- C. Bauer and H. Giessen, *Light harvesting enhancement in solar cells with quasicrystalline plasmonic structures*, Opt. Express **21**, A363 (2013).

- C. Bauer, G. Kobiela, and H. Giessen, *2D quasiperiodic plasmonic crystals*, Nature Sci. Rep. **2**, 681 (2012).

- C. Bauer, G. Kobiela, and H. Giessen, *Optical properties of two-dimensional quasicrystalline plasmonic arrays*, Phys. Rev. B **84**, 193104 (2011).

On international conferences:

- C. Bauer, G. Kobiela, and H. Giessen, *2D metallic photonic quasicrystals*, European Materials Research Society (E-MRS) Spring Meeting, Talk N14.8, Strasbourg, France (2012).

- C. Bauer, G. Kobiela, and H. Giessen, *2D metallic photonic quasicrystals*, Quantum Electronics and Laser Science Conference (QELS), Talk QF2D.2, San Jose, USA (2012).

- C. Bauer, G. Kobiela, and H. Giessen, *Simulation model of 2D metallic photonic quasicrystals*, DPG Spring Meeting, Talk HL 54.6, Regensburg, Germany (2010).

- G. Kobiela, C. Bauer, and H. Giessen, *Quasicrystalline Metamaterials*, European Quantum Electronics Conference (EQEC), Poster EJ.P4 (2009).

- C. Bauer, D. Nau, S. Zhukovsky, and H. Giessen, *Quasiperiodic structures in metallic photonic crystals*, DPG Spring Meeting, Poster HL 36.26, Berlin, Germany (2008).

Additional scientific publications that are not presented in this thesis:

- H. Schweizer, L. Fu, M. Hentschel, T. Weiss, C. Bauer, P. Schau, K. Frenner, W. Osten, and H. Giessen, *Resonant multimeander-metasurfaces: A model system for superlenses and communication devices*, phys. stat. sol. (b) **249**, 1415 (2011).

- A. Christ, G. Lévêque, O. J. F. Martin, T. Zentgraf, J. Kuhl, C. Bauer, H. Giessen, and S. G. Tikhodeev, *Near-field induced tunability of surface plasmon polaritons in composite metallic nanostructures*, J. Microsc. **229**, 344 (2008).

- D. Nau, A. Schönhardt, A. Christ, T. Zentgraf, Ch. Bauer, J. Kuhl, and H. Giessen, *Optical properties of disordered metallic photonic crystal slabs*, phys. stat. sol. (a) **204**, 3848 (2007).

- D. Nau, A. Schönhardt, Ch. Bauer, A. Christ, T. Zentgraf, J. Kuhl, M. W. Klein, and H. Giessen, *Correlation effects in disordered metallic photonic crystal slabs*, Phys. Rev. Lett. **98**, 133902 (2007).

- D. Nau, A. Schönhardt, C. Bauer, A. Christ, T. Zentgraf, J. Kuhl, and H. Giessen, *Disorder issues in metallic photonic crystals*, phys. stat. sol. (b) **243**, 2331 (2006).

CONTENTS

CHAPTER 1

INTRODUCTION

It has been known for centuries that glasses containing small metal particles appear in bright colors. The Lycurgus Cup is an example for such a colored glass. This cup is green when light is reflected by the cup and changes its color to red for transmitted light [1]. These optical properties were achieved by adding a small amount of gold and silver colloids to the glass during the production process [2]. Already in 1857, the optical properties of such small metal particles were studied by Faraday [3]. However, it was not before 1908 that a detailed theory was developed to describe the optical properties of small spherical metal particles [4].

In the second half of the 19th century, first investigations on one-dimensional photonic crystals were performed [5–7] observing a one-dimensional photonic stop-band. However, the idea of Yablonovitch that three-dimensional photonic crystals can be used to suppress the spontaneous emission in semiconductors [8] as well as the idea of John that a reasonable disorder amount within a three-dimensional photonic crystal is able to strongly localize photons [9] were the breakthroughs in this area of research in 1987. Two years later, Yablonovitch introduced the name *photonic crystal* [10], which is commonly used thereafter.

A huge number of applications has been proposed in the subsequent years. Among these suggestions is the use of photonic crystals as waveguides to guide light around sharp corners [11], as beam splitters [12], or as photonic crystal fibers [13, 14]. Photonic crystals can also be used for sensing [15–19] as well as for enhancing the efficiency of LEDs [20–22] and solar cells [23–25].

Most of the photonic crystal designs are based on a refractive index variation of dielectric materials. However, metallic photonic crystals, where one of the materials is a metal, have also been studied [26–30]. Among these designs are metallic photonic crystals possessing a one-dimensional (1D) or a two-dimensional (2D) metallic

grating on top of a waveguide material [31–33]. The nonlinear properties have also been investigated [34–38]. Metallic photonic crystals have also been used for several applications, just as photonic crystal slab lenses [39], optical switches [40], or sensors [41–43].

After the discovery of quasicrystals in 1982 by Shechtman and his first publication in 1984 [44], Levine and Steinhardt found that Shechtman's diffraction patterns and their computed ones assuming an icosahedral quasicrystal match very well [45] identifying for the first time the occurrence of a quasicrystal. These computed diffraction patterns are based on the findings of Mackay [46], who was the first person to find the diffraction pattern of a model consisting of circles on the vertices of a Penrose tiling [47, 48]. In the subsequent years, quasicrystals gained the interest of numerous researchers. A lot of different quasicrystals have been discovered since then [49–52] and many applications have been presented like a non-sticking frying pan due to a quasicrystalline coating [53], the use of quasicrystals as catalysts [53, 54], or as solar light absorbers [53, 55, 56]. For the discovery of quasicrystals, Shechtman won the Nobel Prize in Chemistry 2011 [57].

Not only quasicrystalline metallic alloys have been investigated, but also other quasicrystals like colloidal [58–60] or phononic quasicrystals [61, 62]. Quasicrystalline structures have also been studied theoretically [63–66]. Another area of research are photonic quasicrystals. Such photonic quasicrystals have been studied in one-dimensional [67], two-dimensional [68–70], and three-dimensional [71–73] structural arrangements.

All these photonic quasicrystals have in common that no metals are involved. However, also metallic photonic quasicrystals have been investigated. Whereas the quasicrystalline arrangement of nanoholes in a metallic film has been studied by several groups [74–76], the optical properties of the inverse structures have not been examined so far. The above mentioned metallic photonic crystal designs with a metallic grating on top of a waveguide material are all based on a *periodic* grating structure. Also disordered metallic photonic crystals have been studied in our group for 1D structural arrangements [77–79] as well as for 2D structural arrangements [80]. However, quasiperiodic structures have not been investigated up to now.

Since quasicrystalline structures are much more isotropic than periodic ones [81], it is interesting to study the optical properties of such structures. In this thesis, such quasiperiodic structures are measured and analyzed for 1D as well as 2D structural arrangements. A theoretical model for normal as well as for oblique light incidence is developed in order to be able to model the optical properties of such 2D structures.

This model is based on the 1D model for disordered structures introduced by D. Nau [78]. The model is experimentally confirmed by several measurements. Additionally, this model is used to predict the enhanced absorption of such quasicrystalline structures on solar cells. In this thesis, the optical properties of 1D disordered and 1D fractal structures are investigated as well.

The outline of this thesis is as follows: In Chapter 2, the optical properties of metallic photonic crystals are introduced. First, the focus is on metal particles and then on waveguide modes. Afterwards, the optical properties of the combined structure are presented. In the next parts, the concept of disordered structures as well as of fractal structures is presented. Different construction methods for 1D as well as for 2D quasicrystals are introduced in the following part. The last part in Chapter 2 presents the simulation model for 1D disordered structures.

Chapter 3 explains the fabrication method of the samples by electron-beam lithography as well as the experimental setup and the measurement procedure.

Chapter 4 focuses on the 1D plasmonic structures. In the first part, the spectra of the disordered structures are shown and the coupling strengths between the plasmonic mode and the waveguide mode for normal light incidence are determined. The spectra for oblique light incidence are shown next and the different behavior of the individual disorder samples is analyzed. Afterwards, the optical properties of the 1D quasicrystalline structures as well as of the fractal structures are presented.

The optical properties of the 2D plasmonic structures are presented in Chapter 5. This chapter focuses on the normal incidence spectra of different samples first. Then, a theoretical model for 2D structures and normal light incidence based on the 1D disorder model of D. Nau [78] is developed. The calculated spectra are compared for all samples to the measured ones verifying the model. Afterwards, the spectra measured for oblique light incidence are presented. The theoretical model for normal light incidence is then expanded for oblique light incidence and the calculated spectra are compared to the measured ones. The last part in this chapter presents a possible application and predicts the absorption enhancement of a plasmonic solar cell with a quasicrystalline gold disk arrangement compared to one with a periodic gold disk arrangement. As waveguide layer serves the silicon layer of the solar cell.

The last chapter summarizes the results and a short outlook on future research projects is presented.

CHAPTER 2

THEORETICAL BACKGROUND

2.1 Metallic photonic crystals

Photonic crystals usually consist of a periodic arrangement of different refractive indices with a periodicity in the order of the wavelength of the incident light [82]. The modulation of the refractive index can be changed in one, two, or three directions which corresponds to one-dimensional (1D), two-dimensional (2D), or three-dimensional (3D) photonic crystals [83].

Examples for natural photonic crystals are butterfly wings [84], peacock feathers [85], or opals [86, 87], where different materials are placed in such a manner that these beautiful colors arise. This is due to the photonic band gap, which means that specific wavelengths are reflected leading to the different colors [83]. Photonic crystals exhibiting band structures for photons are the electromagnetic analog to natural crystals with band structures for electrons [83]. Since the photons in such structures show a similar behavior as electrons in normal crystals, these materials are called *photonic crystals* [10].

Materials with such photonic band structures are interesting for plenty of applications. Yablonovitch had the idea that the photonic band gap can suppress the spontaneous emission of semiconductors [8]. John recommended the introduction of a moderate amount of disorder into a three-dimensional periodic lattice in order to obtain a strong localization of photons [9]. Other applications are the use of photonic crystals for fast all-optical switches on a silicon chip [88], for waveguide couplers [89], and for splitters [12].

Most photonic crystals consist of different *dielectric* materials. However, it is also possible to replace at least one of the components by a metal. Therefore, these structures are more specifically called *metallic photonic crystals* [79]. By using such

metallic photonic crystals, large stop bands can be obtained [26]. As an example, these structures can be utilized as metallic photonic crystal filters [90, 91].

The structures studied here consist of metallic wires or dots on top of a dielectric waveguide corresponding to 1D or 2D metallic photonic crystals. The properties of the metallic nanostructures, the waveguide modes, as well as the complete system are presented in the following subsections.

2.1.1 Metallic nanostructures

Metals possess electrons in the conduction band. These electrons can be considered to move freely in the metal [92]. With this assumption, most of the electronic and optical properties of metals can be described. Therefore, it is crucial to have a look at the Drude-Lorentz-Sommerfeld model [93]. This simple model describes the behavior of the free electron gas when an external electromagnetic field $\mathbf{E} = \mathbf{E}_0 \, e^{-i\omega t}$ with amplitude $\mathbf{E}_0$ and frequency ω is incident on the metal. It assumes that n conduction band electrons of the metal show the same response to the external force as one electron multiplied by the number of electrons [93]. The motion of the conduction band electrons can be described by a damped harmonic oscillator model leading to the following equation of motion

$$\ddot{\mathbf{r}} + \Gamma\dot{\mathbf{r}} = -\frac{e}{m_e}\mathbf{E}_0 \, e^{-i\omega t} \tag{2.1}$$

with e as the elementary charge, m_e as the electron mass, and Γ as the damping constant. In Eq. (2.1) the restoring force is assumed to be zero [94] meaning that the electrons are not influenced by the ionic lattice. By using the ansatz $\mathbf{r} = \mathbf{r}_0 \, e^{-i\omega t}$, Eq. (2.1) can be solved. Together with the polarization

$$\mathbf{P} = -en\mathbf{r} = \varepsilon_0\chi_{DS}\mathbf{E}, \tag{2.2}$$

the free-electron Drude-Sommerfeld susceptibility

$$\chi_{DS} = -\frac{\omega_p^2}{\omega^2 + \Gamma^2} + i\frac{\Gamma\omega_p^2}{\omega(\omega^2 + \Gamma^2)} \tag{2.3}$$

as well as the dielectric function

$$\varepsilon = 1 + \chi_{DS} = 1 - \frac{\omega_p^2}{\omega^2 + \Gamma^2} + i\frac{\Gamma\omega_p^2}{\omega(\omega^2 + \Gamma^2)} \tag{2.4}$$

can be obtained. The Drude plasma frequency ω_p is defined by

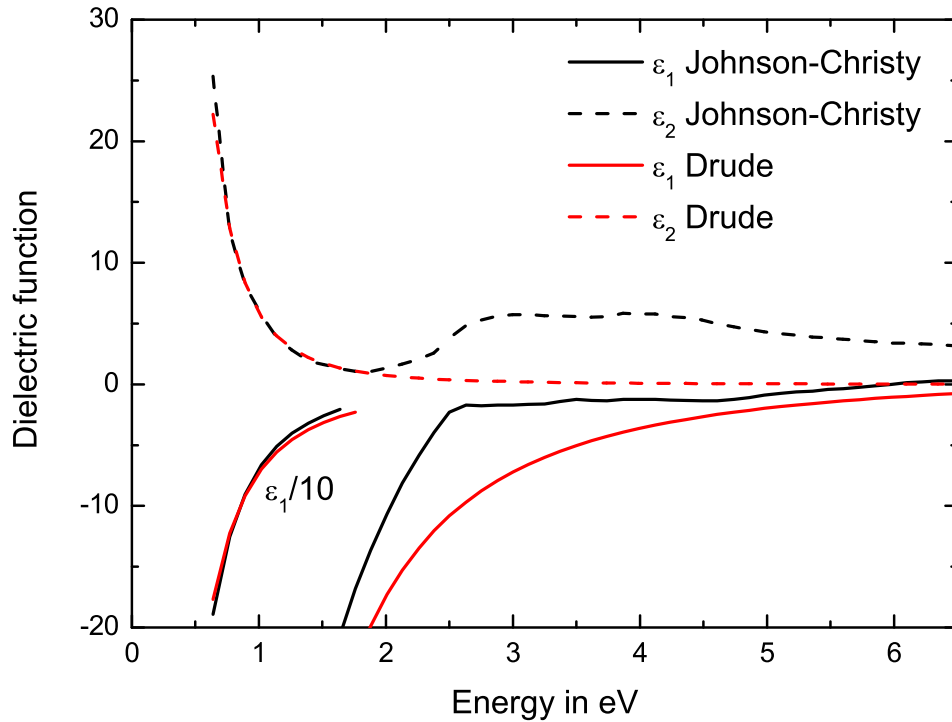$$\omega_p = \sqrt{\frac{e^2 n}{\varepsilon_0 m_e}} \tag{2.5}$$

Figure 2.1: The real part (solid lines) and the imaginary part (dashed lines) of the dielectric function of gold. The black curves show the measured data of Ref. [95]. The red curves are modeled by using the Drude-Lorentz-Sommerfeld model with $\hbar\omega_p = 8.6\,\text{eV}$ and $\hbar\Gamma = 0.08\,\text{eV}$.

with ε_0 being the vacuum permittivity.

Up to now only the conduction band electrons have been considered. However, the interband transitions of electrons in deeper levels play a crucial role [93]. Therefore, the dielectric function given in Eq. (2.4) has to be expanded by an additional term, the interband susceptibility χ_{IB}, leading to

$$\varepsilon = 1 + \chi_{DS} + \chi_{IB}. \tag{2.6}$$

Especially for gold these interband transitions are important. This can be seen when the measured dielectric function is compared to the Drude modeled values. The real and imaginary parts of the dielectric function of gold ε_1 and ε_2 measured by Johnson and Christy [95] are shown as black solid and black dashed curves in Fig. 2.1. The red curves in this figure are modeled by using Eq. (2.4) with the Drude plasma frequency $\hbar\omega_p = 8.6\,\text{eV}$ and the damping constant $\hbar\Gamma = 0.08\,\text{eV}$. Especially for the imaginary part the agreement between the measured and the modeled curves is quite

good up to an energy of about $2\,\mathrm{eV}$. The deviations are much higher for energies above $2\,\mathrm{eV}$. The increased values of the experimentally obtained dielectric function are due to the above mentioned interband transitions. However, the measured values of Johnson and Christy [95] are used in the following parts of this thesis. A deeper insight into the theory of interband transitions is given in Ref. [93].

The metal structures in this thesis are either gold wires or gold disks with lengths in two or three dimensions being much smaller than the wavelength of the incident light. Due to this spatial confinement, so-called *particle plasmons* [96] (also called *localized surface plasmons* [97]) can be excited. These particle plasmons can be directly excited by light incident on the metal particle. The atomic cores are assumed to stay at fixed positions, whereas the conduction band electrons are forced by the external light field to oscillate collectively around the positions of the atomic cores [93]. Since the particle size is much smaller than the incident wavelength, the electrons are assumed to respond immediately to the incoming electromagnetic field [98]. This means that retardation is neglected, which is known as the *quasi-static approximation* [98]. Whereas the scattering and absorption efficiencies of spherical particles can be described by the Mie theory [4], this exact theory is not applicable for differently shaped particles. Therefore, the quasi-static approximation has to be used for ellipsoidal particles. As already mentioned above, the conduction band electrons follow the electric field of the incident light. This means that the electrons are collectively displaced with respect to the positive background at a specific time leading to a charge separation. Therefore, a small particle can be approximated by an electric dipole with dipole moment [94]

$$\mathbf{p} = \varepsilon_m \boldsymbol{\alpha} \mathbf{E}_0, \qquad (2.7)$$

where ε_m is the permittivity of the medium surrounding the particle, $\boldsymbol{\alpha}$ is the polarizability tensor, and $\mathbf{E}_0$ is the incoming static electric field. When we assume an ellipsoidal particle with semiaxes r_1, r_2, and r_3 consisting of a material with permittivity $\varepsilon_p = \varepsilon_p' + i\,\varepsilon_p''$, the polarizability α_j along one of the principal axes in direction $\mathbf{e}_j$ is defined to be [94]

$$\alpha_j = \frac{4\pi}{3}\, r_1 r_2 r_3 \, \frac{\varepsilon_p - \varepsilon_m}{\varepsilon_m(1 - L_j) + L_j \varepsilon_p} \qquad (2.8)$$

with $j = 1$, 2, or 3. This polarizability tensor only possesses the main axis elements α_j. The form factors L_j are dependent on the geometry of the particle and are given by

$$L_j = \frac{r_1 r_2 r_3}{2} \int_0^\infty \frac{1}{(r_j^2 + q) f(q)} \, \mathrm{d}q \qquad (2.9)$$

with $f(q) = \sqrt{(q + r_1^2)(q + r_2^2)(q + r_3^2)}$. This means that L_j with $L_1 + L_2 + L_3 = 1$ is always a value between zero and one. For spherical particles, all three form factors are equal to $\frac{1}{3}$. Reducing one of the main axis diameters results in a larger form factor while the other two form factors become smaller [80]. The extinction, scattering, and absorption of light by a particle are characterized by the extinction, scattering, and absorption cross sections $C_{ext,j}$, $C_{sc,j}$, and $C_{a,j}$ for an incident electric field vector along one of the principal axes. These values can be calculated via [94]

$$C_{ext,j} = k \operatorname{Im}(\alpha_j), \tag{2.10}$$

$$C_{sc,j} = \frac{k^4}{6\pi} |\alpha_j|^2, \tag{2.11}$$

$$C_{a,j} \approx C_{ext,j} = k \operatorname{Im}(\alpha_j) \tag{2.12}$$

with k being the propagation constant of the incoming light. Note that $C_{a,j}$ and $C_{ext,j}$ are approximately the same due to the negligibly small scattering cross section of small particles [94]. By inserting Eq. (2.8) into Eq. (2.10), the following equation is obtained:

$$C_{ext,j} = k \frac{4\pi}{3} r_1 r_2 r_3 \frac{\varepsilon_m \varepsilon_p''}{[\varepsilon_m + L_j(\varepsilon_p' - \varepsilon_m)]^2 + [L_j \varepsilon_p'']^2}. \tag{2.13}$$

In order to calculate $C_{ext,j}$, the frequency dependent dielectric functions of the particle and the surrounding material have to be used.

The resonance frequency of the particle plasmon is then given by the frequency when Eq. (2.13) is maximum meaning that $[\varepsilon_m + L_j(\varepsilon_p' - \varepsilon_m)]^2 + [L_j \varepsilon_p'']^2$ has to be minimum. By assuming the imaginary part of the particle's dielectric function ε_p'' to be either small or almost constant in the vicinity of the resonance, the condition $\varepsilon_p' = -\varepsilon_m \frac{1 - L_j}{L_j}$ has to be fulfilled [93]. If ε_m was changed to higher values, the resonance frequency of the particle plasmon would appear at a value corresponding to a lower ε_p'. This would lead to a shift to lower resonance frequencies (see real part of the dielectric function of gold in Fig. 2.1) for all three particle plasmons. If the form factor changed to higher values, the particle plasmon should shift to higher resonance frequencies. At the same time, the resonance frequency of at least one of the other particle plasmons should shift to lower values due to the condition $L_1 + L_2 + L_3 = 1$. The assumption that ε_p'' is either small or almost constant in the vicinity of the resonance is not necessarily true. This assumption is only used to get a feeling for the behavior of the resonance frequencies when one parameter is changed.

Since the particles in this thesis are surrounded by different materials above and below, the dielectric function ε_m can be averaged by [93, 99]

$$\varepsilon_m \approx \frac{1}{2}(\varepsilon_{air} + \varepsilon_{sub}). \tag{2.14}$$

ε_{air} and ε_{sub} in this equation denote the dielectric functions of air and substrate material, respectively.
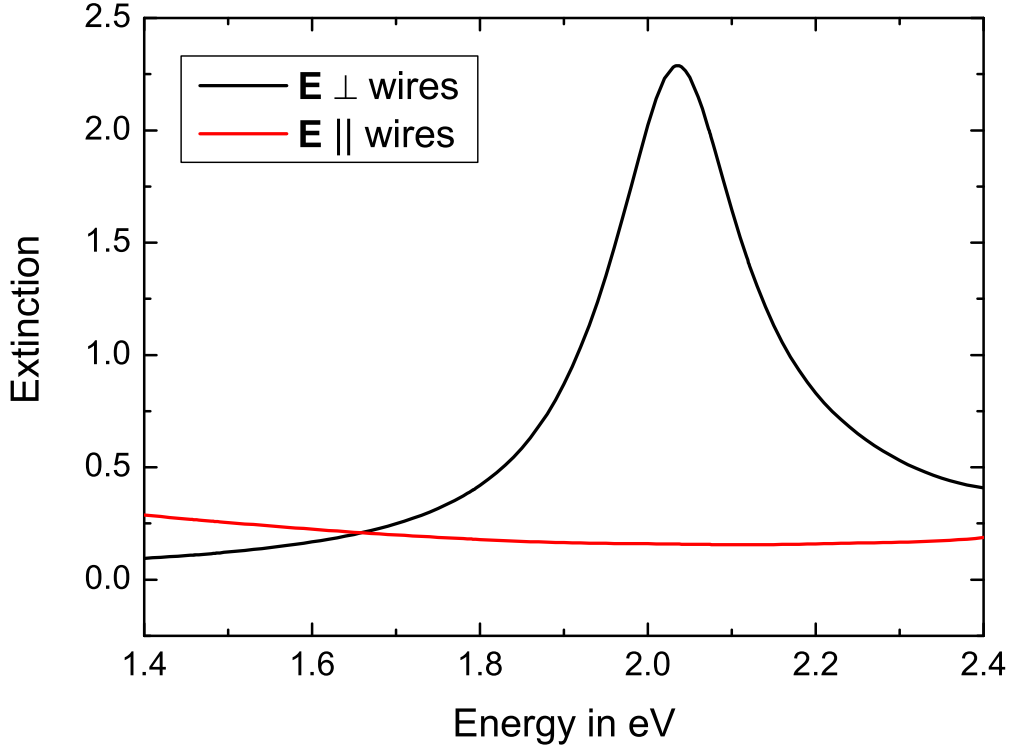

Figure 2.2: Simulated extinction spectra of a gold nanowire array on top of quartz for normally incident light with a polarization perpendicular to the wires (black) as well as parallel to the wires (red). The gold wires of 20 nm height and 100 nm width are periodically arranged with a periodicity of 300 nm.

A special case of structures in this thesis is given by a gold wire array. These wires possess a spatial confinement in only two dimensions, which is in our case the height and the width. The extinction spectra of a gold nanowire array on top of a quartz substrate, which are calculated by using a scattering matrix (S-matrix) formalism, are shown in Fig. 2.2. Each wire has a width of 100 nm and a height of 20 nm, the period of the grating is 300 nm. The special feature can be seen by looking at the two different spectra. When the polarization of the normally incident light has a polarization perpendicular to the wires (black line), a particle plasmon resonance can be excited. Thus, a broad peak is visible in the spectrum. The resonance energy of this particle plasmon is determined by the cross section of the wire, namely the width and the height. When the normally incident light is polarized along the wires, no particle plasmon can be excited. Therefore, only a flat line can be obtained in

the spectrum (red line). This is due to the length of the wire, which is too long for a particle plasmon to be excited. Only a surface plasmon along the wire could be excited with the help of a grating coupler along this direction or a prism. However, this is not treated within this work.

In another part of this thesis, the optical properties of gold disks are investigated. These disks are elliptically shaped cylinders. However, they can be approximated by an ellipsoid. According to the quasi-static approximation presented above, the excited particle plasmons along the three principal axes possess three different resonance energies. Due to the much smaller height compared to the other main axis diameters, the particle plasmon for a polarization parallel to the height is located outside the measured energy range.
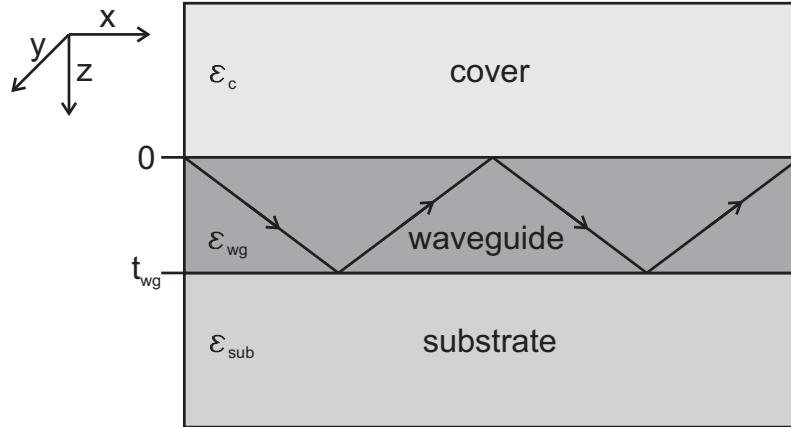
2.1.2 Waveguide modes

Figure 2.3: Schematic view of a waveguide slab of the thickness t_{wg} and the dielectric constant ε_{wg} sandwiched between a cover layer with ε_c and a substrate with ε_{sub}.

A waveguide is a dielectric material with a higher index of refraction than the surrounding medium [100], which in the samples studied here is a system of three layers with the waveguide layer of thickness t_{wg} in the center (Fig. 2.3). The dielectric constants of the cover, the waveguide, and the substrate are given by ε_c, ε_{wg}, and ε_{sub}. Waves can propagate in such a waveguide when t_{wg} is greater than a specific minimum thickness t_{min} [101]. It can be considered that a wave inside the waveguide follows a path from the top surface in x-z direction to the bottom surface, where it is reflected by total internal reflection, and then going back to the top surface, where it is again totally reflected [102] (see Fig. 2.3). For such waves, either the electric field vector **E** or the magnetic field vector **H** is perpendicular to the direction of propagation $\boldsymbol{\beta}_p$, which is called transverse electric (TE) or transverse

magnetic (TM) polarization, respectively. This means that for TE polarization, the $\mathbf{E}$ vector has only a component in y direction ($\mathbf{E} = E_y\mathbf{e}_y$), whereas the $\mathbf{H}$ vector has components in x as well as in z direction ($\mathbf{H} = H_x\mathbf{e}_x + H_z\mathbf{e}_z$). However, for TM polarization the $\mathbf{H}$ vector exhibits a y component and the $\mathbf{E}$ vector one in x and one in z direction ($\mathbf{H} = H_y\mathbf{e}_y$, $\mathbf{E} = E_x\mathbf{e}_x + E_z\mathbf{e}_z$). The waves in the waveguide layer are assumed to be planar, whereas the fields outside are evanescent. Therefore, the field amplitudes can be described by [80, 103, 104]

$$E_{y,\,c} = A_{TE}\,e^{pz}\,e^{i(\beta_p\,x-\omega t)} \qquad\qquad \text{for } z < 0, \qquad (2.15)$$

$$E_{y,\,wg} = (B_{TE}\,e^{ik_zz} + C_{TE}\,e^{-ik_zz})\,e^{i(\beta_p\,x-\omega t)} \qquad \text{for } 0 \leq z \leq t_{wg}, \qquad (2.16)$$

$$E_{y,\,sub} = D_{TE}\,e^{-qz}\,e^{i(\beta_p\,x-\omega t)} \qquad\qquad \text{for } z > t_{wg} \qquad (2.17)$$

for TE polarization and by

$$H_{y,\,c} = A_{TM}\,e^{pz}\,e^{i(\beta_p\,x-\omega t)} \qquad\qquad \text{for } z < 0, \qquad (2.18)$$

$$H_{y,\,wg} = (B_{TM}\,e^{ik_zz} + C_{TM}\,e^{-ik_zz})\,e^{i(\beta_p\,x-\omega t)} \qquad \text{for } 0 \leq z \leq t_{wg}, \qquad (2.19)$$

$$H_{y,\,sub} = D_{TM}\,e^{-qz}\,e^{i(\beta_p\,x-\omega t)} \qquad\qquad \text{for } z > t_{wg} \qquad (2.20)$$

for TM polarization. The corresponding H_x and H_z components for TE polarization as well as E_x and E_z components for TM polarization can be obtained by using Maxwell's equations. In the equations above, p, q, and k_z correspond to the propagation constants in z direction in the different materials. β_p is the propagation constant of the waveguide mode in x-y direction, ω the angular frequency of the light, and t the time. The field amplitudes given in Eqs. $(2.15) - (2.17)$ and Eqs. $(2.18) - (2.20)$ have to fulfill the wave equation [80] leading to

$$p^2 - \beta_p^2 = -k_0^2\varepsilon_c, \qquad (2.21)$$

$$-k_z^2 - \beta_p^2 = -k_0^2\varepsilon_{wg}, \qquad (2.22)$$

$$q^2 - \beta_p^2 = -k_0^2\varepsilon_{sub} \qquad (2.23)$$

with $k_0 = \omega/c$ as the free space wavevector and c the speed of light. At the surfaces of the different layers, the field components E_y and H_x for TE polarization as well as H_y and E_x for TM polarization have to be equal in the different materials. In order to obtain a non-trivial solution for the components A_n, B_n, C_n, and D_n (n = TE or TM), the system of four linear equations for each polarization has to be solved leading to the dispersion relations given by [80, 100, 104]

$$t_{wg}\sqrt{k_0^2\varepsilon_{wg} - \beta_p^2} = \arctan\left(\sqrt{\frac{k_0^2(\varepsilon_{wg} - \varepsilon_c)}{k_0^2\varepsilon_{wg} - \beta_p^2} - 1}\right) +$$

$$\arctan\left(\sqrt{\frac{k_0^2(\varepsilon_{wg} - \varepsilon_{sub})}{k_0^2\varepsilon_{wg} - \beta_p^2} - 1}\right) + m\pi \qquad (2.24)$$

for TE polarization and

$$
\begin{aligned}
t_{wg}\sqrt{k_0^2\varepsilon_{wg} - \beta_p^2} = {} & \arctan\left(\frac{\varepsilon_{wg}}{\varepsilon_c}\sqrt{\frac{k_0^2(\varepsilon_{wg} - \varepsilon_c)}{k_0^2\varepsilon_{wg} - \beta_p^2} - 1}\right) + \\
& \arctan\left(\frac{\varepsilon_{wg}}{\varepsilon_{sub}}\sqrt{\frac{k_0^2(\varepsilon_{wg} - \varepsilon_{sub})}{k_0^2\varepsilon_{wg} - \beta_p^2} - 1}\right) + m\pi
\end{aligned} \tag{2.25}
$$

for TM polarization and the mth waveguide mode. The cover layer and the substrate usually do not consist of the same material. This means that waves in such an asymmetric system cannot be guided below a specific cutoff energy, which is given by [80]

$$
E_{TE,\,cut} = \frac{\hbar c}{t_{wg}\sqrt{\varepsilon_{wg} - \varepsilon_{sub}}}\left(\arctan\left(\sqrt{\frac{\varepsilon_{sub} - \varepsilon_c}{\varepsilon_{wg} - \varepsilon_{sub}}}\right) + m\pi\right) \tag{2.26}
$$

for TE polarization and

$$
E_{TM,\,cut} = \frac{\hbar c}{t_{wg}\sqrt{\varepsilon_{wg} - \varepsilon_{sub}}}\left(\arctan\left(\frac{\varepsilon_{wg}}{\varepsilon_c}\sqrt{\frac{\varepsilon_{sub} - \varepsilon_c}{\varepsilon_{wg} - \varepsilon_{sub}}}\right) + m\pi\right) \tag{2.27}
$$

for TM polarization.

The dispersion curves of Eqs. (2.24) and (2.25) for guided waves in a waveguide layer with a dielectric constant $\varepsilon_{wg} = 3.1684$ and a thickness $t_{wg} = 180\ nm$ are shown as black solid (TE) and red dashed (TM) curves in Fig. 2.4 (a). As a reference, also the light lines of the cover ($\varepsilon_c = 1$) and the substrate ($\varepsilon_{sub} = 2.1904$) are plotted as black dotted and black dash-dotted lines. Due to the fact that the waveguide dispersion curves are always below the light lines of the surrounding media, the guided modes cannot be excited by light impinging from the top or the bottom [80, 101]. Therefore, an additional momentum in the direction of propagation is needed. For the samples in this thesis a grating on top of the waveguide layer is introduced, where the momentum is defined by the reciprocal lattice vector $\mathbf{g}$ with $g = \frac{2\pi}{d}$ and d as the grating period. The incoming light is diffracted at the grating and coupled into the waveguide layer. The waves inside the waveguide are no longer *guided waves* since the grating also allows that the waves are coupled to the photon continua of the surrounding media [105]. Therefore, these waves are called *quasiguided modes* [105]. Due to the periodic arrangement of the grating, the dispersion curves of the guided modes can be folded into the first Brillouin zone with boundaries at $\pm\pi/d$. The dispersion curves of the TE and TM quasiguided modes for a grating with period d = 500 nm are shown in Fig. 2.4 (b). One can see that dispersion curves for the quasiguided modes are always above the substrate light line meaning that quasiguided waveguide modes can be excited.
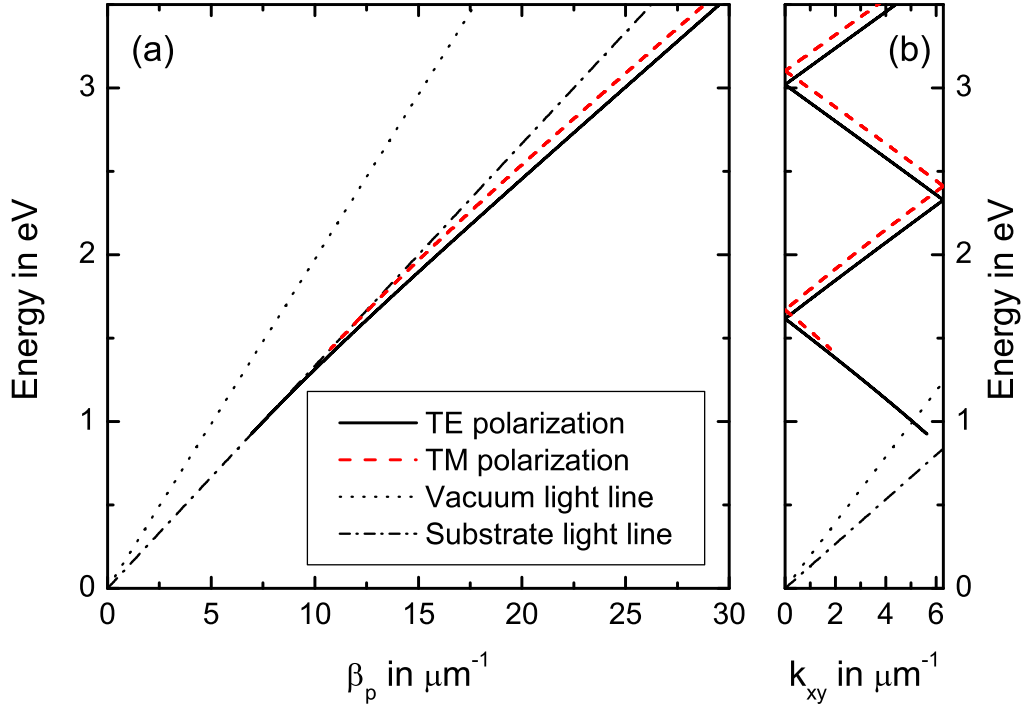
Figure 2.4: Waveguide dispersion for (a) a guided wave and (b) a quasiguided wave with a grating period d = 500 nm. The dielectric constants of the cover, the waveguide, and the substrate are $\varepsilon_c = 1$, $\varepsilon_{wg} = 3.1684$, and $\varepsilon_{sub} = 2.1904$, respectively.

The wave vector of the incident light can also possess a component $\mathbf{k}_{xy}$ parallel to the sample surface leading to the overall propagation constant

$$\boldsymbol{\beta}_p = \mathbf{k}_{xy} + \mathbf{g}. \tag{2.28}$$

$k_{xy} = k_0 \sin(\vartheta)$ is dependent on the angle of incidence ϑ and on the absolute value of the incident wavevector k_0. For normal incidence k_{xy} is equal to zero meaning that the propagation constant in this case is only dependent on $\mathbf{g}$. In Fig. 2.4 (b), the case for normal incidence is given by a vertical line with $k_{xy} = 0$. A straight line with the angle ϑ to the energy axis at $k_{xy} = 0$ would give the k_{xy} values for the corresponding incidence angle ϑ. The excited waveguide mode resonances correspond to the energies when this straight line crosses the dispersion curves. However, this is an empty lattice approximation. Deviations of the dispersion curves in the center of the Brillouin zone and the Brillouin zone edge are present. This is explained in detail in section 2.1.4.

For a 1D photonic crystal, the grating is only modulated in one direction and,

therefore, integer numbers of g have to be added to k_{xy}. However, for a 2D photonic crystal, meaning a modulation in two directions, one needs to consider the vector addition given in Eq. (2.28) [80].
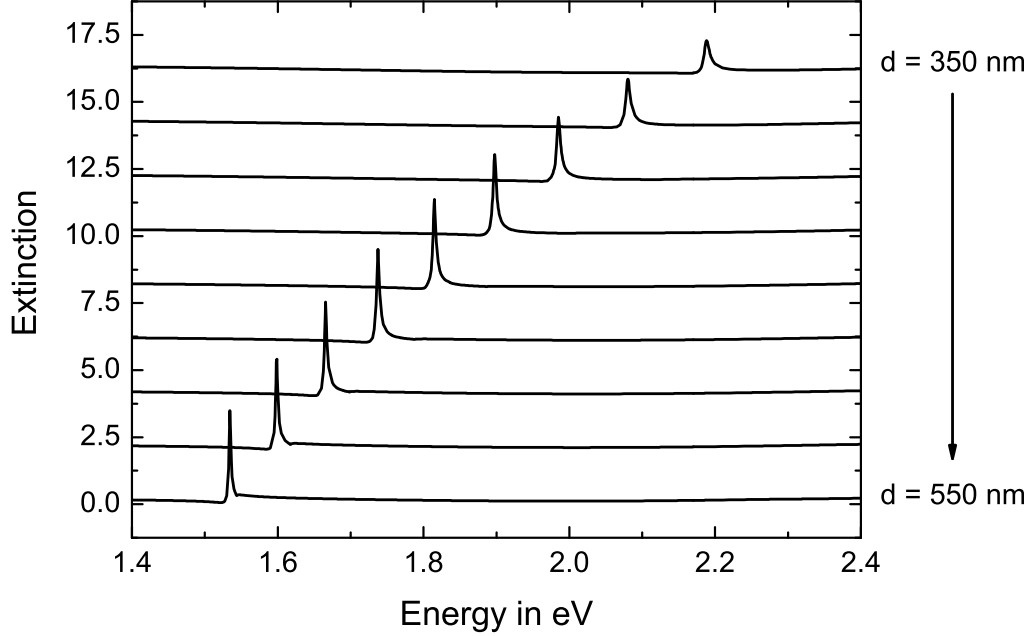

Figure 2.5: Simulated normal incidence spectra of TE polarized quasiguided modes with the grating period varied between 350 nm (top) and 550 nm (bottom) in steps of 25 nm. The spectra are shifted upward for clarity.

The line shape in an absorbance spectrum of such quasiguided modes is that of a Fano resonance and is given by [106]

$$\alpha(E) = A \frac{\left(q + \frac{E - E_0}{\gamma/2}\right)^2}{1 + \left(\frac{E - E_0}{\gamma/2}\right)^2} \tag{2.29}$$

with A as the amplitude, E_0 as the resonance energy, and γ as the natural line width of the resonance. This is due to the interaction between the discrete quasiguided modes and the directly transmitted wave, which is a continuum [31]. The ratio q describes the probability that a discrete state transfers into a continuum. For a 1D photonic crystal and normal incidence, only the symmetric waveguide mode can be excited [107] leading to one sharp Fano resonance in the extinction spectrum. This is shown in Fig. 2.5 for grating periods varying between 350 nm (Fig. 2.5 at the top) and 550 nm (Fig. 2.5 at the bottom). The TE polarized modes in these S-matrix calculated spectra were guided in a 180 nm thick layer of Indium-Tin-Oxide

(ITO) on top of a quartz substrate. One can see that the waveguide mode is shifted to lower energies for larger grating periods. This can be understood by the fact that the Brillouin zone edge is dependent on the grating period as mentioned above. Thus, the dispersion curves are folded differently into the first Brillouin zone for each grating period. Since the Brillouin zone edge is inversely proportional to the grating period, the dispersion curves at the center of the Brillouin zone (corresponding to normal incidence) possess a lower energy for a larger grating period.
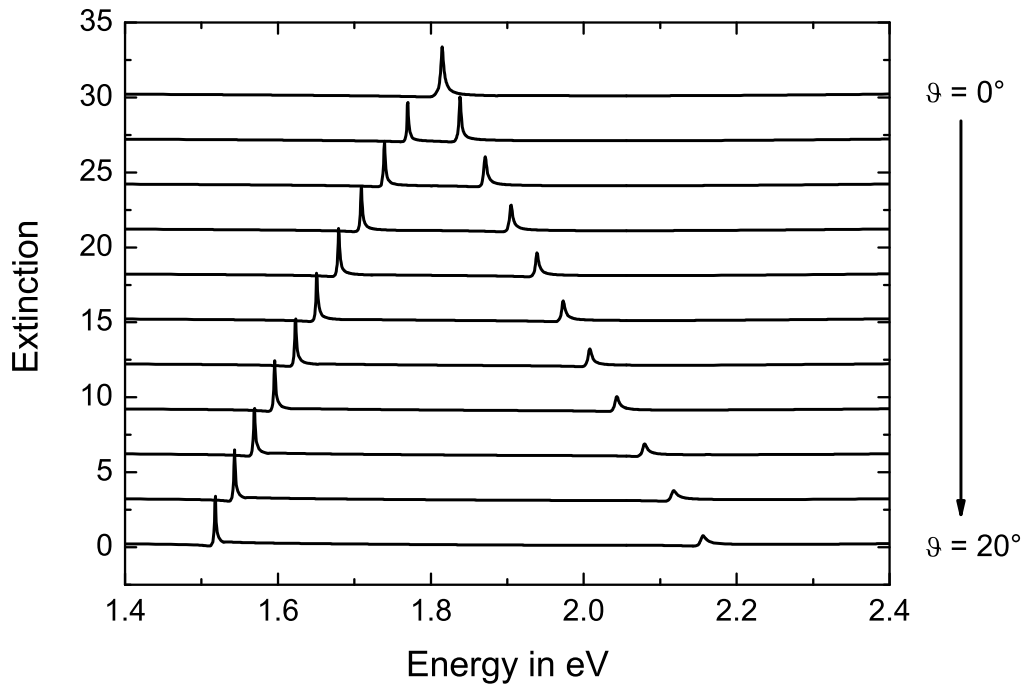
Figure 2.6: Simulated spectra of TE polarized quasiguided modes with the angle of incidence varied between 0° (top) and 20° (bottom) in steps of 2°. The grating period was 450 nm. The spectra are shifted upward for clarity.

However, for an oblique angle of incidence, two resonances are visible in the spectrum corresponding to the propagation constants given in Eq. (2.28) (see Fig. 2.6). The additional peak is due to the antisymmetric waveguide mode that cannot be excited for normal light incidence. The distance between the two peaks is increased for a larger angle of incidence; one resonance is shifted to lower energies, whereas the other resonance is shifted to higher energies (see Fig. 2.6). This can be understood by looking at the dispersion curves in the first Brillouin zone (see Fig. 2.4 (b)). As already explained above, the waveguide mode resonances correspond to the energies when a straight line with angle ϑ to the axis with $k_{xy} = 0$ crosses the dispersion

curves. The dispersion curve is crossed by the straight line twice around the normal incidence energy. For larger angles ϑ, this straight line has a more gentle slope. Thus, the lower energy crossing point is shifted to lower energy values, whereas the higher energy crossing point is shifted to higher energy values leading to an increased energy difference between the two peaks. All spectra in Fig. 2.6 are S-matrix calculations and are shown for a 180 nm thick ITO waveguide layer on top of a quartz substrate and a grating period of 450 nm. For incidence angles close to normal incidence, only one of the peaks is approaching the energy of the peak at normal incidence. However, the other resonance approximates a value $E - \Delta E$, where ΔE is the photonic band gap (not shown). This behavior is due to the interaction between the two waveguide modes close to the center of the first Brillouin zone [104]. A more detailed analysis of the band structure is given in section 2.1.4.

2.1.3   Coupled system

The previous sections covered particle plasmons as well as waveguide modes. However, both kinds of resonances were discussed in absence of the respective other one. In this section, a system is considered, where both resonances are present.

The energy of the particle plasmon is only dependent on the cross section of the metal particle as well as on the dielectric functions of the metal and the surrounding medium, whereas the waveguide mode is dependent on the grating period. This means that a variation of the grating period only shifts the resonance energy of the waveguide mode while that of the particle plasmon stays constant. For simplicity, everything is discussed for 1D metallic photonic crystals. The special feature in this case is that the particle plasmon can only be excited when the polarization of the incident light is perpendicular to the metallic nanowire, which is called TM polarization. However, for TE polarization only the waveguide mode can be excited.

When both resonances are in the same energy range, an interaction between the particle plasmon and the waveguide mode occurs leading to a new quasi-particle, the so-called waveguide-plasmon-polariton [31]. This means that the normal incidence spectrum always shows two peaks with a finite energy difference between the peaks. For small grating periods, the energy of the waveguide mode is higher than that of the particle plasmon. In the spectrum, the broad particle plasmon peak and the sharp waveguide mode are visible (see upper spectra in Fig. 2.7). By increasing the grating period, the energy of the waveguide mode is decreased as already explained for TE polarization. In the region, where both resonances are coupled, two broader peaks are visible; the two branches of the waveguide-plasmon-polariton. By further
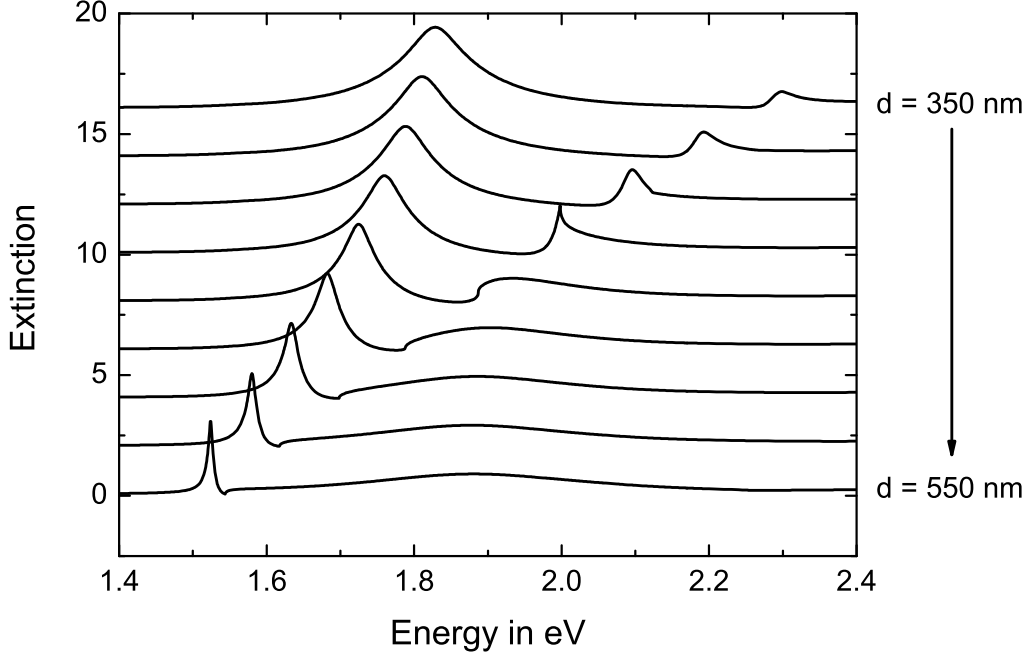
Figure 2.7: Simulated normal incidence spectra of a metallic photonic crystal slab in TM polarization with the grating period of the gold wires varied between 350 nm (top) and 550 nm (bottom) in steps of 25 nm. The spectra are shifted upward for clarity.

increasing the grating period, the two resonances become decoupled again. The sharp waveguide mode is now at the lower energy side of the particle plasmon. The spectra for different grating periods are visible in Fig. 2.7 showing the just described behavior. As above for the TE polarized spectra, the waveguide layer consists of a 180 nm thick ITO layer on top of a quartz substrate. The grating is placed on top of the waveguide layer and consists of gold wires with a thickness of 20 nm and a width of 100 nm. Again, all spectra are S-matrix simulations.

The line shape of such coupled resonances can be described by a coupled oscillator model given by [108]

$$\alpha(E) = A_{Pl} \frac{4\Gamma_{Pl}^2 E^2 \left[E^2 - E_{wg}^2 - (q_{wg}/q_{Pl})E_c^2\right]^2}{\left[(E^2 - E_{Pl}^2)(E^2 - E_{wg}^2) - E_c^4\right]^2 + 4\Gamma_{Pl}^2 E^2 (E^2 - E_{wg}^2)^2} . \qquad (2.30)$$

A_{Pl} in this equation is the amplitude of the plasmon resonance and E_c^2 is the coupling strength between the two oscillators in the energy range E. The spectral half widths, the energies of the individual resonances, and the oscillator strengths of the uncoupled systems are given by Γ_j, E_j, and q_j with $j = wg$ or Pl.

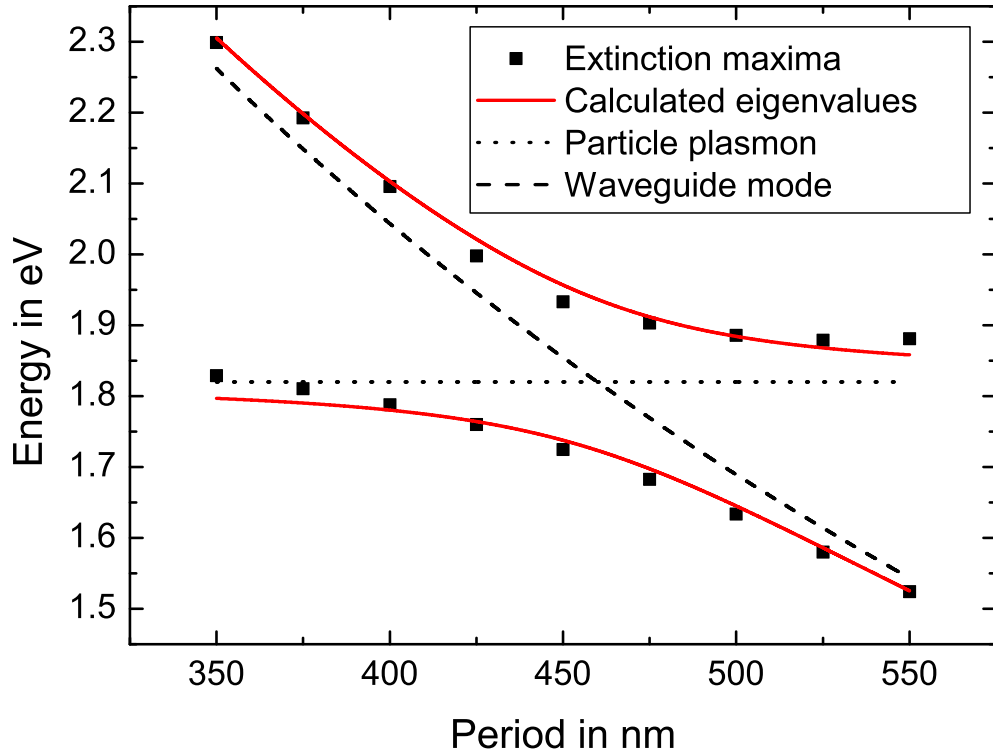Plotting the resonance energies of the two peaks from the spectra in Fig. 2.7 versus

Figure 2.8: Anti-crossing behavior of the extinction maxima (black squares) of Fig. 2.7 as well as the fitted eigenvalues of the Hamiltonian (red solid curves) for $E_{Pl} = 1.82$ eV, $V_2 = 0.075$ eV, and $V_1 = 0.02$ eV. The uncoupled particle plasmon energies (black dotted curve) as well as the uncoupled TM waveguide mode energies (black dashed curve) are plotted as well.

the corresponding grating period visualizes the above described anti-crossing behavior. This is shown as black squares in Fig. 2.8. In this plot it is obvious that the resonance energies from the two polariton branches (black squares) deviate from the energies of the waveguide mode (dashed curve) and the particle plasmon (dotted curve). The deviation of the polariton branches from the energies of the uncoupled resonances is especially large in the region around 450 nm grating period, where the energy of the particle plasmon peak and the energy of the waveguide mode are approximately the same. The polariton curves do not cross each other, but the transitions from the waveguide mode to the particle plasmon (upper black squares) and from the particle plasmon to the waveguide mode (lower black squares) are visible. The minimum distance between the two polariton branches is the so-called polariton splitting ΔE [109], which is dependent on the coupling constant V_2 between the two modes.

Even though only one waveguide mode can be excited for normal incidence due to symmetry reasons, theoretically two waveguide mode resonances exist. These two waveguide modes are coupled together by the halfwidth of the photonic band gap V_1, and each of the waveguide modes is coupled to the particle plasmon via V_2. In order to describe the anti-crossing behavior, the following Hamiltonian has to be used:

$$H = \begin{pmatrix} E_{wg}(d) & V_1 & V_2 \\ V_1 & E_{wg}(d) & V_2 \\ V_2 & V_2 & E_{Pl} \end{pmatrix} \tag{2.31}$$

with $E_{wg}(d)$ as the energy of the waveguide mode dependent on the grating period d and E_{Pl} as the energy of the particle plasmon resonance. Equation (2.31) is based on Eq. (4.10) of Ref. [104]. However, instead of the waveguide mode energies for different incidence angles, the bare waveguide mode energies for different grating periods and normal incidence are used here. By rearranging this Hamiltonian, an effective energy matrix E_{eff} can be obtained given by

$$E_{eff} = \begin{pmatrix} E_{wg}(d) + V_1 & 0 & \sqrt{2}V_2 \\ 0 & E_{wg}(d) - V_1 & 0 \\ \sqrt{2}V_2 & 0 & E_{Pl} \end{pmatrix}. \tag{2.32}$$

It is obvious that the second row is decoupled from the other part of the matrix. Therefore, the second row as well as the second column can be left out leading to the 2×2 energy matrix given by

$$E_{eff} = \begin{pmatrix} E_{wg}(d) + V_1 & \sqrt{2}V_2 \\ \sqrt{2}V_2 & E_{Pl} \end{pmatrix}. \tag{2.33}$$

By calculating the eigenenergies of this energy matrix, the above mentioned anti-crossing behavior can be obtained. These eigenenergies are plotted for a particle plasmon energy $E_{Pl} = 1.82$ eV, a coupling constant $V_2 = 0.075$ eV, and a photonic band gap halfwidth $V_1 = 0.02$ eV as red solid curves in Fig. 2.8. It can be seen that the extinction maxima (black squares) and the eigenenergies (red solid curves) agree very well.

With this approach, a specific coupling constant can be assigned to the anti-crossing behavior of such structures. By varying the coupling constant, the anti-crossing behavior as well as the polariton splitting is changed. For a particle plasmon resonance with $E_{Pl} = 1.82$ eV, a halfwidth of the photonic band gap $V_1 = 0.02$ eV, and TM polarized waveguide modes in a 180 nm thick ITO layer on quartz, the polariton branches for coupling energies of $V_2 = 75$ meV, $V_2 = 50$ meV, and $V_2 = 25$ meV
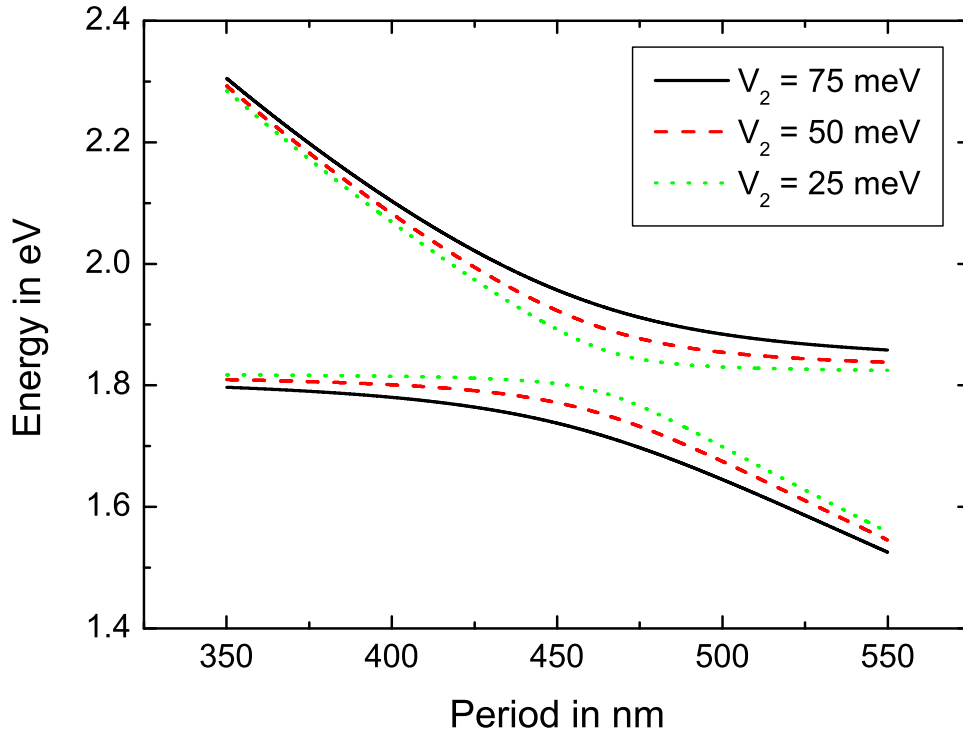
Figure 2.9: Anti-crossing behavior for different coupling constants V_2. The particle plasmon energy was kept constant to a value of $E_{Pl} = 1.82$ eV. The halfwidth of the photonic band gap was $V_1 = 0.02$ eV.

are shown as black solid, red dashed, and green dotted curves in Fig. 2.9, respectively. It can be clearly seen that a larger polariton splitting belongs to a higher coupling constant. Those two parameters are connected via $\Delta E = \sqrt{V_1^2 + 8V_2^2}$. The variation of the coupling constant is especially important in the case of disordered structures as it has been shown in Ref. [101]. Section 4.1.2 of this thesis is making use of this property.

The spectra in Fig. 2.7 were all calculated for normal incidence. For oblique light incidence, however, three resonances instead of two are visible as shown in Fig. 2.10. These three resonances arise due to the excitation of the particle plasmon as well as two waveguide modes. As already explained for TE polarization, the second waveguide mode corresponds to the antisymmetric waveguide mode that cannot be excited for normal incidence. Both waveguide modes are coupled to the particle plasmon forming a waveguide-plasmon-polariton. By increasing the angle of incidence, the energy difference between the two waveguide modes also increases. The lower energy waveguide mode shifts to lower energies, whereas the higher energy
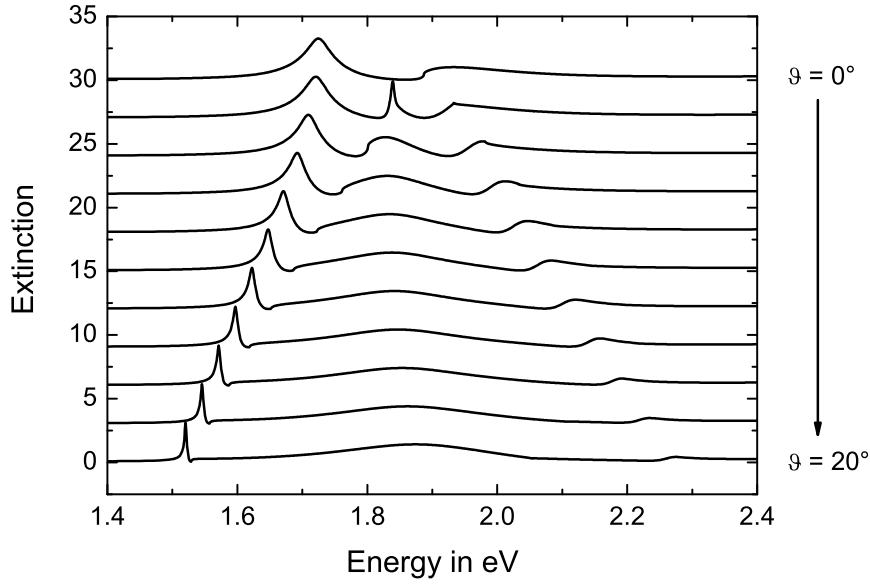
Figure 2.10: Spectra of a metallic photonic crystal slab in TM polarization with the angle of incidence varied between 0° (top) and 20° (bottom) in steps of 2°. The grating period of the gold wires was 450 nm. The spectra are shifted upward for clarity.

waveguide mode shifts to higher energies. This can be obtained in Fig. 2.10 as two dips moving apart from each other. For higher incidence angles especially the waveguide mode on the lower energy side of the particle plasmon is visible as a sharp peak like in the spectra with TE polarization. However, the symmetry of the line shape for the lower energy waveguide mode of the 20° spectrum in TM polarization (see bottom curve in Fig. 2.10) is reversed when compared to the corresponding resonance in TE polarization (see bottom curve in Fig. 2.6). This indicates a remaining influence of the particle plasmon on the TM quasiguided mode.

While the outer two peaks are shifting to lower and higher energies, the resonance energy of the central peak stays approximately constant at a value of about 1.85 eV. The spectral width of the peak in the center increases for larger angles of incidence, whereas the spectral widths of the other two peaks decrease. Again, all S-matrix calculations were performed for an ITO waveguide layer of 180 nm thickness and a grating period of 450 nm.

2.1.4   Band structure

The band structure of a 1D metallic photonic crystal is obtained by plotting the energy position E of the extinction maxima versus the x component of the incident
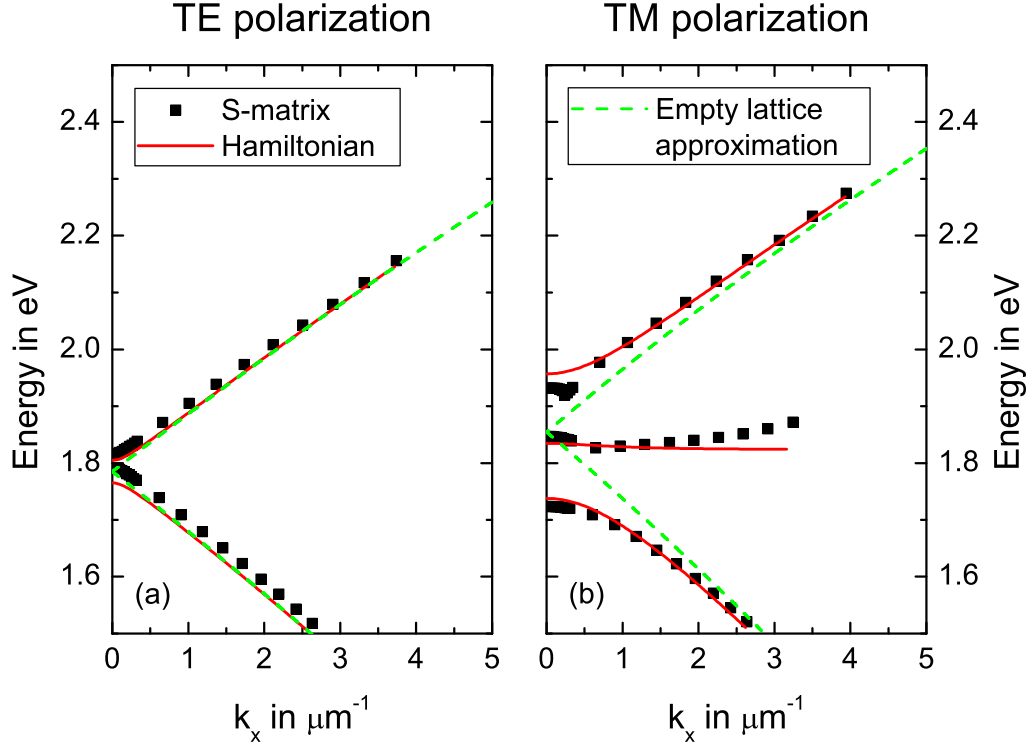
Figure 2.11: Band structure of a 1D metallic photonic crystal in (a) TE polarization and (b) TM polarization. The peak maxima of the extinction spectra calculated with S-matrix (black squares) are compared to the eigenenergies of a Hamiltonian (red solid line) as well as to the empty lattice approximation (green dashed line).

k vector k_x. k_x and the angle of incidence ϑ are connected via $k_x = \frac{E}{\hbar c} \sin(\vartheta)$ with $\hbar$ as the reduced Planck constant and c as the speed of light. The peak maxima of Figs. 2.6 and 2.10 are shown as black squares in Fig. 2.11 (a) and (b), respectively.

A first step to approximate the energy positions of the extinction peak maxima is the use of the above mentioned empty lattice approximation. Due to the periodic arrangement of the metal wires, the TE and TM waveguide dispersion relations (Eqs. (2.24) and (2.25)) can be folded into the first Brillouin zone. The energy positions of the folded dispersion curves at a specific k_x value are the energy positions of the quasiguided modes in a first approximation. These folded TE and TM waveguide dispersion relations are plotted in Fig. 2.11 (a) and (b) as green dashed curves, respectively. The energy positions for larger k_x values are described quite well with this approach. However, close to the center of the first Brillouin zone one can recognize deviations from the empty lattice approximation. In TE polarization, a splitting, which is called a band gap, can be seen for the black squares in Fig. 2.11

(a) around $k_x = 0$. Such a band gap is not visible in the empty lattice approximation (green dashed curves). At the edge of the first Brillouin zone such deviations can also be obtained (not shown). The splitting is due to an interaction between the symmetric and the antisymmetric quasiguided mode, which can be described by the following Hamiltonian:

$$H = \begin{pmatrix} E_{wg}(k_x + \frac{2\pi}{d}) & V_1 \\ V_1 & E_{wg}(k_x - \frac{2\pi}{d}) \end{pmatrix}. \tag{2.34}$$

$E_{wg}(k)$ in this equation are the energies of the bare waveguide modes with momenta $k_x \pm \frac{2\pi}{d}$ and V_1 is the halfwidth of the photonic band gap [104]. The waveguide mode energies can be approximated by $E_{wg}(k_x \pm \frac{2\pi}{d}) \approx E_0 \pm \tilde{c} k_x$ with E_0 as the bare waveguide mode energy and $\tilde{c}$ as the group velocity at $k_x \approx \pm \frac{2\pi}{d}$ [31]. Equation (2.34) is true for TE quasiguided modes as well as for TM quasiguided modes when no particle plasmon can be excited. Due to the fact that the dispersion relations of the TE and the TM waveguide modes are different, also the energy regions of the band gaps are different. Therefore, usually no full band gap, i.e., a band gap independent of the incident polarization [31], exists.

By calculating the eigenvalues of Eq. (2.34), the energy positions including the interaction between the two quasiguided modes can be obtained. This is shown as red solid curves in Fig. 2.11 (a) for $V_1 = 0.02$ eV and TE polarization. The agreement between the energy positions of the peak maxima in the S-matrix calculated extinction spectra (black squares) and the eigenvalues of the Hamiltonian is quite good. However, the eigenvalues of the Hamiltonian are slightly smaller than the energy positions of the peak maxima. This is due to the fact that the peak maxima of Fano resonances are slightly shifted when compared to the energies of the corresponding excited quasiguided modes.

In TM polarization also a particle plasmon with energy E_{Pl} can be excited. Therefore, also the interaction between the quasiguided modes and the particle plasmon has to be considered. This interaction is expressed by the coupling constant V_2. The Hamiltonian describing such a system is given by [31, 104]

$$H = \begin{pmatrix} E_{wg}(k_x + \frac{2\pi}{d}) & V_1 & V_2 \\ V_1 & E_{wg}(k_x - \frac{2\pi}{d}) & V_2 \\ V_2 & V_2 & E_{Pl} \end{pmatrix}. \tag{2.35}$$

Again, the waveguide mode energies can be approximated by the linear function $E_{wg}(k_x \pm \frac{2\pi}{d}) \approx E_0 \pm \tilde{c} k_x$. By using this approximation, Eq. (2.35) can be rearranged,

just like Eq. (2.31), leading to an effective energy matrix [31, 104]

$$E_{eff} = \begin{pmatrix} E_0 + V_1 & \tilde{c}k_x & \sqrt{2}V_2 \\ \tilde{c}k_x & E_0 - V_1 & 0 \\ \sqrt{2}V_2 & 0 & E_{Pl} \end{pmatrix}. \tag{2.36}$$

The eigenenergies of Eq. (2.36) describe now the behavior in the center of the first Brillouin zone. This is plotted as red solid curves in Fig. 2.11 (b) for $E_{Pl} = 1.82$ eV, $V_2 = 0.075$ eV, and $V_1 = 0.02$ eV. It can be seen that the behavior of the resonances in the center of the first Brillouin zone is well described by the eigenenergies of Eq. (2.36).

When more resonances are present in the specific energy range, all of these modes interact with each other. This leads to the following Hamiltonian [101]:

$$H = \begin{pmatrix} E_1 & V_{1,2} & V_{1,3} & V_{1,4} & \cdots \\ V_{2,1} & E_2 & V_{2,3} & V_{2,4} & \cdots \\ V_{3,1} & V_{3,2} & E_3 & V_{3,4} & \cdots \\ \vdots & \vdots & \ddots & \ddots & \ddots \end{pmatrix}, \tag{2.37}$$

where E_i are the resonance energies and $V_{i,j} = V_{j,i}$ are the coupling constants between the ith and the jth resonance. Equation (2.37) is important for 2D metallic photonic crystals, where several waveguide modes as well as a particle plasmon resonance can be excited. Furthermore, this equation can be used for aperiodic structures, where also several waveguide modes can be excited.

2.2 Disordered structures

The study of samples with specific types and degrees of disorder is very interesting. In this thesis two different types of disorder are studied: frozen-phonon disorder and long-range disorder. In frozen-phonon disordered samples the coordinates of the wires fluctuate around the location of a periodic grating. The analog of this is an electronic crystal at different temperatures, where at 0 K all atoms are placed at a specific periodic position. However, a temperature in this crystal being larger than 0 K leads to fluctuations of the atoms around the equilibrium positions [92], which are called phonons [110]. Increasing the temperature leads to bigger deviations from the initial positions. This behavior is studied in the frozen-phonon disordered samples (or uncorrelated disordered samples), where different degrees of disorder correspond to different temperatures. The nth coordinate of the wires is given by [77]

$$x_n = x_0 + nd_0 + \Delta x_n \tag{2.38}$$

with x_0 as the location of the first wire, d_0 as the period of the periodic grating, and Δx_n as the deviation of the nth wire from the location of the periodic wire position. The degree of disorder is given by [77]

$$D[\%] = \frac{FWHM}{d_0} \, 100, \tag{2.39}$$

where $FWHM$ is the full width at half maximum of the distribution function.

The displacements of the nanowires around the periodic wire positions in this thesis are either uniformly distributed (uniform distribution) or normally distributed (Gaussian distribution). The uniform distribution is characterized by having the same probability p for the wire to be placed around the initial wire position. This is described by the function

$$p(x) = \begin{cases} \frac{1}{FWHM} & \text{for } -\frac{FWHM}{2} \leqslant x - x_0 \leqslant \frac{FWHM}{2} \\ 0 & \text{else.} \end{cases} \tag{2.40}$$

In contrast, the probability of a wire with Gaussian distribution to be found at the initial wire position is highest and decreases exponentially for larger displacements. However, also wire positions with deviations of more than FWHM/2 are possible. The probability of a Gaussian distribution is given by

$$p(x) = \frac{1}{\sigma\sqrt{2\pi}} \exp\left\{-\frac{(x-x_0)^2}{2\sigma^2}\right\} \tag{2.41}$$

with the standard deviation σ defined by

$$\sigma = \frac{FWHM}{\sqrt{8\ln(2)}}. \tag{2.42}$$

The other disorder type studied in this thesis, the long-range disorder, corresponds to amorphous materials [111]. It is also called correlated disorder since the deviations of the wire positions of the nth wire is dependent on all $n-1$ previous wires. Therefore, the nth coordinate of the wires is in this case given by [77]

$$x_n = x_0 + nd_0 + \sum_{k=1}^{n} \Delta x_k. \tag{2.43}$$

As for frozen-phonon disorder, the degree of disorder for long-range disorder can be obtained by Eq. (2.39). The distribution functions used for long-range disorder are the same as for frozen-phonon disorder, namely a uniform distribution (Eq. (2.40)) as well as a Gaussian distribution (Eq. (2.41)).

2.3   Fractal structures

Another type of structures studied in this thesis are 1D fractal structures. These structures are self-similar meaning that a similar structural arrangement can be found in different magnification levels [112]. This can be seen by looking at the Cantor sequence. Here, the basic element is

$$LSL$$

with L being a long distance between two wires and S a short distance. When we assume the distance of two neighboring wires to be either L_0 as a long distance or S_0 as a short distance and the first basic element to be $L_0 S_0 L_0$, then the second basic element consists of $L_1 = L_0 S_0 L_0$ and $S_1 = S_0 S_0 S_0$ leading to

$$\underbrace{L_0 S_0 L_0}_{L_1} \ \underbrace{S_0 S_0 S_0}_{S_1} \ \underbrace{L_0 S_0 L_0}_{L_1}.$$

This procedure can be continued to the Nth basic element $L_{N-1} \ S_{N-1} \ L_{N-1}$ with $L_{N-1} = L_{N-2} S_{N-2} L_{N-2}$ and $S_{N-1} = S_{N-2} S_{N-2} S_{N-2}$. It can be seen that one basic element consists of several smaller basic elements.

A Cantor sequence can be generated by using an *initiator* and a *generator* [113]. The initiator for the Cantor set is a line with the length L_i and the generator is the shape applied to the initiator, namely the division into the sequence LSL. This generator is applied N times to the corresponding initiator. The whole construction rule can be written as follows. The generator consists of G parts numbered from 0 to $G-1$, where a subset $\mathbf{C} \subset \{0, 1, ..., G-1\}$ is exchanged. The whole procedure is repeated N times leading to a structure that can be written as $(G, \mathbf{C}, N)$ [114]. A Cantor set can be written as $(3, \{1\}, N)$ when the generator consists of the sequence LSL. This means that subset number 1 of the $G = 3$ elements with length L is replaced by a block of length S. The fractal dimensionality D_F of such a Cantor set is given by [115]

$$D_F = \frac{\ln\left(\frac{G+1}{2}\right)}{\ln\left(G\right)}. \tag{2.44}$$

Two different kinds of Cantor-like sets are used in this thesis, namely the $(3, \{1\}, 5)$ set and the $(6, \{1, 4\}, 3)$ set. Whereas the LSL sequence is applied 5 times for the first Cantor set, the sequence $LSLLSL$ for the latter one is repeated 3 times. The latter Cantor set is also called *Cantor-6 sequence* in this thesis.

2.4   Quasicrystals

In 1982, Shechtman discovered a material with 10-fold symmetry in the diffraction pattern after he has rapidly chilled the molten mixture of aluminum and manganese [116]. The first paper about this discovery was then published in 1984 [44]. In 2011, he won the Nobel Prize in chemistry for the discovery of quasicrystals [57].

Quasicrystals are neither periodic nor random. Quasicrystals show long-range orientational order as well as long-range *quasiperiodic* translational order [117]. However, no *periodic* translational order can be observed. Although they do not show any lattice periodicity, such structures exhibit a Fourier transform with essentially discrete Fourier peaks [118] which is due to the long-range order. In this thesis 1D as well as 2D quasicrystals are considered. Therefore, the following sections cover the different methods in order to construct 1D as well as 2D quasicrystals.

2.4.1   1D quasicrystals

The Fibonacci sequence is an example of a 1D quasicrystal. There are several methods in order to obtain this sequence. The first method explained here is making use of deflation rules. The starting point is a block L, and in the following steps each L is replaced by LS and each S by L [119]. This leads to the following steps:

$$
\begin{array}{ccccc}
L & & & & \\
L & & S & & \\
L & & S & L & \\
L & S & L & L & S \\
\vdots & & & &
\end{array}
$$

Repeating these steps a large number of times leads to the whole Fibonacci sequence. As above for the fractal structures, the L is used for a long distance between two wires and the S for a short distance between two wires. In the real Fibonacci sequence the definition

$$L = \tau S \tag{2.45}$$

is used with τ as the golden ratio [117]

$$\tau = \frac{1 + \sqrt{5}}{2}. \tag{2.46}$$

However, in this thesis the ratio between the long distance L and the short distance S is not the golden ratio, but an arbitrary number higher than 1. Therefore, the sequences used here are only Fibonacci-like sequences.
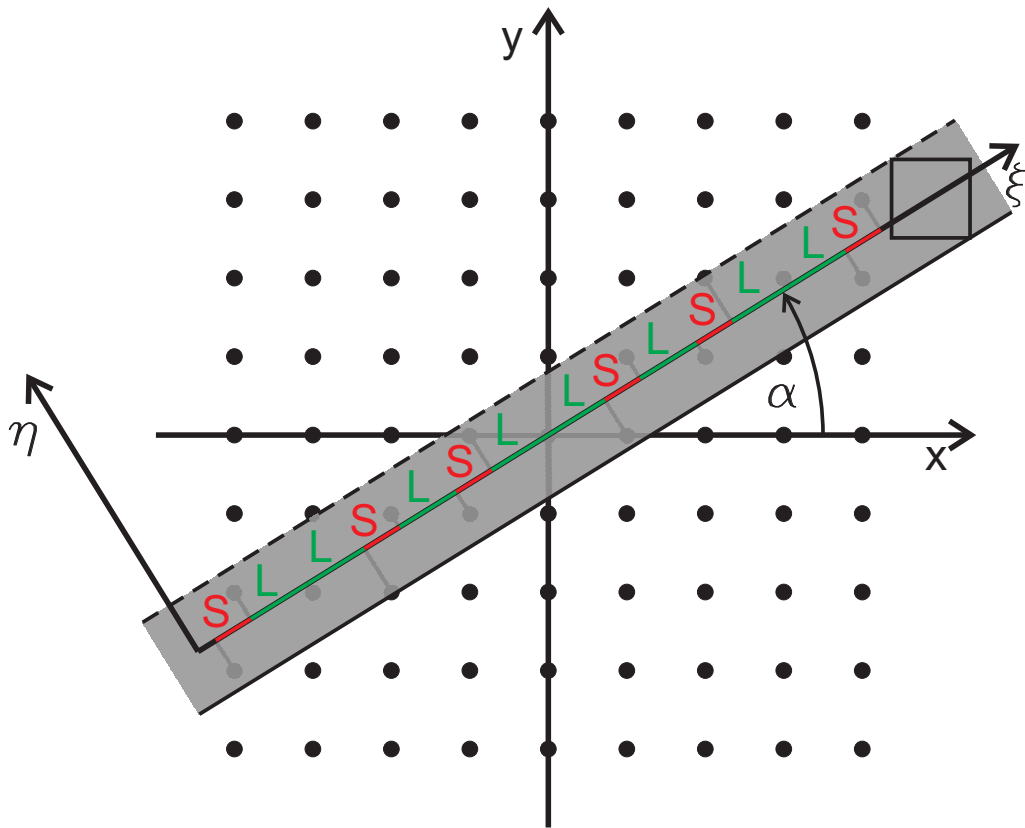
Figure 2.12: The vertices within the shaded area are projected on ξ. When the angle α between the x axis and the ξ axis is irrational, a 1D quasiperiodic string is obtained.

Another possibility to obtain the Fibonacci sequence is the projection method [120, 121], also called the cut-and-project method [122]. In this method a subset of a periodic grid in a higher dimension is used and the vertices are projected onto a plane in a lower dimension [122]. This is displayed in Fig. 2.12 for the Fibonacci chain. A square periodic grid in 2 dimensions parallel to the x and the y direction is used with a periodicity of a, since two different lengths are wanted in the Fibonacci chain. The line ξ is called the physical space and is rotated by an angle α with respect to the x axis of the periodic grid. The line η orthogonal to ξ is called the perpendicular space. By translating the unit square along the physical space ξ, a strip is formed (see shaded area in Fig. 2.12). All vertices within this strip are projected onto ξ. Whereas the vertices on the solid line belong to the strip, the vertices on the dashed line are not part of the strip. When $\cot\alpha$ is an irrational number, then the obtained sequence is quasiperiodic [123], which is for the Fibonacci sequence $\cot\alpha = \tau$. The sequence on ξ is then the Fibonacci chain, which is visualized by the green (long, L) as well as the red (short, S) segments. The long (short) segments are due to the projection of two neighboring vertices connected along the x axis (y axis) leading to $L = a\cos\alpha$ ($S = a\sin\alpha$).

Quasicrystals can be approximated by the so-called approximants [123]. In order to construct such approximants, the angle $\widetilde{\alpha}$ between the x axis of the periodic grid and the direction of the projection strip is not equal to the angle α. The expression $\cot \widetilde{\alpha}$ is given by a rational number approximating τ [123]. This produces a periodic sequence of the above mentioned distances L and S. The closer $\widetilde{\alpha}$ approximates α, the larger the unit cell is and the closer this sequence is to the real quasiperiodic one.

In order to obtain the Fibonacci-like sequences mentioned above, a rectangular periodic grid with period a in x direction and period b in y direction is used in the higher dimensional space. The angle α_{new} between ξ and the x axis of the periodic grid is then given by $\tan \alpha_{new} = \frac{b}{a\tau}$. Here, a as well as b are the crucial parameters for the lengths S and L. The short and long distances in the Fibonacci-like sequence are now given by $S = b \sin \alpha_{new}$ and $L = a \cos \alpha_{new}$. This construction method assures that the short and long segments are placed exactly in the order of the Fibonacci sequence. However, the ratio between the segments L and S in this sequence is not equal to τ.

A similar method to the *projection method* is the *cut formalism*. The difference between these two methods is that the projection method projects all vertices in the shaded area (see Fig. 2.12) onto ξ, whereas the cut formalism uses line segments perpendicular to ξ that are placed on every vertex of the higher dimensional periodic grid (see Fig. 2.13). The length h of a line segment is obtained by projecting the unit square in the perpendicular space η. These line segments represent atomic surfaces in the periodic lattice [123]. Due to the finite length of the line segments, only some intersect the physical space. At each of the intersections an atom is placed. For an irrational slope of the physical space, a quasiperiodic sequence is obtained. The slope for the Fibonacci sequence is given by $\alpha = \arctan\left(\frac{1}{\tau}\right)$.

The cut formalism is also a good method to obtain the Fourier transform of the quasiperiodic chain [123]. The periodic grid including the atomic surfaces on every vertex has to be Fourier-transformed. The periodic grid in real space is also a periodic grid in reciprocal space, whereas the atomic surfaces, i.e. a rectangular function, correspond to sinc functions in reciprocal space (see Fig. 2.14). The sinc function is given by

$$\mathrm{sinc}\left(\frac{k_\eta h}{2\pi}\right) = \frac{\sin\left(\frac{k_\eta h}{2}\right)}{\frac{k_\eta h}{2}}. \tag{2.47}$$

The intensity of the sinc function at the intersections is equal to the intensity of the Fourier-transformed quasiperiodic lattice in physical space. Due to the fact that the sinc function has values not equal to zero even for large distances from the
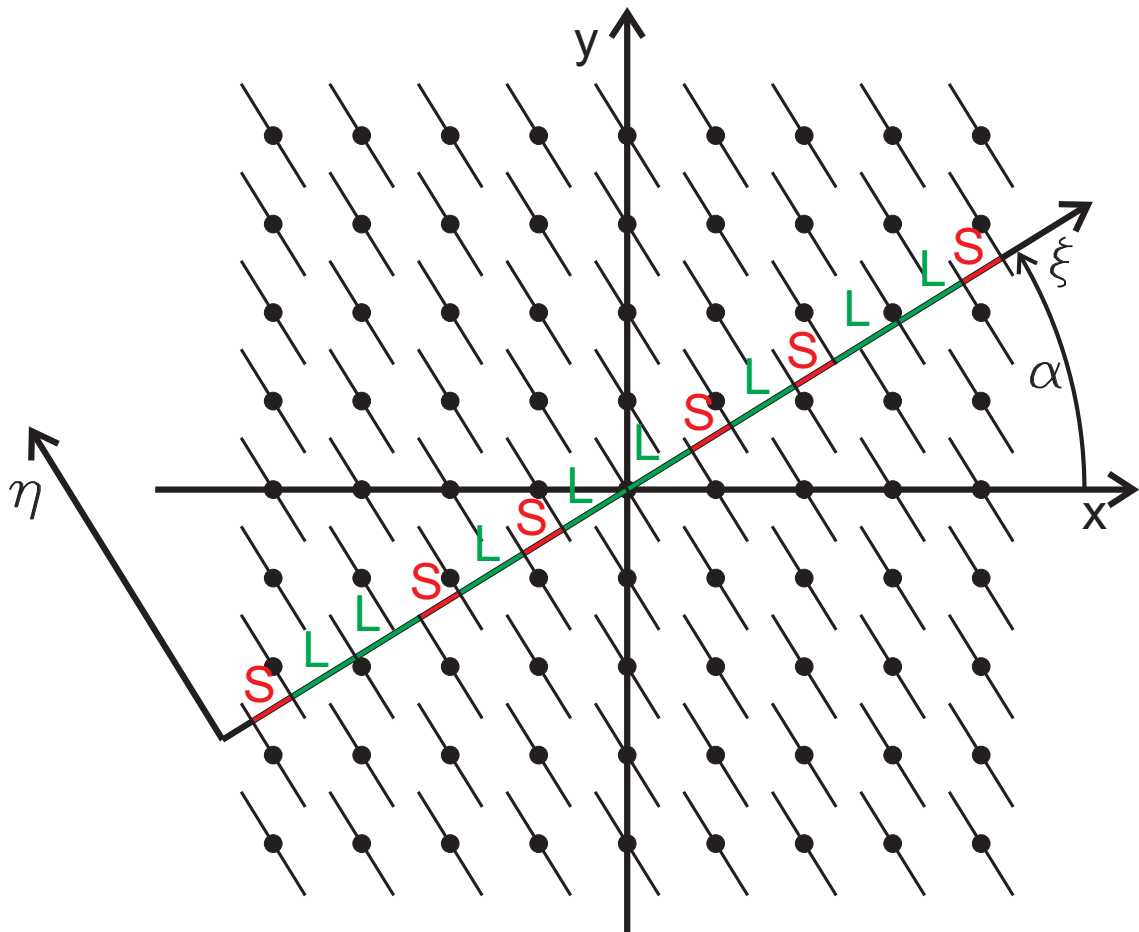
Figure 2.13: The line segments intersecting the physical space ξ cut the physical space into small segments of lengths L and S. When the angle α between the x axis and the ξ axis is irrational, a 1D quasiperiodic string is obtained.

center, *all* vertices of the periodic grid have a contribution to the Fourier transform. This leads to a Fourier transform with a dense set of Fourier peaks [124]. However, the Fourier peaks are more or less pronounced. Therefore, one can see essentially discrete Fourier peaks.

2.4.2   2D quasicrystals

The corresponding quasicrystal to the Fibonacci chain in 2D is the Penrose tiling. It is also possible to use matching rules in order to obtain this lattice [125]. Therefore, two different rhombi are used; a skinny rhombus with interior angles of 36° and 144° and a fat rhombus with interior angles of 72° and 108°. The matching rules are making use of decorated tiles (see red rhombi in Fig. 2.15), where only two tiles are allowed to share one side when both the number and the direction of the arrows correspond to each other. In that way it is possible to obtain the whole Penrose
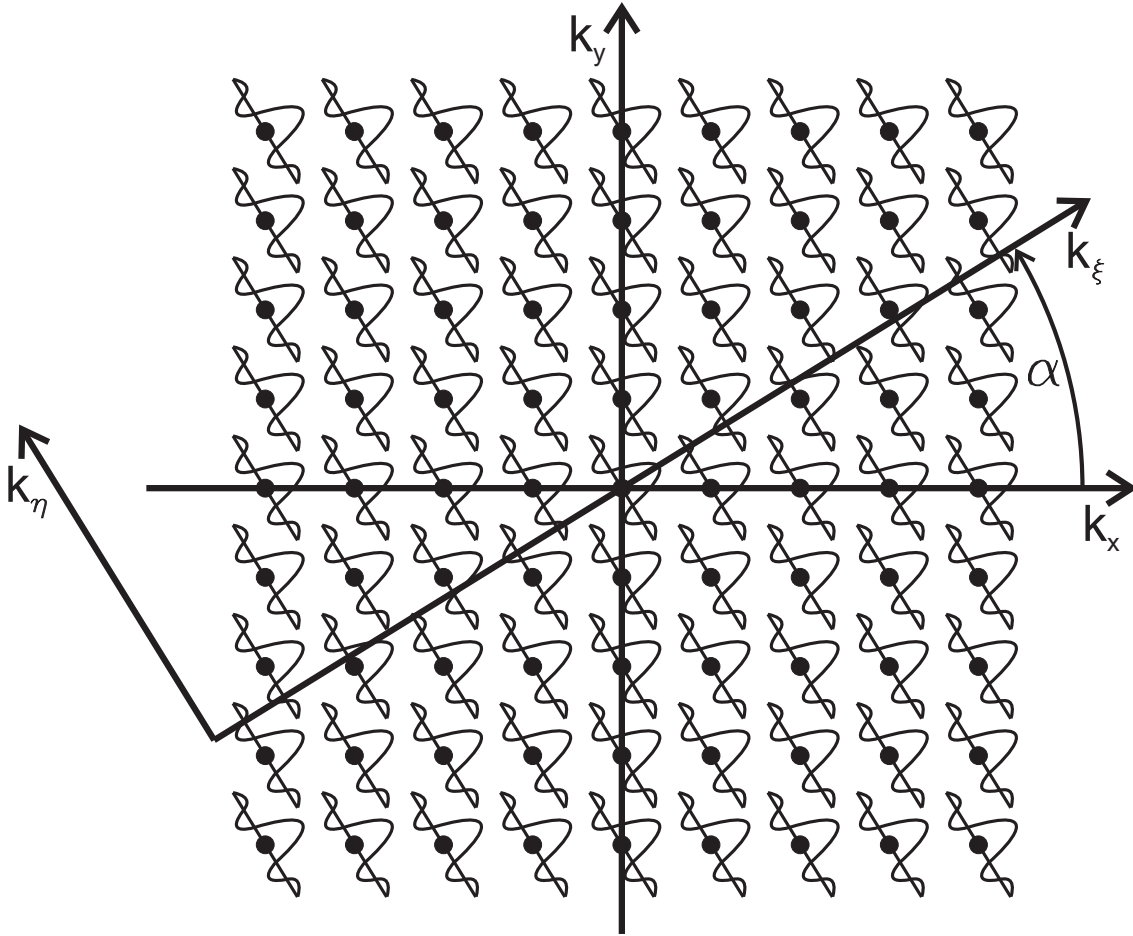
Figure 2.14: Fourier transform of the periodic grid and the atomic surfaces. The intensity of the sinc function at the intersections leads to the Fourier transform of the quasiperiodic lattice in physical space.

tiling (see Fig. 2.15).

Another possibility to obtain the Penrose tiling is using the pentagrid method [125–127]. Each one of the five grids consists of a periodic arrangement of parallel lines. The individual grids are rotated by an angle of $72°$ with respect to the previous grid. The parallel lines in each grid are perpendicular to one of the five directions of a star vector with [119]

$$\mathbf{e}_n = \begin{pmatrix} \cos\left(\frac{2\pi n}{5}\right) \\ \sin\left(\frac{2\pi n}{5}\right) \end{pmatrix} \tag{2.48}$$

and n as an integer value between 0 and 4. The length of $\mathbf{e}_n$ also determines the distance between two parallel lines of the nth grid. The five star vectors are the projections of the five basis vectors from a five-dimensional periodic hypercubic lattice into the two-dimensional physical space [128]. Therefore, a vector with the dimension 5x1 can be used to describe the position of each vertex. The five components
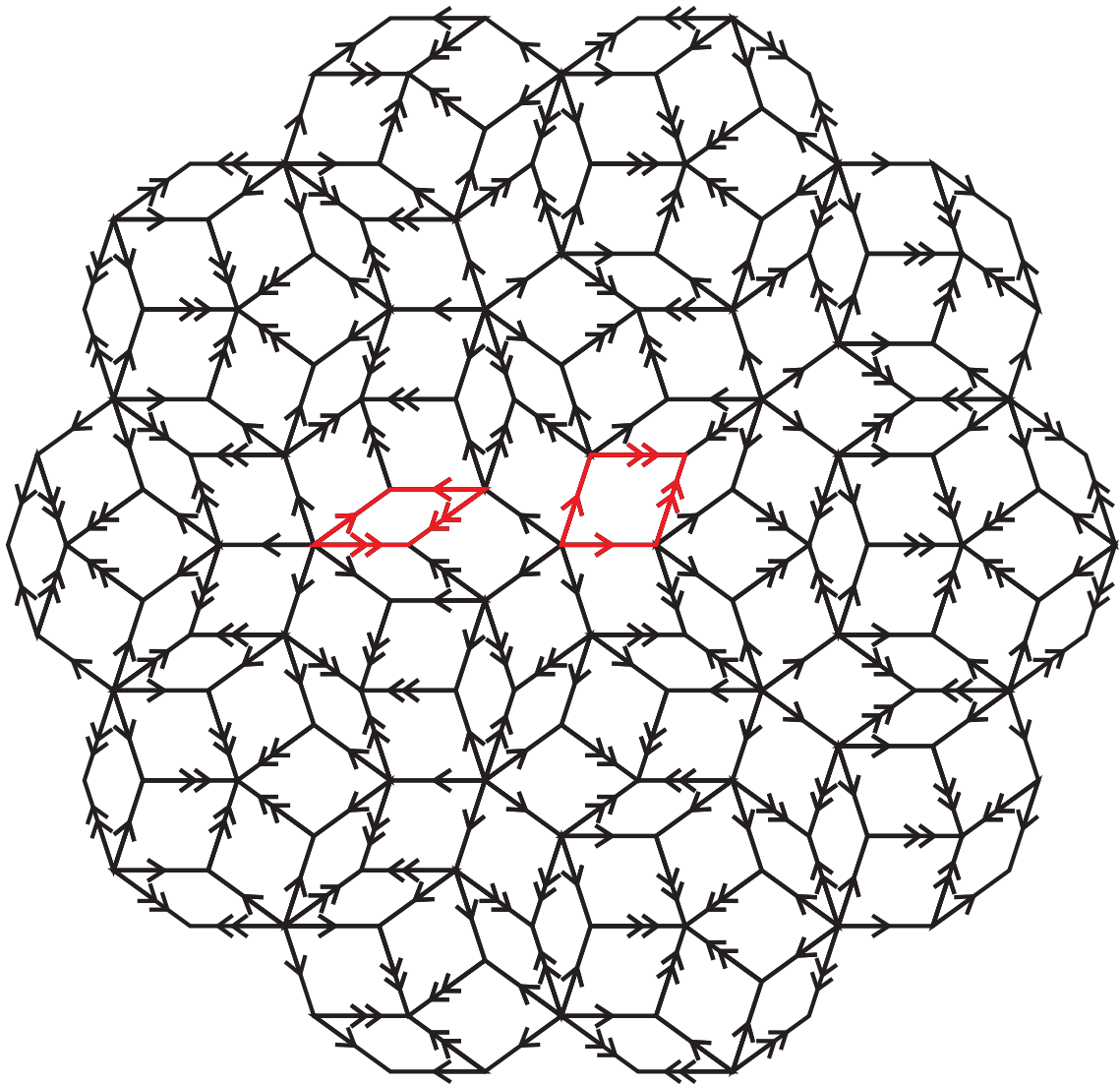
Figure 2.15: Penrose tiling obtained by using decorated fat and skinny rhombi. A fat and a skinny rhombus are shown in red with the different arrows used for the matching rules.

in this vector correspond to one of the five star vectors since all vertices in the five-dimensional space are described by the five basis vectors.

Each line of the grids is numbered from $-\infty$ to $+\infty$ and the nth grid is shifted by the value γ_n in direction $\mathbf{e}_n$. In order to obtain the Penrose tiling given in Fig. 2.15, the condition $\sum_{n=0}^{4} \gamma_n = 0$ has to be fulfilled [119, 125]. In a regular grid there should be only two grid lines intersecting with each other [125].

Such a pentagrid is shown in Fig. 2.16, where the different grids are colored differently. The corresponding star vectors are also shown. The area between two lines of one grid belongs to the line with the lower number. To the areas between the grid lines of all grids (see brown shaded area in Fig. 2.16) five numbers are
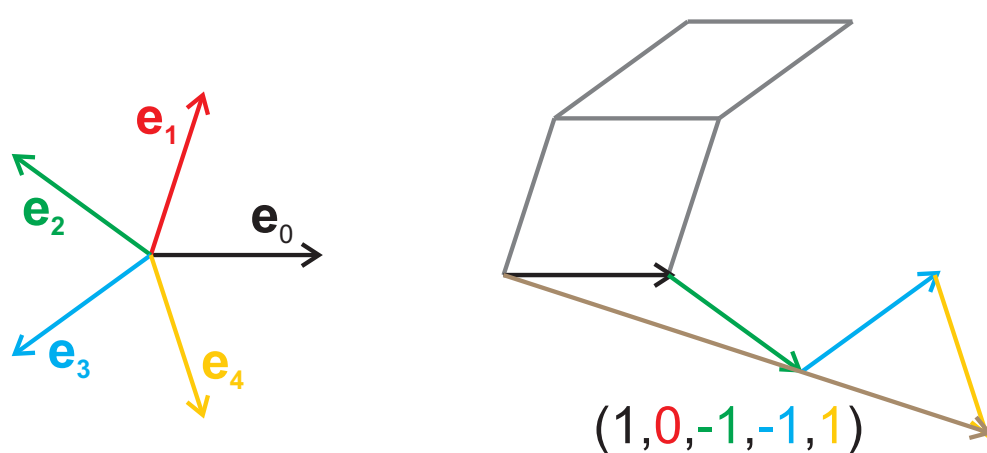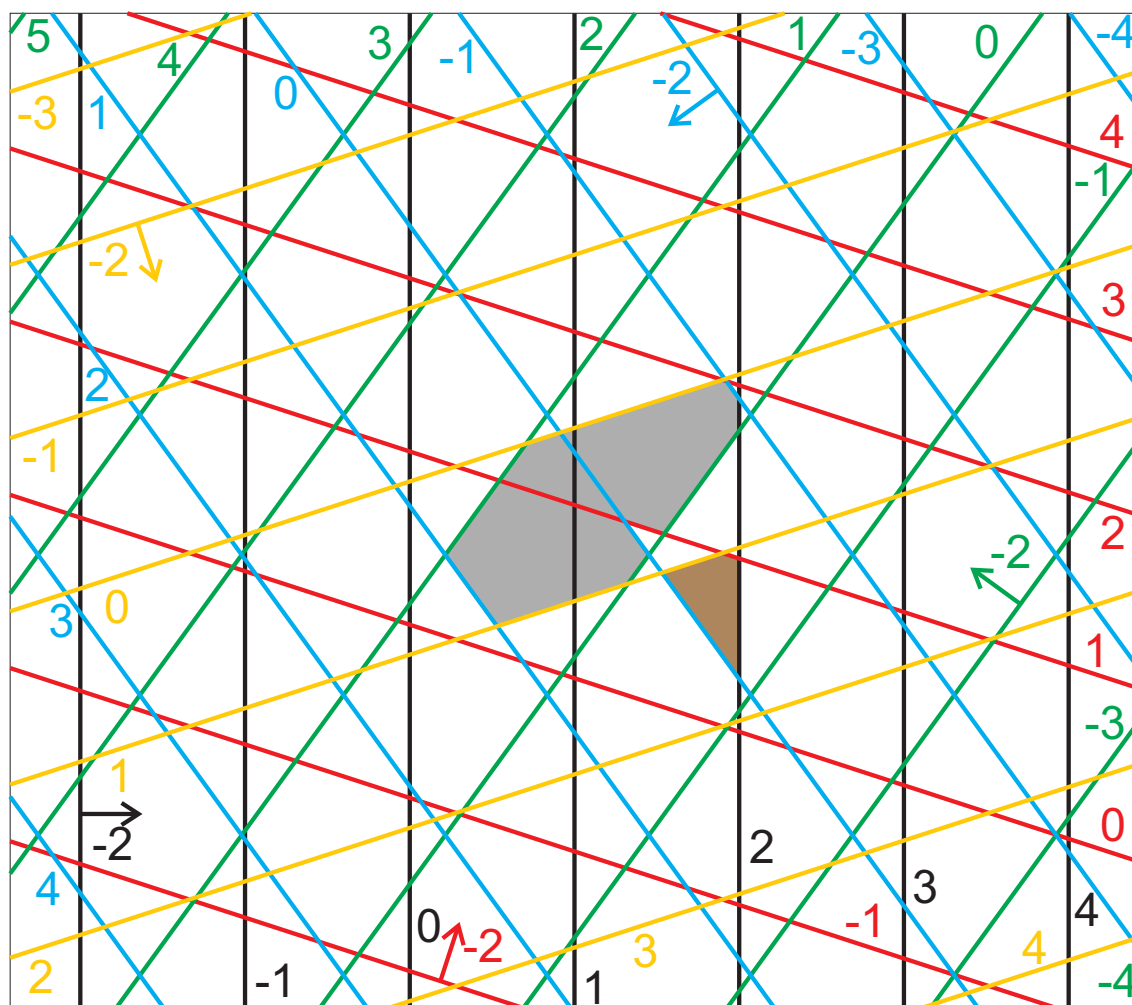
Figure 2.16: The five grids of the pentagrid method are displayed in different colors. Two lines of the nth grid are separated by the vector $\mathbf{e}_n$. The corresponding five star vectors, a fat and a skinny rhombus, as well as the vector to one specific vertex are shown at the bottom.

assigned; each number belonging to one grid. As an example, the shaded area has the numbers 1, 0, -1, -1, and 1. In order to obtain the coordinate of one vertex, a vector addition has to be performed by using the directions $\mathbf{e}_n$ of the star vectors and multiplying these with the specific number from the corresponding area. This vector addition for the shaded area is also shown in Fig. 2.16. The gray shaded areas in Fig. 2.16 correspond to the vertices of a fat and a thin rhombus, which can be seen at the bottom of this figure. By taking all areas into account, the Penrose tiling is obtained.

As already mentioned above, the five star vectors $\mathbf{e}_n$ are the projections of the basic vectors from a five-dimensional hyperspace into physical space. However, these basic vectors can also be projected into the perpendicular space. This perpendicular space is three-dimensional and can be divided into a two-dimensional as well as a one-dimensional space. By projecting the basic vectors of the five-dimensional space into the two-dimensional part of the perpendicular space, another five star vectors are obtained. This time, the rotation between two neighboring star vectors is 144° instead of the 72° in physical space [128]. This can be expressed by the five directions

$$\mathbf{e}_n^{\perp} = \begin{pmatrix} \cos\left(\frac{4\pi n}{5}\right) \\ \sin\left(\frac{4\pi n}{5}\right) \end{pmatrix} \tag{2.49}$$

with n as the corresponding integer value between 0 and 4. The basic vectors $\mathbf{k}_n$ in the five-dimensional hyperspace with

$$\mathbf{k}_0 = \begin{pmatrix} 1 \\ 0 \\ 0 \\ 0 \\ 0 \end{pmatrix}, \mathbf{k}_1 = \begin{pmatrix} 0 \\ 1 \\ 0 \\ 0 \\ 0 \end{pmatrix}, \mathbf{k}_2 = \begin{pmatrix} 0 \\ 0 \\ 1 \\ 0 \\ 0 \end{pmatrix}, \mathbf{k}_3 = \begin{pmatrix} 0 \\ 0 \\ 0 \\ 1 \\ 0 \end{pmatrix}, \mathbf{k}_4 = \begin{pmatrix} 0 \\ 0 \\ 0 \\ 0 \\ 1 \end{pmatrix}$$

are projected into physical space as well as into perpendicular space and form the star vectors in Eqs. (2.48) and (2.49). The projection $\mathbf{p}_n$ of the basic vectors $\mathbf{k}_n$ is given by

$$\mathbf{p}_n = \mathbf{M} \cdot \mathbf{k}_n = \begin{pmatrix} \mathbf{e}_n \\ \mathbf{e}_n^{\perp} \\ x_{5n} \end{pmatrix} \tag{2.50}$$

with $\mathbf{M}$ being the projection matrix. Since two different projection vectors are orthogonal to each other, each coordinate x_{5n} has to be equal to $1/\sqrt{2}$. This leads

to the projection matrix

$$
\mathbf{M} = \begin{pmatrix}
1 & \cos\left(\frac{2\pi}{5}\right) & \cos\left(\frac{4\pi}{5}\right) & \cos\left(\frac{6\pi}{5}\right) & \cos\left(\frac{8\pi}{5}\right) \\
0 & \sin\left(\frac{2\pi}{5}\right) & \sin\left(\frac{4\pi}{5}\right) & \sin\left(\frac{6\pi}{5}\right) & \sin\left(\frac{8\pi}{5}\right) \\
1 & \cos\left(\frac{4\pi}{5}\right) & \cos\left(\frac{8\pi}{5}\right) & \cos\left(\frac{2\pi}{5}\right) & \cos\left(\frac{6\pi}{5}\right) \\
0 & \sin\left(\frac{4\pi}{5}\right) & \sin\left(\frac{8\pi}{5}\right) & \sin\left(\frac{2\pi}{5}\right) & \sin\left(\frac{6\pi}{5}\right) \\
1/\sqrt{2} & 1/\sqrt{2} & 1/\sqrt{2} & 1/\sqrt{2} & 1/\sqrt{2}
\end{pmatrix} \tag{2.51}
$$

$$
= \begin{pmatrix}
1 & 1/(2\tau) & -\tau/2 & -\tau/2 & 1/(2\tau) \\
0 & \tau\sqrt{3-\tau}/2 & \sqrt{3-\tau}/2 & -\sqrt{3-\tau}/2 & -\tau\sqrt{3-\tau}/2 \\
1 & -\tau/2 & 1/(2\tau) & 1/(2\tau) & -\tau/2 \\
0 & \sqrt{3-\tau}/2 & -\tau\sqrt{3-\tau}/2 & \tau\sqrt{3-\tau}/2 & -\sqrt{3-\tau}/2 \\
1/\sqrt{2} & 1/\sqrt{2} & 1/\sqrt{2} & 1/\sqrt{2} & 1/\sqrt{2}
\end{pmatrix},
$$

which is also given in Ref. [129]. In order to obtain the whole Penrose tiling, a subset of the vertices in the five-dimensional hyperspace is projected into physical space. This subset is obtained by projecting all vertices into perpendicular space. Only those vertices whose projections in perpendicular space lie within a specific *acceptance domain* are allowed to be projected into physical space [129].

By approximating the golden mean τ in perpendicular space, i.e. the last three rows of $\mathbf{M}$, by a rational number, the 2D approximant structures are obtained. The fact that τ is not approximated in physical space, i.e. the first two rows of $\mathbf{M}$, keeps the size and the shape of the fat and skinny rhombi constant [129].

2.5   Theoretical model for 1D structures

A theoretical model for disordered 1D metallic photonic crystals has been introduced by D. Nau [78, 101]. This model is described in the following and then expanded for 2D metallic photonic crystals for normal and oblique light incidence in sections 5.3 and 5.6, respectively.

In a 1D metallic photonic crystal, gold nanowires are placed on top of a waveguide layer with the modulation in x direction of the sample (see Fig. 2.17). The location of the nanowires can be described by setting a Dirac delta function at each wire coordinate x_n

$$
f(x) = \sum_n \delta(x - x_n). \tag{2.52}
$$

For disordered structures, x_n is given by Eqs. (2.38) or (2.43). This function is
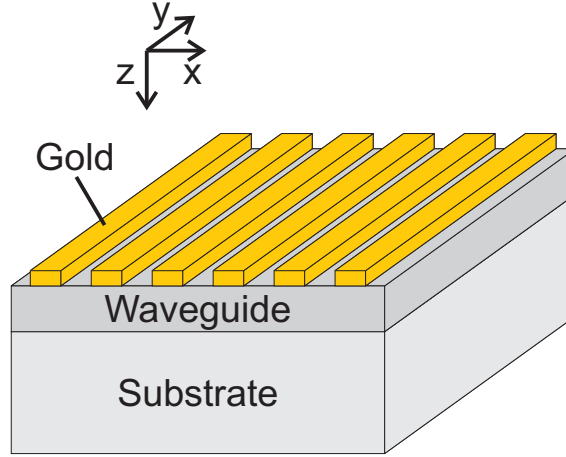
Figure 2.17: Structure design of a 1D metallic photonic crystal on top of a waveguide layer.

Fourier-transformed leading to

$$F(k_x) = \sum_n \int_{-\infty}^{\infty} \delta(x - x_n) \exp(-ik_x x) \, dx = \sum_n \exp(-ik_x x_n). \qquad (2.53)$$

The main steps of the simulation model are illustrated in Fig. 2.18. The Fourier transform of the spatial arrangement calculated with Eq. (2.53) is used for the relevant propagation constants (see Fig. 2.18 (a)). The propagation constants k_j of the Fourier peaks with amplitudes A_j are transferred to the corresponding energies E_j by using the TE and TM waveguide dispersion relations (Eqs. (2.24) and (2.25)), which is indicated for three Fourier peaks in Fig. 2.18 (b). By using the Fano formula given in Eq. (2.29), the TE extinction spectrum in the specific energy range can be calculated (Fig. 2.18 (c)). Since several resonances might be present in a spectrum, Eq. (2.29) has to be slightly modified by using the sum over all Fano resonances [78, 101]

$$\alpha(E) = \sum_j A_j \frac{\left(q + \frac{E_j - E_0}{\gamma/2}\right)^2}{1 + \left(\frac{E_j - E_0}{\gamma/2}\right)^2}. \qquad (2.54)$$

Equation (2.54) describes the TE polarized spectra quite well (see Ref. [78]). However, in TM polarization also the particle plasmon is present in the spectra. As already explained above, the waveguide mode and the particle plasmon are coupled to each other when they are in the same energy range. Therefore, the dispersion relation for the waveguide-plasmon-polariton (eigenenergies of Eq. (2.33)) is different when compared to the uncoupled TM waveguide dispersion relation (Eq. (2.25)). This means that the energies of the waveguide-plasmon-polariton are shifted in
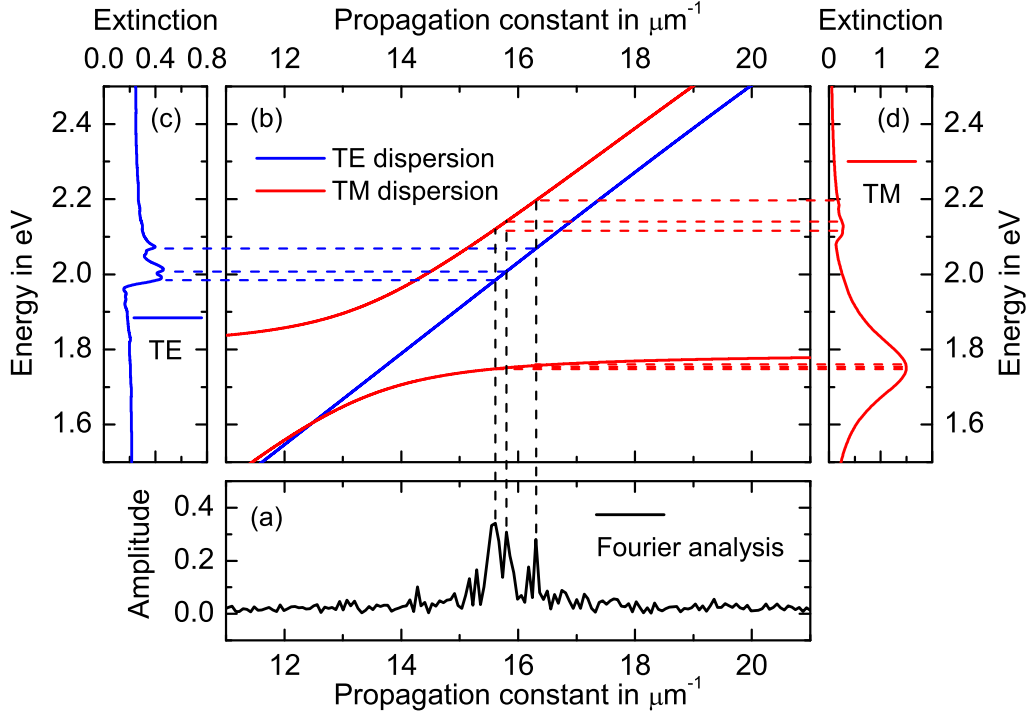
Figure 2.18: (a) Fourier transform of the desired structure for the relevant propagation constants. (b) The TE (blue) and TM (red) dispersion relations connect the propagations constants to the corresponding energies. (c) Extinction spectrum in TE polarization with peak amplitudes of the waveguide modes given by the corresponding Fourier peak amplitudes. (d) Extinction spectrum in TM polarization with peak amplitudes of the waveguide modes given by the corresponding Fourier peak amplitudes.

comparison to the plain waveguide mode energies. The extinction spectra in TM polarization can be obtained by using Eq. (2.30). However, for several quasiguided modes, the sum over all coupled oscillators has to be used leading to

$$\alpha(E) = \sum_j A_{j,Pl} \frac{4\Gamma_{Pl}^2 E^2 \left[E^2 - E_{j,wg}^2 - (q_{wg}/q_{Pl})E_c^2\right]^2}{\left[(E^2 - E_{Pl}^2)(E^2 - E_{j,wg}^2) - E_c^4\right]^2 + 4\Gamma_{Pl}^2 E^2 (E^2 - E_{j,wg}^2)^2} \ . \quad (2.55)$$

The calculated spectrum of such a coupled system is shown in Fig. 2.18 (d).

The model described here is used for 1D quasiperiodic and disordered metallic photonic crystals. However, it has to be expanded for 2D metallic photonic crystals. This is done in sections 5.3 and 5.6 for normal and oblique light incidence as already mentioned above.

Chapter 3

Experimental considerations

3.1 Sample fabrication

The samples in this thesis consist of a Silicon dioxide SiO_2 substrate and a waveguide layer on top. The waveguide layer is either a 180 nm thick layer of Hafnium dioxide (HfO_2) or a 180 nm thick layer of Indium-Tin-Oxide (ITO). In order to pattern the sample, two layers of Polymethylmethacrylate (PMMA) are spin coated on the waveguide layer (Fig. 3.1 (b)) after the sample was cleaned in an ultrasonic bath of acetone (Fig. 3.1 (a)). The molecular weight of the lower PMMA layer is usually 200 K with a concentration of 3.5% in chlorobenzene, whereas the molecular weight of the upper PMMA layer is 950 K with a concentration of 1.5%. The lower PMMA layer is more sensitive to electrons than the upper one leading to an undercut of the exposed areas. The photoresist is then exposed by using electron-beam lithography in order to structure the sample with the desired geometry (Fig. 3.1 (c)). The samples with an ITO layer are directly exposed after the spin coating of the photoresist since the ITO layer is conductive. Therefore, it minimizes charging effects. However, the HfO_2 layer is not conductive. In order to minimize charging effects for this material, a thin layer of Chromium (Cr) has to be evaporated on top of the PMMA layers. After exposure, the sample is developed in a mixture with one part of methyl isobutyl ketone (MIBK) and three parts of propanol (Fig. 3.1 (d)), where the exposed areas of the PMMA are removed. The undercut is clearly visible in Fig. 3.1 (d). Before developing the HfO_2 samples, the Cr layer has to be etched away by using a chrome etch solution. The next step in the sample fabrication is the use of an oxygen plasma in order to remove small fractions of PMMA remaining on the structured areas (Fig. 3.1 (e)). Then, the desired thickness of gold is evaporated (Fig. 3.1 (f)), and, finally, a lift-off process is used to remove the PMMA mask (Fig. 3.1 (g)). The solution
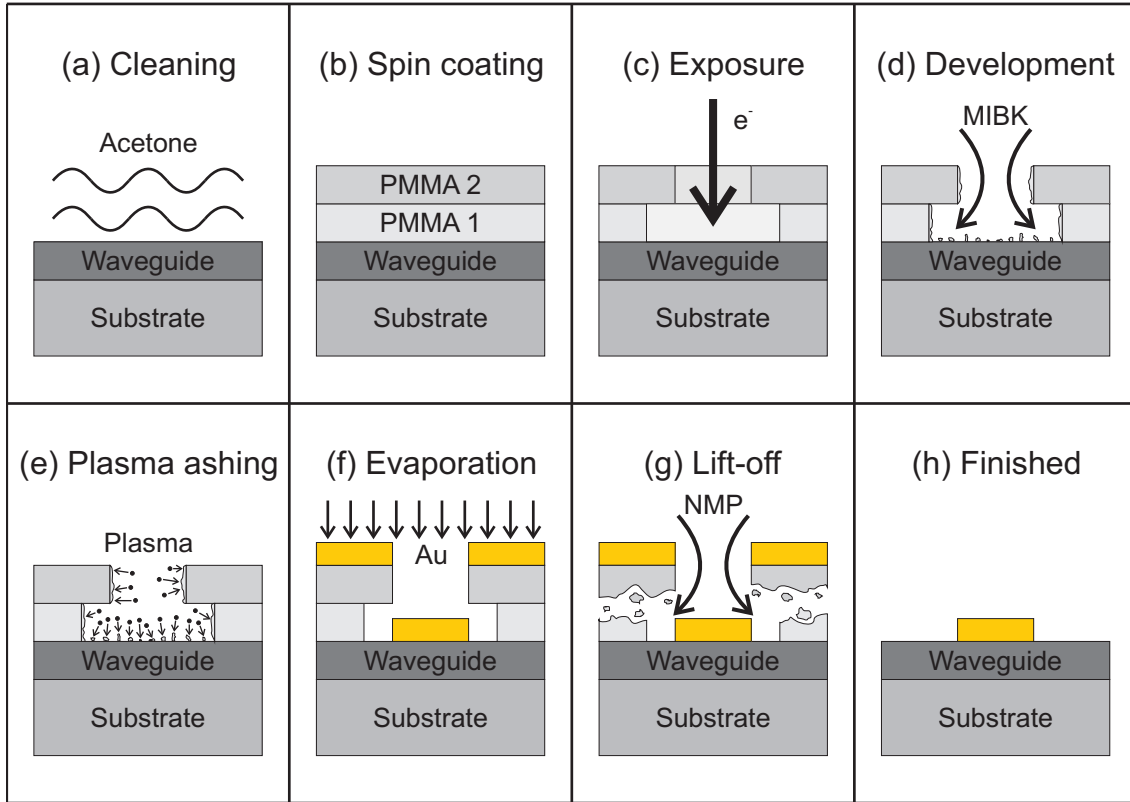
Figure 3.1: Schematic overview of the sample fabrication process. (a) Cleaning of the sample, (b) spin coating of the double layer photoresist, (c) electron-beam exposure, (d) developing the sample, (e) plasma ashing, (f) evaporation of gold, (g) finished structure.

for the lift-off process is the commercially available N-Methyl-2-pyrrolidone (NMP). After lift-off, the desired pattern is left on the waveguide layer (Fig. 3.1 (h)). The structured areas usually have a size of about 100 μm $\times$ 100 μm.

3.2   Experimental setup

The fabricated samples are measured in a white light transmission setup. The schematic view of the setup is shown in Fig. 3.2. As white light source serves a halogen lamp that is collimated by lens L1. In order to produce a point source, lenses L2 and L3 with pinhole P1 in the focal point are used. The polarizer is mounted on a rotation stage so that the linearly polarized light behind the polarizer is variable in its x-y direction. The objective L4 (Zeiss, A-Plan, 10$\times$ magnification, numerical aperture = 0.25) focuses the light on the sample that is mounted on a rotation stage in order to be able to vary the angle of incidence on the sample. In order to assure a focal point diameter of approximately 100 μm, pinhole P2 with a diameter of 600 μm is inserted in front of the objective. The beam behind the sample is recollimated
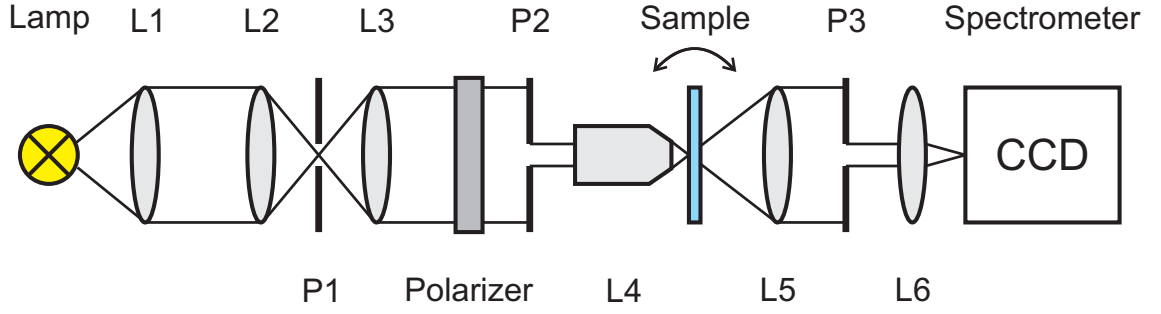
Figure 3.2: Experimental white light transmission setup.

by lens L5 and, finally, focused by lens L6 on the spectrometer. In order to reduce the aperture angle of the light from the sample to 0.2°, pinhole P3 with a diameter of 100 μm is used [130]. Lens L6 can be replaced by a cylindrical lens so that the whole CCD-chip (CCD: charge-coupled device) from the camera attached to the spectrometer can be read out with the wavelength information in the columns of the chip and the different angles of incidence in the rows of the chip. This cylindrical lens was used for the measurements in section 4.1.3, where the band structure of the different metallic photonic crystals can be observed.

In the spectrometer a grating with 150 lines/mm is used in order to split up the incident light into the different spectral components. The CCD camera of the spectrometer is cooled by liquid nitrogen and it is read out by a LabView program for measuring the extinction spectra. First, the background I_b is measured, which is subtracted from the reference spectrum I_r (spectrum through the substrate and the waveguide layer) as well as from the spectrum through the structure I_f. The measured extinction spectrum is defined by the negative logarithm of the transmission T and is calculated by

$$Ext = -\ln(T) = -\ln\left(\frac{I_f - I_b}{I_r - I_b}\right). \tag{3.1}$$

CHAPTER 4

1D PLASMONIC STRUCTURES

4.1 Disordered structures

D. Nau studied in his PhD thesis [101] the optical properties of disordered metallic photonic crystals. Two different disorder types (frozen-phonon and long-range disorder) were analyzed, each of them for two different distribution functions (Uniform and Gaussian distribution). Additionally, the behavior of the coupling strength V_2 in dependence on the disorder amount for each disorder type and each distribution function was calculated (see Fig. 4.1, taken from [101]). However, this behavior was not experimentally confirmed. Therefore, several samples were fabricated in order to confirm the predicted behavior.
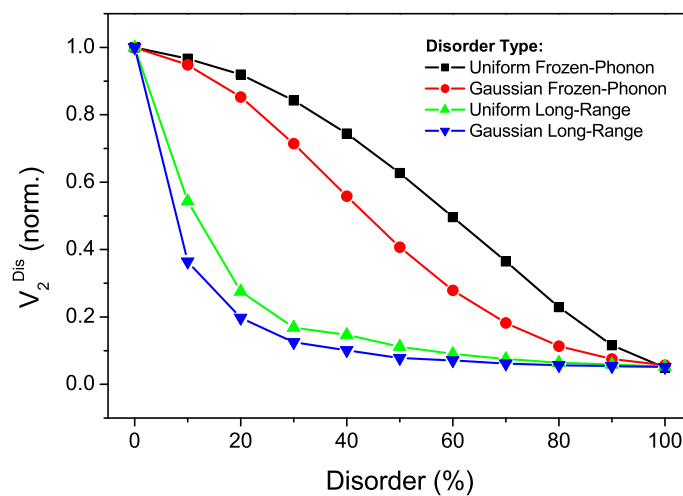
Figure 4.1: Normalized calculated coupling strength V_2^{Dis} as a function of disorder for different disorder types. Taken from [101].

4.1.1　Sample designs

Figure 4.2: Arrangement of the different arrays on a sample with disorder. The average grating period was varied between 400 nm and 475 nm and the disorder amount was changed between 0% and 80%.

Four different samples were fabricated by using electron-beam-lithography, whose fabrication method is described in section 3.1. These four samples are attributed to different disorder types and different distribution functions, namely *uniform frozen-phonon disorder*, *uniform long-range disorder*, *Gaussian frozen-phonon disorder*, and *Gaussian long-range disorder*. The different disorder types and distributions are described in section 2.2. Each one of the samples consists of 20 different $100\,\mu$m $\times$ $100\,\mu$m-large arrays, which is shown in Fig. 4.2. The period of the perfectly ordered grating structure d_0 is changed between 400 nm and 475 nm in steps of 25 nm, whereas the degree of disorder is increased from 0% to 80% in steps of 20%. The gold wires have a width of 100 nm and a height of 20 nm. They are placed on top of an Indium-Tin-Oxide (ITO) layer with a thickness of 180 nm.

4.1.2　Normal incidence extinction spectra

The extinction spectra of the above mentioned structures were measured for normal light incidence. Figure 4.3 shows these spectra for *uniform frozen-phonon disorder* with an average grating period of (a) 400 nm, (b) 425 nm, (c) 450 nm, and (d) 475 nm. The TM polarized spectra are shown as black curves and the TE polarized spectra as red curves in each panel. The spectra with different degrees of disorder are shifted upward with the spectra of 0% disorder at the top and those of 80% disorder at the bottom. In TE polarization (red curves), only the waveguide mode can be excited. One can see that the energy of the waveguide mode changes to lower energies for an increasing grating period (see spectra with 0% disorder in Fig.

Figure 4.3: Extinction spectra of samples with uniform frozen-phonon disorder for normal light incidence in TM (black lines) and TE (red lines) polarization. The average grating period d_0 is (a) 400 nm, (b) 425 nm, (c) 450 nm, and (d) 475 nm. The disorder amount in each panel is changed between 0% (top) and 80% (bottom). The different spectra are shifted upward for clarity in each panel.

4.3 (a) − (d)), which is expected from theory (see section 2.1.2). The amplitude of the resonance peak is decreased for larger uniform frozen-phonon disorder, which is visible for all average grating periods. For a disorder amount of 80%, the quasiguided mode is almost vanished. Due to the fact that no additional Fourier components arise around $k = \frac{2\pi}{d_0}$ for this disorder type, the optical properties are only characterized by a reduction in amplitude but not with a broadening of the peak [101]. In TM polarization, the particle plasmon can be additionally excited leading to a more (see Fig. 4.3 (c) or (d)) or less (see Fig. 4.3 (a)) coupled system between waveguide mode and particle plasmon. In all perfectly ordered structures the upper and lower polariton branches are visible [31]. By increasing the grating period from 400 nm to 475 nm, only the energy of the waveguide mode is shifted. This means that the energy difference between the two maxima is changed as expected, which can be observed in Fig. 4.3 (compare to Fig. 2.7). It can be seen in Fig. 4.3 that the contrast of the two peaks in the spectra and the dip in-between is reduced

for an increased disorder amount. This can be obtained for all average grating periods. This corresponds to the reduced peak amplitude as observable in the TE polarized spectra. Again, no additional peaks are visible corresponding to Fourier components only at $k = \frac{2\pi}{d_0}$. For a disorder amount of 80%, almost only one broad peak is recognizable. Additionally, a broadening of the lower energy peak can be observed in Fig. 4.3 (a) and (b). These findings agree with the optical properties of such structures studied in Ref. [101]. Furthermore, an increase in extinction of the minimum between the two resonances is found, which is either due to the reduced amplitude (Fig. 4.3 (c) and (d)) or to the broadened particle plasmon resonance (Fig. 4.3 (a) and (b)). Depending on d_0, the amplitude reduction affects either one of the peaks (higher energy peak in Fig. 4.3 (a)) or the dip in-between (Fig. 4.3 (d)). However, the general behavior that the amplitude of the waveguide mode reduces for an increasing uniform frozen-phonon disorder and that no additional peaks arise is independent of the individual grating period.
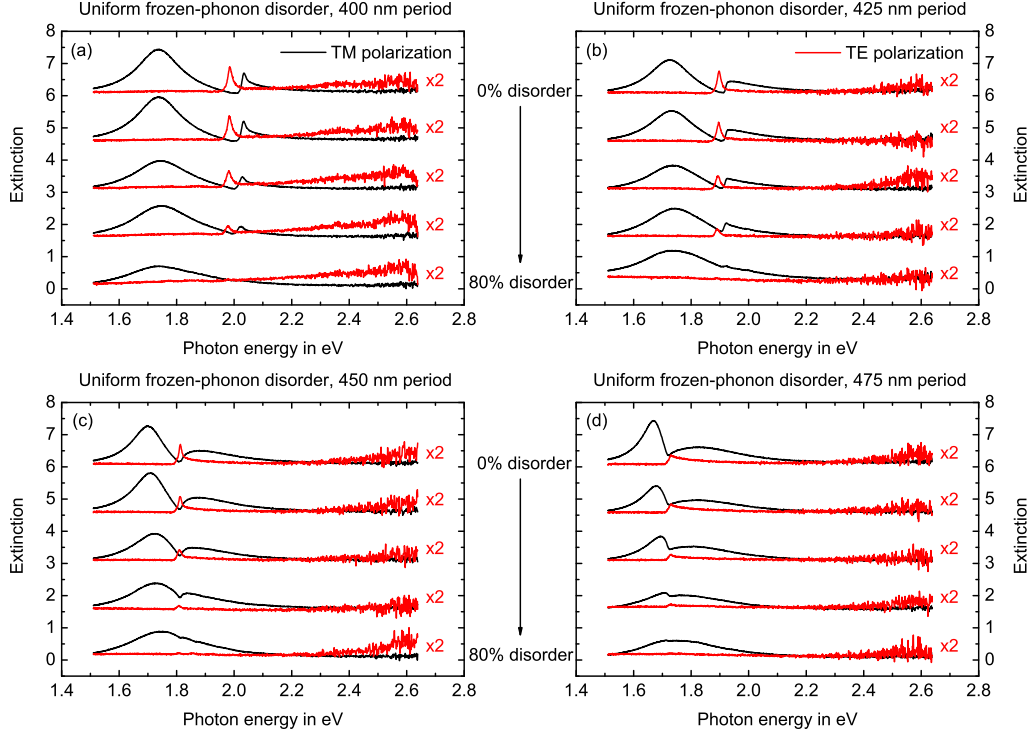

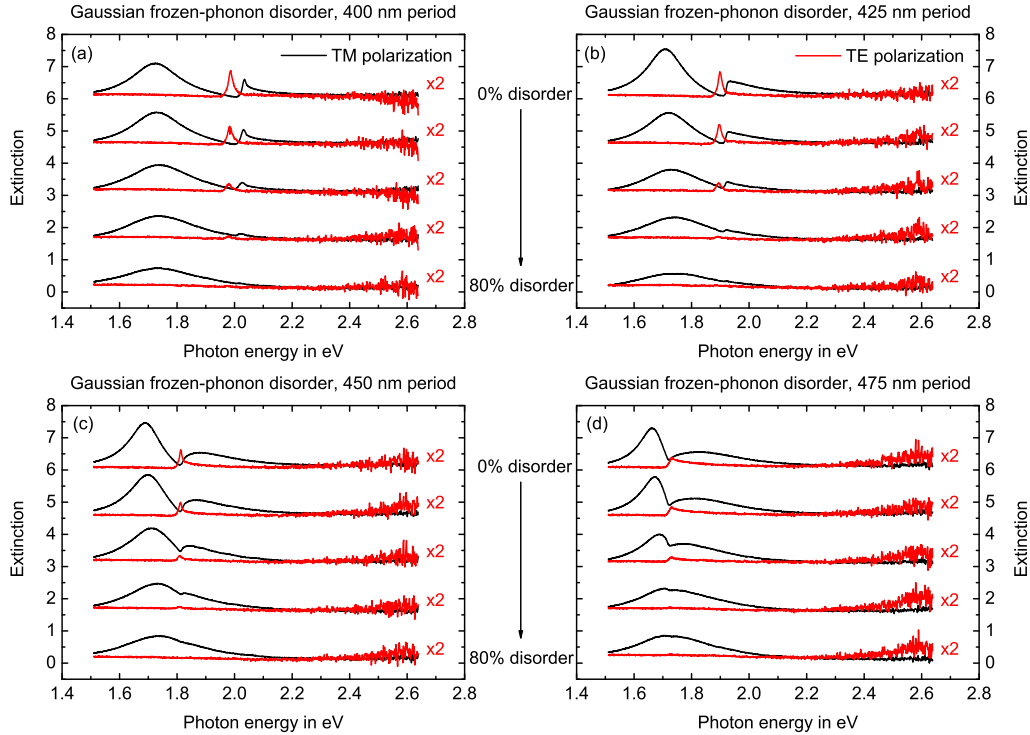**Figure 4.4:** Extinction spectra of samples with Gaussian frozen-phonon disorder for normal light incidence in TM (black lines) and TE (red lines) polarization. The average grating period d_0 is (a) 400 nm, (b) 425 nm, (c) 450 nm, and (d) 475 nm. The disorder amount in each panel is changed between 0% (top) and 80% (bottom). The different spectra are shifted upward for clarity in each panel.

In comparison, a sample with *Gaussian frozen-phonon disorder* was measured (Fig. 4.4). Again, the average grating period was changed between 400 nm and 475 nm (see Fig. 4.4 (a) − (d)) and the disorder amount was varied between 0% and 80%. Basically, a similar behavior is observed. In TE polarization, only the waveguide mode can be excited and its resonance energy shifts to lower values for larger grating periods. As it can be also seen for uniform frozen-phonon disorder, the resonance amplitude reduces until it disappears for about 80% disorder. However, the peak height decreases faster when compared to uniform frozen-phonon disorder. One can recognize that the waveguide mode for 60% disorder is almost vanished for Gaussian frozen-phonon disorder (Fig. 4.4), whereas this resonance is still clearly visible for uniform frozen-phonon disorder (Fig. 4.3). Once again, only one waveguide mode corresponding to a Fourier component with $k = \frac{2\pi}{d_0}$ can be excited in this energy range. In TM polarization, both the particle plasmon and the waveguide mode can be excited. As it is already described for uniform frozen-phonon disorder, the energy difference between the two resonances is changed for different grating periods. Increasing the Gaussian frozen-phonon disorder amount decreases the contrast between the peaks and the dip, but this decrease is again faster when compared to uniform frozen-phonon disorder. This can be obtained for a disorder amount of 60%, where the waveguide mode is nearly vanished for Gaussian frozen-phonon disorder (see Fig. 4.4) in comparison to a clearly visible waveguide mode for uniform frozen-phonon disorder. As above, the spectral width of the particle plasmon is slightly increased. Also here, the extinction in the dip between the two polariton branches is increased for larger disorder amounts. Therefore, the principle behavior is similar for these two distributions. However, the amplitude decrease is faster for the Gaussian frozen-phonon disorder. This is reasonable since the deviations from the perfectly ordered grating positions can be larger than the half width at half maximum (HWHM) for the Gaussian distribution, whereas the largest possible deviation for the uniform distribution is exactly given by HWHM.

Additionally, the optical properties of samples with *uniform long-range disorder* (Fig. 4.5) and *Gaussian long-range disorder* (Fig. 4.6) were measured. Again, the average grating period was changed between 400 nm and 475 nm (panels (a) − (d) in each figure) and the disorder amount was increased from 0% to 80%. Note that the TE polarized spectra of all four sample types are multiplied by a factor of 2. However, comparing these spectra to those with frozen-phonon disorder (Fig. 4.3 and Fig. 4.4) reveals obvious differences. Even though the amplitude of the waveguide modes in TE polarization (red curves) decreases for increasing disorder amounts as it was observed for frozen-phonon disorder, a huge broadening of the

Figure 4.5: Extinction spectra of samples with uniform long-range disorder for normal light incidence in TM (black lines) and TE (red lines) polarization. The average grating period d_0 is (a) 400 nm, (b) 425 nm, (c) 450 nm, and (d) 475 nm. The disorder amount in each panel is changed between 0% (top) and 80% (bottom). The different spectra are shifted upward for clarity in each panel.

spectral width can be obtained. Moreover, various peaks can be recognized. This broadening is due to the fact that several Fourier components arise in the vicinity of $k = \frac{2\pi}{d_0}$ for the long-range disorder. So, in principle, the broadened peak consists of several waveguide mode resonances at slightly different energy positions. Due to the dense occurrence of these resonances, they appear like one broad peak. Whereas the waveguide mode resonances in the spectra with frozen-phonon disorder are visible to a disorder amount of at least 60%, they are almost completely vanished at this degree of disorder for long-range disorder, even for the uniform distribution. For Gaussian long-range disorder the decrease is even stronger as it has been observed for the frozen-phonon disorder. However, for long-range disorder this behavior is more difficult to recognize. In TM polarization, both polariton branches are visible for the perfectly ordered samples. For increasing long-range disorder, several other waveguide mode peaks in addition to a broadening of the original two polariton peaks can be observed. The extinction in the region between the polariton peaks
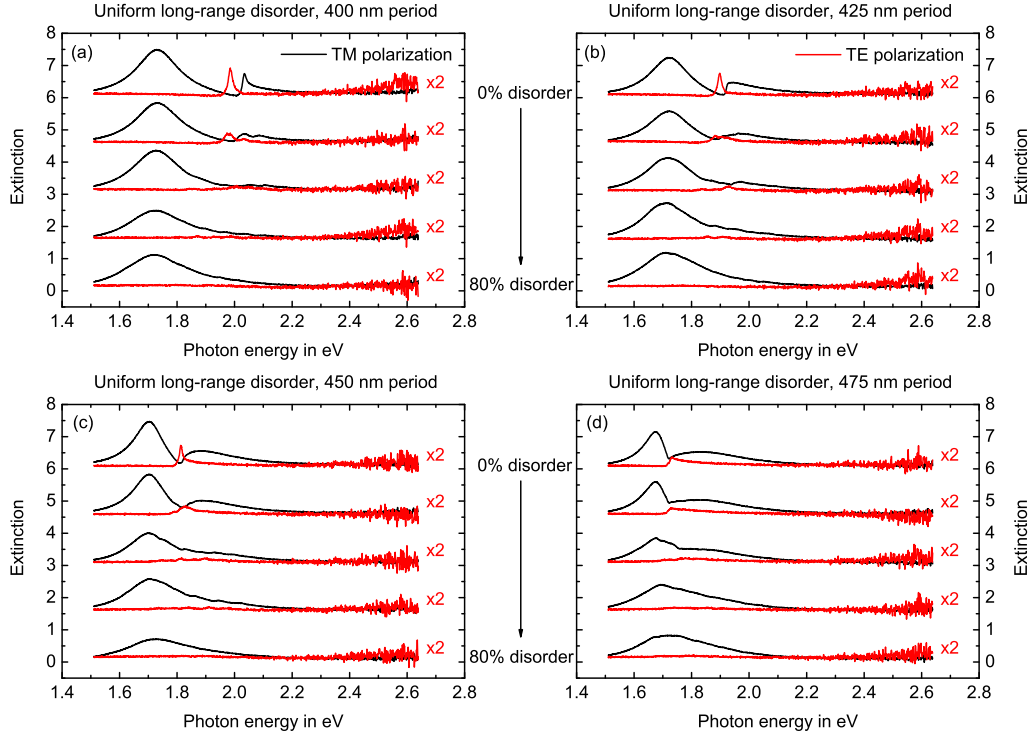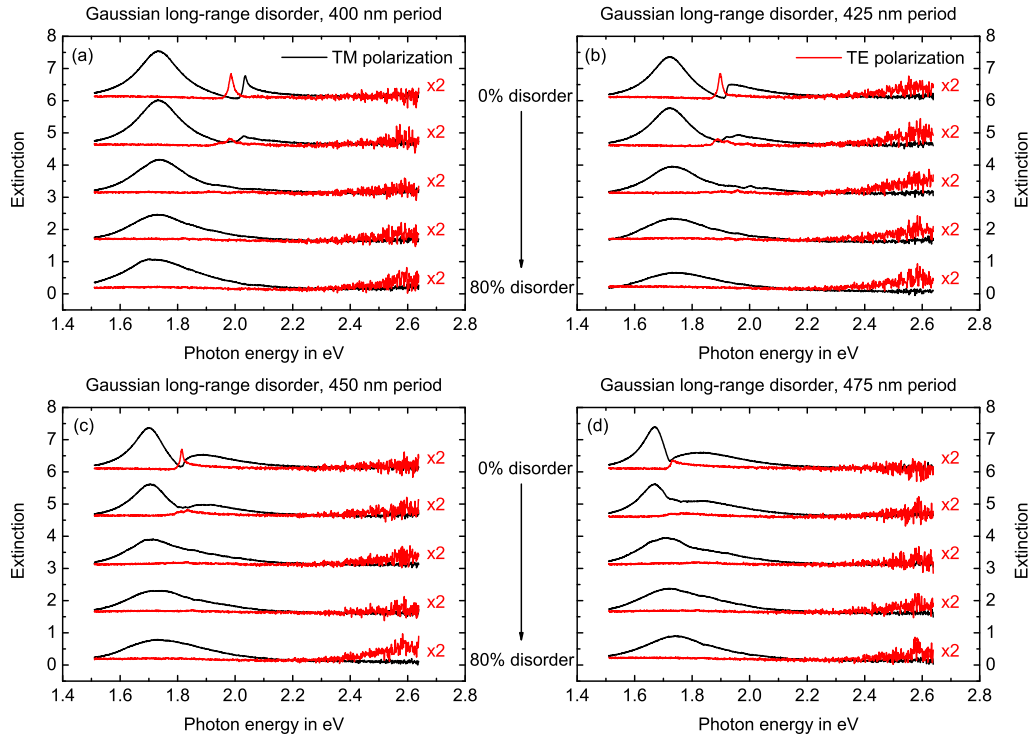
Figure 4.6: Extinction spectra of samples with Gaussian long-range disorder for normal light incidence in TM (black lines) and TE (red lines) polarization. The average grating period d_0 is (a) 400 nm, (b) 425 nm, (c) 450 nm, and (d) 475 nm. The disorder amount in each panel is changed between 0% (top) and 80% (bottom). The different spectra are shifted upward for clarity in each panel.

is increased due to the appearance of the additional waveguide mode resonances. Therefore, this energy gap is filled up with additional modes quite easily. By looking at the spectra with $d_0 = 475$ nm and 60% disorder, one can recognize a quite rough lineshape for uniform long-range disorder (Fig. 4.5) in the spectral range around 1.7 eV due to the additional waveguide modes. In comparison to this curve, the spectrum for the same periodicity and degree of disorder with uniform frozen-phonon disorder (Fig. 4.3) shows a very smooth lineshape. In addition to that, the minimum between the two main peaks is shifted to higher energies for the uniform long-range disorder. For Gaussian long-range disorder, this minimum is not visible anymore. Only the shoulder on the higher energy side indicates the previous separation of the two polariton branches. This means that the broadening for this distribution is even stronger than for the uniform distribution, which is consistent to the behavior of the Gaussian frozen-phonon disorder compared to that of the uniform frozen-phonon disorder. These findings, namely the broadening of the resonance peaks and the

Table 4.1: Coupling strength V_2 for uniform frozen-phonon disorder compared to Gaussian frozen-phonon disorder for different disorder amounts D.

	$D = 0\%$	$D = 20\%$	$D = 40\%$	$D = 60\%$	$D = 80\%$
Uniform	54.5 meV	48.8 meV	36.2 meV	23.2 meV	9.8 meV
Gaussian	54.5 meV	46.8 meV	29.4 meV	12.0 meV	4.5 meV

additionally excited waveguide modes for the long-range disorder in comparison to the behavior of the frozen-phonon disordered samples, are in agreement with the observations in Ref. [101].

In order to analyze the behavior of the coupling strength with increasing frozen-phonon disorder, the energy positions of the peak maxima are plotted versus the corresponding grating periods (filled squares in Fig. 4.7). This anti-crossing behavior is shown for uniform frozen-phonon disorder on the left side of Fig. 4.7 and for Gaussian frozen-phonon disorder on the right side. The degree of disorder increases from 0% in the top panels to 80% in the bottom panels in steps of 20%. The plots for both distribution functions have in common that the peaks in the region of the polariton splitting converge for larger disorder amounts indicating a decrease of the coupling strength between the particle plasmon and the waveguide modes. By comparing the uniform distribution to the Gaussian distribution, one can see that the peak positions for the Gaussian distribution are closer to each other meaning a lower coupling strength. This can be observed especially for 40% and 60% disorder. As explained in section 2.1.3, such an anti-crossing behavior can be described by a Hamiltonian, which is given in Eq. (2.33). The eigenvalues of the corresponding Hamiltonian are plotted as red curves in Fig. 4.7. The coupling strength V_2 was a fitting parameter, whereas E_{Pl} and $E_{wg}(d)$ are the energies of the undisturbed particle plasmon and the undisturbed waveguide modes for the grating period d, respectively. The half width of the photonic band gap is given by $V_1 = 10$ meV. The fitted values for the coupling strength are given in the corresponding labels in Fig. 4.7 as well as in Table 4.1. These values decrease for increasing disorder amounts as expected from the above described behavior. This is reasonable since an increasing disorder amount results in a smaller overlap between the electric fields of the waveguide mode and the particle plasmons as described in Ref. [101]. Additionally, the values for Gaussian frozen-phonon disorder are slightly smaller than those for uniform frozen-phonon disorder. This was also expected as the peak distance around the polariton splitting was smaller for Gaussian frozen-phonon disorder. This can be understood by looking at the two distribution functions. For a uniform distribution the maximum deviation from the perfectly ordered grating positions is given
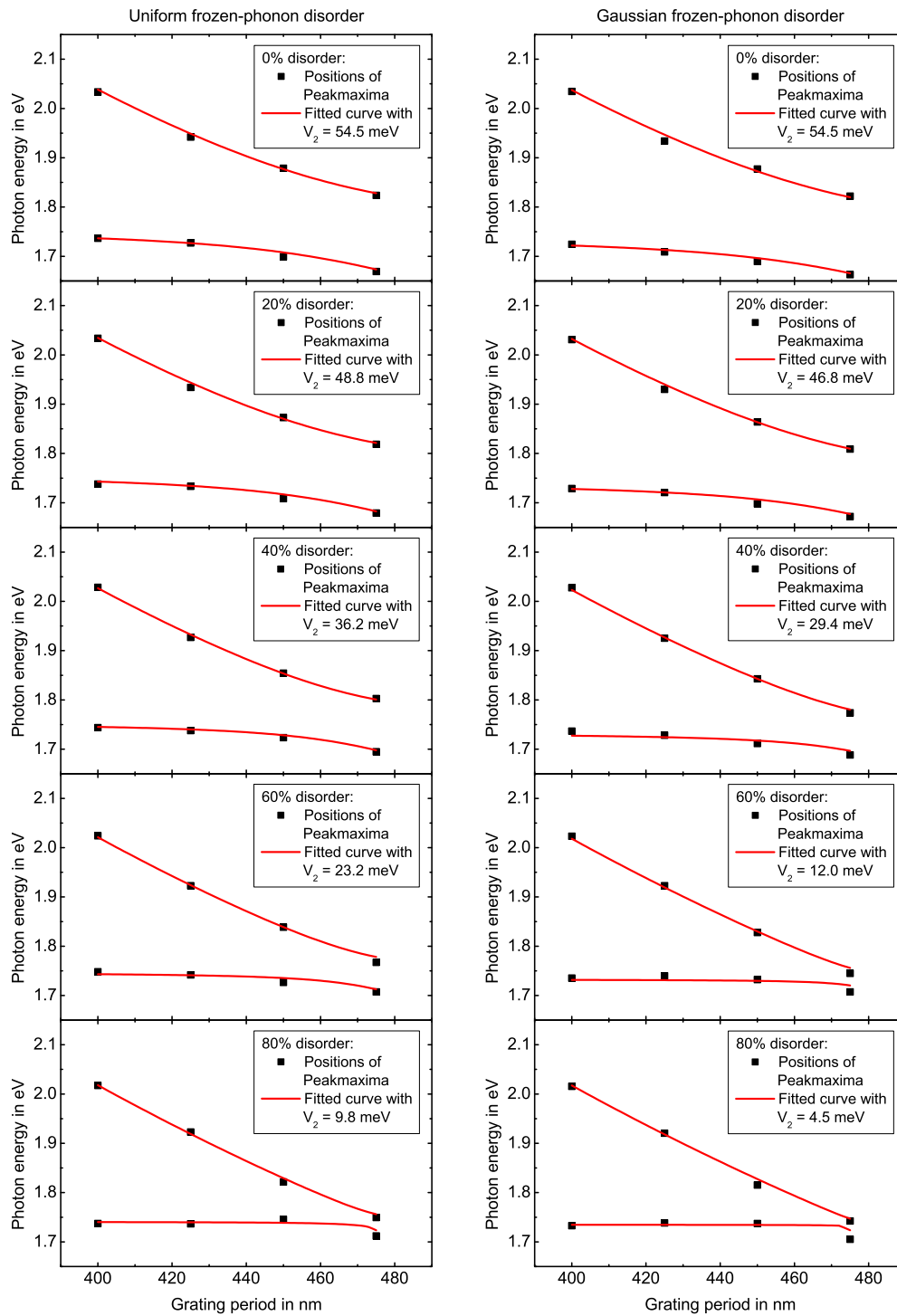
Figure 4.7: Anti-crossing behavior for samples with uniform frozen-phonon disorder (left) and Gaussian frozen-phonon disorder (right). The disorder amount increases from 0% (top) to 80% (bottom).

by HWHM, whereas larger deviations are possible for a Gaussian distribution as
already mentioned above.
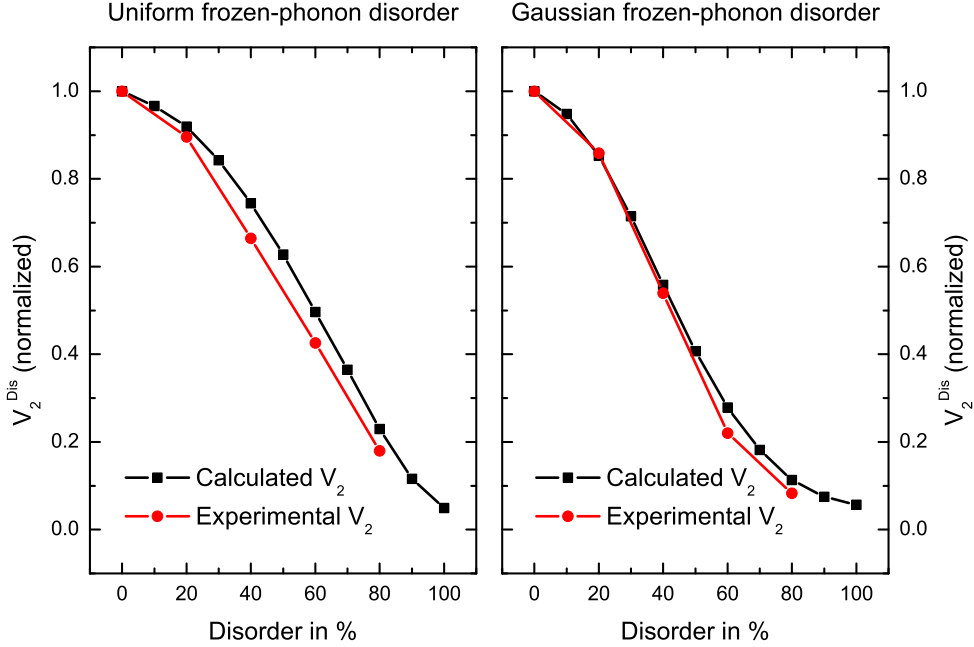
Figure 4.8: Calculated (black lines) and experimental (red lines) coupling strength V_2
versus degree of disorder for uniform frozen-phonon disorder (left) and Gaussian frozen-
phonon disorder (right).

The fitted values for the coupling strength are plotted in Fig. 4.8 versus the dis-
order amount as red curves for uniform frozen-phonon disorder (left) and Gaussian
frozen-phonon disorder (right). These values are compared to the calculated ones of
Ref. [101] shown as black curves in Fig. 4.8. The principle behavior between theo-
retical and experimental curves is quite good, especially for Gaussian frozen-phonon
disorder. The experimental values for the coupling strength for uniform frozen-
phonon disorder are slightly smaller than the theoretical values (see left panel of
Fig. 4.8). However, by comparing the fitted values of the coupling strength of the
uniform frozen-phonon disorder to the calculated ones for both distributions, one
can recognize a smaller deviation to the curve with uniform frozen-phonon disorder.
This is especially true for higher disorder amounts. These deviations can be due
to imperfections of the fabricated structure. It is possible that the positions of the
gold wires deviate slightly from the desired positions leading to an increase of the
disorder amount and thus a decrease of the coupling strength. Another possibility
can be due to problems finding the exact energy position of the peak maximum,

especially for the broader peaks. Furthermore, the deviations can arise due to the simple model for the coupling strength calculation [101]. However, the behavior of the coupling strength is described quite well with the theoretical model.

The behavior of the coupling strength for the experimental data with increasing disorder is shown here for frozen-phonon disorder. However, the coupling strength for long-range disorder cannot be obtained experimentally due to the large amount of additional waveguide modes arising for these samples. Therefore, a different method has to be found in order to compare the experimentally obtained values of V_2 to the theoretically predicted ones. It is well-known that the absorption tail of disordered structures shows an exponential behavior [131–134]. This is the Urbach rule, where the absorption α in the specific region is defined by [132–134]

$$\alpha = \alpha_0 \exp\left(\frac{E - E_0}{E_U}\right) \tag{4.1}$$

with α_0 and E_0 as two constants being almost independent of the disorder amount and E_U as the Urbach energy. For semiconductors and insulators it is known that an increase of the disorder amount results in a more gentle slope of the absorption tail when $\ln(\alpha)$ is plotted versus the energy E [133]. In other words, a higher disorder amount possesses a lower value of the slope $m = 1/E_U$. By looking at the behavior of the coupling strength (see Fig. 4.1 and Fig. 4.8), one can also recognize a decrease for larger disorder amounts. Therefore, there might be a relation between the Urbach slope and the coupling strength.
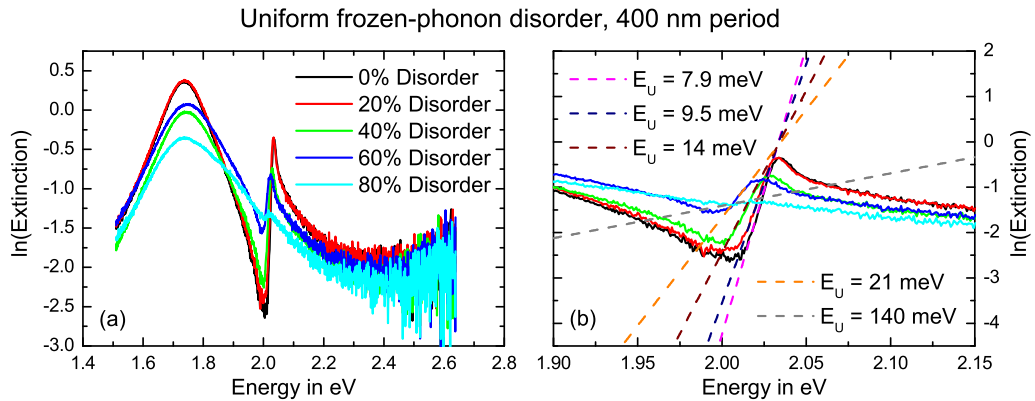

Figure 4.9: (a) The natural logarithm of the extinction ($\ln(Ext)$) is plotted versus the photon energy of the whole measured spectral range. (b) The same plot as in (a), but with the spectral range restricted to the region around the resonance at higher energies. A line is fitted to the resonance slope in order to obtain the Urbach energy.

Table 4.2: Fitted Urbach energies E_U of the samples with uniform as well as with Gaussian frozen-phonon disorder for different disorder amounts D and different grating periods d_0.

		$D = 0\%$	$D = 20\%$	$D = 40\%$	$D = 60\%$	$D = 80\%$
Uniform	400 nm	7.9 meV	9.5 meV	14 meV	21 meV	140 meV
	425 nm	6 meV	6.5 meV	9.1 meV	17.8 meV	350 meV
	450 nm	13.5 meV	16 meV	19 meV	44 meV	400 meV
	475 nm	54 meV	81 meV	220 meV	500 meV	–
Gaussian	400 nm	8.1 meV	13 meV	23 meV	53 meV	–
	425 nm	5.4 meV	8 meV	18 meV	55 meV	–
	450 nm	13.5 meV	18 meV	40 meV	120 meV	–
	475 nm	54 meV	73 meV	250 meV	1500 meV	–

Since the extinction spectra can be treated as absorption spectra (see chapter 7.2 in Ref. [35]), the natural logarithm of the extinction is plotted versus the photon energy for our disorder samples. This is exemplarily shown in Fig. 4.9 for the sample with uniform frozen-phonon disorder and an average grating period of 400 nm. However, the following procedure to obtain the Urbach energies is in principle the same for all samples. In Fig. 4.9 (a), the whole $\ln(Ext)$ spectrum is plotted versus the photon energy. It can be seen that the peak height as well as the steepness of the resonance slopes decrease for a larger disorder amount. In order to better recognize the steepness of the slope, the spectral range in Fig. 4.9 (b) is restricted to the region around the higher energy resonance. To every spectrum the linear equation

$$\ln(Ext) = \ln(Ext_0) + \left(\frac{E - E_0}{E_U}\right) \tag{4.2}$$

is fitted, which can be obtained by applying the natural logarithm to Eq. (4.1). These linear fits are shown as dashed curves in Fig. 4.9 (b) and the fitted Urbach energy values are also specified therein. It can be seen that the slope of each curve is quite nicely reproduced by the linear fits. However, the gentle slope of the sample with 80% disorder is difficult to recognize. As expected, the Urbach energy increases for higher disorder amounts.

As already mentioned above, the Urbach energy is fitted to the higher energy peak of all frozen-phonon spectra. The obtained Urbach energies of the samples with uniform as well as Gaussian frozen-phonon disorder are shown in Table 4.2 for different disorder amounts and different grating periods. For some 80% spectra, it was not possible to determine the Urbach energy. It can be seen that the Urbach energy

becomes larger for all samples by increasing the disorder amount. Furthermore, the Urbach energy increases faster for the Gaussian distribution when compared to the corresponding grating periods of the uniform distribution. This is expected since larger deviations than FWHM/2 from the perfect periodic grating position are possible only for the Gaussian distribution. It can also be seen in Table 4.2 that the Urbach energy strongly depends on the grating period. This is reasonable since the spectra also change significantly by varying the grating period. However, the relation of the grating period and the Urbach energy is not clear up to now.
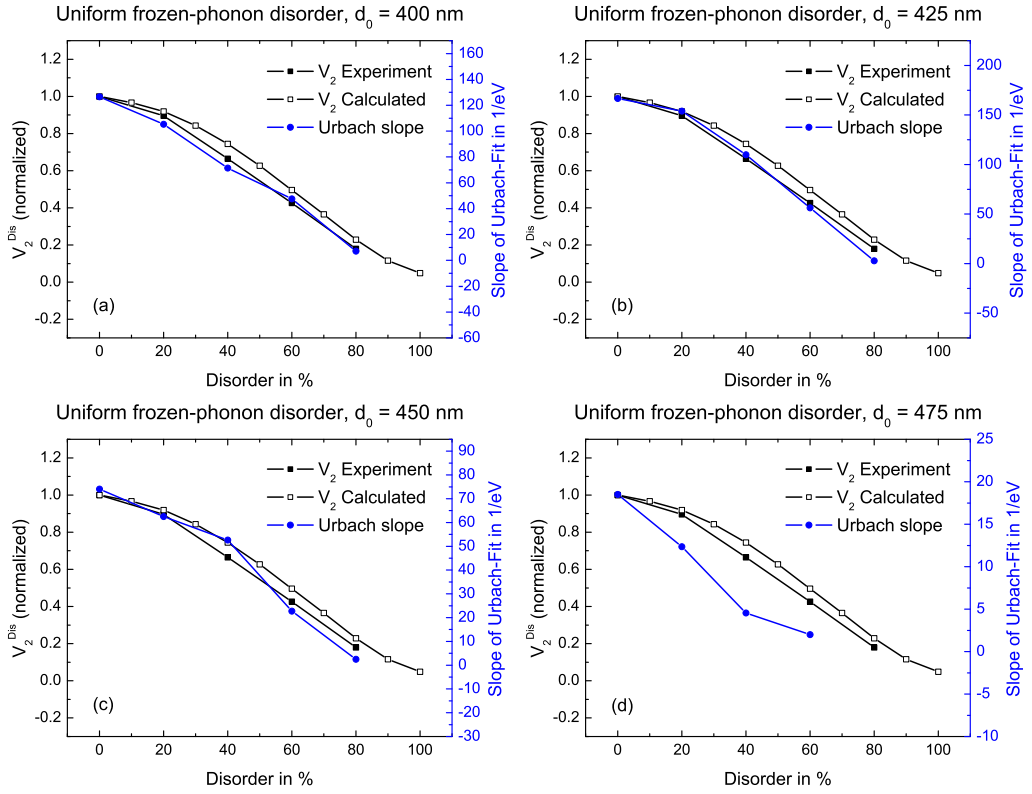
Figure 4.10: Experimental (filled squares) and calculated (open squares) normalized coupling constants (black) compared to the behavior of the Urbach slopes (blue filled circles) for uniform frozen-phonon disorder and a periodicity (a) $d_0 = 400\,\text{nm}$, (b) $d_0 = 425\,\text{nm}$, (c) $d_0 = 450\,\text{nm}$, and (d) $d_0 = 475\,\text{nm}$.

In order to see if the coupling constant of the disordered samples V_2^{Dis} and the slope m of the Urbach energy show a similar behavior, V_2^{Dis} and $m = \frac{1}{E_U}$ are both plotted versus the disorder amount for both distributions and all grating periods. This is shown in Fig. 4.10 for uniform frozen-phonon disorder and in Fig. 4.11 for Gaussian frozen-phonon disorder. The behavior for different average grating
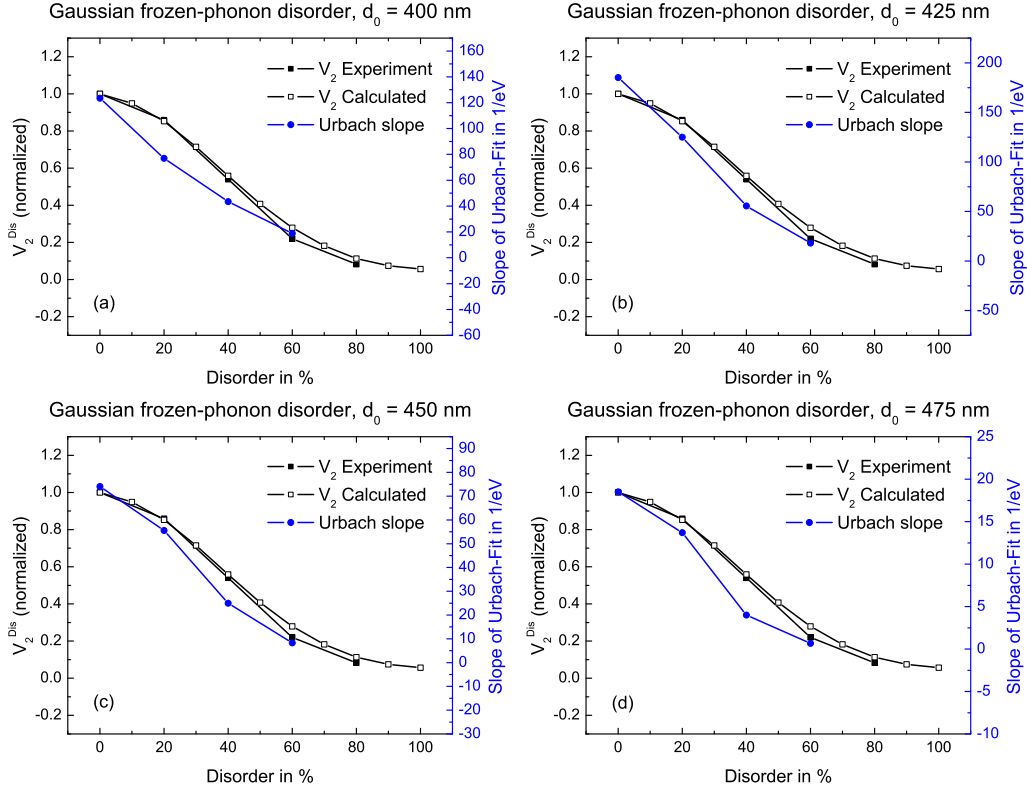
Figure 4.11: Experimental (filled squares) and calculated (open squares) normalized coupling constants (black) compared to the behavior of the Urbach slopes (blue filled circles) for Gaussian frozen-phonon disorder and a periodicity (a) $d_0 = 400\,\text{nm}$, (b) $d_0 = 425\,\text{nm}$, (c) $d_0 = 450\,\text{nm}$, and (d) $d_0 = 475\,\text{nm}$.

periods $d_0 = 400\,\text{nm} - 475\,\text{nm}$ is displayed in panels (a) $-$ (d), respectively. Due to the unknown relation between the coupling constant and the Urbach energy slope, two independent y axes are used. The relation between the two y axes is different for the individual grating periods, however, it is equal for the same grating period and the two different distributions. It can be seen in Figs. 4.10 and 4.11 that the behavior of the Urbach energy slope (blue) is quite similar to the behavior of the disorder dependent coupling constant (black). This is true for both the experimentally obtained and the calculated normalized coupling constants. Some deviations are visible like in Fig. 4.10 (d) or in Fig. 4.11 (a), which can be due to the fitting process. However, the general behavior is reproduced quite well. Even the faster decrease of the Gaussian frozen-phonon disorder when compared to the uniform distribution can be seen.

Table 4.3: Fitted Urbach energies E_U of the samples with uniform as well as with Gaussian long-range disorder for different disorder amounts D and different grating periods d_0.

		$D = 0\%$	$D = 20\%$	$D = 40\%$	$D = 60\%$	$D = 80\%$
Uniform	400 nm	8 meV	24 meV	160 meV	500 meV	500 meV
	425 nm	5.5 meV	30 meV	175 meV	650 meV	550 meV
	450 nm	15 meV	100 meV	400 meV	550 meV	–
	475 nm	44 meV	550 meV	7 eV	10 eV	10 eV
Gaussian	400 nm	8 meV	40 meV	430 meV	4000 meV	–
	425 nm	5.5 meV	50 meV	800 meV	1000 meV	6000 meV
	450 nm	15 meV	125 meV	1000 meV	1200 meV	–
	475 nm	44 meV	2000 meV	7 eV	10 eV	10 eV

Since the behavior of the coupling constants and the slopes of the Urbach energies is quite similar for frozen-phonon disorder, the Urbach energies are also fitted to the samples with long-range disorder. However, it is more difficult to fit Eq. (4.2) to the spectra of the long-range disorder samples. The fitted Urbach energies are shown in Table 4.3 for the uniform distribution as well as the Gaussian distribution. By comparing the values in this table to those for frozen-phonon disorder (Table 4.2), it can be observed that the values for long-range disorder are much higher than expected. Additionally, also the Urbach energies for the Gaussian distribution are higher than those for the uniform distribution. This is expected and consistent with the findings for frozen-phonon disorder. It is also found that the Urbach energies are strongly dependent on the grating period as above. However, the order of magnitude for the four different samples having the same grating period is comparable, which is true for all grating periods.

Since the correct tendency of the Urbach energies is found, the same plots as in Figs. 4.10 and 4.11 are shown for uniform and Gaussian long-range disorder in Figs. 4.12 and 4.13, respectively. However, the Urbach energy slopes (blue filled circles) are only compared to the calculated normalized coupling constants (black open squares) since it was not possible to experimentally obtain the coupling constants due to the large amount of additionally excited waveguide modes. Panels (a) − (d) of Figs. 4.12 and 4.13 again show the different results for the samples with average periodicities $d_0 = 400\,\text{nm} - 475\,\text{nm}$. As above, the y axes of the Urbach slopes are different for the varying grating periods. However, the scale is exactly the same for one specific grating period but other sample designs. By comparing the black and the blue curves, it can be seen that the agreement is good for all

Figure 4.12: Calculated normalized coupling constants (black open squares) compared to the behavior of the Urbach slopes (blue filled circles) for uniform long-range disorder and a periodicity (a) $d_0 = 400\,\text{nm}$, (b) $d_0 = 425\,\text{nm}$, (c) $d_0 = 450\,\text{nm}$, and (d) $d_0 = 475\,\text{nm}$.

grating periods and both distributions. Although the fitting procedure was more difficult, also for long-range disorder the behavior of the coupling constants is quite well reproduced by the behavior of the Urbach slopes. As above, the faster decrease of the sample with Gaussian distribution can be obtained. Additionally, it can be seen that the samples with long-range disorder reach much lower values for the same disorder amount when compared to the corresponding values of the samples with frozen-phonon disorder.

These findings indicate that the coupling constant is somehow related to the slope of the Urbach energy. However, this relation is not known up to now. It can just be said that the Urbach slope is strongly dependent on the grating period. In order to find this relation, further investigations have to be made, which is subject to future research.
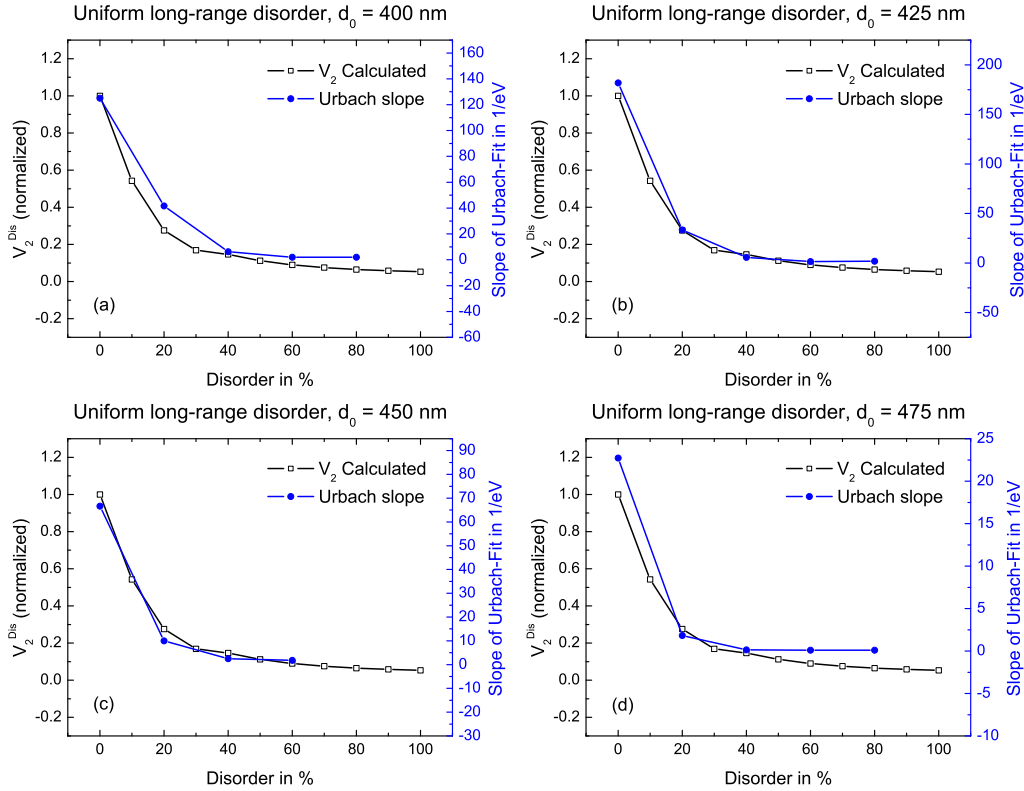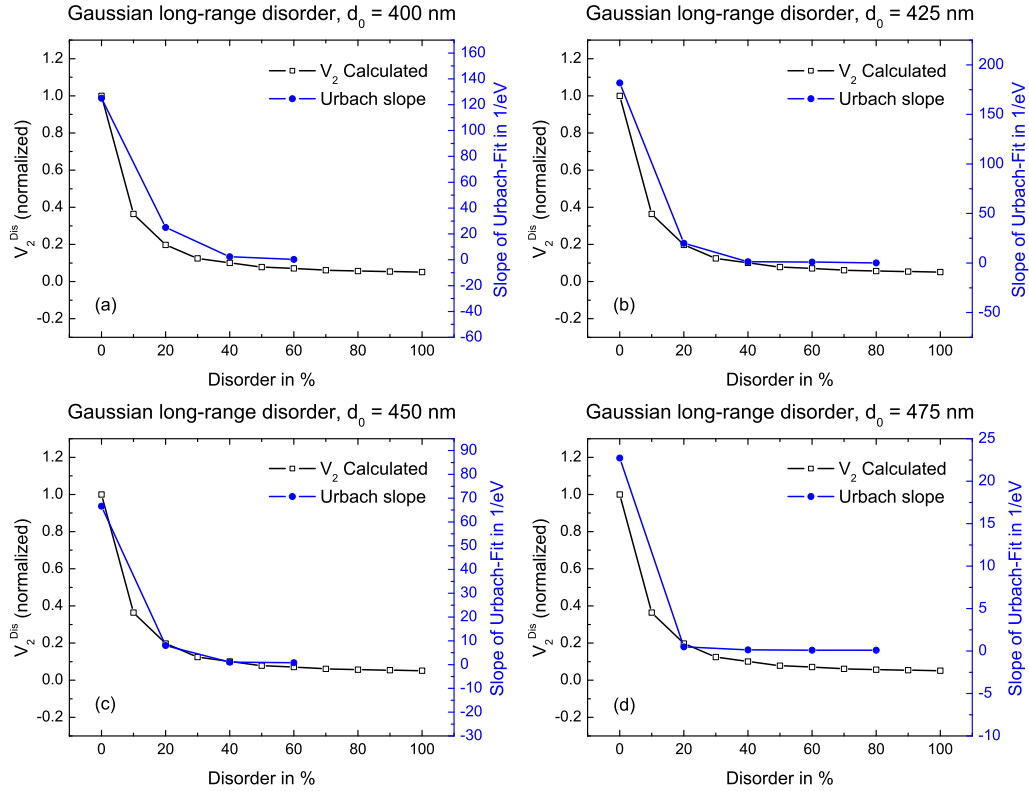
Figure 4.13: Calculated normalized coupling constants (black open squares) compared to the behavior of the Urbach slopes (blue filled circles) for Gaussian long-range disorder and a periodicity (a) $d_0 = 400\,\text{nm}$, (b) $d_0 = 425\,\text{nm}$, (c) $d_0 = 450\,\text{nm}$, and (d) $d_0 = 475\,\text{nm}$.

4.1.3 Angular extinction spectra

The disorder samples described in section 4.1.1 were also measured with oblique light incidence. For these measurements the cylindrical lens mentioned in section 3.2 was used and the whole CCD chip was read out. The measured angular extinction spectra in TE polarization are shown in Fig. 4.14 for uniform frozen-phonon disorder (panels (a) − (e)) as well as for uniform long-range disorder (panels (f) − (j)). The extinction is color-coded and it is plotted versus the photon energy and the angle of incidence ϑ. These measurements are exemplarily shown for an average periodicity $d_0 = 450\,\text{nm}$. However, the behavior for the other grating periods is similar. The two panels at the top (Fig. 4.14 (a) and (f)) show the measurements for a perfect periodic grating arrangement. The disorder is increased for the panels below. For oblique light incidence on the periodic samples, two waveguide modes are visible. The splitting between these resonances decreases for smaller incidence angles. Whereas

Figure 4.14: Measured angular extinction spectra in TE polarization with (a) − (e) uniform frozen-phonon disorder and (f) − (j) uniform long-range disorder. The disorder amount is increased from top (panels (a) or (f)) to bottom (panels (e) or (j)). The color-coded extinction is plotted versus the photon energy and the angle of incidence.

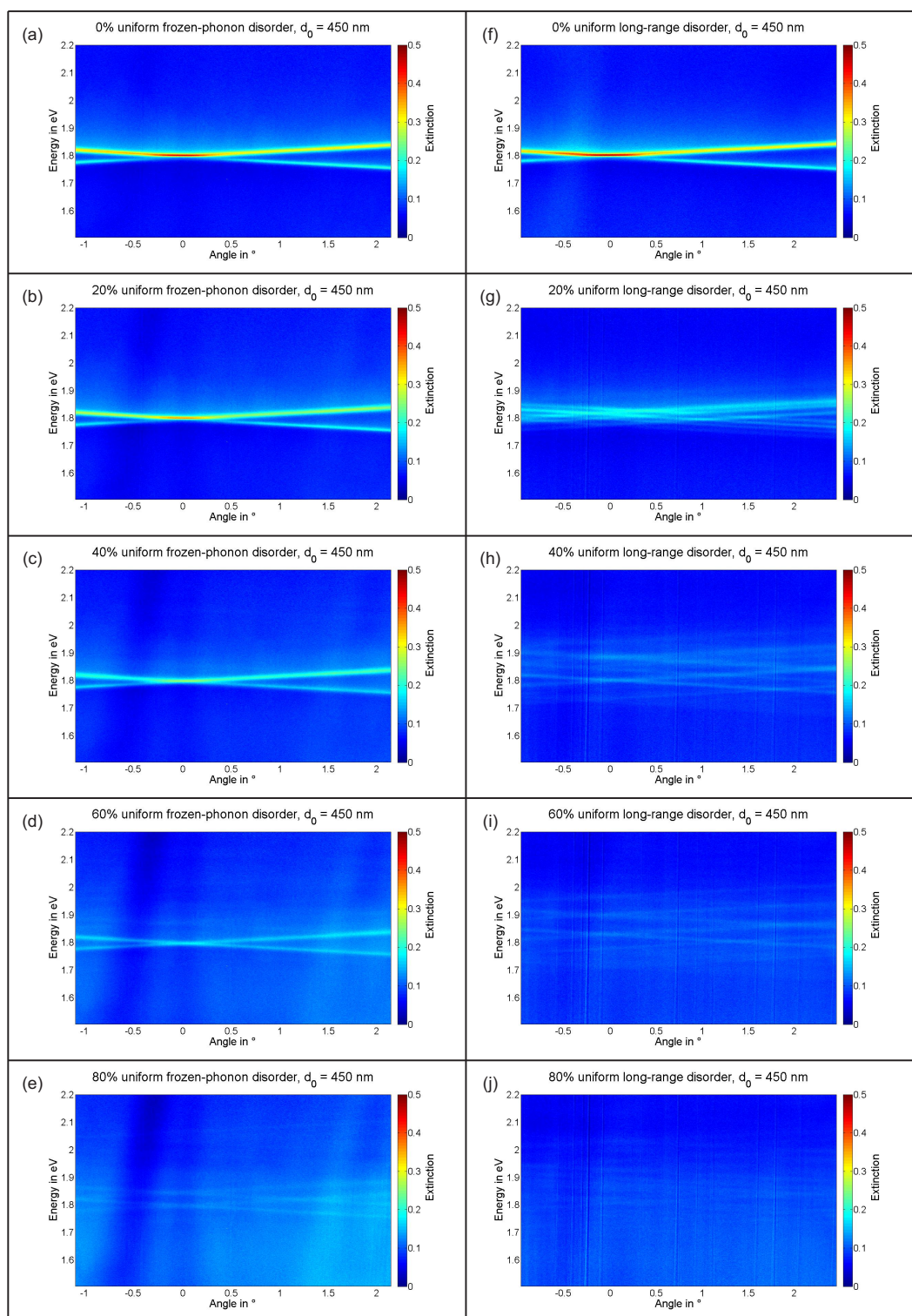the upper energy waveguide mode is always visible, the lower energy waveguide mode vanishes for normal incidence and small angles of incidence. It can be seen that the upper energy waveguide mode stays at approximately the same energy for $\vartheta \approx 0°$. The lower energy waveguide mode stays also at almost constant energies for $\vartheta \approx 0°$, however, at a slightly lower energy value. This is not clearly visible due to the decreased extinction values for this waveguide mode. The energy difference between the upper and the lower energy waveguide modes is the photonic band gap. It can be seen that the behavior is equal for positive and negative incidence angles.

Increasing the uniform frozen-phonon disorder amount results in a reduction of the resonance height and a smaller waveguide mode separation (see Fig. 4.14 (a) − (e)). However, the general behavior of a larger splitting between the two waveguide modes for increasing incidence angles is preserved. The band gap between the two waveguide modes disappears for a disorder amount of approximately 60%. For a disorder amount of 80% additional weak waveguide modes at slightly higher energies are visible. The peak heights are about the same for all resonances due to the strongly decreased waveguide modes of the perfect photonic crystal and the simultaneously increased background. However, for higher disorder amounts it is expected that no waves can be coupled into the waveguide layer and thus leading to no visible resonances in the spectrum.

For increased uniform long-range disorder (see Fig. 4.14 (f) − (j)) the peak heights of the waveguide modes are also reduced. However, additional resonances arise since the long-range order is not preserved. All of these waveguide modes split up into two modes for oblique light incidence and the energy difference between these two modes increases. This can be seen by the larger energy range for bigger incidence angles. However, for small angles of incidence the individual waveguide modes are hardly visible due to the large amount of additional resonances. By increasing the uniform long-range disorder amount, the energy range in which the waveguide modes are spread out becomes larger. The peak heights for the same disorder amount are smaller for long-range disorder when compared to frozen-phonon disorder. Therefore, also the excited waveguide modes vanish for smaller disorder amounts. This can be seen for a disorder amount of 80%. Hardly any resonances are visible for uniform long-range disorder, whereas the waveguide modes for uniform frozen-phonon disorder can still be seen. For uniform frozen-phonon disorder, it is even possible to observe the splitting of the waveguide modes for oblique light incidence.

Figure 4.15 shows the same plots as in Fig. 4.14 but for Gaussian frozen-phonon disorder (panels (a) − (e)) and for Gaussian long-range disorder (panels (f) − (j)).
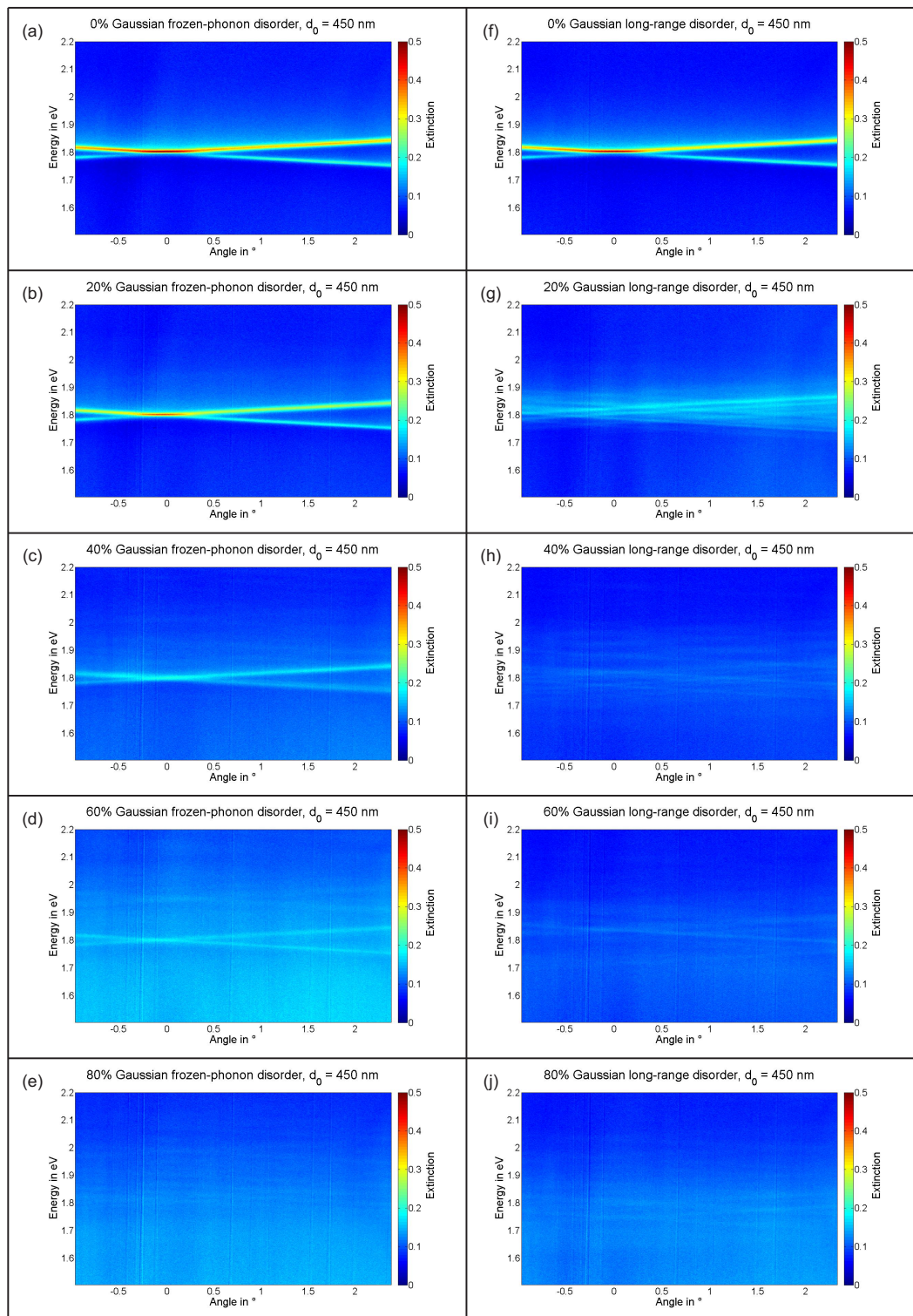
Figure 4.15: Measured angular extinction spectra in TE polarization with (a) − (e) Gaussian frozen-phonon disorder and (f) − (j) Gaussian long-range disorder. The disorder amount is increased from top (panels (a) or (f)) to bottom (panels (e) or (j)). The color-coded extinction is plotted versus the photon energy and the angle of incidence.

The principle behavior is similar to that already explained for uniform distribution. However, the peak heights decrease faster for Gaussian distribution. This can be seen especially for 80% frozen-phonon disorder, where the waveguide modes are clearly visible for uniform distribution but hardly observable for Gaussian distribution. For 20% long-range disorder, it can be seen that the waveguide modes of the Gaussian distribution are spread out over are larger energy range in comparison to the uniform distribution. Whereas the waveguide modes for 40% uniform long-range disorder can still clearly be seen, the resonances for 40% Gaussian long-range disorder are already very weak. This is consistent with the findings of the previous section.

All samples were also measured in TM polarization, which is again exemplarily shown in Figs. 4.16 and 4.17 for an average grating period $d_0 = 450$ nm. The measurements of the samples with uniform distribution are shown in Fig. 4.16 and those with Gaussian distribution can be seen in Fig. 4.17. In TM polarization, not only the waveguide modes can be excited but also the particle plasmon as already mentioned earlier. For $d_0 = 450$ nm, the waveguide modes and the particle plasmon are coupled leading to the waveguide-plasmon-polariton. Therefore, the waveguide modes in these plots are visible as extinction dips within the broad particle plasmon. The behavior of the waveguide modes in TM polarization is similar to that in TE polarization. For frozen-phonon disorder (panels $(a) - (e)$ in Figs. 4.16 and 4.17), the dip between the polariton-branches decreases by increasing the disorder amount. As above, this decrease is faster for the Gaussian distribution. This can be observed by the weaker contrast between the dips and the neighboring peaks for the same disorder amount. For 60% uniform frozen-phonon disorder the dips are still visible, whereas the waveguide modes for 60% Gaussian frozen-phonon disorder cannot be recognized anymore. Instead, only the particle plasmon peak is visible. The amplitude of the particle plasmon also decreases for larger disorder amounts, which is true for both distributions.

In the spectra with long-range disorder, additional waveguide modes arise. The waveguide modes cover a broader energy range with a smaller amplitude when compared to the frozen-phonon measurements. Especially in the images with 20% long-range disorder, this is clearly visible. In comparison to the samples with 40% frozen-phonon disorder, hardly any waveguide mode resonances are visible for 40% long-range disorder. The contrast between neighboring peaks and dips is very low. As above, the waveguide modes of the samples with Gaussian distribution possess lower amplitudes and they are also located in a broader energy range in comparison to the waveguide modes of the samples with uniform distribution. For a disorder amount of 40% and Gaussian long-range disorder it is already hard to distinguish the

Figure 4.16: Measured angular extinction spectra in TM polarization with (a) − (e) uniform frozen-phonon disorder and (f) − (j) uniform long-range disorder. The disorder amount is increased from top (panels (a) or (f)) to bottom (panels (e) or (j)). The color-coded extinction is plotted versus the photon energy and the angle of incidence.
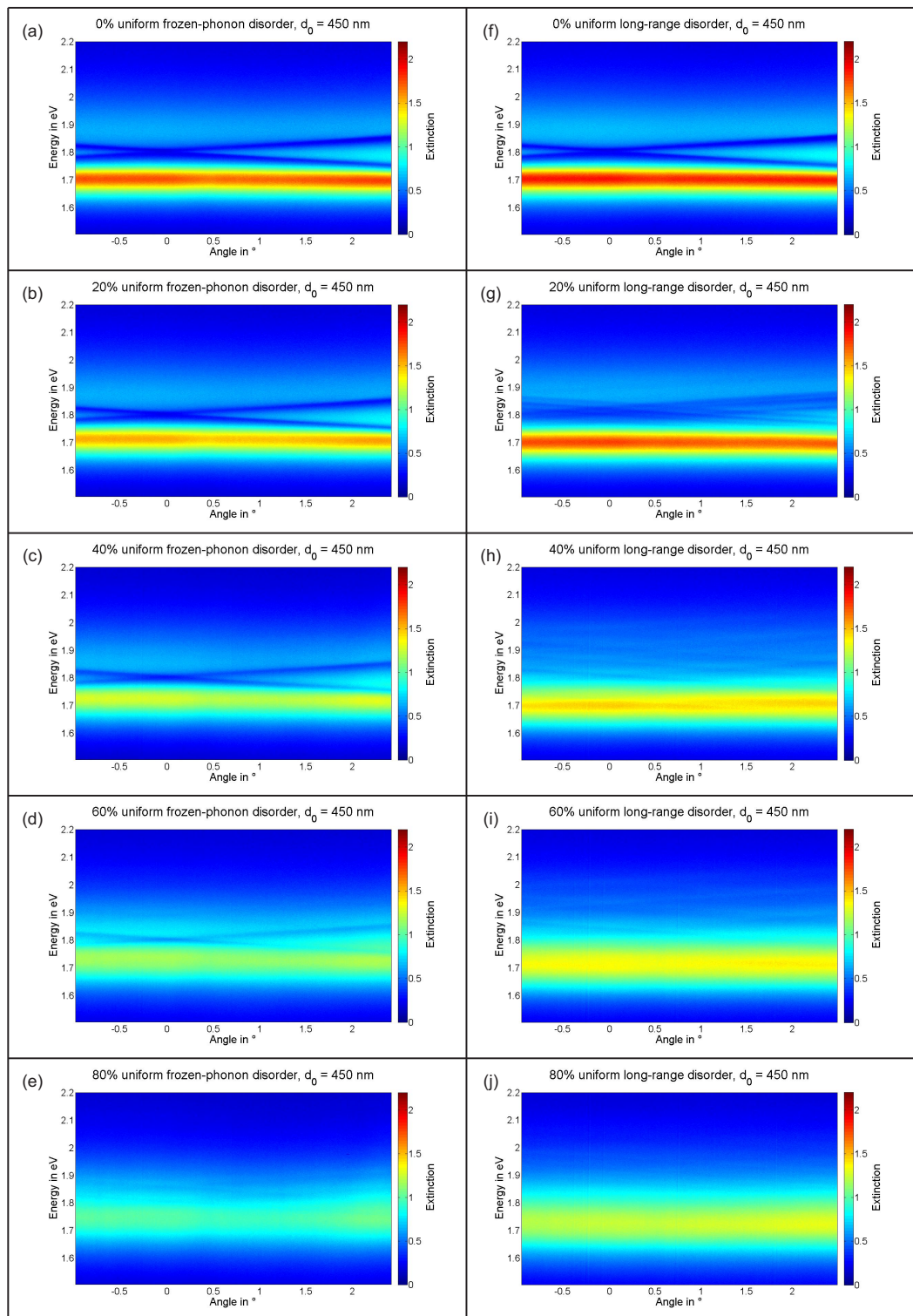
Figure 4.17: Measured angular extinction spectra in TM polarization with (a) − (e) Gaussian frozen-phonon disorder and (f) − (j) Gaussian long-range disorder. The disorder amount is increased from top (panels (a) or (f)) to bottom (panels (e) or (j)). The color-coded extinction is plotted versus the photon energy and the angle of incidence.
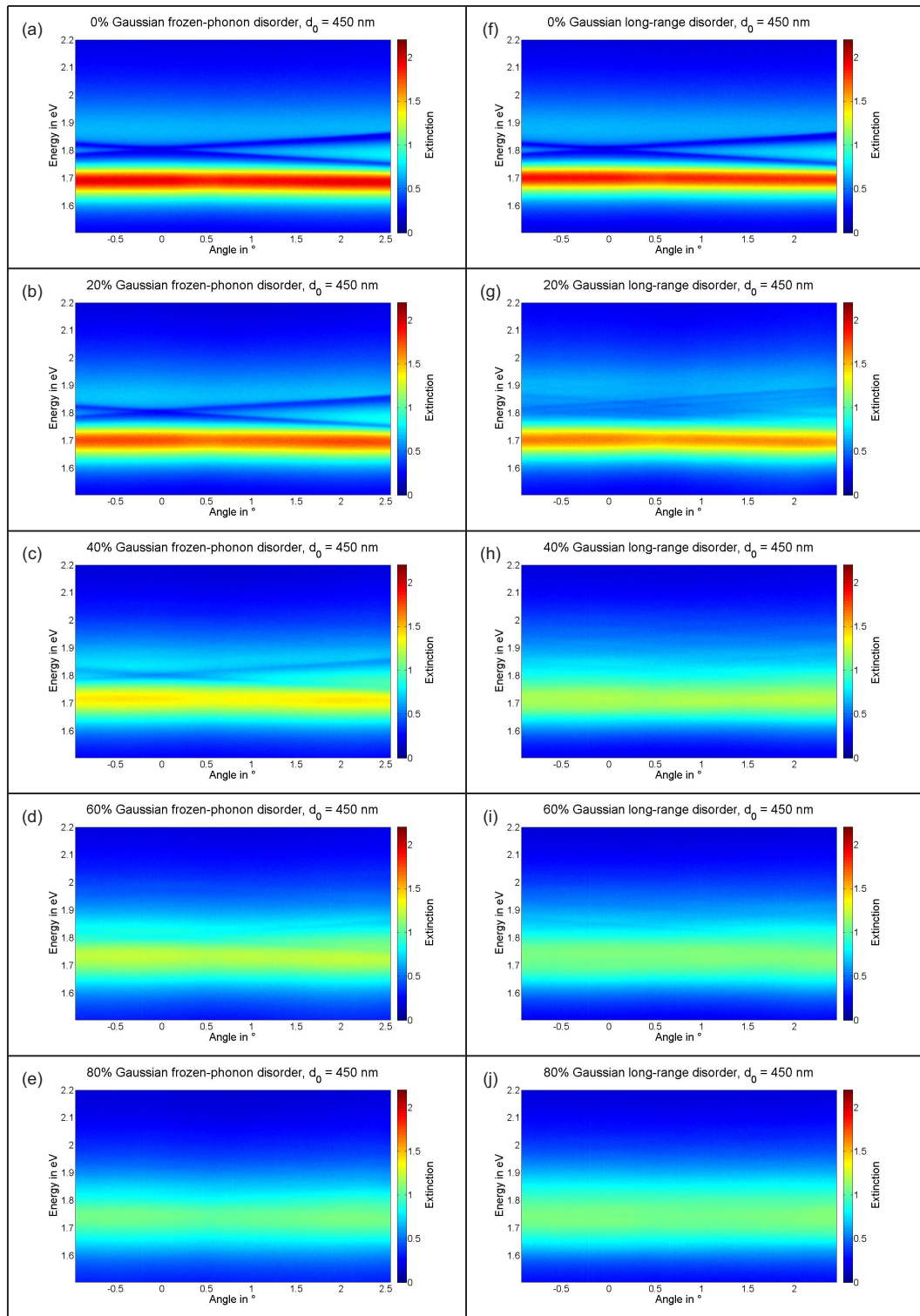
individual waveguide modes, whereas they are still recognizable for uniform long-range disorder and the same disorder amount. As soon as the waveguide modes are vanished, only the broad particle plasmon peak is visible. Also for long-range disorder, the particle plasmon amplitude decreases by increasing the disorder amount.

4.2   Quasiperiodic and fractal structures

In this section, the optical properties of 1D photonic crystals are studied for different samples with quasiperiodic as well as fractal gold wire arrangements. All samples are measured for normal light incidence as well as for oblique light incidence.

4.2.1   Sample designs

Table 4.4: Short, long, and average distances of the different Fibonacci samples.

	short distance	long distance	average distance
Sample F1	≈ 360 nm	425 nm	400 nm
Sample F2	≈ 319 nm	450 nm	400 nm
Sample F3	≈ 279 nm	475 nm	400 nm
Sample F4	≈ 385 nm	450 nm	425 nm
Sample F5	≈ 344 nm	475 nm	425 nm
Sample F6	≈ 410 nm	475 nm	450 nm
Sample F7	400 nm	≈ 440 nm	425 nm
Sample F8	400 nm	≈ 481 nm	450 nm
Sample F9	400 nm	≈ 521 nm	475 nm
Sample F10	425 nm	≈ 465 nm	450 nm
Sample F11	425 nm	≈ 506 nm	475 nm
Sample F12	450 nm	≈ 490 nm	475 nm
Sample F13	400 nm	425 nm	≈ 415 nm
Sample F14	400 nm	450 nm	≈ 431 nm
Sample F15	400 nm	475 nm	≈ 446 nm
Sample F16	425 nm	450 nm	≈ 440 nm
Sample F17	425 nm	475 nm	≈ 456 nm
Sample F18	450 nm	475 nm	≈ 465 nm

The gold wires of the quasiperiodic photonic crystal samples are arranged in a Fibonacci-like sequence, as mentioned in section 2.4.1, with the short and long

segments S and L between two neighboring wires. The distances S and L and thus also the average grating period are varied for the different quasiperiodic arrays and are given in Table 4.4.

Table 4.5: Short, long, and average distances of the different Cantor samples.

	short distance	long distance	average distance
Sample C1	≈ 396 nm	425 nm	400 nm
Sample C2	≈ 392 nm	450 nm	400 nm
Sample C3	≈ 389 nm	475 nm	400 nm
Sample C4	≈ 421 nm	450 nm	425 nm
Sample C5	≈ 417 nm	475 nm	425 nm
Sample C6	≈ 446 nm	475 nm	450 nm
Sample C7	400 nm	≈ 590 nm	425 nm
Sample C8	400 nm	≈ 780 nm	450 nm
Sample C9	400 nm	≈ 970 nm	475 nm
Sample C10	425 nm	≈ 615 nm	450 nm
Sample C11	425 nm	≈ 805 nm	475 nm
Sample C12	450 nm	≈ 640 nm	475 nm
Sample C13	400 nm	425 nm	≈ 403 nm
Sample C14	400 nm	450 nm	≈ 407 nm
Sample C15	400 nm	475 nm	≈ 410 nm
Sample C16	425 nm	450 nm	≈ 428 nm
Sample C17	425 nm	475 nm	≈ 432 nm
Sample C18	450 nm	475 nm	≈ 453 nm

As already mentioned in section 2.3, two different Cantor-like sets, namely the $(3, \{1\}, 5)$ set (Cantor) and the $(6, \{1, 4\}, 3)$ set (Cantor-6), are used as fractal structures. The dimensions of the short, long and average distances are given in Tables 4.5 and 4.6 for the Cantor set and the Cantor-6 set, respectively. For comparison, also periodic gold wire arrangements with grating periods of 400 nm, 425 nm, 450 nm, and 475 nm are fabricated. All samples substrates consist of quartz with a 180 nm thick ITO waveguide layer on top. The gold wires with a width of 100 nm, a thickness of 20 nm, and a length of 100 μm are placed on the waveguide material and were fabricated via electron-beam-lithography and a subsequent evaporation process as described in section 3.1. Each array has a size of 100 μm $\times$ 100 μm.

Table 4.6: Short, long, and average distances of the different Cantor-6 samples.

	short distance	long distance	average distance
Sample C6-1	≈ 389 nm	425 nm	400 nm
Sample C6-2	≈ 379 nm	450 nm	400 nm
Sample C6-3	≈ 368 nm	475 nm	400 nm
Sample C6-4	≈ 414 nm	450 nm	425 nm
Sample C6-5	≈ 404 nm	475 nm	425 nm
Sample C6-6	≈ 439 nm	475 nm	450 nm
Sample C6-7	400 nm	≈ 484 nm	425 nm
Sample C6-8	400 nm	≈ 569 nm	450 nm
Sample C6-9	400 nm	≈ 653 nm	475 nm
Sample C6-10	425 nm	≈ 509 nm	450 nm
Sample C6-11	425 nm	≈ 594 nm	475 nm
Sample C6-12	450 nm	≈ 534 nm	475 nm
Sample C6-13	400 nm	425 nm	≈ 407 nm
Sample C6-14	400 nm	450 nm	≈ 415 nm
Sample C6-15	400 nm	475 nm	≈ 422 nm
Sample C6-16	425 nm	450 nm	≈ 432 nm
Sample C6-17	425 nm	475 nm	≈ 440 nm
Sample C6-18	450 nm	475 nm	≈ 457 nm

4.2.2   Normal incidence extinction spectra

The normal incidence extinction spectra of the periodic gold wire arrangements were measured as a reference. The TM (black lines) and TE polarized (red lines) spectra are shown in Fig. 4.18. The grating period was changed between $d_0 = 400$ nm (bottom) and $d_0 = 475$ nm (top) in steps of 25 nm. It can be seen that only one waveguide mode is excited for all spectra. However, the resonance peak of the waveguide mode is shifted to lower energies for larger grating periods. This is expected and has already been explained in sections 2.1.2 and 2.1.3.

The first measured samples with normal light incidence are the Fibonacci samples. The different spectra of samples $F1 - F6$, $F7 - F12$, and $F13 - F18$ are shown in Fig. 4.19, Fig. 4.20, and 4.21, respectively. Whereas TE polarized light (red lines) can only excite the waveguide modes, TM polarized light (black lines) additionally excites the particle plasmon. By looking at the TE polarized spectra of samples $F1 - F3$, it is found that the main waveguide mode is excited at the same energy position. The only visible difference is the changing resonance amplitude. This is also found
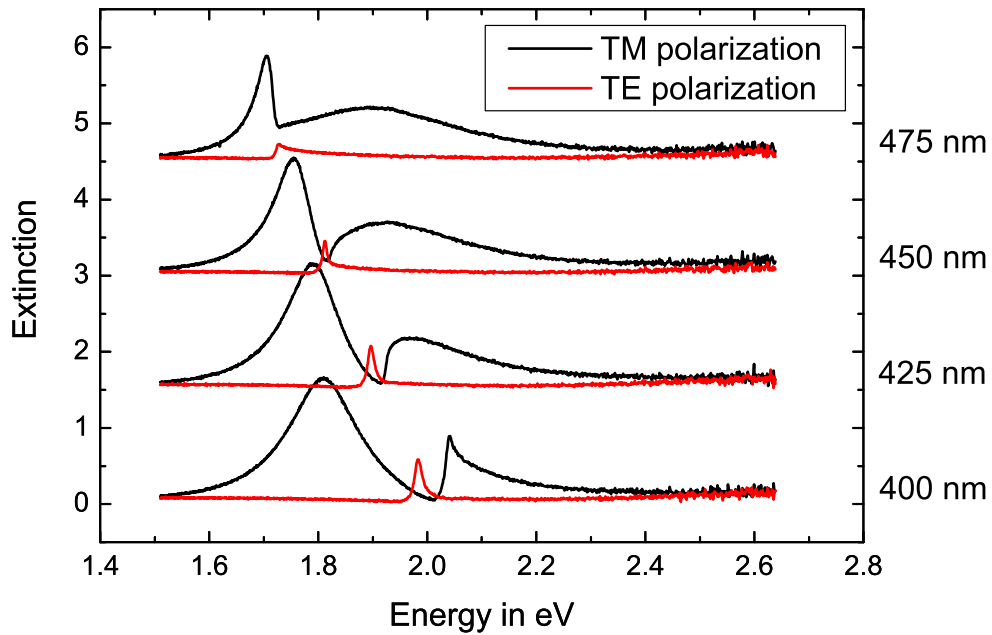
Figure 4.18: Extinction spectra of samples with periodic gold wire arrangements for normal light incidence in TM (black lines) and TE (red lines) polarization. The grating period d_0 is changed from 400 nm (bottom) to 475 nm (top) in steps of 25 nm. The different spectra are shifted upward for clarity.

for samples F4 and F5. However, the waveguide mode resonance is shifted to lower energies when compared to samples F1 − F3. The energy of sample F6 is again shifted to lower values. By looking at the specifications of these samples (Table 4.4), it is found that samples F1 − F3 possess an average wire distance of 400 nm and samples F4 and F5 an average distance of 425 nm. The average wire distance of sample F6 is 450 nm. The resonance energies of the periodic samples coincide with those of the Fibonacci samples with the according average wire distance. This indicates that the average wire distance is responsible for the location of the main waveguide mode. The same is true for the TM polarized spectra. Only the particle plasmon is additionally excited.

If this finding that the average wire distance is responsible for the main resonance energy was true, samples F8 and F10 as well as samples F9, F11, and F12 should possess the same resonance energy (see Fig. 4.20). Indeed, this can be obtained for the corresponding measurements. By comparing the spectra in Figs. 4.18, 4.19, and 4.20, the waveguide modes of the samples with the same average wire distance appear at the same energies.
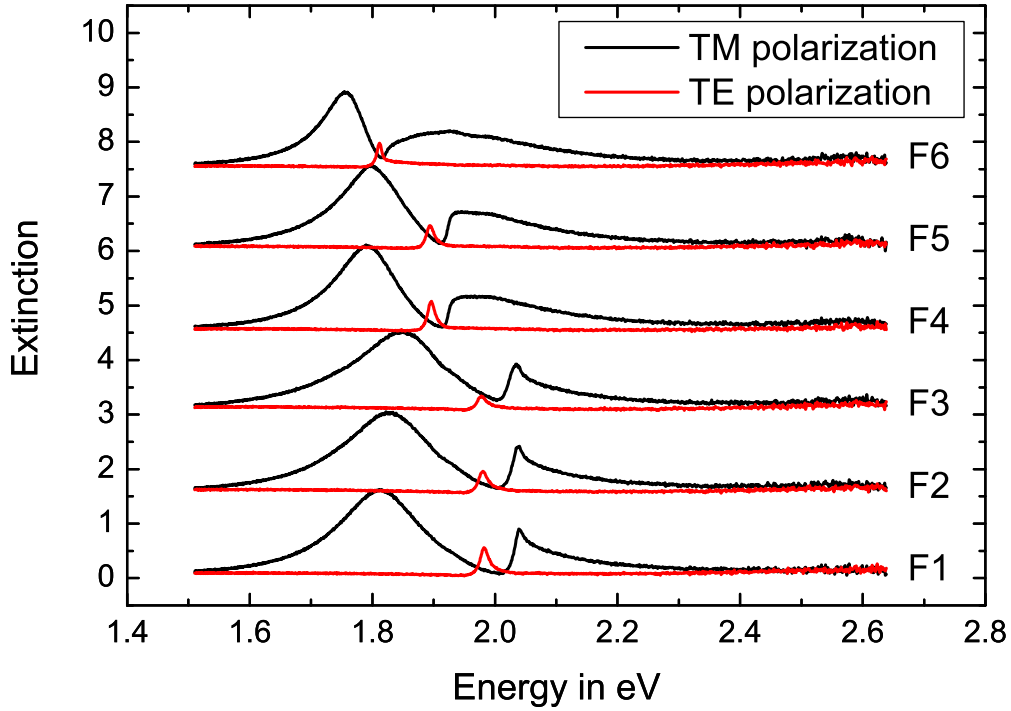
Figure 4.19: Extinction spectra of the Fibonacci samples F1 to F6 for normal light incidence in TM (black lines) and TE (red lines) polarization. The different spectra are shifted upward for clarity.

The waveguide mode resonance of samples F13 − F15 as well as of samples F16 − F18 is shifted to lower energies by increasing the sample number (Fig. 4.21). In contrast to the spectra in Figs. 4.19 and 4.20, the resonance energies are always different for each of the six individual samples. This can be explained by the corresponding average wire distances, which are never the same for these samples (Table 4.4). The average wire distance increases from sample F13 to sample F15. The same is true for sample F16 to F18. The average wire distance of sample F16 lies between that of samples F14 and F15. This can also be obtained in the spectra, where the waveguide mode energy of sample F16 is between that of the other two samples.

All the measurements of the Fibonacci samples have in common that the average wire distance determines the energy position of the main waveguide mode resonance as well as that the resonance amplitude is dependent on the other sample parameters. However, the latter finding is not yet analyzed in detail. In order to understand this behavior, the Fourier transform of the individual samples has to be considered. The Fourier transform is calculated by a computer program and the analysis of the Fourier peaks is done by following the procedure described in Ref. [135]. The
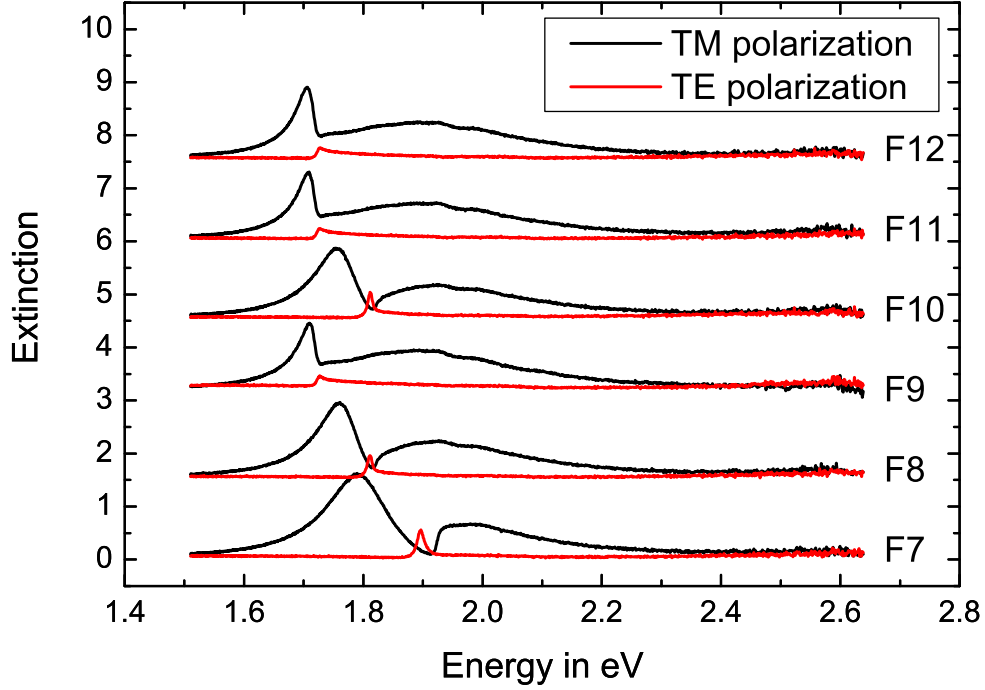
Figure 4.20: Extinction spectra of the Fibonacci samples F7 to F12 for normal light incidence in TM (black lines) and TE (red lines) polarization. The different spectra are shifted upward for clarity.

starting point is the higher-dimensional periodic real lattice (see Fig. 4.22 (a)) and its corresponding lattice in reciprocal space (see Fig. 4.22 (b)). Since the samples in this section are only Fibonacci-like structures, a rectangular lattice with lattice constants a in x direction and b in y direction has to be used (compare to Figs. 2.13 and 2.14 for the Fibonacci sequence). As already mentioned in section 2.4.1, the angle α_{new} between the physical space ξ and the x axis of the periodic grid is given by $\tan(\alpha_{new}) = \frac{b}{a\tau}$. This angle is maintained in reciprocal space. The short and long wire distances S and L are defined by $S = b\sin\alpha_{new}$ and $L = a\cos\alpha_{new}$, the average wire distance M is given by $M = \frac{S+\tau L}{1+\tau}$ [136]. As it is explained in Ref. [135], the reciprocal lattice points connected by a straight line (see Fig. 4.22 (b)) show periodic contributions to the Fourier transform of the Fibonacci sequence. The yellow dashed line segment in Fig. 4.22 (b) is repeated periodically in reciprocal physical space k_ξ and is given by

$$k_1 = \frac{2\pi/a}{\cos(\psi)}\cos(\psi - \alpha_{new}) = \ldots = 2\pi\frac{\tau+1}{S+\tau L} = \frac{2\pi}{M}. \tag{4.3}$$
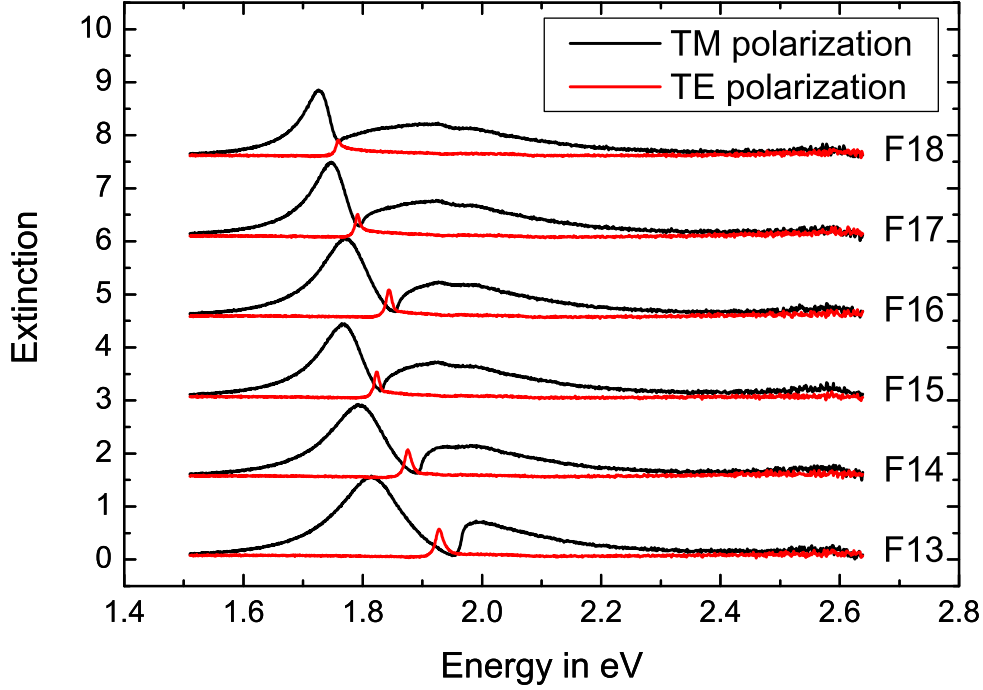
Figure 4.21: Extinction spectra of the Fibonacci samples F13 to F18 for normal light incidence in TM (black lines) and TE (red lines) polarization. The different spectra are shifted upward for clarity.

Equation (4.3) indeed proves that a waveguide mode resonance is present with an energy corresponding to the average distance M.

When a straight line in 2D reciprocal space crosses k_ξ, the amplitude is maximum at this crossing point. By increasing the k_ξ values, the distance of all the points on this line to the k_ξ axis also increases. Thus, the amplitude of the Fourier peaks varies with the sinc function given in Eq. (2.47). Therefore, the absolute value of the sinc function is the envelope curve of all peaks lying on a straight line in 2D reciprocal space. Two straight lines (dotted lines) with angle ψ to the k_x axis are plotted in Fig. 4.22 (b). One of these two lines crosses the k_ξ axis in the center of the reciprocal space, whereas the other one is shifted by $\frac{2\pi}{a}$ in k_x direction. Thus, the crossing point of the second line is given by $\left(\frac{2\pi a\tau}{\tau a^2 - b^2} / \frac{2\pi b}{\tau a^2 - b^2}\right)$. Therefore, the envelope curve corresponding to this second straight line is shifted by the value k_2 (red line segment in Fig. 4.22 (b)), which is given by

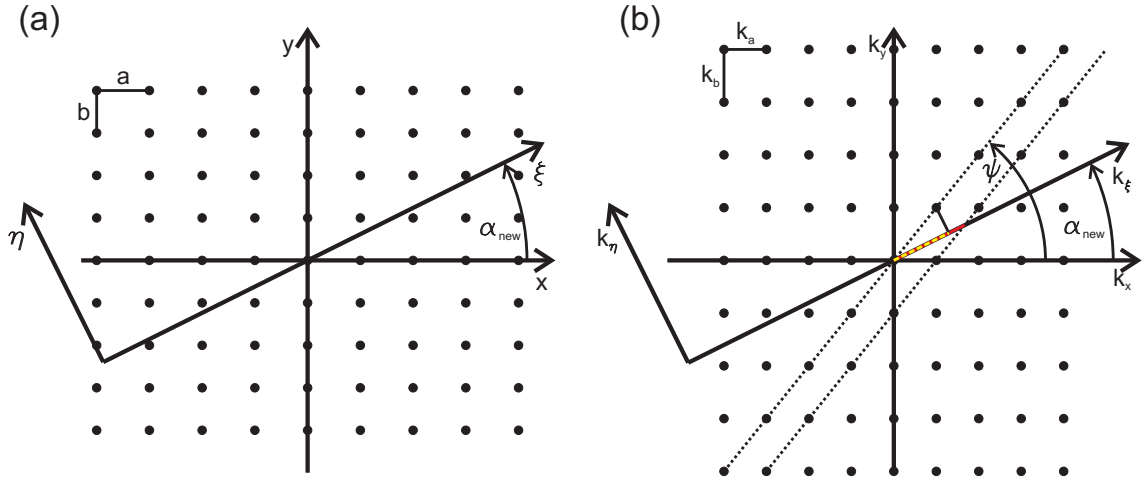$$k_2 = \frac{2\pi a\tau}{(\tau a^2 - b^2)\cos(\alpha_{new})} = \ldots = \frac{2\pi}{L - S}. \tag{4.4}$$

Figure 4.22: (a) A 2D periodic lattice with periods a and b in x and y direction in order to obtain the Fibonacci-like sequence in physical space ξ. (b) The corresponding 2D reciprocal lattice with periods $k_a = \frac{2\pi}{a}$ and $k_b = \frac{2\pi}{b}$ in k_x and k_y direction in order to obtain the Fourier transform of the Fibonacci-like sequence.

All the points in 2D reciprocal space are covered by periodically shifting the straight line in $\pm k_x$ direction leading to periodically shifted envelope functions. This is also found in Ref. [135], which is shown there in Fig. 4. However, in the paper of Wolny the diffraction pattern is shown (sinc^2), whereas in this thesis the Fourier transform is analyzed ($|\mathrm{sinc}|$).

The Fourier transforms of four different samples together with three envelope curves are exemplarily shown in Figs. 4.23 and 4.24. The red envelope function corresponds to the line through the center of the 2D reciprocal space with a slope $\frac{a}{b}$. The green and blue envelope curves correspond to straight lines with the same slope but with a shift of $\frac{2\pi}{a}$ and $\frac{4\pi}{a}$ in k_x direction, respectively. Note that the Fourier peaks do not reach the amplitude of the corresponding envelope function, which might be due to numerical limitations of the Fourier transform calculations. The small peaks around the main Fourier components belong to a shifted envelope function.

Sample F1 and sample F2, whose Fourier transforms are plotted in Fig. 4.23 (a) and (b), possess the same average wire distance ($M = 400\,\mathrm{nm}$). This means that the spectral distance between two neighboring Fourier peaks corresponding to the same envelope function is $k_1 = \frac{2\pi}{M} \approx 1.57 \times 10^7\,\frac{1}{\mathrm{m}}$ for both samples. However, the difference $L - S$ is about $85\,\mathrm{nm}$ for sample F1 and about $131\,\mathrm{nm}$ for sample F2. Thus, the shift k_2 between two neighboring envelope functions is different for both samples. This also means that the first zero of the envelope function, which also appears at k_2, is different for both samples. Since $L - S$ is bigger for sample F2, the halfwidth of the envelope function is smaller for this sample leading to a faster
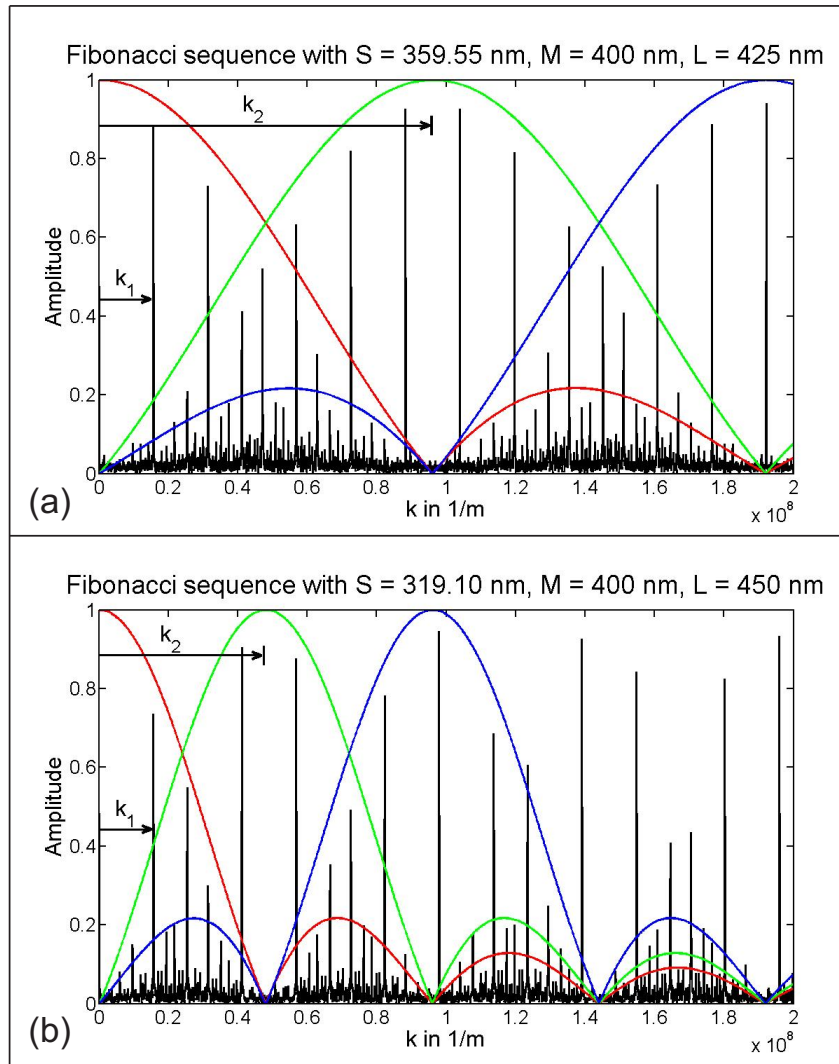
Figure 4.23: Fourier transforms for (a) sample F1 and (b) sample F2. The average wire distance is $M = 400\,\mathrm{nm}$ for both samples, but the difference $L - S$ is higher for sample F2. Three different envelope curves are also plotted for both samples.

reduction of the peak height. Therefore, the peak height strongly depends on k_2 when k_1 is kept constant. This is also seen in the measured spectra, where the waveguide mode resonance of samples F1 and F2 appears at the same energy with a slightly smaller amplitude of the sample F2 resonance. Note that *all* Fourier peaks of sample F1 appear at exactly the same position as those of sample F2 even though the two Fourier transforms look completely different. This is due to the different k_2 values of the two samples.

Samples F14 and F17, whose Fourier transforms are displayed in Fig. 4.24 (a) and (b), possess the same difference $L - S$ but a different average wire distance M. Since $L - S$ is equal to $50\,\mathrm{nm}$ for both samples, the halfwidths, the zeros, and the shift of the corresponding envelope functions are the same. However, due to the smaller
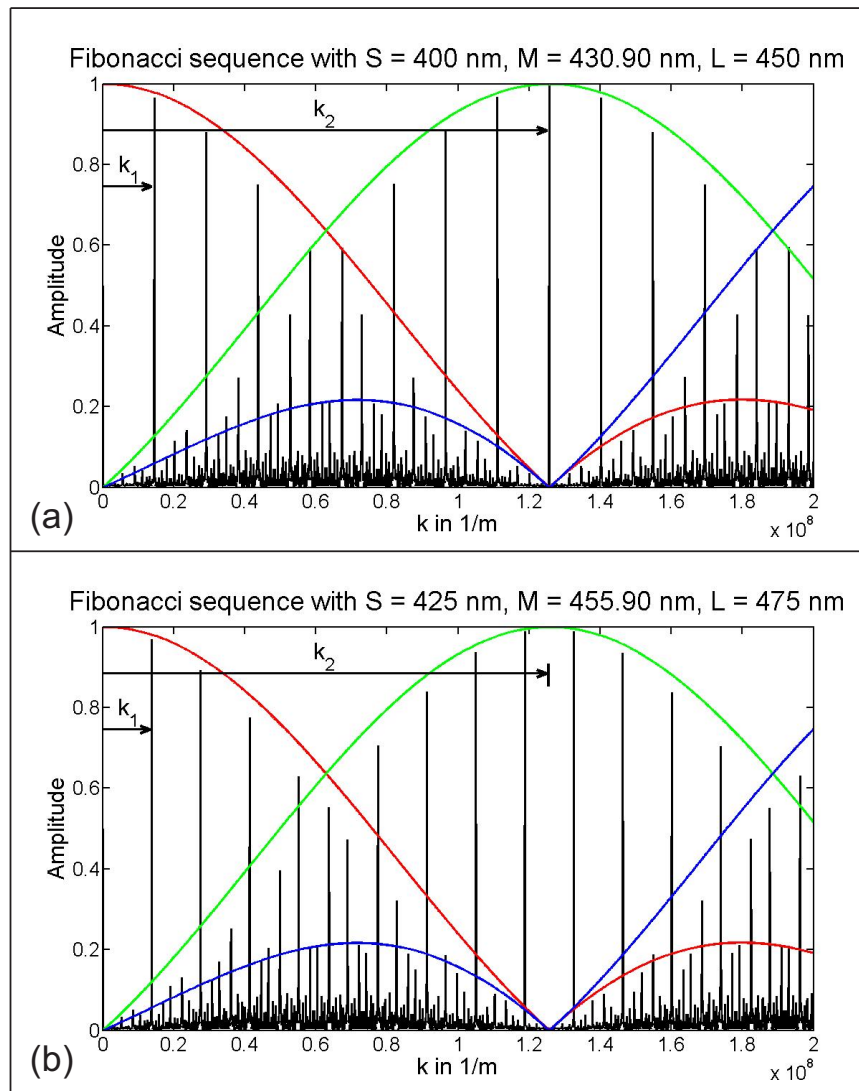
Figure 4.24: Fourier transforms for (a) sample F14 and (b) sample F17. The difference $L-S$ is equal to $50\,\text{nm}$ for both samples, but the average wire distance is higher for sample F17. Three different envelope curves are also plotted for both samples.

average wire distance of sample F14, two Fourier peaks of the same envelope function are further apart than for sample F17. Thus, the Fourier peaks of the two samples are *not* at the same position. Also in the spectra of these two samples the energy shift of the main waveguide mode resonance is visible.

The different spectra of all measured Fibonacci samples are consistent with the findings presented here. By using this approach, it is possible to tailor the sample parameters in order to obtain the desired resonances. The individual resonances can be shifted to other energies and the amplitudes of the resonances can be tuned.

The next measured samples are the Cantor samples. The spectra of samples $C1 - C6$, $C7 - C12$, and $C13 - C18$ are shown in Figs. 4.25, 4.26, and 4.27, respectively.
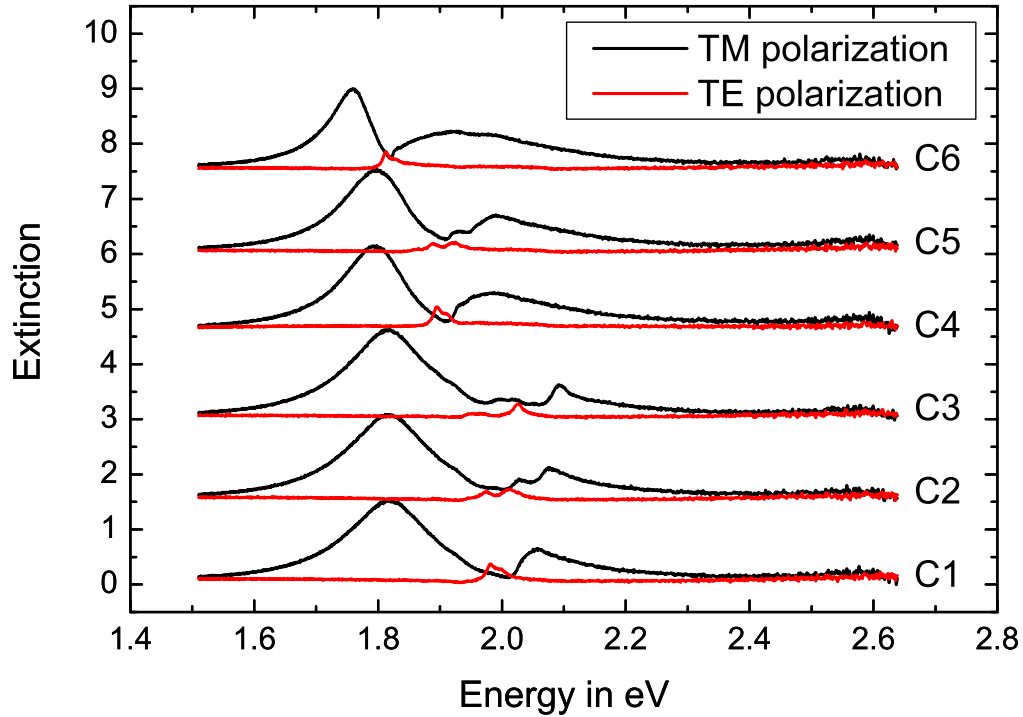
Figure 4.25: Extinction spectra of the Cantor samples C1 to C6 for normal light incidence in TM (black lines) and TE (red lines) polarization. The different spectra are shifted upward for clarity.

As above for the Fibonacci samples, the TM polarized spectra are shown as black curves and the TE polarized spectra as red curves. By looking at the spectra with TE polarization for samples C1 − C6, those of samples C1, C4, and C6 seem to be quite similar but with a shift of the resonance energies. All of these three spectra show a small double peak with approximately the same separation. The main resonances are located around the energy positions of the average wire distance. However, the short wire distance is also close to the average wire distance (see Table 4.5). Therefore, it is not clear whether the two peaks surround the location of the average wire distance or the short wire distance. Additionally, it cannot be clearly identified if one of the peaks is located at the resonance position of the average or the short wire distance. The TE spectra of samples C2 and C5 possess two clearly separated main peaks with approximately the same energy difference between them, but at different energy positions. It seems that the two peaks in each spectrum are shifted to slightly higher and lower energy positions when compared to the resonance position corresponding to the average wire distance. Whereas the amplitude of the lower energy peak is the bigger one in the spectra of samples C1, C4, and C6, the higher
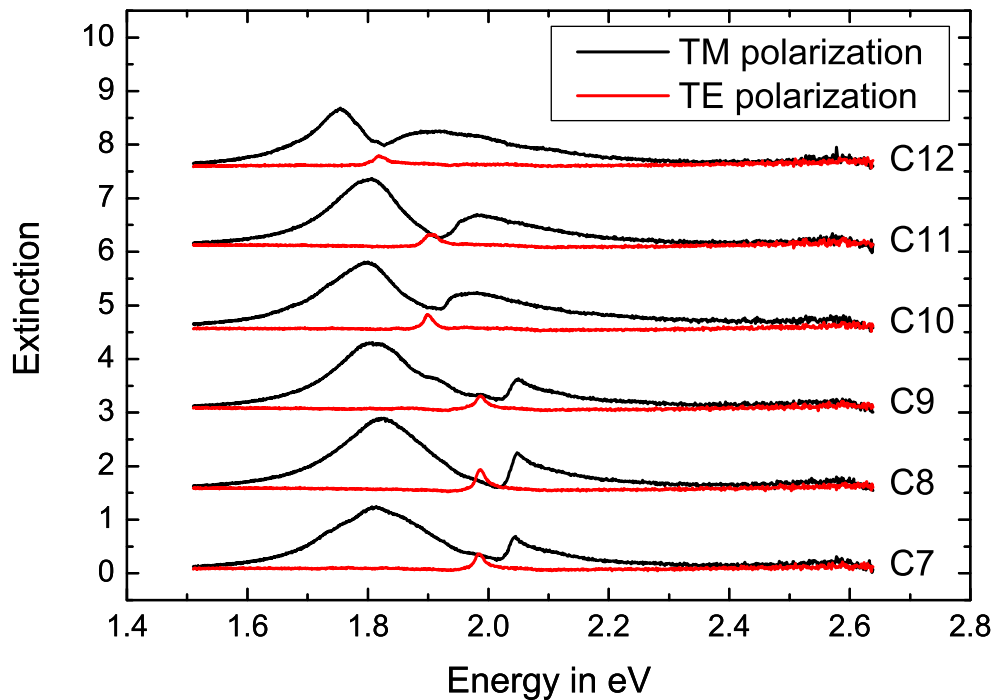
Figure 4.26: Extinction spectra of the Cantor samples C7 to C12 for normal light incidence in TM (black lines) and TE (red lines) polarization. The different spectra are shifted upward for clarity.

energy peak in the spectra of samples C2 and C5 has a slightly bigger amplitude. The two main peaks are further separated in the TE spectra of sample C3. They are again located around the energy position of the average wire distance. However, the lower energy peak is a quite broad peak with a low amplitude. It seems that this peak consists of at least two nearby resonances. The TM polarized spectra show in principle the same behavior with an additionally excited particle plasmon. However, the double peaks in the spectra of samples C1, C4, and C6 cannot be clearly obtained. By comparing the TM spectrum of sample C1 to that of the periodic sample with grating period 400 nm (see Fig. 4.18), the resonance positions appear at approximately the same energies. However, the higher energy resonance of sample C1 is much broader, which is due to the two waveguide modes with the small energy difference. In the TM spectra of samples C2 and C5, the two resonances of the mainly excited waveguide modes can be clearly obtained. The separation of the peaks can also be recognized in the TM spectrum of sample C3. In comparison to the TE spectrum of sample C3, the double peak of the lower energy waveguide
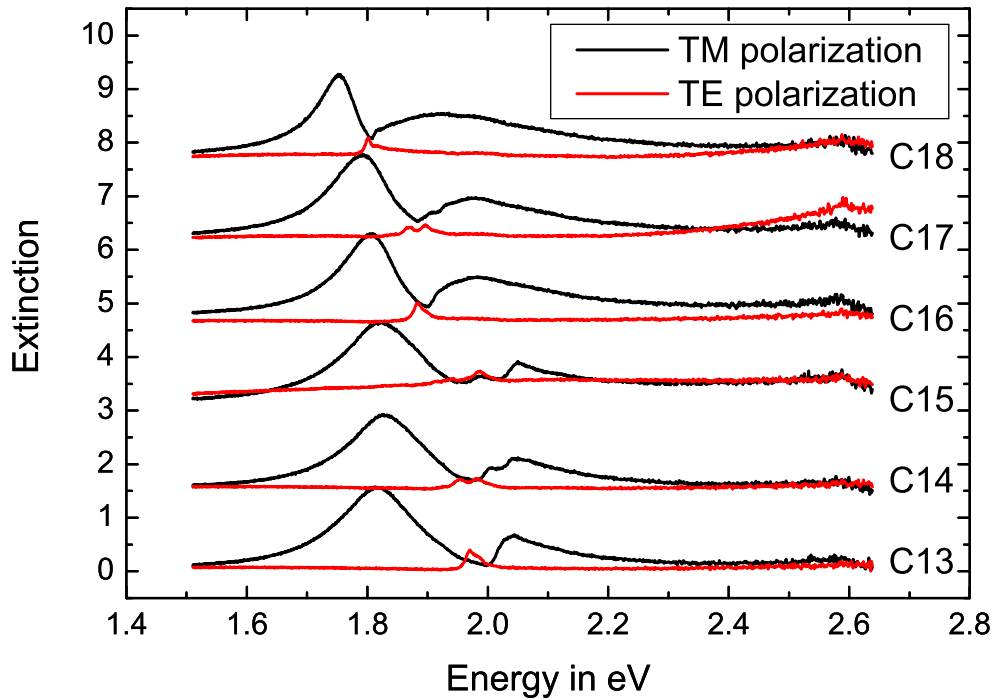
Figure 4.27: Extinction spectra of the Cantor samples C13 to C18 for normal light incidence in TM (black lines) and TE (red lines) polarization. The different spectra are shifted upward for clarity.

mode can be seen much better in the TM spectrum. Summing up the findings of samples C1 − C6, the main waveguide mode resonances arise at energy positions around the average wire distance with none of the peaks located at exactly the resonance corresponding to this distance. The separation between the waveguide mode resonances increases for a bigger large wire distance. It seems that the lower energy peak consists of several resonances that are further apart from each other for a bigger large wire distance.

In each TE polarized spectrum of samples C7 − C12 (see Fig. 4.26) only one main peak is visible. By comparing these resonance positions to the ones in the spectra of the periodic gratings (see Fig. 4.18), it is found that they are located at the energy positions of the corresponding short wire distance. The other resonances visible in the spectra of samples C1 − C6 cannot be obtained here. Since all the resonances should appear around the corresponding average wire distance, the separation between these peaks must be quite large. In the spectra of samples C1 − C6 it is also found that the lower energy peak consists of several resonances. These

resonances are distributed over a larger energy range with a smaller amplitude when the large wire distance is bigger. Therefore, it is probably hard to measure these resonances for samples $C7 - C12$. In the TM polarized spectra some modulations in the particle plasmon resonance are visible, especially for samples C7 and C9. These modulations are due to excited waveguide modes. However, it is not clear which sample parameters are responsible for these resonances.

The spectra of samples $C13 - C18$ in Fig. 4.27 are quite similar to those of samples $C1 - C6$ in Fig. 4.25. However, the separation between the two excited main peaks is a little bit smaller for samples $C13 - C18$. It has been said for samples $C1 - C6$ that the separation between the waveguide mode resonances increases for a bigger large wire distance. Since the large wire distance is the same in the corresponding spectra of samples $C1 - C6$ and $C13 - C18$, the increasing separation might be due to the increasing difference $L - S$. By comparing the spectra of samples $C13 - C18$ to those of the periodic samples, it is found that the higher energy resonance corresponds to the waveguide mode of the periodic sample with a grating period equal to the short wire distance of the Cantor sample. This is in agreement with the findings above. It is also found that the lower energy peak consists of several resonances that are distributed over a larger energy range for a larger difference $L - S$.

In summary, the resonances in the Cantor spectra are located around the energy corresponding to the average wire distance and the higher energy mode corresponds to the individual short wire distance. The lower energy peak consists of several resonances that are distributed over a larger energy range for an increased difference $L - S$. The separation between higher and lower energy peaks is dependent on the difference $L - S$. However, a detailed analysis of the Fourier transform as in the case of the Fibonacci-like sequence is not possible since there is no similar construction method of the Cantor sequence making use of a higher-dimensional space. Therefore, it is not known which sample parameters are responsible for all the Fourier peaks. However, all the resonances are in agreement with the Fourier peaks in the numerically calculated Fourier transform of the corresponding Cantor lattices.

The last measured samples were those with the Cantor-6 structured gold wire arrays. The TM (black lines) and TE (red lines) spectra of samples $C6\text{-}1 - C6\text{-}6$, $C6\text{-}7 - C6\text{-}12$, and $C6\text{-}13 - C6\text{-}18$ are shown in Figs. 4.28, 4.29, and 4.30, respectively. In all spectra multiple waveguide mode resonances are excited. It can be seen in the TE spectra of samples C6-1, C6-4, and C6-6 that these resonances are excited
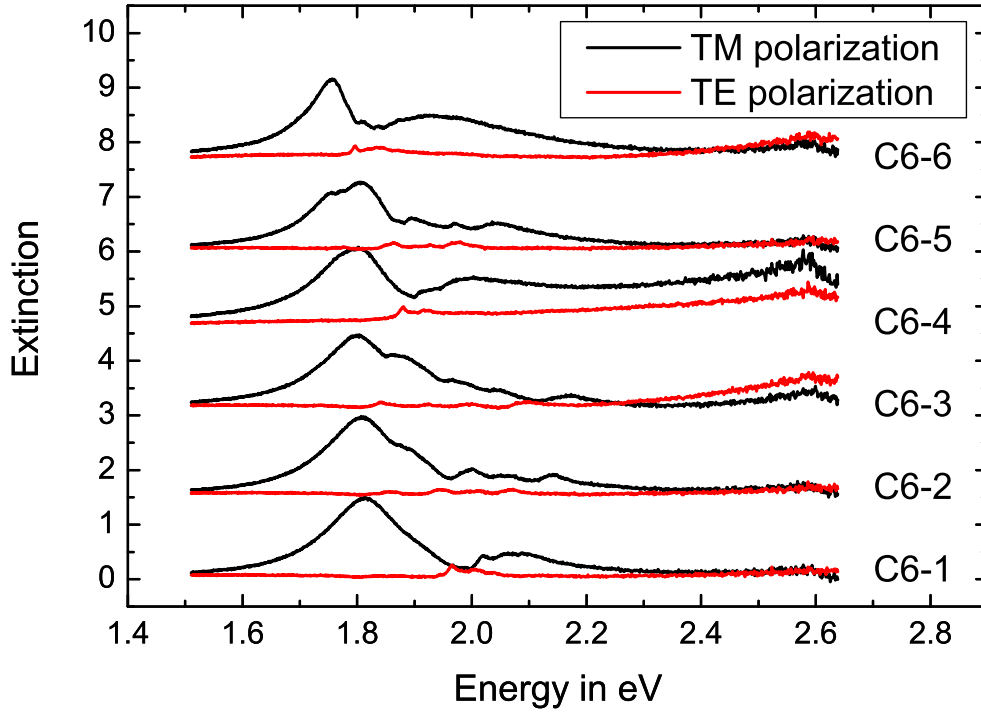
Figure 4.28: Extinction spectra of the Cantor-6 samples C6-1 to C6-6 for normal light incidence in TM (black lines) and TE (red lines) polarization. The different spectra are shifted upward for clarity.

over a small energy range with a shift to lower energies for a higher average wire distance. By comparing these spectra to the periodic ones, it is found that the resonance corresponding to the average wire distance is located between the two main resonances of the Cantor-6 samples. In the spectra of samples C6-2 and C6-6 four main peaks are visible. They are spread over a larger energy range when compared to samples C6-1, C6-4, and C6-6. The resonances of sample C6-2 are located at higher energies than the resonances of sample C6-5 due to the lower average wire distance. As for samples C6-1, C6-4, and C6-6, the main peaks of samples C6-2 and C6-6 are centered around the k value corresponding to the average wire distance. In the spectrum of sample C6-3 also four main peaks centered around $\frac{2\pi}{M}$ are visible. These peaks cover a relatively broad energy range. As it has been observed for the Cantor samples, the main peaks of the Cantor-6 samples are located around the average wire distance. The energy range over which the resonances are excited also increases for a larger difference $L - S$. However, in comparison to the Cantor samples, more resonances are excited for the Cantor-6 samples which are spread over a larger energy range.
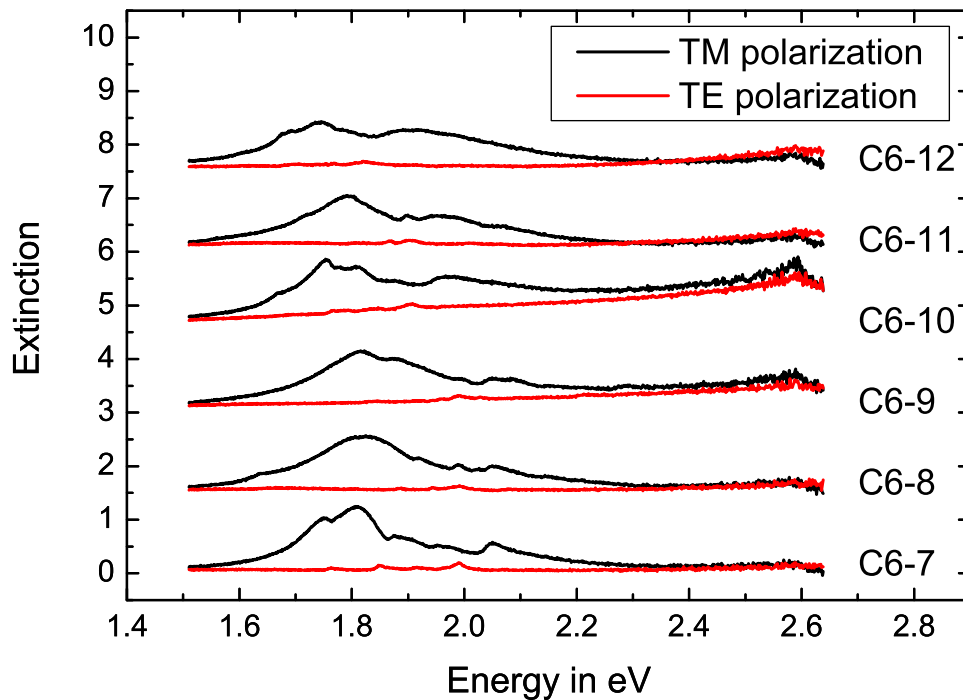
Figure 4.29: Extinction spectra of the Cantor-6 samples C6-7 to C6-12 for normal light incidence in TM (black lines) and TE (red lines) polarization. The different spectra are shifted upward for clarity.

The second set of Cantor-6 measurements (samples C6-7 − C6-12) is shown in Fig. 4.29. In the spectra of samples C6-7, C6-10, and C6-12 three or four main peaks are visible. The separation between the individual peaks is comparable for these three spectra. The peaks are located around the energy position of the average wire distance. The energy range covered by the excited resonances is already large when compared to the spectra of samples C6-1 − C6-6. This can be explained by the fact that $L − S$ is quite large for these samples. The peak with the highest energy is approximately located at the resonance position corresponding to the short wire distance. This has also been observed for the Cantor samples. Samples C6-8, C6-9, and C6-11 also possess a resonance at the energy of about the short wire distance. However, this is not necessarily at the peak possessing the highest energy. It cannot be observed in these three spectra that the peaks are located around the energy position corresponding to the average wire distance. This can be due to the weaker amplitudes of the lower energy peaks. Another possibility might be that these waveguide modes cannot be excited due to an energy below cutoff.
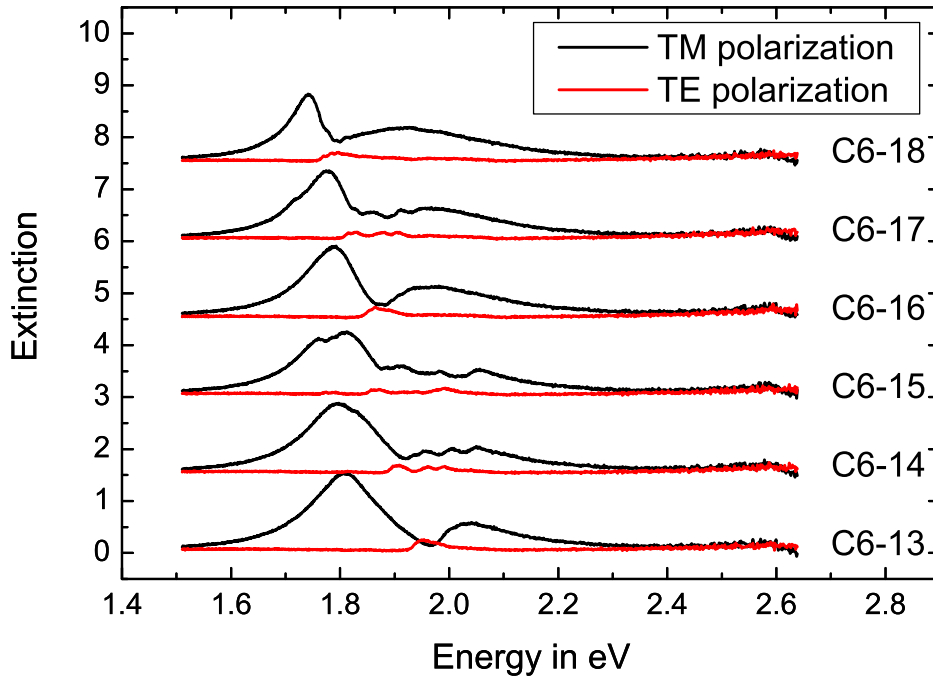
Figure 4.30: Extinction spectra of the Cantor-6 samples C6-13 to C6-18 for normal light incidence in TM (black lines) and TE (red lines) polarization. The different spectra are shifted upward for clarity.

The measurements of the samples C6-13 − C6-18 are consistent with the findings above. The resonance of a periodic grating with a periodicity corresponding to the short wire distance is always at the peak positions of one of the higher energy peaks. The covered energy range of the main peaks is larger for a larger difference between the L and the S segment. All the peaks are approximately located around the energy corresponding to the average wire distance. These findings are consistent with those of the Cantor sample. However, for the Cantor-6 samples more waveguide modes are excited and the main peaks are spread over a larger energy range. As already mentioned for the Cantor set, a detailed analysis of the Fourier transform as in the case of the Fibonacci-like sequence is also not possible for the Cantor-6 set.

CHAPTER 5

2D PLASMONIC STRUCTURES

In this chapter the measurements of 2D quasiperiodic and 2D periodic plasmonic crystals are compared. First, the normal incidence spectra are presented. Afterwards, a theoretical model is developed for 2D metallic photonic crystals with normal light incidence. Next, measurements for oblique light incidence are shown. The theoretical model is then expanded for inclined light incidence. In the last section, the theoretical model is used to predict the absorbance spectra of 2D quasiperiodic plasmonic solar cells.

5.1 Sample designs

The samples in this chapter are 2D metallic photonic crystals with gold disks on top of a hafnium dioxide (HfO_2) waveguide layer with a thickness of $t_{wg} = 180\,\mathrm{nm}$, which is shown in Fig. 5.1 (a) and (b). The gold disks of 25 nm height are elliptically shaped and rotated by the angle γ around the x axis of the sample. The short main axis diameter of the gold disk has a length d_u and the long main axis diameter a length d_v (see Fig. 5.1 (c) and (d)). The arrangement of the gold dots is either periodic with a periodicity of P_x in x direction and with P_y in y direction (Fig. 5.1 (b) and (d)) or it is quasiperiodic with the gold disks placed on the vertices of a Penrose tiling with an edge length of $P = 530\,\mathrm{nm}$ (Fig. 5.1 (a) and (c)). Note that the Penrose tiling is not a real Penrose tiling but an approximant, where the golden mean τ in perpendicular space is approximated by the rational number $\tau' = \frac{8}{5}$ (see Eq. (2.51) in section 2.4.2). However, in the following sections it is just called a Penrose tiling. Two different periodic structures were fabricated: a square lattice with $P_x = P_y = 530\,\mathrm{nm}$ and a rectangular lattice with $P_x = 492\,\mathrm{nm}$ and $P_y = 570\,\mathrm{nm}$. The diameters of the gold disks d_u and d_v as well as the rotation of
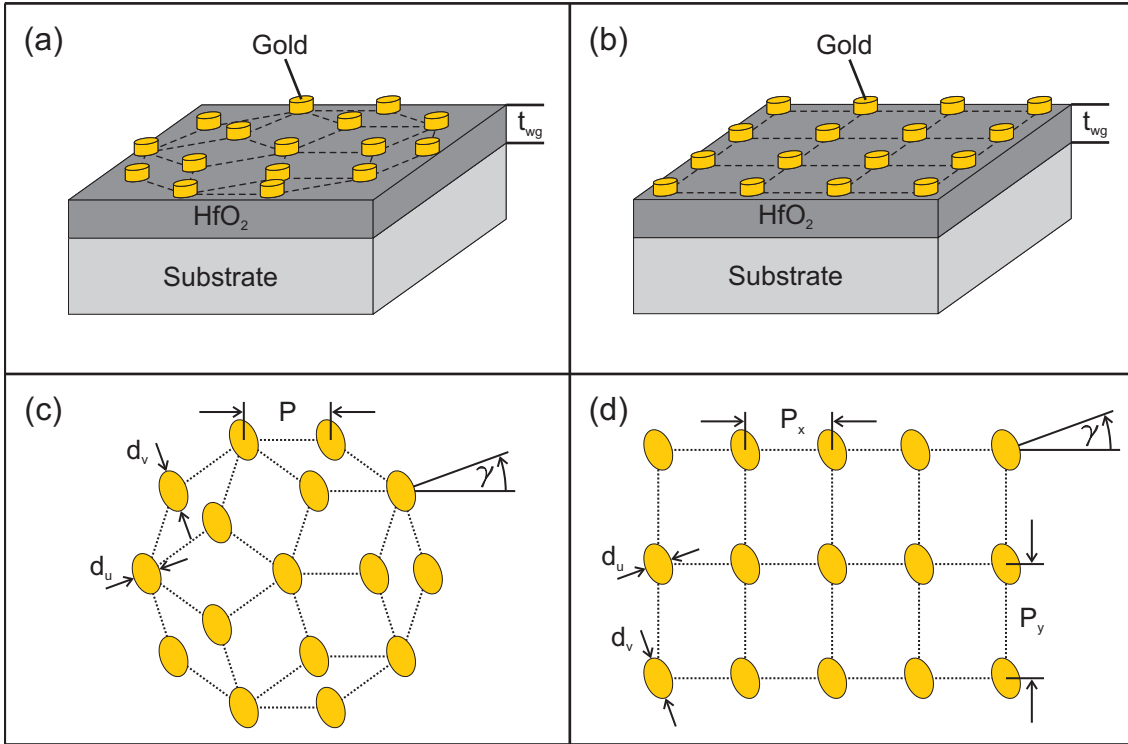
Figure 5.1: Sample design of (a) a 2D quasiperiodic arrangement and (b) a 2D periodic arrangement of gold disks on top of a 180 nm thick HfO_2 waveguide layer and a quartz substrate. The elliptically shaped dots with main axis diameters d_u and d_v and a rotation of γ around the sample x axis are arranged (c) on the vertices of a Penrose tiling with an edge length P and (d) in a periodic fashion with periodicities P_x and P_y.

the disks around the x axis are varied for different samples. This is indicated for the specific measurements in this chapter.

5.2   Normal incidence extinction spectra

The gold disks of sample 1 possess an average short main axis diameter of $d_u = 120$ nm, an average long main axis diameter of $d_v = 130$ nm, and a rotation of $\gamma = 0°$ around the sample x axis. For this sample, a second layer of 25 nm high gold disks separated by 50 nm of magnesium fluoride (MgF_2) is present as well. The intension was a coupling of the two excited particle plasmons. When the disks in both gold particle layers are equal in size, the particle plasmons should appear at the same photon energy. Due to the close distance to the other gold particle, both resonances should be coupled leading to shifts to lower energies as well as to higher energies. However, the diameters of the gold disks in the upper layer are much smaller than those of the lower layer. Therefore, the particle plasmon energy of the

gold disks in the upper layer is at higher energies and not in the energy range of the measured spectra. Thus, the two particle plasmons are not coupled to each other. The particle plasmon of the upper gold layer is not considered in the following. Two different structure designs were fabricated: a Penrose tiling with an edge length $P = 530\,\text{nm}$ and a periodic lattice with $P_x = P_y = 530\,\text{nm}$. These measurements have already been shown in Ref. [137]. However, these results are shown here in order to compare them to other geometries of the gold disks.
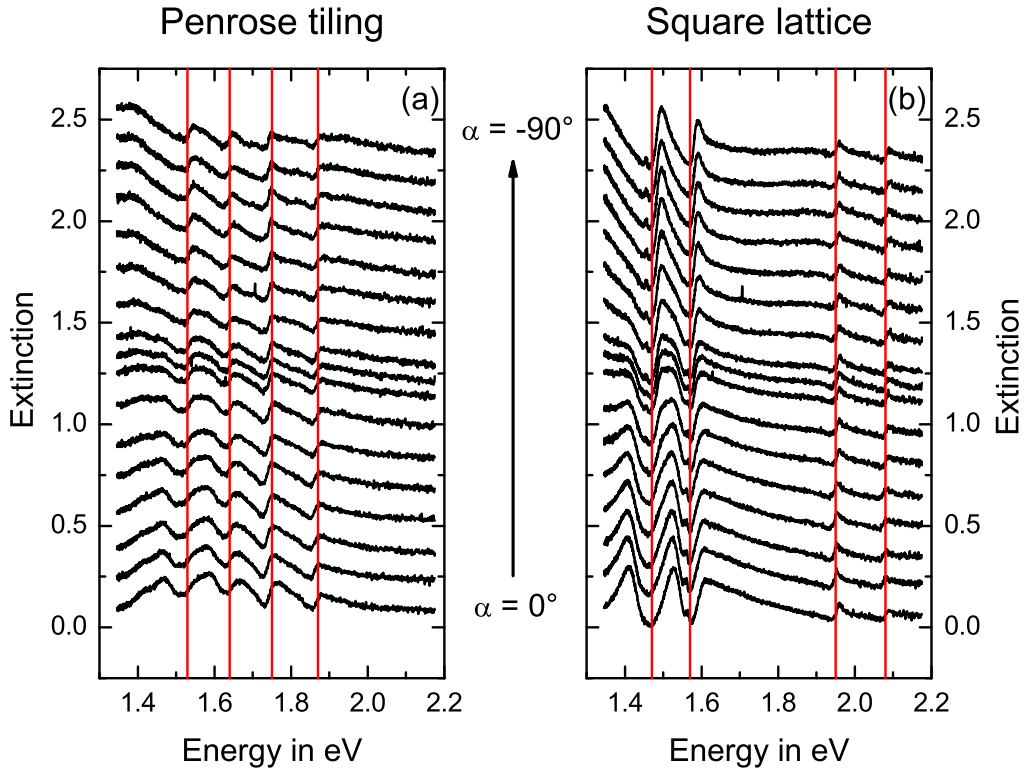

Figure 5.2: Extinction spectra of (a) a Penrose tiling with $P = 530\,\text{nm}$ and of (b) a square lattice with $P_x = P_y = 530\,\text{nm}$. The main axis diameters of the gold disks are $d_u = 120\,\text{nm}$ and $d_v = 130\,\text{nm}$ with a rotation of $\gamma = 0°$ around the sample x axis. The incident polarization was changed from $\alpha = 0°$ (bottom) to $\alpha = -90°$ (top). The spectra are shifted upward for clarity.

The extinction spectra of the Penrose tiling and the square lattice are displayed in Fig. 5.2 (a) and (b), respectively. The incident polarization is changed between $\alpha = 0°$ and $\alpha = -90°$ in steps of $-6°$. The spectrum in the center has a polarization of $45°$. This means that the polarization difference is $3°$ when compared to the previous and the following spectra. This is indicated by the smaller offset between the spectra. The particle plasmon for an incident polarization of $\alpha = 0°$ is located

at higher energies (approximately at $1.6\,\text{eV}$) when compared to the particle plasmon for a polarization of $\alpha = -90°$ (approximately at $1.4\,\text{eV}$). This is due to the fact that the main axis diameter of the gold disks in x direction (corresponding to $\alpha = 0°$) is shorter than the one in y direction. In the theory section 2.1.1 it is explained that a smaller main axis diameter results in a larger form factor. Thus, the resonance frequency (or energy) is shifted to higher values. The red lines in Fig. 5.2 (a) and (b) indicate the location of the expected waveguide modes. For the Penrose tiling, TE and TM polarized waveguide modes propagating in directions $0°$, $36°$, ... excite the first two resonances, and TE and TM polarized waveguide modes in directions $18°$, $54°$, ... excite the last two resonances. For the square lattice, the first two resonances are due to TE and TM polarized waveguide modes along the sample x or y direction, whereas the last two resonances arise due to TE and TM polarized waves in diagonal direction. A more detailed description of the expected positions of the waveguide modes is given in section 5.3. The lower energy waveguide modes are located within the particle plasmon resonance leading to a coupling between the waveguide modes and the particle plasmon. This can be seen by the fact that the expected waveguide mode energy is not at a peak position but rather at a dip position. For the waveguide mode resonances at approximately $1.65\,\text{eV}$ and $1.75\,\text{eV}$ of the Penrose tiling (Fig. 5.2 (a)), it can be seen that the red line is almost at the energy position of a peak maximum for a polarization $\alpha = -90°$. However, due to the fact that the particle plasmon shifts to higher energies for a polarization of $\alpha = 0°$, the coupling between the waveguide modes and the particle plasmon is stronger leading to an extinction maximum at slightly higher energies than the expected ones for the waveguide modes. In the spectra of both the quasiperiodic lattice and the periodic lattice, waveguide mode resonances at four different energies are visible for normal incidence. However, the waveguide modes differ in their energy positions when the spectra of the Penrose tiling are compared to those of the square lattice. The situation changes for oblique light incidence what will be discussed in section 5.5.

The gold disks of sample 2 possess an average short main axis diameter of $d_u = 97\,\text{nm}$, an average long main axis diameter of $d_v = 118\,\text{nm}$, and a rotation of $\gamma = 40°$ around the sample x axis. For this sample, only one layer of gold particles is present as shown in Fig. 5.1 (a) and (b). The quasiperiodic sample is a Penrose tiling with an edge length of $P = 530\,\text{nm}$ and the two periodic samples are one sample with a square lattice and $P_x = P_y = 530\,\text{nm}$ as well as one sample with a rectangular lattice and $P_x = 492\,\text{nm}$ and $P_y = 570\,\text{nm}$.
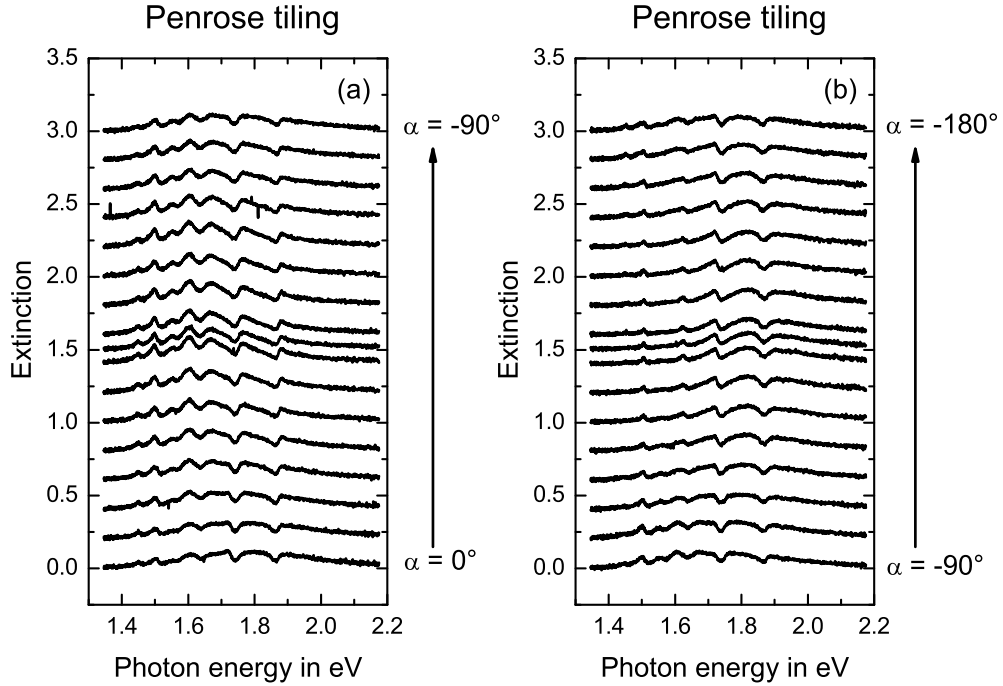
Figure 5.3: Extinction spectra of a Penrose tiling with $P = 530\,\text{nm}$. The main axis diameters of the gold disks are $d_u = 97\,\text{nm}$ and $d_v = 118\,\text{nm}$ with a rotation of $\gamma = 40°$ around the sample x axis. The incident polarization was changed from (a) $\alpha = 0°$ (bottom) to $\alpha = -90°$ (top) and from (b) $\alpha = -90°$ (bottom) to $\alpha = -180°$ (top). The spectra are shifted upward for clarity.

The extinction spectra for the Penrose tiling, the square lattice, and the rectangular lattice are shown in Figs. 5.3, 5.4, and 5.5, respectively. The polarization of the normally incident light is changed from (a) $\alpha = 0°$ to $\alpha = -90°$ and from (b) $\alpha = -90°$ to $\alpha = -180°$ in steps of $-6°$. Measurements with a polarization of $\alpha = -45°$ as well as with $\alpha = -135°$ are also included. The spectra of the different sample designs have in common that a particle plasmon at a photon energy of approximately $1.6\,\text{eV}$ is visible for a polarization of about $\alpha = -50°$ as well as a particle plasmon at approximately $1.8\,\text{eV}$ for $\alpha = -140°$. This is due to the fact that the short main axis of the gold disks is rotated by $40° = -140°$ and the long main axis by $130° = -50°$ with respect to the x axis of the sample. Especially in the spectrum of the square lattice with $\alpha = 0°$ it is visible that two particle plasmon resonances are excited, namely that along the short main axis and that along the long main axis. In the bottom curve of Fig. 5.4 (a), this can be obtained by the broad resonance at about $1.8\,\text{eV}$ and the shoulder at lower energies. This is due to the fact that particle plasmons can only be excited along the principal axes [93, 94].
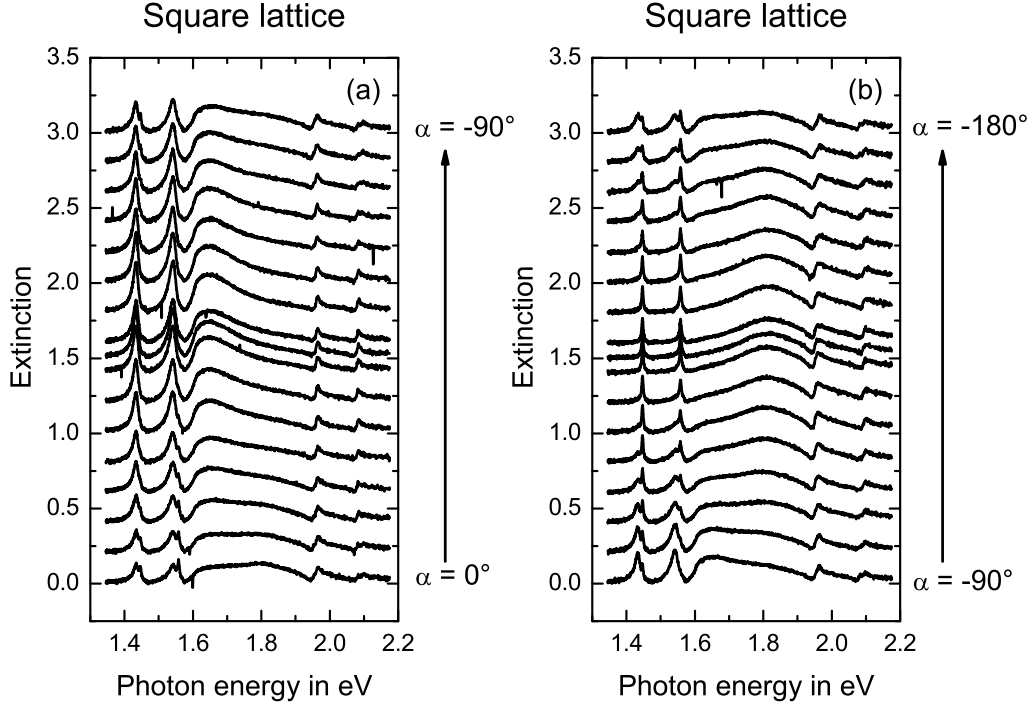
Figure 5.4: Extinction spectra of a square lattice with $P_x = P_y = 530\,\text{nm}$. The main axis diameters of the gold disks are $d_u = 97\,\text{nm}$ and $d_v = 118\,\text{nm}$ with a rotation of $\gamma = 40°$ around the sample x axis. The incident polarization was changed from (a) $\alpha = 0°$ (bottom) to $\alpha = -90°$ (top) and from (b) $\alpha = -90°$ (bottom) to $\alpha = -180°$ (top). The spectra are shifted upward for clarity.

The particle plasmon resonances are modulated by the waveguide mode resonances leading to waveguide-plasmon-polaritons. As already described for Fig. 5.2, the first two and the last two waveguide mode resonances for the Penrose tiling are due to TE and TM polarized waves propagating along the directions $0°$, $36°$, ... as well as to TE and TM polarized waves propagating along $18°$, $54°$, ..., respectively. At approximately $1.45\,\text{eV}$ and $1.55\,\text{eV}$, additional resonances are more or less visible. The energies of these additional resonances correspond to TE and TM polarized waves with a propagation constant of approximately $\frac{2\pi}{530\,\text{nm}}$. However, it is not clear why these resonances arise since there are no main Fourier peaks for the Penrose tiling for this k value. It might be possible that the Fourier peaks with this k value are enhanced in comparison to the other Fourier peaks due to sample imperfections.

For the square lattice, the first two resonances arise due to TE and TM polarized waves propagating in x or y direction. The last two resonances stem from TE and TM waves propagating in diagonal direction. As it can be seen in the bottom curve
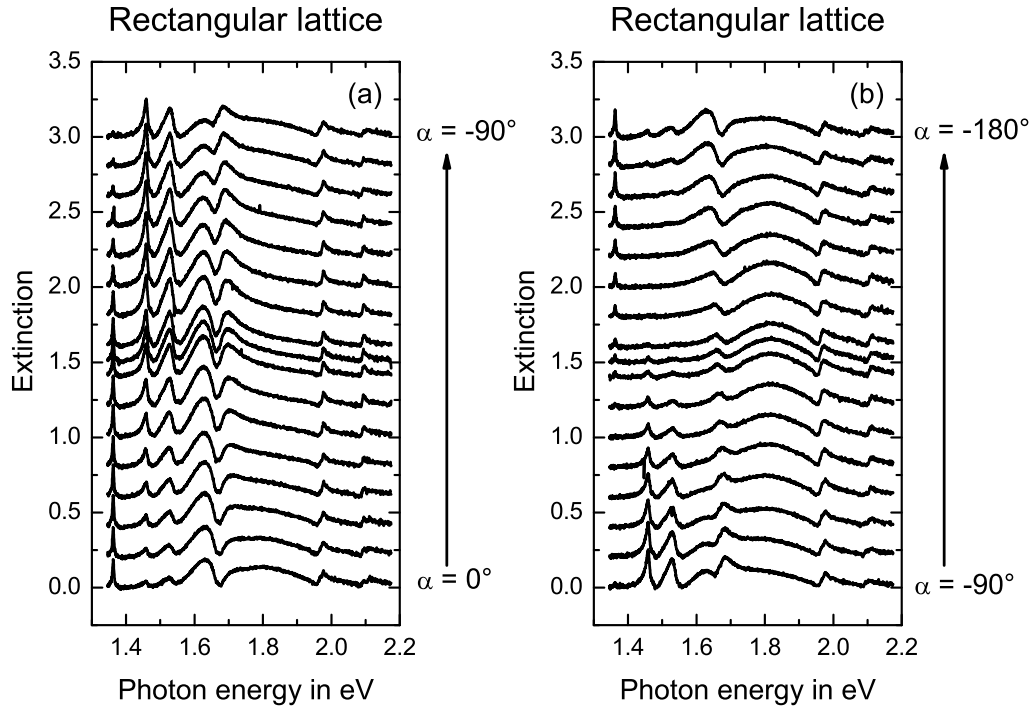
Figure 5.5: Extinction spectra of a rectangular lattice with $P_x = 492\,\text{nm}$ and $P_y = 570\,\text{nm}$. The main axis diameters of the gold disks are $d_u = 97\,\text{nm}$ and $d_v = 118\,\text{nm}$ with a rotation of $\gamma = 40°$ around the sample x axis. The incident polarization was changed from (a) $\alpha = 0°$ (bottom) to $\alpha = -90°$ (top) and from (b) $\alpha = -90°$ (bottom) to $\alpha = -180°$ (top). The spectra are shifted upward for clarity.

of Fig. 5.4 (a), the first two resonances consist of double peaks indicating a slight deviation of the two periodicities in x and y direction.

The waveguide mode resonances of the rectangular lattice are due to TE and TM polarized waves propagating in y direction, in x direction as well as in diagonal direction. The individual resonances are more or less pronounced since TE and TM waves in x or y direction cannot always be excited. It is expected that only a TE polarized wave can be excited in y direction (resonance at about $1.35\,\text{eV}$) and only a TM polarized wave can be excited in x direction (resonance at about $1.65\,\text{eV}$) for $\alpha = 0°$. By looking at the bottom spectrum of Fig. 5.5 (a), there are resonances clearly visible that are due to TM polarized waves propagating in y direction (resonance at about $1.45\,\text{eV}$) as well as due to TE polarized waves propagating in x direction (resonance at about $1.55\,\text{eV}$). This deviation is connected to the particle plasmons and will be explained in detail in section 5.3.
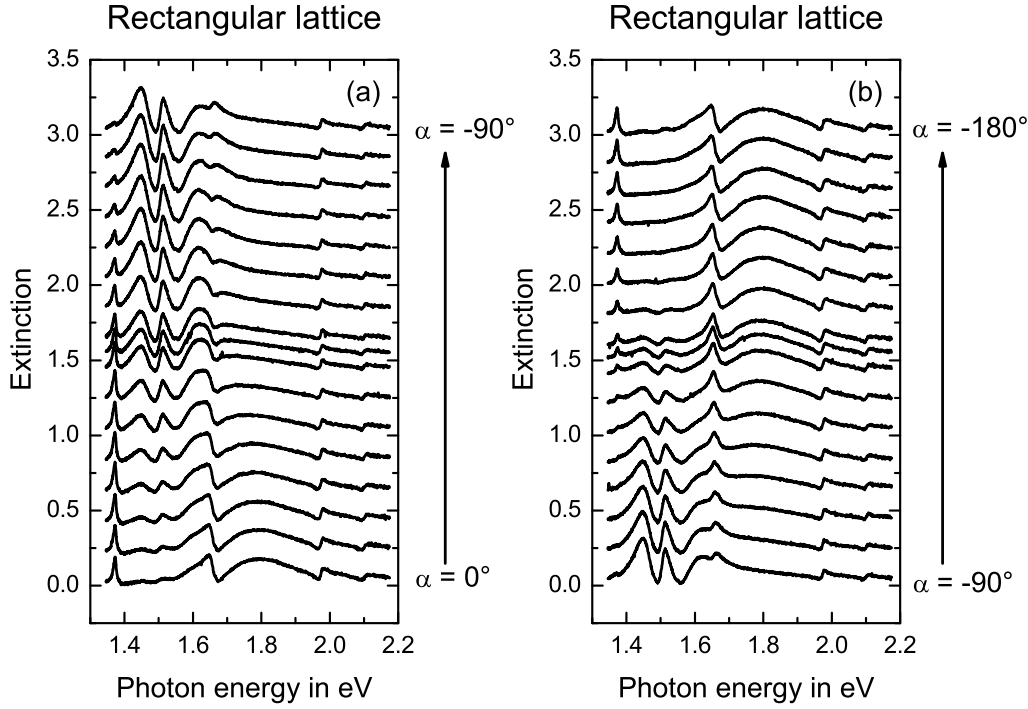
Figure 5.6: Extinction spectra of a rectangular lattice with $P_x = 492\,\mathrm{nm}$ and $P_y = 570\,\mathrm{nm}$. The main axis diameters of the gold disks are $d_u = 88\,\mathrm{nm}$ and $d_v = 120\,\mathrm{nm}$ with a rotation of $\gamma = 25°$ around the sample x axis. The incident polarization was changed from (a) $\alpha = 0°$ (bottom) to $\alpha = -90°$ (top) and from (b) $\alpha = -90°$ (bottom) to $\alpha = -180°$ (top). The spectra are shifted upward for clarity.

Another sample (sample 3) consisting of gold disks with average main axis diameters $d_u = 88\,\mathrm{nm}$ and $d_v = 120\,\mathrm{nm}$ as well as a rotation of $\gamma = 25°$ around the x axis of the sample was fabricated. The second layer of smaller gold particles separated by $50\,\mathrm{nm}$ $\mathrm{MgF_2}$ is also present for this sample. However, the particle plasmons of the upper gold disk layer do not influence the spectra in the measured energy range due to the much smaller particle diameters. In order to study the above mentioned influence of the particle plasmons due to the rotated, elliptical gold particles in the lower gold disk layer, a rectangular arrangement of gold disks with $P_x = 492\,\mathrm{nm}$ and $P_y = 570\,\mathrm{nm}$ is regarded. The extinction spectra of this sample are shown in Fig. 5.6 for normally incident light with the polarization changed from $\alpha = 0°$ to $\alpha = -90°$ (panel (a)) as well as from $\alpha = -90°$ to $\alpha = -180°$ (panel (b)) in steps of $-6°$. At first sight, the spectra of sample 3 (Fig. 5.6) are similar to those of sample 2 (Fig. 5.5). However, one can see that the lower energy particle plasmon resonance of sample 3 is shifted to lower energies when compared to the

spectra of sample 2. This can be clearly seen by looking at the distance between the waveguide mode at approximately $1.35\,\text{eV}$ and the lower energy particle plasmon (see spectra with $\alpha \approx -48°$ of Fig. 5.5 and with $\alpha \approx -66°$ of Fig. 5.6). The higher energy particle plasmon stays approximately at the same energy (see spectra with $\alpha \approx -138°$ of Fig. 5.5 and with $\alpha \approx -156°$ of Fig. 5.6). However, it is expected that the higher energy particle plasmon should shift to larger energies and the lower energy particle plasmon to only slightly lower energies due to the different particle geometry (different form factor). This different behavior can be explained by the fact that the gold particles of sample 3 possess an MgF_2 layer on top, whereas there is only air above the particles of sample 2. The slightly higher refractive index shifts both particle plasmons to lower energies (see Eq. (2.13) and the discussion about the resonance frequency in section 2.1.1) when compared to the same particle geometry with air above the particles. Additionally, it seems that the resonances at about $1.45\,\text{eV}$ and $1.55\,\text{eV}$ are less pronounced in the $\alpha = 0°$ spectrum of sample 3 (bottom curve in Fig. 5.6 (a)) when compared to the corresponding spectrum of sample 2 (bottom curve in Fig. 5.5 (a)).

In order to compare the behavior of the waveguide modes, the peak heights of the first two waveguide modes, namely a TE as well as a TM polarized wave propagating in y direction of the sample, are plotted in Fig. 5.7. For the peak heights in Fig. 5.7, the difference between the maximum extinction value of the specific resonance and the minimum value on the higher energy side is used. A similar behavior can be recognized for samples 2 (black) and 3 (red). However, small deviations are visible. The peak heights for the TE polarized wave propagating in the sample y direction (Fig. 5.7 (a)) show a minimum value at about $\alpha = -108°$ with a small shift to higher polarization angles for sample 3 when compared to sample 2. The minimum peak height for the TM wave propagating in y direction (Fig. 5.7 (b)) is at about $\alpha = -156°$ for sample 2 and at about $\alpha = -168°$ for sample 3. This deviation is due to the differently shaped particles and the different rotation angles around the sample x axis. A detailed explanation of this behavior will be given in section 5.4.

5.3 Theoretical model for 2D structures

A theoretical model for 1D disordered and quasiperiodic metallic photonic crystals has been introduced in section 2.5 as well as in Refs. [101] and [78]. However, for 2D metallic photonic crystals, this model has to be expanded. The first step of the 2D theoretical model is the same as for the 1D model: the spatial arrangement of the plasmonic particles is described by a delta function at each lattice point. For
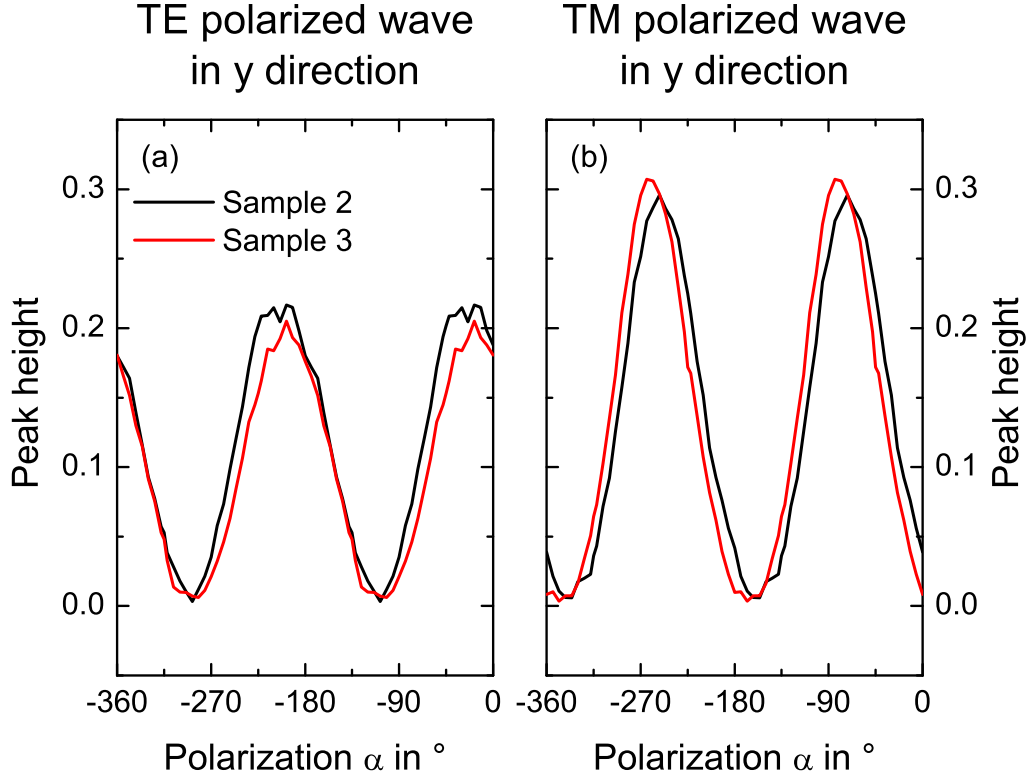
Figure 5.7: Behavior of the peak heights of sample 2 (black) compared to the peak heights of sample 3 versus the incident polarization α. The peak heights of these two samples are compared for (a) a TE polarized wave propagating in y direction as well as for (b) a TM polarized wave propagating in y direction.

the 2D case, this is given by

$$f(x, y) = \sum_{n} \delta(x - x_n)\,\delta(y - y_n). \tag{5.1}$$

The nth nanodisk has the coordinates x_n and y_n. Next, the 2D Fourier transform is taken. In order to reduce the calculation time of the 2D Fourier transform, the projection slice theorem is used [138, 139]. The projection slice theorem is sketched in Fig. 5.8. It states that the 2D Fourier transform

$$F(k_\xi, k_\eta) = \int_{-\infty}^{\infty} \int_{-\infty}^{\infty} f(\xi, \eta) e^{-i(k_\xi \xi + k_\eta \eta)}\, d\xi\, d\eta \tag{5.2}$$

of a structure (Fig. 5.8 on the left) can be obtained by projecting the structure coordinates onto a line with the angle β (Fig. 5.8 at the top)

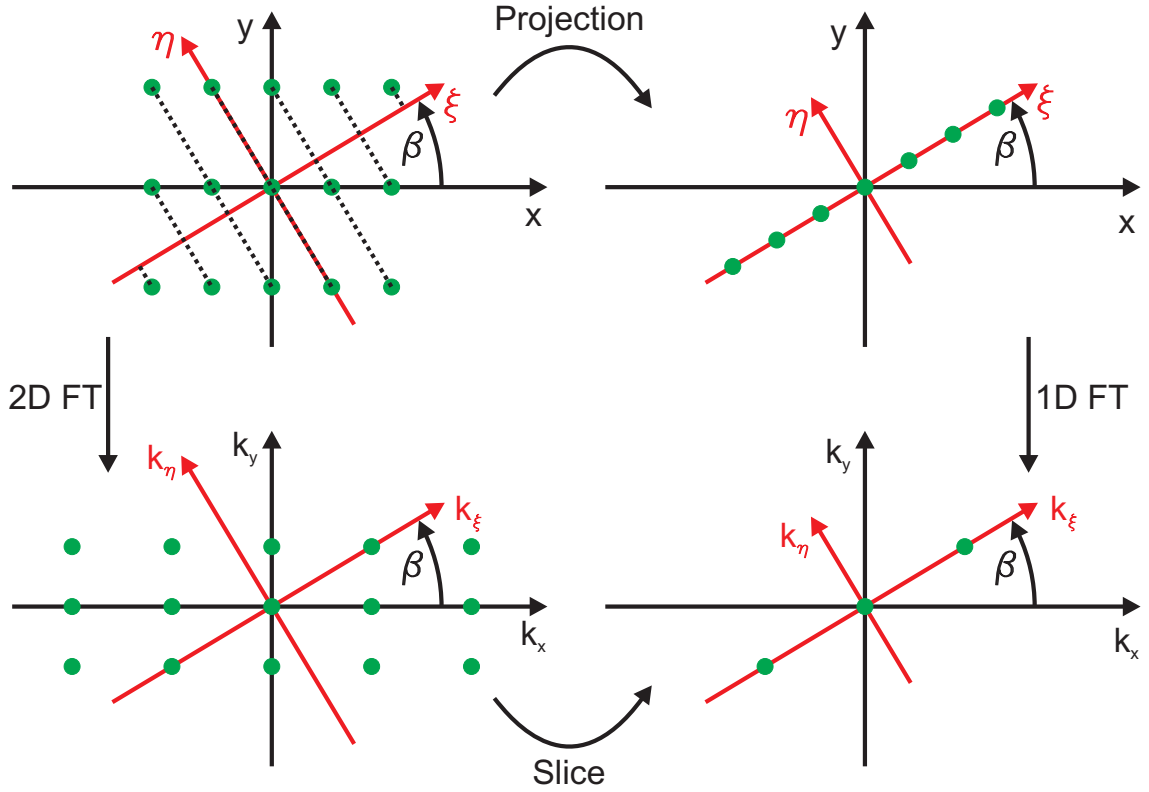$$P_\beta(\xi) = \int_{-\infty}^{\infty} f(\xi, \eta)\, d\eta \tag{5.3}$$

Figure 5.8: Sketch of the projection slice theorem. The projection of a 2D lattice onto a line in direction β (top) and the subsequent 1D Fourier transform (right) is equal to the 2D Fourier transform (left) and the inspection of a slice in direction β (bottom).

and performing the 1D Fourier transform of this line (Fig. 5.8 on the right)

$$S_\beta(k_\xi) = \int_{-\infty}^{\infty} P_\beta(\xi) e^{-ik_\xi \xi} \, d\xi \tag{5.4}$$

$$= \int_{-\infty}^{\infty} \left[\int_{-\infty}^{\infty} f(\xi, \eta) \, d\eta \right] e^{-ik_\xi \xi} \, d\xi.$$

$S_\beta(k_\xi)$ is then the slice of $F(k_\xi, k_\eta)$ in direction β through the center of the Fourier transform with $k_\eta = 0$ (Fig. 5.8 at the bottom). The whole Fourier transform is obtained for varying β between $0°$ and $180°$. However, due to the fact that the Fourier transform of periodic as well as quasiperiodic lattices show essentially discrete values [118], only these angles β have to be considered, where the main Fourier peaks are expected.

This Fourier transform is crucial in order to know which waveguide modes can be excited. The normally incident light is diffracted at the grating and coupled into the waveguide layer in the directions of the Fourier components with the specific propagation constants k. Incident light with a polarization $\mathbf{E}_\alpha$, whose electric field vector is rotated by the angle α around the sample x axis, can excite a TE as well as a TM polarized waveguide mode in direction β (see Fig. 5.9 (a)). The TE (TM)
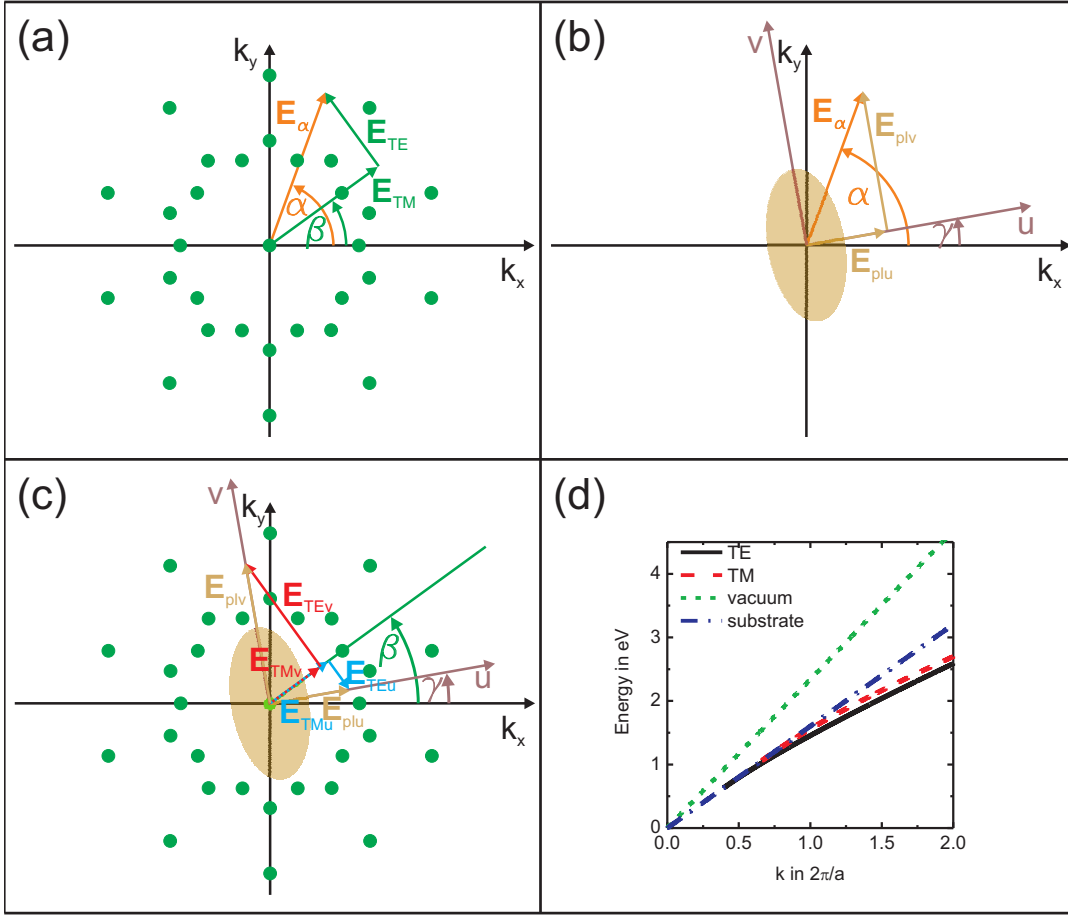
Figure 5.9: (a) TE and TM waves propagating in direction β with $\mathbf{E}_{TE}$ and $\mathbf{E}_{TM}$ as the vector addition of the incident polarization $\mathbf{E}_\alpha$. (b) The incident polarization excites one particle plasmon in u and one in v direction of an elliptical metal particle. (c) Each particle plasmon can excite a TE as well as a TM polarized wave in direction β. (d) Dispersion relations of a TE (black solid) and a TM polarized (red dashed) waveguide mode as well as those of vacuum (green short-dashed) and quartz (blue dash-dotted) for a 180 nm thick HfO_2 waveguide on quartz.

polarized waveguide mode is defined to have the electric field vector (magnetic field vector) on a plane perpendicular to the propagating wave [140]. The components obtained by splitting the incident polarization into a TE as well as a TM polarized wave are given by [141]

$$C_{TE} = C_\alpha \sin(\alpha - \beta), \tag{5.5}$$

$$C_{TM} = C_\alpha \cos(\alpha - \beta) \tag{5.6}$$

with C_α as a factor that is dependent on the incident wave. This means that an incident polarization with $\alpha = 0°$ can only excite a TM polarized wave in x direction ($\beta = 0°$) and a TE polarized wave in y direction ($\beta = 90°$). For a rectangular

arrangement of the nanodisks, no TE polarized wave with a propagation constant $k = \frac{2\pi}{P_x}$ as well as no TM polarized wave with $k = \frac{2\pi}{P_y}$ can be excited. However, for a quasiperiodic lattice, the TE as well as the TM polarized wave is present for any propagation constant k. By looking at the spectra of Fig. 5.5, one can recognize that both the TE polarized wave in x direction (resonance at $1.55\,\text{eV}$) and the TM polarized wave in y direction (resonance at $1.45\,\text{eV}$) are still present for $\alpha = 0°$. This can only be explained by also considering the particle plasmons.

It is well-known that the electric field vector of an incident polarization $\mathbf{E}_\alpha$ can only excite particle plasmons along the principal axes u and v of a metallic particle [93, 94]. Therefore, $\mathbf{E}_\alpha$ has to be split into one electric field component $\mathbf{E}_{plu}$ in u direction as well as into one electric field component $\mathbf{E}_{plv}$ in v direction leading to [141]

$$C_{plu} = C_\alpha C_u \cos(\alpha - \gamma), \tag{5.7}$$

$$C_{plv} = C_\alpha C_v \sin(\alpha - \gamma) \tag{5.8}$$

for an elliptically shaped particle with a rotation γ around the x axis of the sample (see Fig. 5.9 (b)). C_u and C_v are factors dependent on the eccentricity as well as on the size of the particle. These factors are related to the extinction cross section at the corresponding resonance energy. It is possible now to treat these two particle plasmons as two independent polarizations incident on the sample. Each individual electric field vector of the particle plasmon can excite a TE as well as a TM polarized waveguide mode in direction β leading to the electric field components $\mathbf{E}_{TEu}$ and $\mathbf{E}_{TMu}$ for the plasmon in u direction and $\mathbf{E}_{TEv}$ and $\mathbf{E}_{TMv}$ for the plasmon in v direction. This is visualized in Fig. 5.9 (c) as blue arrows for the u plasmon and as red arrows for the v plasmon. The obtained components are given by [141]

$$C_{TEu} = -C_{plu} \sin(\beta - \gamma), \tag{5.9}$$

$$C_{TMu} = C_{plu} \cos(\beta - \gamma), \tag{5.10}$$

$$C_{TEv} = C_{plv} \cos(\beta - \gamma), \tag{5.11}$$

$$C_{TMv} = C_{plv} \sin(\beta - \gamma) \tag{5.12}$$

with C_{plu} and C_{plv} of Eqs. (5.7) and (5.8), respectively. The $-$ sign in Eq. (5.9) is needed since $\mathbf{E}_{TEu}$ is pointing in the opposite direction than $\mathbf{E}_{TE}$ and $\mathbf{E}_{TEv}$ (see Fig. 5.9 (a) and (c)).

The complete components $C_{TE,add}$ and $C_{TM,add}$ for a TE and a TM polarized wave in direction β are obtained by adding the individual components (Eqs. (5.5), (5.9), and (5.11) for the TE wave and Eqs. (5.6), (5.10), and (5.12) for the TM wave)

leading to [141]

$$C_{TE,add} = C_{TE} + C_{TEu} + C_{TEv}, \tag{5.13}$$

$$C_{TM,add} = C_{TM} + C_{TMu} + C_{TMv}. \tag{5.14}$$

The Fourier transform $S_\beta(k_\xi)$ in direction β is weighted with the square value of $C_{TE,add}$ as well as $C_{TM,add}$. The total intensity of the waveguide modes can be calculated by integrating the weighted $S_\beta(k_\xi)$ over all angles β leading to [141]

$$F_{tot,TE} = \int_{0°}^{360°} S_\beta(k_\xi)\, C_{TE,add}^2\, d\beta, \tag{5.15}$$

$$F_{tot,TM} = \int_{0°}^{360°} S_\beta(k_\xi)\, C_{TM,add}^2\, d\beta. \tag{5.16}$$

The part of $S_\beta(k_\xi)$ with positive k_ξ is used for $0° \leqslant \beta < 180°$ and that with negative k_ξ for $180° \leqslant \beta < 360°$. Note that no particle plasmons can be excited for dielectric nanodisks. In this case, C_{TEu}, C_{TEv}, C_{TMu}, and C_{TMv} are zero. For circular metal particles, C_u is equal to C_v.

As already mentioned above, the Fourier components are characterized by a specific k value. However, not the k value but the corresponding energy E is needed in order to calculate the spectrum. Therefore, the k values are transferred to the corresponding energies by using the waveguide dispersion relations. The dispersion relations of TE and TM waves propagating in a 180 nm thick waveguide layer of HfO$_2$ are plotted in Fig. 5.9 (d) as black solid and red dashed curves, respectively. It can be seen that the energy of a TE waveguide mode for a specific k is always lower than the energy of a TM waveguide mode. As a reference, also the dispersion relations of the air cover (green short-dashed) and the quartz substrate (blue dash-dotted) are plotted.

The Fourier components of Eqs. (5.15) and (5.16) are characterized now by amplitudes A_k at energies E_k. In order to calculate the spectrum, a phenomenological model is used [142, 143]. The transmission amplitude t and the reflection amplitude r are given by

$$\begin{aligned} t = {} & t_d\, e^{i\phi_t} - \frac{t_{plu}\, \cos^2(\alpha - \gamma)\, \Gamma_{plu}\, e^{i\phi_{plu}}}{E - E_{plu} + i\, \Gamma_{plu}} \\ & - \frac{t_{plv}\, \sin^2(\alpha - \gamma)\, \Gamma_{plv}\, e^{i\phi_{plv}}}{E - E_{plv} + i\, \Gamma_{plv}} - A \sum_k \frac{A_k\, \Gamma_k\, e^{i\phi_k}}{E - E_k + i\, \Gamma_k}. \end{aligned} \tag{5.17}$$

$$\begin{aligned} r = {} & r_d\, e^{i\phi_r} + \frac{r_{plu}\, \cos^2(\alpha - \gamma)\, \Gamma_{plu}\, e^{i\phi_{plu}}}{E - E_{plu} + i\, \Gamma_{plu}} \\ & + \frac{r_{plv}\, \sin^2(\alpha - \gamma)\, \Gamma_{plv}\, e^{i\phi_{plv}}}{E - E_{plv} + i\, \Gamma_{plv}} + A \sum_k \frac{A_k\, \Gamma_k\, e^{i\phi_k}}{E - E_k + i\, \Gamma_k}. \end{aligned} \tag{5.18}$$

The directly transmitted light is described by the first term of Eq. (5.17) with the amplitude t_d and the phase ϕ_t and the directly reflected wave is given by the first term of Eq. (5.18) with the amplitude r_d and the phase ϕ_r. These values are dependent on the structure without the plasmonic lattice on top. The next two terms in each equation correspond to the excited particle plasmons in u and in v direction with the spectral widths Γ_{plu} and Γ_{plv}, the phases $\phi_{plu} = \phi_{plv} = \frac{\pi}{2}$, and the plasmon energies E_{plu} and E_{plv}. The last term in each equation is the sum over all waveguide modes that can be guided in the energy range E. For this term, the above calculated amplitudes A_k at the corresponding energies E_k are taken together with the spectral width Γ_k and the phase ϕ_k. The spectral widths of the waveguide modes are assumed to be constant for all waveguide modes in the spectrum with a value of about $0.01\,\text{eV}$. It is also assumed that the spectral widths of the two particle plasmons are equal ($\Gamma_{plu} = \Gamma_{plv}$) with a value in the order of $0.1\,\text{eV}$. In the case of dielectric particles, the plasmon amplitudes t_{plu}, t_{plv}, r_{plu}, and r_{plv} are equal to zero. For circular disks, t_{plu} is equal to t_{plv} leading to only one particle plasmon term $\frac{t_{pl}\,\Gamma_{pl}\,e^{i\phi_{pl}}}{E - E_{pl} + i\,\Gamma_{pl}}$. The same is true for the reflected particle plasmon.

The phase of a waveguide mode without the interaction of the particle plasmon has a value $\phi_{j,\infty}$ with j being either t for the transmitted wave or r for the reflected wave. This is true when the energy of the waveguide mode is totally different to the energy of the particle plasmon. When waveguide mode and particle plasmon possess the same energy, the phase of the waveguide mode is shifted by a value of π with respect to the undisturbed waveguide mode. The undisturbed waveguide mode with a lower energy than the particle plasmon possesses the phase $\phi_{j,\infty}$, whereas the phase of the undisturbed waveguide mode with a higher energy than the particle plasmon is given by $\phi_{j,\infty} + 2\pi$. Thus, the phase of the waveguide modes can be described by [141]

$$\phi_k = 2 \arctan\left(\frac{E - E_{plu}}{\Gamma_{plu}}\right) \cos^2(\alpha - \gamma) \tag{5.19}$$
$$+ 2 \arctan\left(\frac{E - E_{plv}}{\Gamma_{plv}}\right) \sin^2(\alpha - \gamma) + \phi_{j,\infty} + \pi.$$

For dielectric particles, the phase of the waveguide modes is just $\phi_{j,\infty}$. The transmittance and the reflectance spectra can be calculated by using $T = |t|^2$ and $R = |r|^2$, respectively. The extinction spectrum is given by $\text{Ext} = -\ln(T)$.

The just described simulation model for an extinction spectrum is sketched in Fig. 5.10. The weighted Fourier components given in Eqs. (5.15) and (5.16) are used to identify the amplitudes at specific k values. In Fig. 5.10 (a) this is shown for one direction β. The waveguide dispersion relations for TE (black) and TM (red)
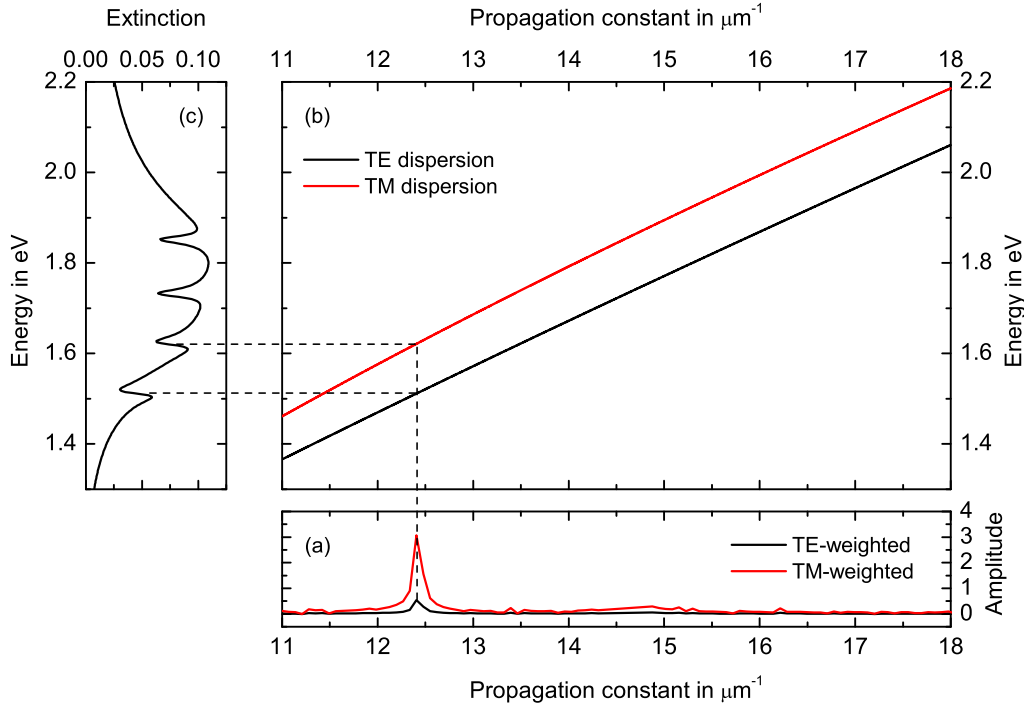
Figure 5.10: (a) Weighted Fourier components in direction β for TE (black) and TM polarization (red) in the relevant k range. (b) The TE (black) and TM (red) dispersion relations assign the corresponding energies to the given propagations constants. (c) Extinction spectrum with peak amplitudes of the waveguide modes given by the corresponding Fourier peak amplitudes.

polarized waves are used to identify the energies to the corresponding k values of the Fourier components (see Fig. 5.10 (b)). This is done for all directions β. Finally, the amplitudes and the corresponding energies are used to calculate the desired extinction spectrum (see Fig. 5.10 (c)).

In order to verify our model, the extinction spectra calculated with the model described above are compared to the measured spectra of section 5.2. The first spectra are calculated for the Penrose tiling as well as for the square lattice of sample 1, which is shown in Fig. 5.11 (a) and (b), respectively. As it has been explained above, the waveguide mode resonances correspond to a TE wave or a TM wave propagating in the directions given by the Fourier peaks. Since the TE waveguide dispersion relation is always below the TM waveguide dispersion relation, the energy of a TE resonance is always smaller than that of a TM resonance for the same propagation constant. For the Penrose tiling, the first two waveguide modes correspond to TE and TM waves propagating in directions $\beta = 0°$, $36°$, ... and the last two to TE and
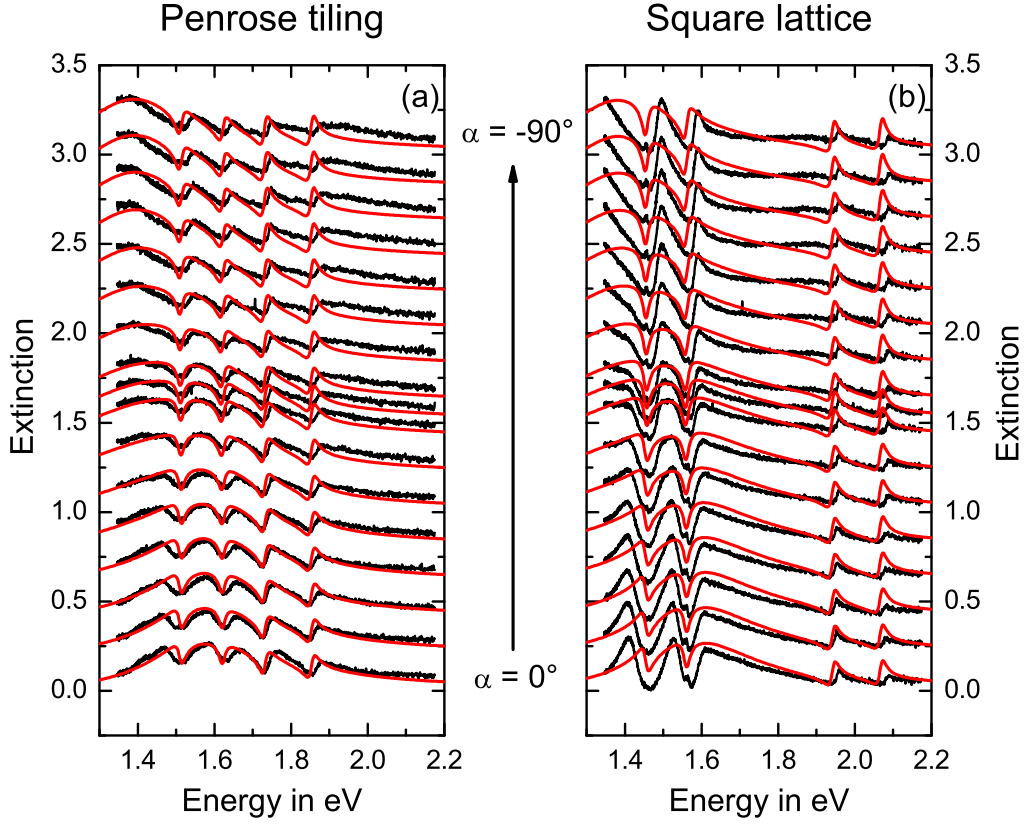
Figure 5.11: Measured (black) and modeled (red) extinction spectra of (a) a Penrose tiling with $P = 530\,\mathrm{nm}$ and of (b) a square lattice with $P_x = P_y = 530\,\mathrm{nm}$. The main axis diameters of the gold disks are $d_u = 120\,\mathrm{nm}$ and $d_v = 130\,\mathrm{nm}$ with a rotation of $\gamma = 0°$ around the sample x axis. The incident polarization was changed from $\alpha = 0°$ (bottom) to $\alpha = -90°$ (top). The spectra are shifted upward for clarity.

TM waves in directions $\beta = 18°$, $54°$, …. The first two resonances for the square lattice are due to TE and TM waves propagating in directions $\beta = 0°$, $90°$, … and the other two are due to TE and TM waves propagating in diagonal direction. For the particle plasmon energies $E_{plu} = 1.555\,\mathrm{eV}$ and $E_{plv} = 1.369\,\mathrm{eV}$, the plasmon spectral widths $\Gamma_{plu} = \Gamma_{plv} = 0.2\,\mathrm{eV}$, the waveguide mode spectral widths $\Gamma_k = 0.01\,\mathrm{eV}$, and amplitude and phase of the directly transmitted light $t_d = 1$ and $\phi_t = 0.085\,\pi$, the extinction spectra (red curves in Fig. 5.11) are calculated by using Eq. (5.17). These parameters are dependent on the particles as well as on the layer specifications of the sample. It is assumed that a directly transmitted wave possesses a transmission amplitude $t_d = 1$. This is not necessarily true since the material without the grating on top can also absorb part of the light leading to a lower transmission amplitude. However, the agreement between measured (black)

and modeled (red) curves is quite good. This is especially true for the Penrose tiling. The fitting parameters $t_{plu} = 0.1434$, $t_{plv} = 0.1580$, and $A = 0.0084$ were obtained by fitting the amplitudes to only one curve. All other spectra were calculated by using the same parameters. The fitting process is necessary so that the correct ratio between the amplitudes is obtained.

This already indicates that the model described above provides reasonable results. However, the spectra are also modeled for the other samples. The Penrose tiling
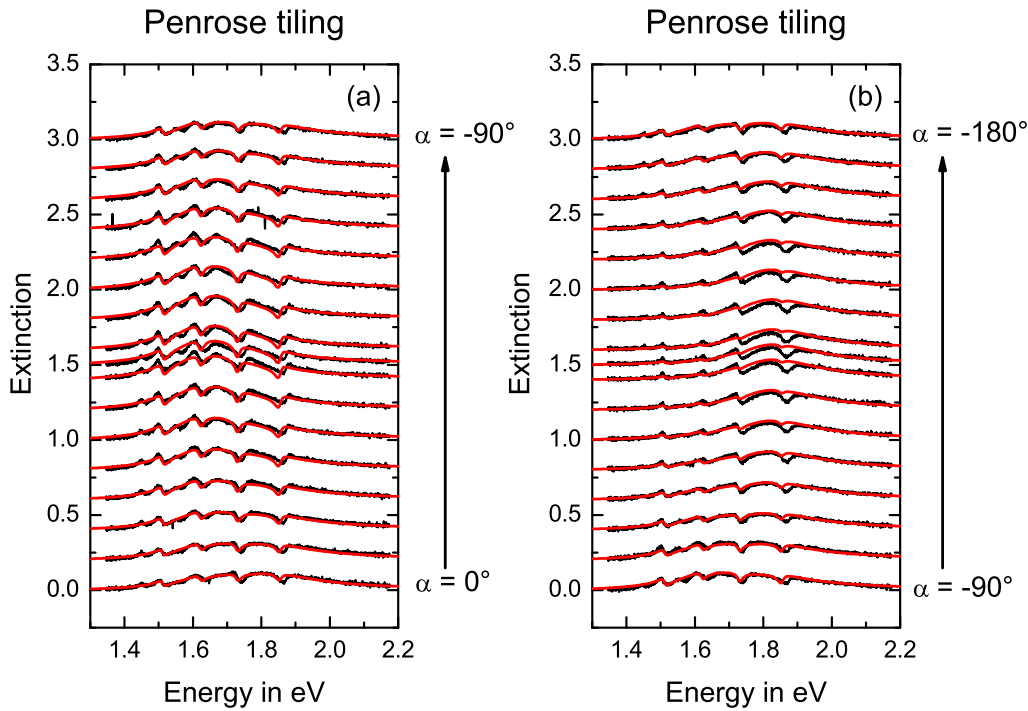

Figure 5.12: Measured (black) and modeled (red) extinction spectra of a Penrose tiling with $P = 530$ nm. The main axis diameters of the gold disks are $d_u = 97$ nm and $d_v = 118$ nm with a rotation of $\gamma = 40°$ around the sample x axis. The incident polarization was changed from (a) $\alpha = 0°$ (bottom) to $\alpha = -90°$ (top) and from (b) $\alpha = -90°$ (bottom) to $\alpha = -180°$ (top). The spectra are shifted upward for clarity.

of sample 2 was measured for different incident polarizations (see Fig. 5.3). The spectra were then modeled and compared to the measured spectra, which is shown as red and black curves in Fig. 5.12. As for sample 1, the directly transmitted light amplitude and phase are assumed to be $t_d = 1$ and $\phi_t = 0.085\,\pi$. However, the energy positions of the particle plasmon are changed to $E_{plu} = 1.813$ eV and $E_{plv} = 1.629$ eV due to the different particle shape. The phases of the particle plasmons are kept constant by $\phi_{plu} = \phi_{plv} = \frac{\pi}{2}$ and the spectral widths of the individual resonances

are given by $\Gamma_{plu} = \Gamma_{plv} = 0.15\,\mathrm{eV}$ and $\Gamma_k = 0.01\,\mathrm{eV}$. The fitting parameters for the individual amplitudes are fitted to just one curve and are given by $t_{plu} = 0.0685$, $t_{plv} = 0.0896$, and $A = 0.001$. All the other curves are calculated with the same parameters. The agreement between the measured and the modeled curves is very good. Only some minor deviations for the dips at $1.75\,\mathrm{eV}$ and $1.85\,\mathrm{eV}$ around a polarization of $\alpha = -135°$ are visible. The rest is modeled very well.
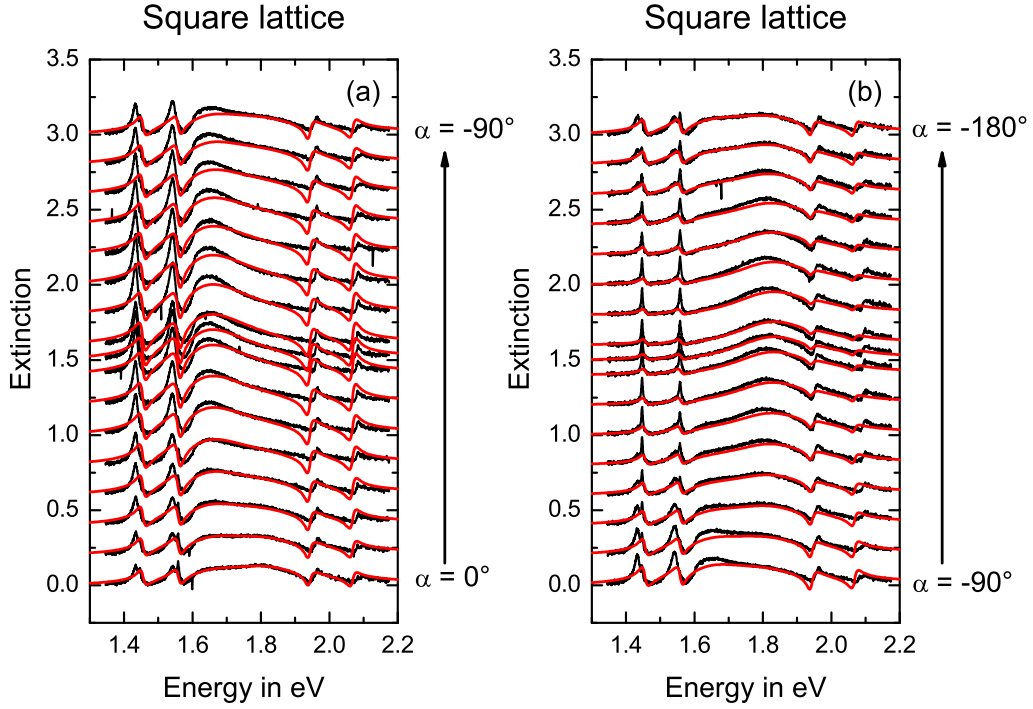

Figure 5.13: Measured (black) and modeled (red) extinction spectra of a square lattice with $P_x = P_y = 530\,\mathrm{nm}$. The main axis diameters of the gold disks are $d_u = 97\,\mathrm{nm}$ and $d_v = 118\,\mathrm{nm}$ with a rotation of $\gamma = 40°$ around the sample x axis. The incident polarization was changed from (a) $\alpha = 0°$ (bottom) to $\alpha = -90°$ (top) and from (b) $\alpha = -90°$ (bottom) to $\alpha = -180°$ (top). The spectra are shifted upward for clarity.

The measured spectra of the square lattice as well as the rectangular lattice of sample 2 were also modeled, which is plotted in Figs. 5.13 and 5.14, respectively. With the fitting parameters $t_{plu} = 0.0784$, $t_{plv} = 0.1169$, and $A = 0.0022$, the spectra were calculated for all polarization angles. A very good agreement between the measured and the calculated curves is achieved for both the square as well as the rectangular lattice. Especially the spectra with the rectangular lattice are interesting since specific resonances disappear for distinct polarizations. As already mentioned above, the waveguide modes initially expected to disappear, namely the TE mode
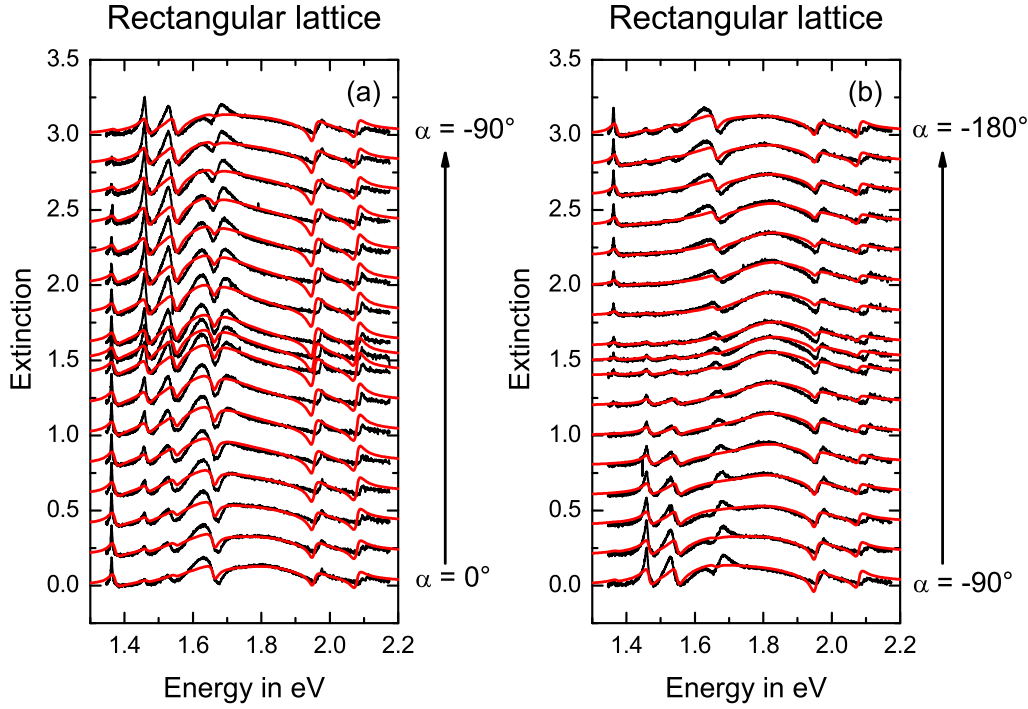
Figure 5.14: Measured (black) and modeled (red) extinction spectra of a rectangular lattice with $P_x = 492\,\text{nm}$ and $P_y = 570\,\text{nm}$. The main axis diameters of the gold disks are $d_u = 97\,\text{nm}$ and $d_v = 118\,\text{nm}$ with a rotation of $\gamma = 40°$ around the sample x axis. The incident polarization was changed from (a) $\alpha = 0°$ (bottom) to $\alpha = -90°$ (top) and from (b) $\alpha = -90°$ (bottom) to $\alpha = -180°$ (top). The spectra are shifted upward for clarity.

propagating in x direction and the TM mode propagting in y direction for $\alpha = 0°$ or the TM mode propagating in x direction and the TE mode propagting in y direction for $\alpha = -90°$, are still present for the corresponding polarization. This is true for both the measured and the modeled spectra. As it was explained for the theoretical model, this is due to the waveguide modes excited by the particle plasmons. In these spectra, the peak height behavior of the waveguide modes is also predicted quite well, which means that the waveguide modes disappear for the same polarizations in the measurements and the model. This is due to the parameters C_u and C_v, which are related to the extinction cross section for the corresponding particle plasmon. A detailed study of this peak height behavior is carried out in section 5.4.

The measured spectra of sample 3 were also compared to the calculated ones, which is shown in Fig. 5.15. Here, the transmission amplitude and phase of the directly transmitted wave, the particle plasmon phases, as well as the individual spectral widths are the same as for sample 2. The particle plasmon energies are changed
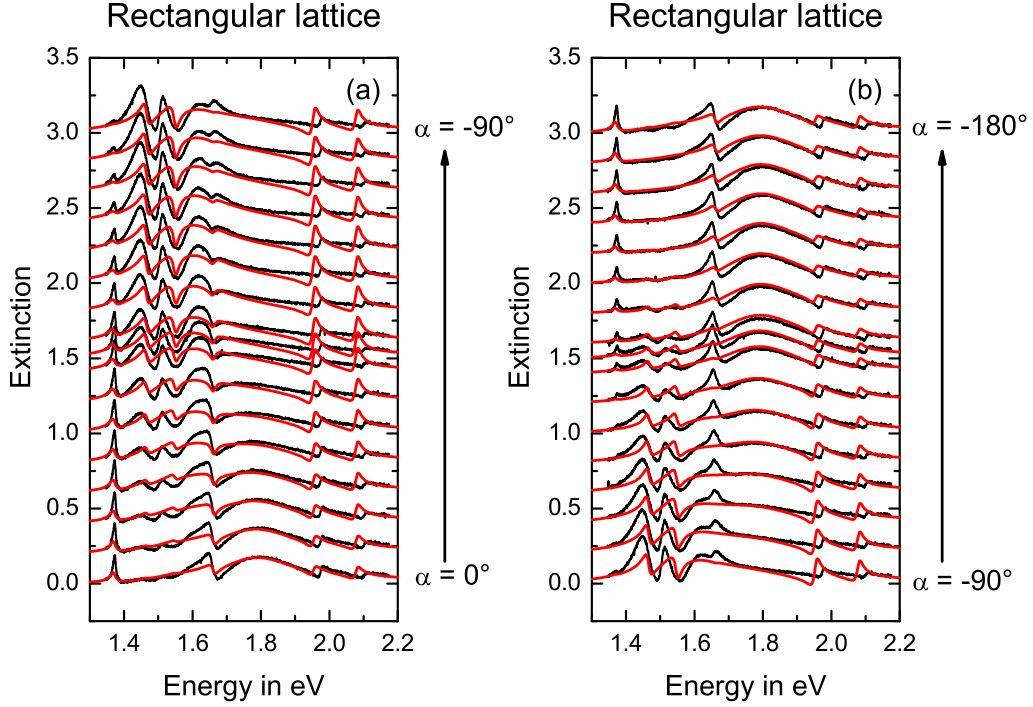
Figure 5.15: Measured (black) and modeled (red) extinction spectra of a rectangular lattice with $P_x = 492$ nm and $P_y = 570$ nm. The main axis diameters of the gold disks are $d_u = 88$ nm and $d_v = 120$ nm with a rotation of $\gamma = 25°$ around the sample x axis. The incident polarization was changed from (a) $\alpha = 0°$ (bottom) to $\alpha = -90°$ (top) and from (b) $\alpha = -90°$ (bottom) to $\alpha = -180°$ (top). The spectra are shifted upward for clarity.

to $E_{plu} = 1.774$ eV and $E_{plv} = 1.563$ eV due to the different particle shape. Again, the amplitudes t_{plu}, t_{plv}, and A were fitted to only one measured spectrum. All red curves in Fig. 5.15 were calculated with the same fitting parameters, namely with $t_{plu} = 0.0999$, $t_{plv} = 0.1125$, and $A = 0.0029$. The agreement between the measured and the modeled curves is good for all polarizations. The peak height behavior is again well described. As already mentioned above, this is due to the parameters C_u and C_v, which are related to the extinction cross sections of the particle plasmons, and will be discussed in section 5.4.

5.4 Peak height behavior

In order to study the peak height behavior of the different waveguide mode resonances in conjunction with different particle eccentricities, different particle sizes,

Table 5.1: Particle parameters for the different S-matrix calculated spectra.

	d_u	d_v	Eccentricity e	Particle size A	Rotation angle
Shape 1	87.5 nm	94.5 nm	0.378	6494 nm^2	30°
Shape 2	100 nm	108 nm	0.378	8482 nm^2	30°
Shape 3	78.75 nm	105 nm	0.661	6494 nm^2	30°
Shape 4	90 nm	120 nm	0.661	8482 nm^2	30°
Shape 5	90 nm	120 nm	0.661	8482 nm^2	60°

and different particle rotations, several spectra were simulated by using S-matrix calculations. The gold particles in the simulations possess the different shapes given in Table 5.1. For each of the two different eccentricities e, two different particle sizes A were used. Additionally, for the eccentricity $e = 0.661$ and the particle size $A = 8482\,\mathrm{nm}^2$, the rotation angle γ of the gold particle was changed. The gold disks are arranged in a rectangular lattice with $P_x = 492\,\mathrm{nm}$ and $P_y = 570\,\mathrm{nm}$. The simulations were performed for the polarizations $\alpha = 0°$, 18°, 45°, 72°, 90°, 108°, 135°, and 162°. The normalized peak heights of a TE polarized and a TM polarized wave propagating in y direction for the different polarizations are plotted in Fig. 5.16 (a) and (b), respectively. It can be seen that the minimum peak height for a TE polarized wave in y direction is at slightly higher polarizations for an eccentricity $e = 0.378$ when compared to the peak heights with $e = 0.661$. For a TM polarized wave in y direction, the minimum peak height of the sample with rotation angle $\gamma = 60°$ is shifted to higher polarizations.

As already mentioned in section 5.3, the values C_u and C_v are related to the extinction cross section at the corresponding particle plasmon resonance energy. In order to verify this assumption, the minimum values of $C_{TE,add}^2$ (see Eq. (5.13)) and $C_{TM,add}^2$ (see Eq. (5.14)) with C_u and C_v as the extinction cross sections at the resonance position are compared to the minimum values of the peak heights of Fig. 5.16. The polarizations of these minimum values are obtained by fitting a $\sin^2$ function to the corresponding curves. These polarizations as well as the predicted ones for the different shapes are given in Table 5.2. The predictions and the fitted values are quite close, especially for Shapes $1 - 3$. Larger deviations are present for Shapes 4 and 5. However, the order of magnitude is still close. These deviations might be due to several reasons. First, the energies of the particle plasmons are close to the waveguide modes, which might influence the peak height behavior. The peak heights are obtained by the difference of the maximum value of the resonance and the minimum on the higher energy side, which should give us the real peak heights. However, there might still be an influence of the particle plasmons. Second, the
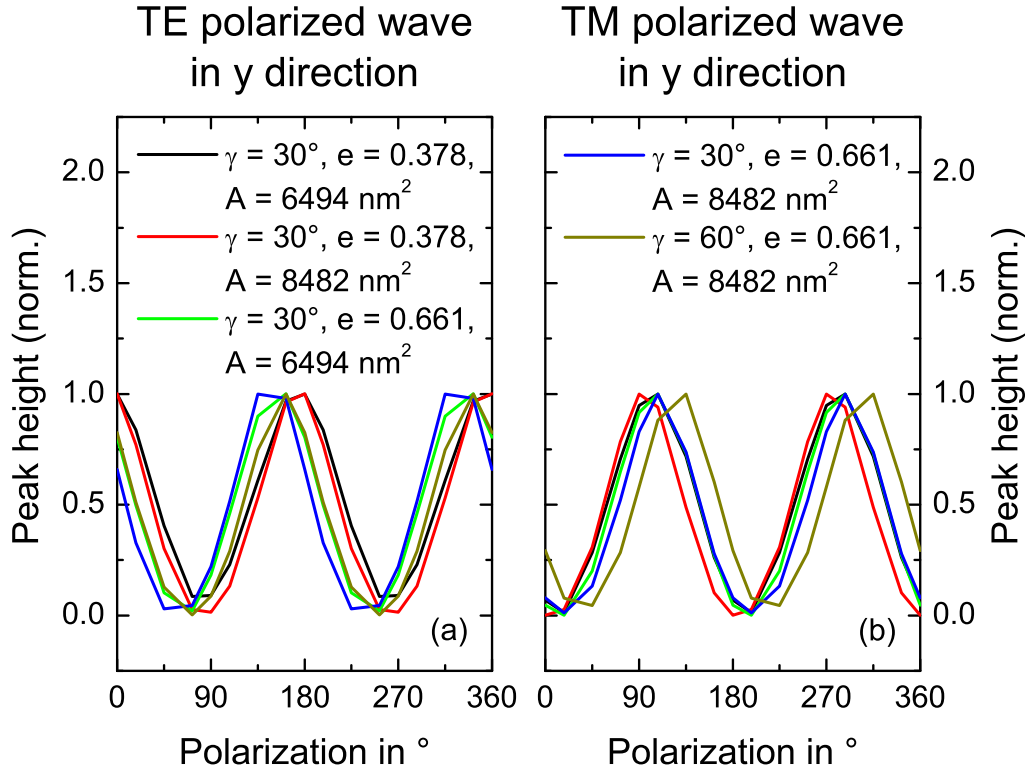
Figure 5.16: Behavior of the peak heights of the different S-matrix spectra with the specifications given in Table 5.1 versus the incident polarization α. The peak heights are compared for (a) a TE polarized wave propagating in y direction as well as for (b) a TM polarized wave propagating in y direction.

extinction is calculated every $2.5\,\text{meV}$ for the S-matrix simulations. It might be possible that the real maximum position of the resonance is at an energy value between two calculated ones. Third, the S-matrix calculations are truncated leading to deviations in the resonance positions as well as the peak heights. Fourth, the calculation of the extinction cross section is based on an approximation. It might be possible that the real extinction cross sections vary from the calculated ones leading to a different position of the minimum peak height. Therefore, the predictions and the polarizations of the S-matrix calculated peak height minima agree quite well. This indicates that the values C_u and C_v are really related to the extinction cross section at the corresponding particle plasmon resonance energy. All calculated spectra of section 5.3 are making use of this ratio between the two extinction cross sections.

Table 5.2: Polarizations of the minimum peak heights of a TE as well as a TM wave propagating in y direction obtained from the S-matrix spectra as well as the predicted ones for the different particle shapes.

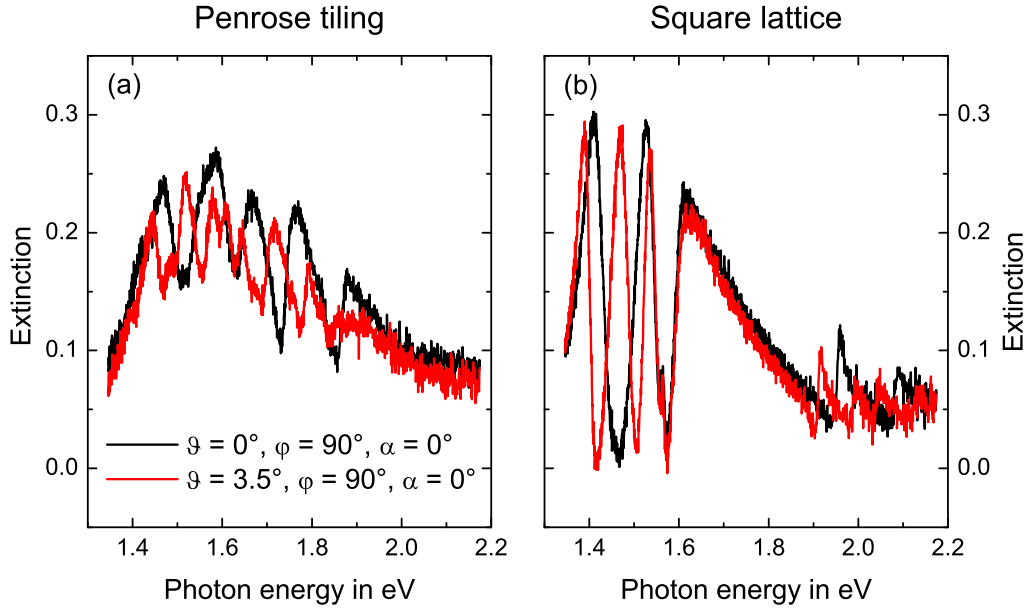|		Shape 1	Shape 2	Shape 3	Shape 4	Shape 5
$\alpha_{min,TEy}$	S-matrix	83.2°	83.3°	64.1°	57.6°	70.1°
	predicted	81.2°	85.4°	64.0°	68.8°	75.0°
$\alpha_{min,TMy}$	S-matrix	13.5°	5.2°	15.6°	19.3°	36.1°
	predicted	7.5°	4.2°	17.3°	15.0°	21.2°

5.5   Angular extinction spectra

Figure 5.17: S-polarized extinction spectra of (a) a Penrose tiling as well as (b) a square lattice for incidence angles $\vartheta = 0°$ (black) and $\vartheta = 3.5°$ (red) and an azimuthal angle $\varphi = 90°$.

Samples 1 and 2 were also measured for different angles of incidence ϑ. The first measurements of sample 1 shown in Fig. 5.17 were performed for $\vartheta = 0°$ (black curves) as well as for $\vartheta = 3.5°$ with the azimuthal angle $\varphi = 90°$ and s-polarized light ($\alpha = 0°$). The spectra were measured for both a Penrose tiling and a square lattice, which are shown in Fig. 5.17 (a) and (b), respectively. The azimuthal angle $\varphi = 90°$ in the angle-dependent spectra means that the waves propagating in x and in $-x$ direction possess the same energy, whereas the energy of the waves propagat-

ing in y and in $-y$ direction is different. Since only a TM wave is propagating in x direction and only a TE wave in y direction for the square lattice with $\alpha = 0°$, only a splitting of the TE polarized wave (resonance at about 1.47 eV) is visible in Fig. 5.17 (b). The TE and TM waves propagating in diagonal direction also show a splitting (see resonances above 1.9 eV). For the Penrose tiling, however, all of the four waveguide mode resonances split up into several modes due to the ten-fold symmetry in reciprocal space (compare to Fig. 5.9 (a)). The resonance at approximately 1.64 eV for normal incidence is due to TM polarized waves propagating in directions $\beta = 0°, 36°, \dots$. For $\vartheta = 3.5°$ this resonance splits up into several different ones, one of them propagating in direction $\beta \approx 0°$. This means that the waveguide mode with this photon energy is still present. In the spectrum, one can see that this dip is indeed at the same energy position. However, TE polarized modes (resonance at about 1.53 eV) with $\beta \approx 0°$ and $\beta \approx 180°$ are not present for $\vartheta = 3.5°$ leading to a peak instead of a dip in the spectrum.
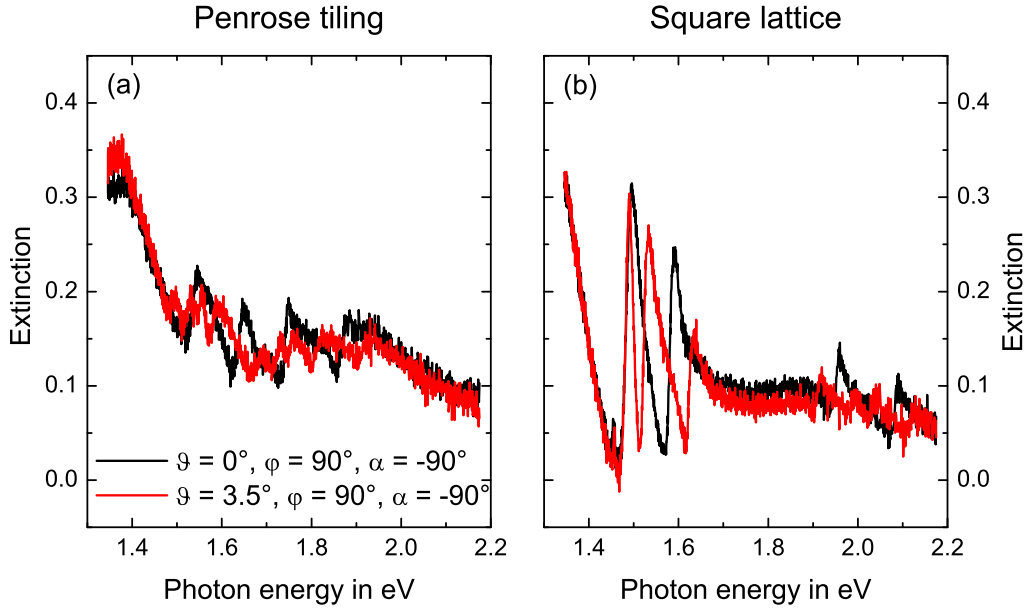

Figure 5.18: P-polarized extinction spectra of (a) a Penrose tiling as well as (b) a square lattice for incidence angles $\vartheta = 0°$ (black) and $\vartheta = 3.5°$ (red) and an azimuthal angle $\varphi = 90°$.

P-polarized ($\alpha = -90°$) spectra of sample 1 with $\varphi = 90°$ for incidence angles $\vartheta = 0°$ and $\vartheta = 3.5°$ were also measured for the Penrose tiling as well as the square lattice. These spectra are shown in Fig. 5.18. The particle plasmon for this polarization is shifted to lower energies due to the longer main axis diameter of the elliptical gold

particles. By comparing the two different incidence angles for the square lattice (Fig. 5.18 (b)), it is clearly visible that the TE polarized waveguide mode stays at the same photon energy (about 1.47 eV), whereas the TM polarized mode splits up into two modes. This can be easily understood by the fact that only a TE mode is propagating in x direction and a TM mode in y direction. As above for $\alpha = 0°$, both waveguide modes propagating in diagonal directions split up into two modes. For normal incidence on the Penrose tiling, the TM polarized waveguide mode propagating in directions $\beta = 0°, 36°, ...$ (photon energy of about 1.64 eV) is almost at a peak position for $\alpha = -90°$ instead of a dip position for $\alpha = 0°$. This is due to the fact that the particle plasmon is shifted to lower energies leading to a less coupled waveguide mode to the particle plasmon. For $\vartheta = 3.5°$ a dip can be obtained at the same energy position indicating that no TM polarized wave is propagating in directions $\beta \approx 0°$ and $\beta \approx 180°$. For a TE polarized wave in direction $\beta = 0°, 36°, ...$, the dip at about 1.53 eV for normal incidence stays approximately at the same energy position indicating that the waveguide mode in $\pm x$ direction is the dominant effect. However, a splitting is visible for this resonance as well.

Sample 2 was also measured for oblique light incidence. The first spectra are shown for the square lattice with s-polarized light (Fig. 5.19) as well as with p-polarized light (Fig. 5.20). The angle of incidence is changed between 0° (bottom) and 6° (top). The azimuthal angle is kept constant at $\varphi = 0°$ in Figs. 5.19 (a) and 5.20 (a). For Figs. 5.19 (b) and 5.20 (b), the azimuthal angle is changed to $\varphi = 90°$. The energy position of the plain normal incidence waveguide modes is indicated by the vertical red dashed lines in all panels. The behavior of the s-polarized (p-polarized) spectra is similar for both azimuthal angles. This is reasonable since the periodicity is equal in x and y direction meaning that it should not be possible to distinguish between the s-polarized (p-polarized) data for $\varphi = 0°$ and $\varphi = 90°$. However, due to the elliptically shaped gold disks, the spectra are still slightly different. Nevertheless, the principle behavior is still comparable. The TE polarized waveguide mode (≈ 1.47 eV) propagating in directions $\beta = 0°$ or $\beta = 90°$ splits up into two main peaks for oblique incidence, whereas the TM polarized waveguide mode (≈ 1.57 eV) stays almost constant. This behavior is expected. However, a small fraction of the TE polarized mode stays at ≈ 1.47 eV and a small fraction of the TM polarized mode splits up into two modes. This can especially be seen for the TM waveguide mode at ≈ 1.57 eV in the s-polarized spectra. While the main peak stays at this energy, an additional resonance is observable on the higher energy side moving to higher energies as the angle of incidence increases. This can only be explained by the elliptical, rotated particles and will be discussed in section 5.6.
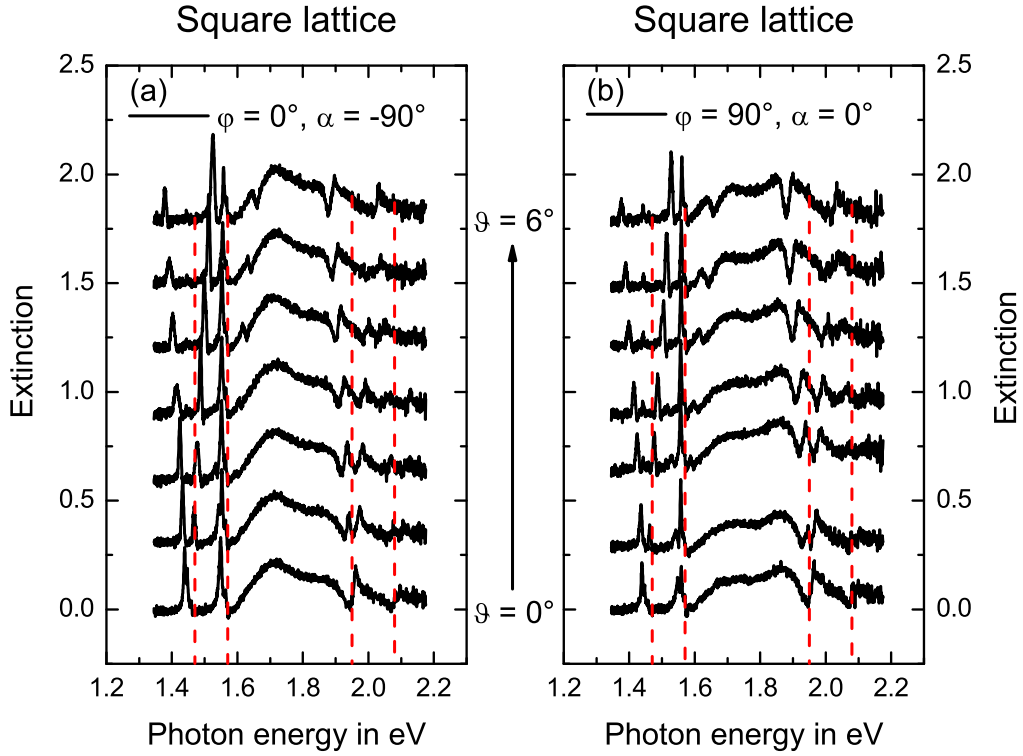
Figure 5.19: S-polarized extinction spectra of a square lattice for (a) $\varphi = 0°$ as well as for (b) $\varphi = 90°$. The angle of incidence is changed between $\vartheta = 0°$ (bottom) and $\vartheta = 6°$ (top) in steps of 1°. The spectra are shifted upward for clarity.

For the p-polarized spectra, the behavior is opposite, meaning that the TE polarized waveguide mode stays approximately constant for oblique light incidence and the TM polarized waveguide mode splits up into two modes as expected. However, a small part of the TE polarized wave splits up into two additional modes and a small part of the TM polarized wave stays at approximately the same photon energy. Again, this is due to the elliptical, rotated particles and will be discussed in section 5.6.

Both the TE and the TM polarized waves propagating in the diagonal directions split up into two modes for s- as well as for p-polarization. The situation changes for $\varphi = 45°$ where either the TE polarized waveguide mode (p-polarization) or the TM polarized waveguide mode (s-polarization) stays approximately constant. In this case, the TE as well as the TM polarized waveguide modes split up into two modes. However, it is not possible to measure this with the current setup.
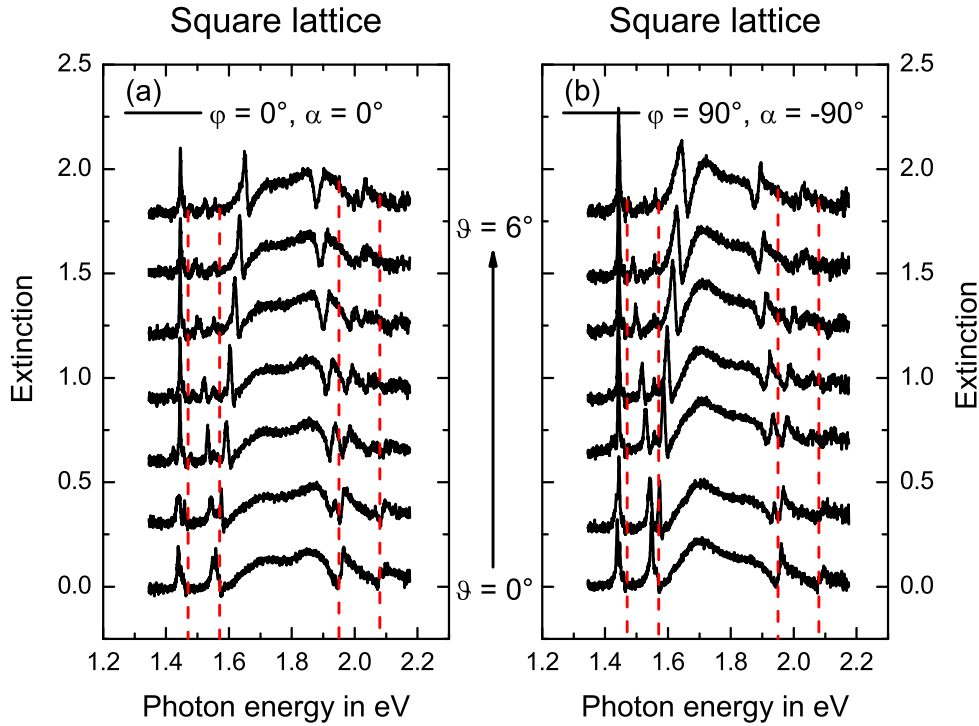
Figure 5.20: P-polarized extinction spectra of a square lattice for (a) $\varphi = 0°$ as well as for (b) $\varphi = 90°$. The angle of incidence is changed between $\vartheta = 0°$ (bottom) and $\vartheta = 6°$ (top) in steps of 1°. The spectra are shifted upward for clarity.

Next, the rectangular lattice of sample 2 was measured in s- and p-polarization, which is shown in Fig. 5.21 and Fig. 5.22, respectively. As above for the square lattice, the angle of incidence was changed between $\vartheta = 0°$ (bottom) and $\vartheta = 6°$ (top) in steps of 1°. Panel (a) shows in both figures the spectra for an azimuthal angle $\varphi = 0°$ and panel (b) the spectra for $\varphi = 90°$. The energy positions of the plain waveguide mode resonances are indicated by the red dashed lines. For $\varphi = 0°$, the TE and TM polarized waveguide modes propagating in y direction stay at an approximately constant energy while the TE and TM polarized waveguide modes propagating in x direction split up into two modes. This is true for both s- and p-polarization (Figs. 5.21 (a) and 5.22 (a)) and can be easily understood by the fact that the absolute values of the modes in $\pm y$ direction are equal whereas those of the modes in $\pm x$ are not. However, the TM polarized waveguide mode in y direction is more pronounced for s-polarization and the TE polarized waveguide mode in y direction for p-polarization. For circularly shaped particles it is expected that the less pronounced resonances cannot be excited at all. Due to the elliptical, rotated particles, a small fraction of these modes is still able to propagate in y direction.
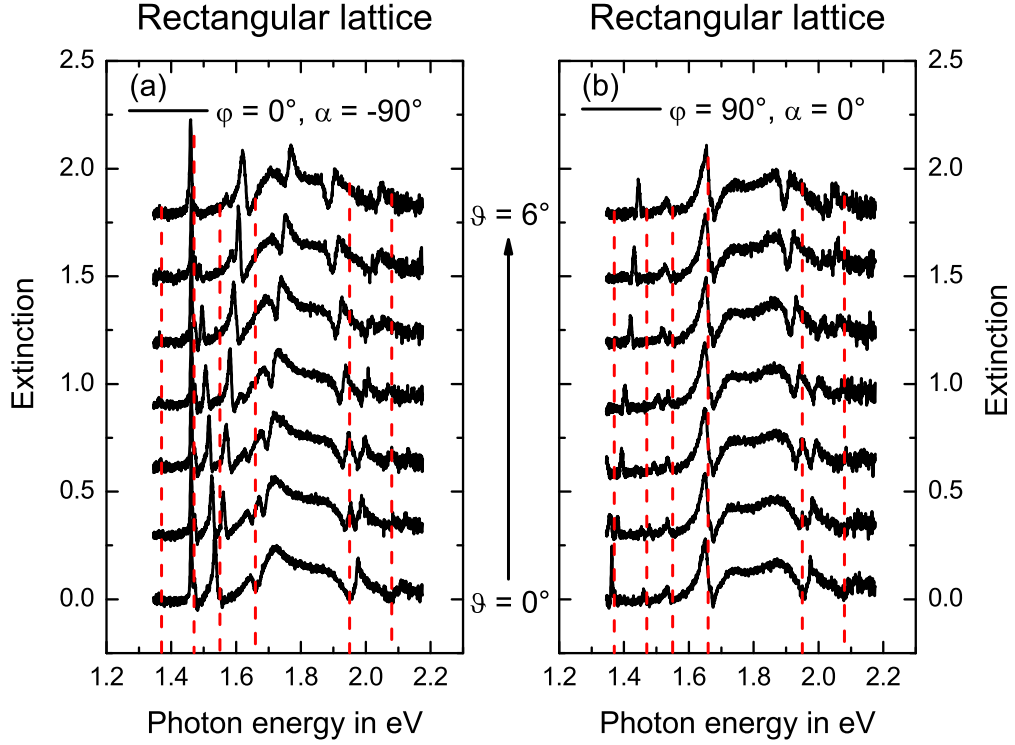
Figure 5.21: S-polarized extinction spectra of a rectangular lattice for (a) $\varphi = 0°$ as well as for (b) $\varphi = 90°$. The angle of incidence is changed between $\vartheta = 0°$ (bottom) and $\vartheta = 6°$ (top) in steps of 1°. The spectra are shifted upward for clarity.

For $\varphi = 90°$, the waveguide modes propagating in y direction split up into two modes and those in x direction stay at an almost constant energy position. The TM polarized waveguide mode in x direction is more pronounced for s-polarization and the TE mode in x direction for p-polarization. Similar considerations as for $\varphi = 0°$ can be made here in order to explain the occurrence of the specific resonances.

The s-polarized spectra have in common that the more pronounced TE wave splits up into two modes and the more pronounced TM wave stays at approximately the same photon energy (Fig. 5.21). This is in agreement with the behavior of the s-polarized spectra of the square lattice. In contrast, the more pronounced TE wave in the p-polarized spectra stays at about the same energy position, whereas the more pronounced TM polarized wave splits up into two modes. Also this behavior is consistent with the findings of the p-polarized spectra of the square lattice.

The last angle-dependent measurements of sample 2 were performed for the Penrose tiling. As above, s-polarized (Fig. 5.23) as well as p-polarized (Fig. 5.24) spectra were measured with the azimuthal angle to be either $\varphi = 0°$ (panels (a)) or $\varphi = 90°$
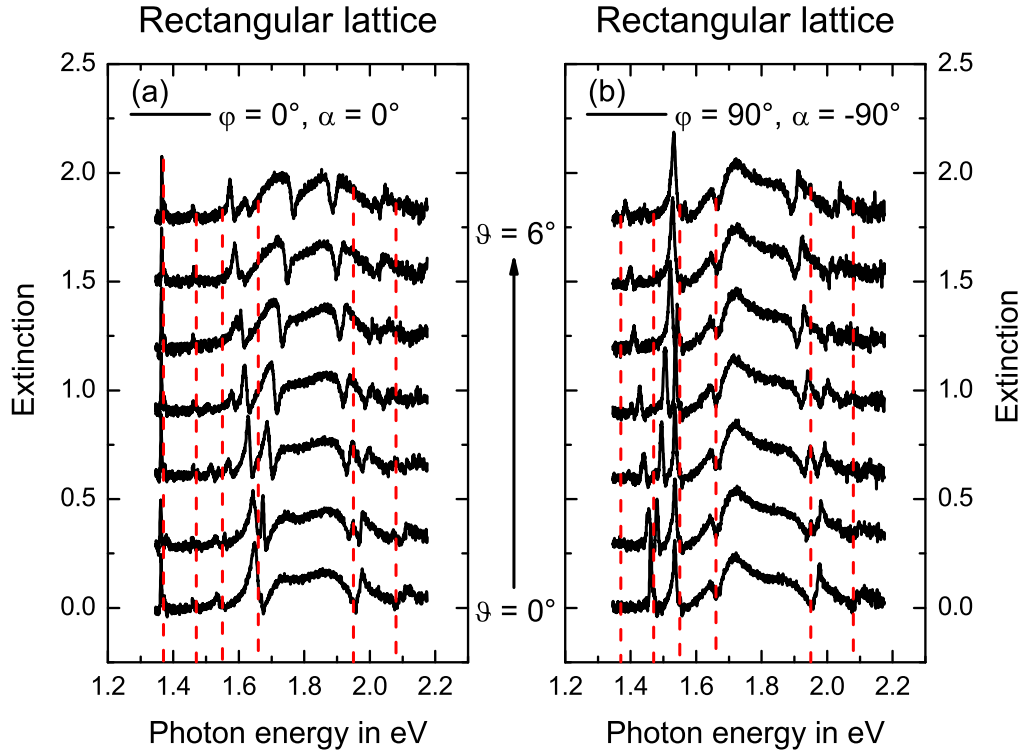
Figure 5.22: P-polarized extinction spectra of a rectangular lattice for (a) $\varphi = 0°$ as well as for (b) $\varphi = 90°$. The angle of incidence is changed between $\vartheta = 0°$ (bottom) and $\vartheta = 6°$ (top) in steps of $1°$. The spectra are shifted upward for clarity.

(panels (b)). The energy positions of the plain normal incidence waveguide modes are again shown by the red dashed lines. As the Penrose tiling possesses ten-fold symmetry in reciprocal space (see Fig. 5.9 (a)), each waveguide mode splits up in up to ten modes for oblique light incidence. For normal incidence, the absolute value of the propagation constants in directions $\beta = 0°$, $36°$, ... is equal for each β. The same is true for $\beta = 18°$, $54°$, ..., however, with a slightly higher propagation constant when compared to directions $\beta = 0°$, $36°$, ... For oblique light incidence, the waves propagating in directions $\beta = 0°$, $36°$, ... ($\beta = 18°$, $54°$, ...) do not possess the same absolute value of the propagation constant. An azimuthal angle $\varphi = 0°$ generates a mirror symmetric behavior of the waveguide modes with respect to the x axis leading to 6 different propagation constants for $\beta = 0°$, $36°$, ... and 5 different propagation constants for $\beta = 18°$, $54°$, ... The mirror symmetric behavior of the waveguide modes for $\varphi = 90°$ is given with respect to the y axis. For this azimuthal angle, the waveguide modes propagating in directions $\beta = 0°$, $36°$, ... split up into 5 modes and those in directions $\beta = 18°$, $54°$, ... into 6 modes. These waveguide modes are
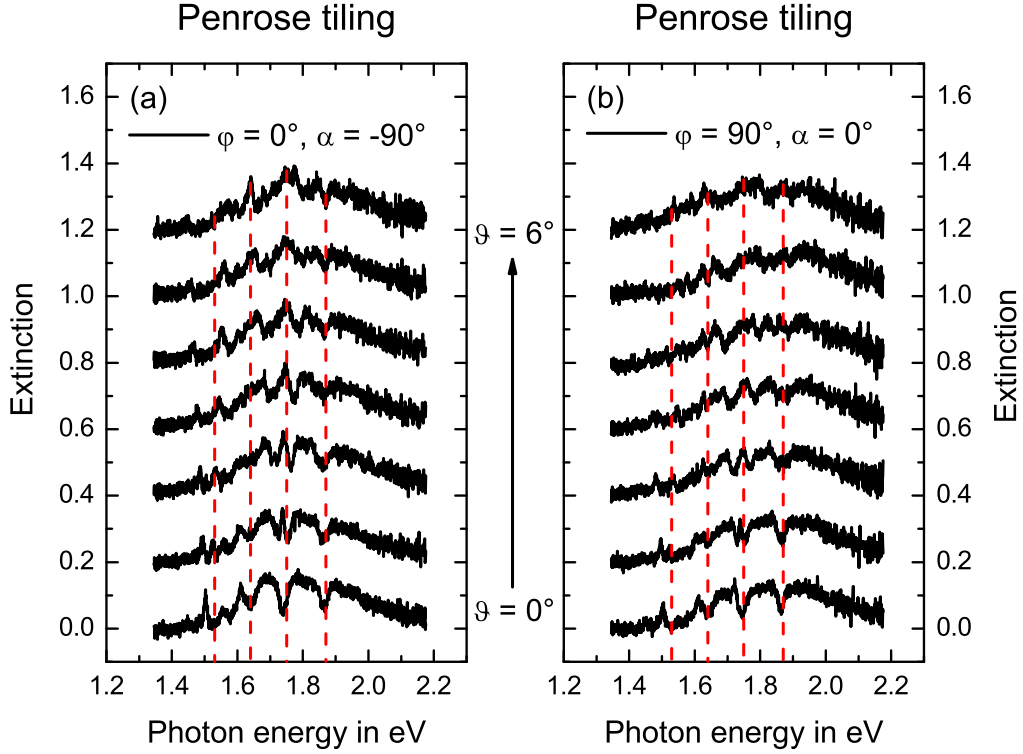
Figure 5.23: S-polarized extinction spectra of a Penrose tiling for (a) $\varphi = 0°$ as well as for (b) $\varphi = 90°$. The angle of incidence is changed between $\vartheta = 0°$ (bottom) and $\vartheta = 6°$ (top) in steps of $1°$. The spectra are shifted upward for clarity.

more or less pronounced, namely a polarization $\alpha = 0°$ results in a maximum value of a TM wave propagating in $\pm x$ direction as well as a maximum value of a TE wave propagating in $\pm y$ direction. The opposite is true for $\alpha = 90°$. This means that the major waveguide mode resonance having about the same energy when compared to the normal incidence spectrum is present for a TM wave propagating in direction $\beta = \pm 90°$ for s-polarization with $\varphi = 0°$ (1.87 eV, Fig. 5.23 (a)) as well as for a TM wave propagating in direction $\beta = \pm 0°$ for s-polarization with $\varphi = 90°$ (1.64 eV, Fig. 5.23 (b)). For p-polarization, the major waveguide modes keeping the resonance energy almost constant are the TE wave propagating in direction $\beta = \pm 90°$ for $\varphi = 0°$ (1.75 eV, Fig. 5.24 (a)) and the TE wave propagating in direction $\beta = \pm 0°$ for $\varphi = 90°$ (1.53 eV, Fig. 5.24 (b)). However, also some minor resonances with higher or lower energies are present in the system. They are simply much less pronounced and, thus, less visible. The TE waves (TM waves) show the opposite behavior for s-polarization (p-polarization).
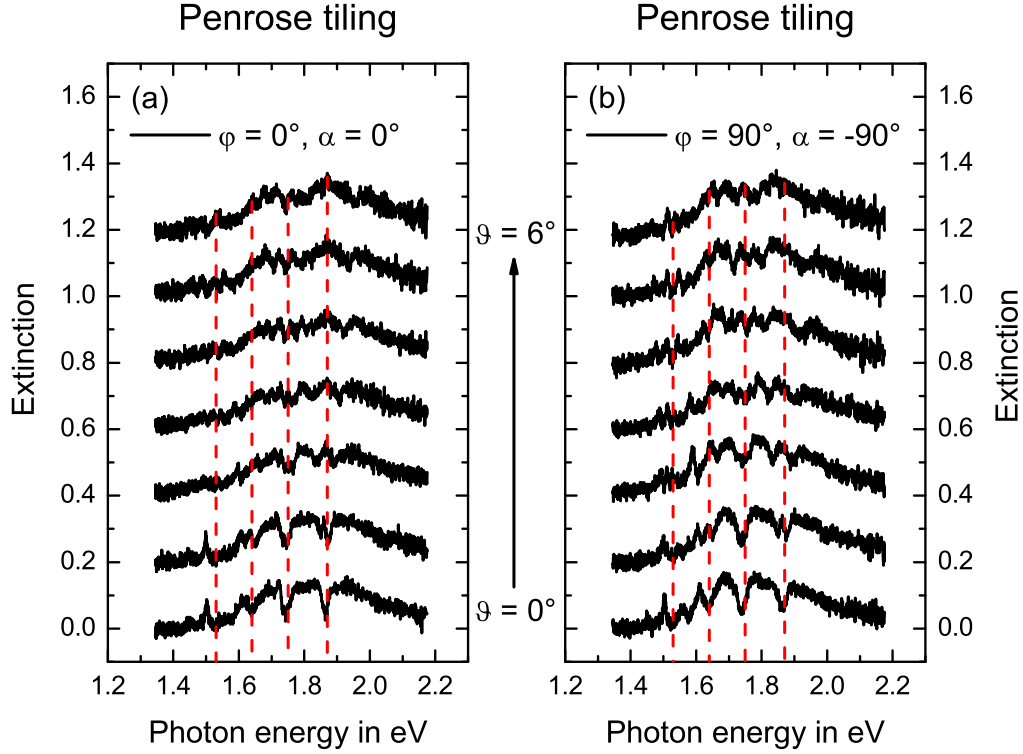
Figure 5.24: P-polarized extinction spectra of a Penrose tiling for (a) $\varphi = 0°$ as well as for (b) $\varphi = 90°$. The angle of incidence is changed between $\vartheta = 0°$ (bottom) and $\vartheta = 6°$ (top) in steps of $1°$. The spectra are shifted upward for clarity.

5.6 2D theoretical model for oblique light incidence

The theoretical model described in section 5.3 was developed for normal incidence. However, in order to model the spectra for oblique light incidence, this model has to be expanded, which is described in this section.

The first step is again the description of the spatial arrangement by Dirac delta functions and the subsequent 2D Fourier transform. This 2D Fourier transform can be calculated with the help of the projection slice theorem [138, 139]. The individual slices in direction β are given by $S_\beta(k_\xi)$ of Eq. (5.4). As it was already described in section 2.1.2, the propagation constants $\boldsymbol{\beta}_p$ are given by

$$\boldsymbol{\beta}_p = \mathbf{k}_{xy} + \mathbf{g} \tag{5.20}$$

with $\mathbf{k}_{xy} = k_0 \sin(\vartheta)$ being the wave vector component parallel to the sample surface (see Fig. 5.25 (a)) and $\mathbf{g}$ being the location of the Fourier components in reciprocal

space. This relation was already given in Eq. (2.28). For normal light incidence, $\mathbf{k}_{xy}$ is equal to zero meaning that the propagation constants of the waveguide modes are just given by the $\mathbf{k}$ vectors of the Fourier peaks. For oblique light incidence, however, $\mathbf{k}_{xy}$ is not equal to zero leading to the vector addition given in Eq. (5.20). This means that the propagation constants for oblique light incidence (filled circles) can be obtained by shifting the Fourier transform (open circles) by $\mathbf{k}_{xy}$, which is displayed in Fig. 5.25 (b). The absolute value of the propagation constants for an angle of incidence ϑ and an azimuthal angle φ is given by [144]

$$\beta_p = \sqrt{k_0^2 \sin^2(\vartheta) + g^2 + 2\, k_0\, \sin(\vartheta)\, g\, \cos(\varphi - \beta_{FT})} \qquad (5.21)$$

with k_0 as the absolute value of the incident wave vector and g as the Fourier component with distance g to the center of the Fourier transform. The directions of the individual Fourier components is denoted by the angle β_{FT}.

Since each Fourier component as well as each component $\mathbf{k}_{xy}$ is dependent on the energy of the incident light with polar angle ϑ, the vector $\mathbf{k}_{xy}$ is different for each Fourier component. Therefore, the TE and TM dispersion relations of Eqs. (2.24) and (2.25) are needed, which are plotted as black solid and red dashed curves in Fig. 5.25 (c), respectively. The energies and the corresponding k_{xy} values are obtained by the intersections of a straight line with angle ϑ to the energy axis and the folded dispersion curves. These k_{xy} values can be utilized to find the location of the angular propagation constants by using Eq. (5.20). The vectors from the center of the Fourier transform that are pointing to the angular propagation constants define the directions in which the waveguide modes are propagating. The angle β defines the angle between the direction of the angular propagation constant and the sample x axis. Due to the fact that the TE and TM dispersion relations are different, the TE waves do not propagate in the same directions as the TM waves for the same Fourier component. However, the Fourier transform in Fig. 5.25 is shifted by a constant $\mathbf{k}_{xy}$ component for all TE and TM propagation constants. In this picture, the TE and TM wave are propagating in the same β direction. This is easier to explain since we do not have to distinguish between the TE and the TM direction. However, we have to keep in mind that the TE and TM directions are different for the real calculations.

The polarization $\mathbf{E}_\alpha$ of the incident light is defined to have the $\mathbf{E}_{\alpha, xy}$ component rotated by the angle α around the sample x axis (see Fig. 5.25 (d)). When light with this polarization is incident on the sample, $\mathbf{E}_\alpha$ has to be split into a TE as well as a TM wave propagating in direction β (see Fig. 5.25 (d)). This leads to the

components [144]

$$C_{TE} = \pm\sqrt{C_{\alpha,xy}^2 \sin^2(\alpha - \beta) + C_{\alpha,z}^2}, \qquad (5.22)$$

$$C_{TM} = C_{\alpha,xy} \cos(\alpha - \beta), \qquad (5.23)$$

where $C_{\alpha,xy}$ and $C_{\alpha,z}$ are defined by

$$C_{\alpha,xy} = \frac{C_\alpha}{\sqrt{1 - \sin^2(\vartheta)\sin^2(\varphi - \alpha)}} \cos(\vartheta), \qquad (5.24)$$

$$C_{\alpha,z} = -\frac{C_\alpha}{\sqrt{1 - \sin^2(\vartheta)\sin^2(\varphi - \alpha)}} \sin(\vartheta)\cos(\varphi - \alpha). \qquad (5.25)$$

The + sign in Eq. (5.22) is used when $0° \leqslant \alpha - \beta < 180°$ and the − sign is used when $180° \leqslant \alpha - \beta < 360°$. The factor C_α in Eqs. (5.24) and (5.25) is dependent on the incident light with polar angle ϑ and azimuthal angle φ. Since $\mathbf{E}_{\alpha,z}$ is always normal to the direction of propagation, only C_{TE} is dependent on $C_{\alpha z}$.

It has been mentioned above that for a square lattice or a rectangular lattice with $\varphi = 0°$ and s-polarization no TM wave is expected to propagate in $\pm x$ direction. However, in Fig. 5.19 (a) as well as in Fig. 5.21 (a) a small resonance is visible for a TM polarized wave propagating in x direction. This resonance is split into two for oblique light incidence. As it has already been explained in section 5.3, this is due to the elliptically shaped particles that are rotated by the angle γ around the sample x axis.

Incident light with polarization $\mathbf{E}_\alpha$ can excite particle plasmons in such metallic particles, but only along the principal axes u, v, and z. The components C_{plu}, C_{plv}, and C_{plz} (see Fig. 5.25 (e)) are given by [144]

$$C_{plu} = C_{\alpha,xy}\, C_u \cos(\alpha - \gamma), \qquad (5.26)$$

$$C_{plv} = C_{\alpha,xy}\, C_v \sin(\alpha - \gamma), \qquad (5.27)$$

$$C_{plz} = C_{\alpha,z}\, C_z \qquad (5.28)$$

with C_u, C_v, and C_z as factors dependent on the eccentricity and size of the metal particles. Each of these excited particle plasmons can be regarded as polarized light that is incident on the sample. As it was explained above for polarized light incident on the sample, each particle plasmon can excite a TE as well as a TM wave propagating in direction β (see Fig. 5.25 (f)). This leads to the following
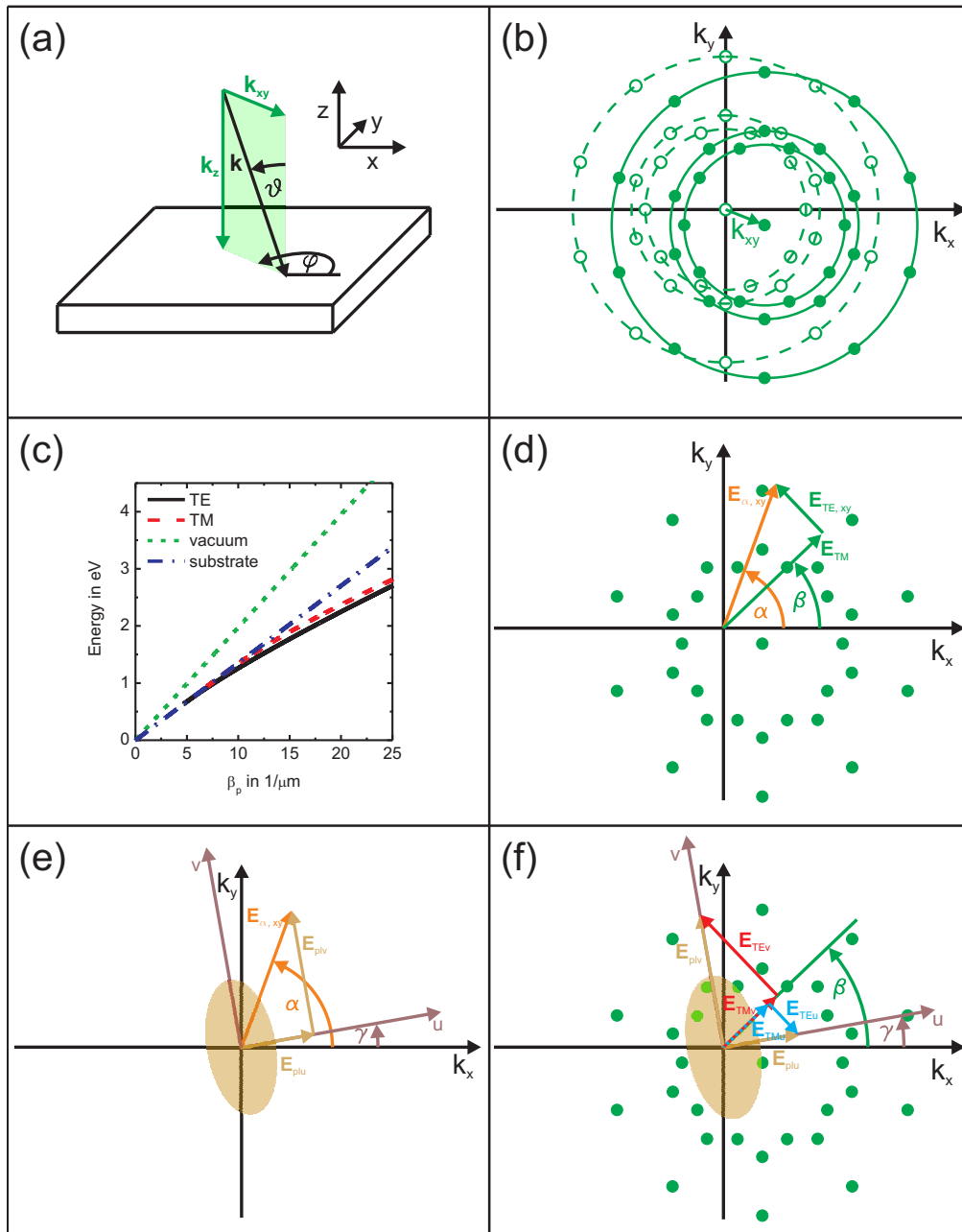
Figure 5.25: (a) **k**-vector incident on the sample for an angle of incidence ϑ and an azimuthal angle φ. (b) The Fourier transform (open circles) is shifted by $\mathbf{k}_{xy}$ in order to obtain the propagation constants for oblique light incidence (filled circles). (c) Dispersion relations of a TE (black solid) and a TM polarized (red dashed) waveguide mode as well as those of vacuum (green short-dashed) and quartz (blue dash-dotted) for a 180 nm thick HfO$_2$ waveguide on quartz. (d) TE and TM waves propagating in direction β with $\mathbf{E}_{TE}$ and $\mathbf{E}_{TM}$ as the vector addition of the incident polarization $\mathbf{E}_\alpha$. (e) The incident polarization excites particle plasmons along the main axes of an elliptical metal particle. (f) Each particle plasmon can excite a TE as well as a TM polarized wave in direction β.

components [144]

$$C_{TEu} = -C_{plu} \sin(\beta - \gamma), \tag{5.29}$$

$$C_{TEv} = C_{plv} \cos(\beta - \gamma), \tag{5.30}$$

$$C_{TEz} = C_{plz}, \tag{5.31}$$

$$C_{TMu} = C_{plu} \cos(\beta - \gamma), \tag{5.32}$$

$$C_{TMv} = C_{plv} \sin(\beta - \gamma). \tag{5.33}$$

The $-$ sign in Eq. (5.29) is needed since $\mathbf{E}_{TEu}$ points in the opposite direction than the other TE components. Note that the electric field vector in z direction can only excite a TE polarized wave as already mentioned above.

The overall components $C_{TE,add}$ for a TE as well as $C_{TM,add}$ for a TM wave are obtained by the addition of the individual components (Eqs. (5.22), (5.29), (5.30), and (5.31) for TE polarized waves as well as Eqs. (5.23), (5.32), and (5.33) for TM polarized waves) [144]

$$C_{TE,add} = C_{TE} + C_{TEu} + C_{TEv} + C_{TEz}, \tag{5.34}$$

$$C_{TM,add} = C_{TM} + C_{TMu} + C_{TMv}. \tag{5.35}$$

As it has been explained for normal incidence, $S_\beta(k_\xi)$ in direction β has to be weighted with the square value of $C_{TE,add}$ as well as with $C_{TM,add}$. However, this is not the initial slice of the Fourier transform but the slice through the center of the reciprocal space and the shifted Fourier peak. The total intensity is then obtained by integrating over all directions β leading to

$$F_{tot,TE} = \int_{0°}^{360°} S_\beta(k_\xi)\, C_{TE,add}^2 \, d\beta, \tag{5.36}$$

$$F_{tot,TM} = \int_{0°}^{360°} S_\beta(k_\xi)\, C_{TM,add}^2 \, d\beta \tag{5.37}$$

with the positive k_ξ axis of $S_\beta(k_\xi)$ for $0° \leqslant \beta < 180°$ and the negative one for $180° \leqslant \beta < 360°$.

The rest of this model is equal to the normal incidence model in section 5.3. As it has been explained there, the transmission and reflection amplitudes are obtained by using Eqs. (5.17) and (5.18) with the phase of the waveguide mode given by Eq. (5.19). The transmittance and reflectance spectra can be calculated by using $T = |t|^2$ and $R = |r|^2$, respectively. The extinction spectrum is given by $\mathrm{Ext} = -\ln(T)$.

For the samples measured with oblique angle of incidence (see spectra in section 5.5), the individual spectra are calculated by using the just described model. The
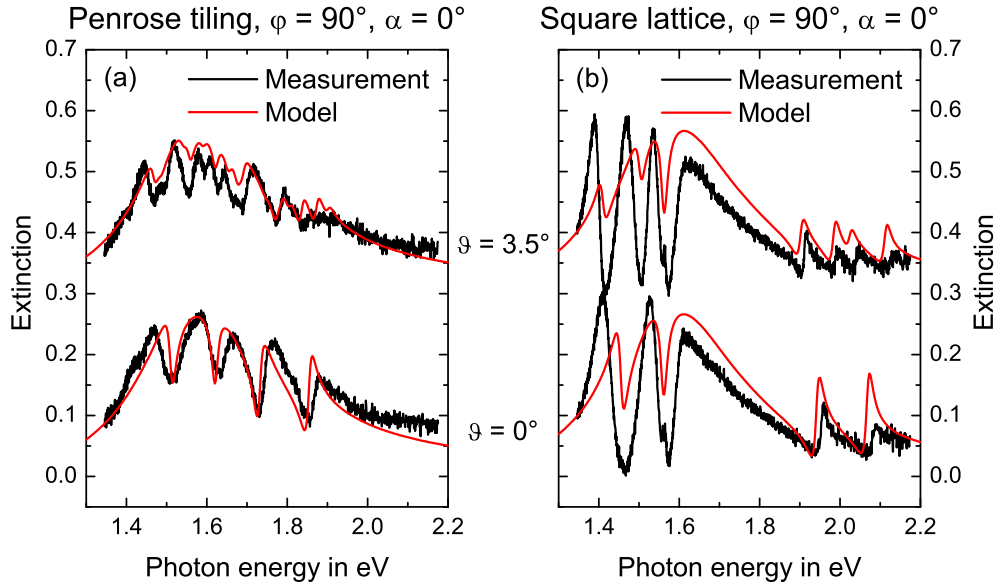
Figure 5.26: Measured (black) and modeled (red) extinction spectra of (a) a Penrose tiling as well as (b) a square lattice in s-polarization for incidence angles $\vartheta = 0°$ (bottom) and $\vartheta = 3.5°$ (top) and an azimuthal angle $\varphi = 90°$. The spectra are shifted upward for clarity.

measured (black) and modeled (red) spectra of sample 1 in s- and p-polarization are shown in Figs. 5.26 and 5.27, respectively. Panels (a) of both figures depict the spectra of the Penrose tiling and panels (b) those of the square lattice. The angle of incidence was changed between $\vartheta = 0°$ (bottom) and $\vartheta = 3.5°$ (top) for an azimuthal angle of $\varphi = 90°$. The fitting parameters $t_{plu} = 0.1434$, $t_{plv} = 0.1580$, and $A = 0.0084$ were used for calculating all spectra. These parameters were obtained by fitting the curve to just one spectrum. The agreement between the measured and the modeled spectra is especially good for the Penrose tiling. The four waveguide mode resonances for normal incidence split up into several peaks for oblique light incidence. This behavior is different for s- and p-polarization. The difference has already been explained for the spectra in Figs. 5.17 and 5.18. Exactly this different behavior is described very well in our model. The location of the resonances in the modeled spectra coincides with those of the measured ones. This behavior can be seen in Fig. 5.26 (a) for s-polarized light ($\varphi = 90°$ and $\alpha = 0°$) as well as in Fig. 5.27 (a) for p-polarized light ($\varphi = 90°$ and $\alpha = -90°$). The location of the resonances for the square lattice is also predicted quite well by our model (see Figs. 5.26 (b) and 5.27 (b)). As it has been already explained in Fig. 5.17 for s-polarization, the TE polarized waveguide mode splits up into two modes for
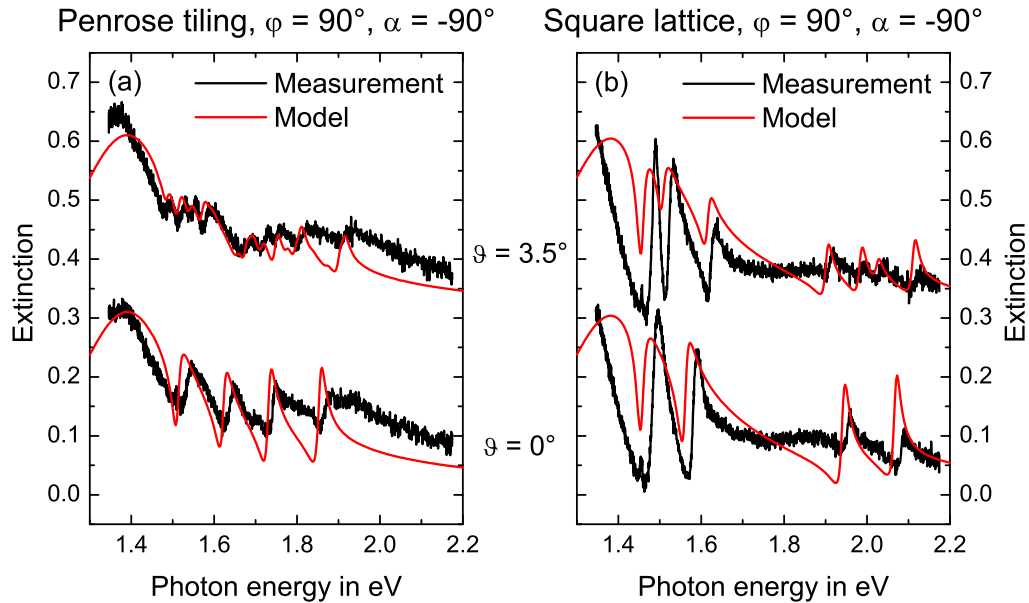
Figure 5.27: Measured (black) and modeled (red) extinction spectra of (a) a Penrose tiling as well as (b) a square lattice in p-polarization for incidence angles $\vartheta = 0°$ (bottom) and $\vartheta = 3.5°$ (top) and an azimuthal angle $\varphi = 90°$. The spectra are shifted upward for clarity.

oblique light incidence, whereas the TM polarized mode stays at about the same energy. This behavior can be seen for both measured and modeled spectra (see Fig. 5.26 (b)). The opposite behavior can be obtained for p-polarization, namely the TE polarized resonance stays at a constant energy and the TM polarized resonance splits up into two modes. Again, this is visible for the measured as well as the modeled spectrum (Fig. 5.27 (b)). Also the splitting of the waveguide modes propagating in diagonal direction is well predicted in the modeled spectra. However, deviations are visible for the waveguide mode resonances within the plasmon resonance. These deviations can also be obtained for normal incidence. The reason of the appearance of these deviations is unknown.

The spectra of sample 2 were also modeled using the theoretical model described above in this section. First, this is shown for s- as well as p-polarized spectra of the square lattice in Figs. 5.28 and 5.29, respectively. The angle of incidence is changed between $\vartheta = 0°$ (bottom) and $\vartheta = 6°$ (top) in steps of 1°. The azimuthal angle is $\varphi = 0°$ in panels (a) and $\varphi = 90°$ in panels (b). The fitting parameters $t_{plu} = 0.0784$, $t_{plv} = 0.1169$, and $A = 0.0022$ were fitted to only one curve and were used for all other spectra.
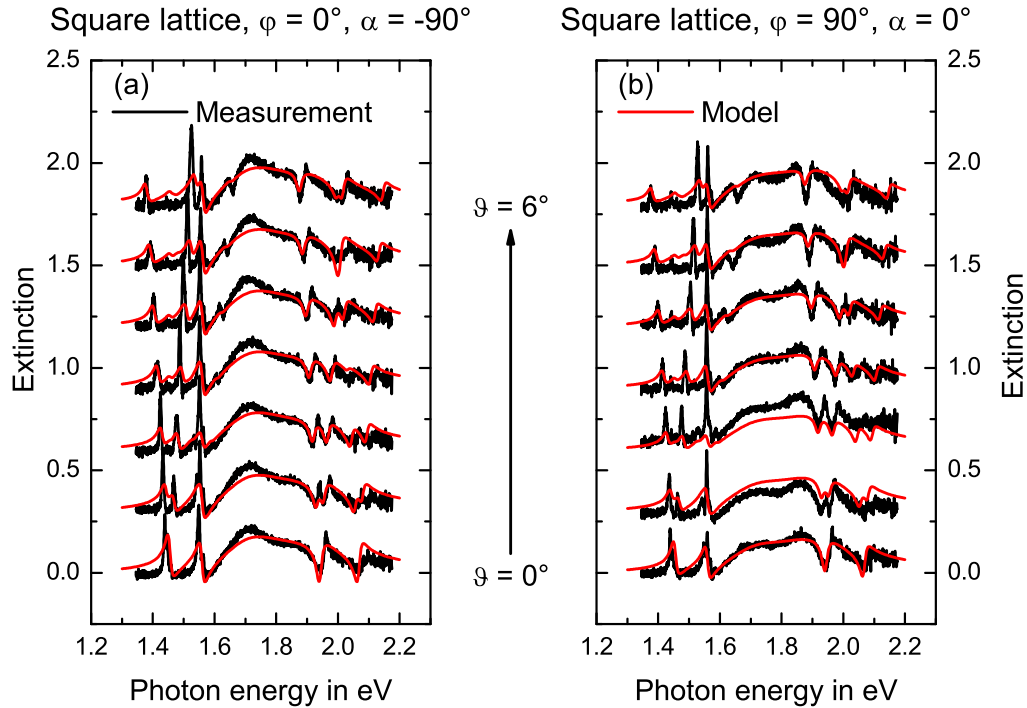
Figure 5.28: Measured (black) and modeled (red) extinction spectra of a square lattice in s-polarization for (a) $\varphi = 0°$ as well as for (b) $\varphi = 90°$. The angle of incidence is changed between $\vartheta = 0°$ (bottom) and $\vartheta = 6°$ (top) in steps of $1°$. The spectra are shifted upward for clarity.

It can be nicely seen that the TE polarized waveguide mode $(1.47\,\text{eV})$ splits up into two modes, whereas the TM polarized waveguide mode $(1.57\,\text{eV})$ stays at approximately constant energies for s-polarization (see Fig. 5.28). However, also a small fraction of the TE polarized mode stays at about $1.47\,\text{eV}$ and a small part of the TM polarized mode splits up into two modes. This behavior is visible in both the measured as well as the modeled spectra. This can only be explained by the elliptically shaped, rotated metal disks. As it has been explained above for the theoretical model, the incident polarization can excite the particle plasmons only along the principal axes. These rotated polarizations can excite waveguide modes propagating in directions β (see Fig. 5.25 (f)). For $\varphi = 0°$ and $\alpha = -90°$ (see Fig. 5.28 (a)), the TE (TM) polarized waves are propagating in $\pm x$ ($\pm y$) direction. Therefore, it is only expected that the TE (TM) waveguide mode splits up into two modes (stays at constant energies). However, due to the fact that the gold disks are elliptically shaped and rotated by $\gamma = 40°$, the excitation of a TE (TM) polarized mode propagating in $\pm y$ ($\pm x$) is possible. This leads to the small fraction
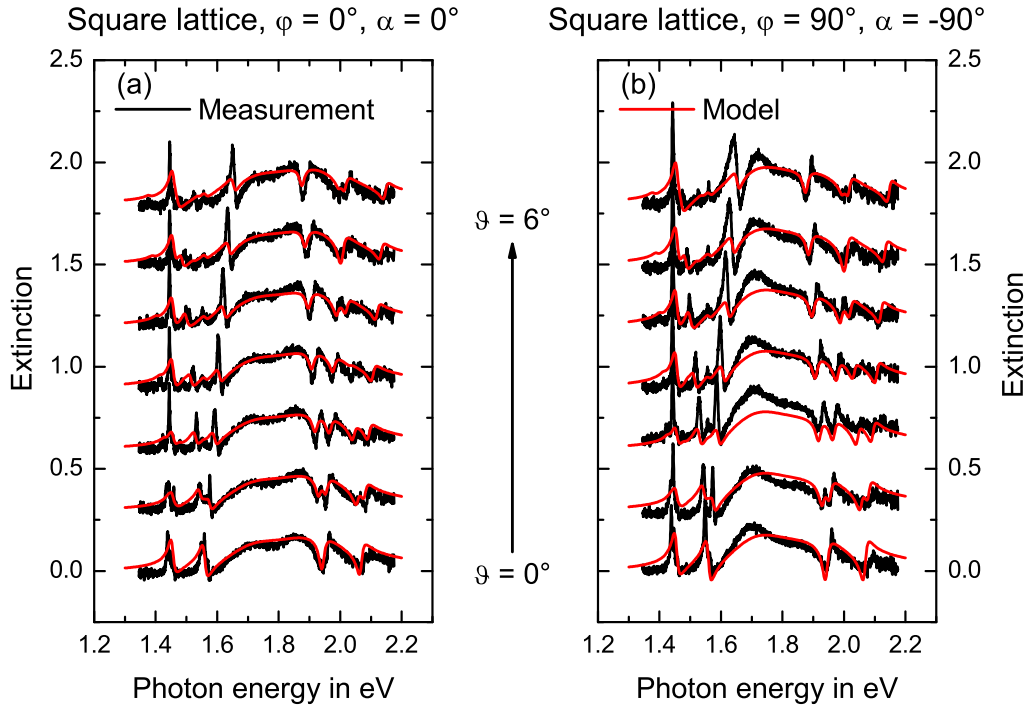
Figure 5.29: Measured (black) and modeled (red) extinction spectra of a square lattice in p-polarization for (a) $\varphi = 0°$ as well as for (b) $\varphi = 90°$. The angle of incidence is changed between $\vartheta = 0°$ (bottom) and $\vartheta = 6°$ (top) in steps of 1°. The spectra are shifted upward for clarity.

of the TE polarized mode staying at approximately constant energies as well as to the small fractions of the TM polarized wave splitting up into two modes. Similar explanations can be given for the s-polarized spectra with $\varphi = 90°$ (see Fig. 5.28 (b)). However, the waves propagating in $\pm x$ direction have to be replaced by waves propagating in $\pm y$ direction and vice versa. The behavior of the measured spectra is very nicely reproduced by the modeled spectra, which verifies our model.

The p-polarized spectra for $\varphi = 0°$ and $\varphi = 90°$ were also calculated using the same fitting parameters as above. Also here, a very nice agreement between measured and modeled curves is achieved. In contrast to s-polarization, the major TE peak stays at constant energies and the major TM peak splits up into two modes. However, a minor TE peak splitting up into two modes as well as a minor TM peak staying at approximately constant energies can be obtained in both the measured as well as the modeled spectra. As above for the s-polarized spectra, this behavior can only be explained by the elliptically shaped, rotated metal disks. For $\varphi = 0°$ and $\alpha = 0°$ (see Fig. 5.29 (a)), a TE polarized wave propagating in $\pm x$ direction as well as a

TM polarized wave propagating in $\pm y$ can only be explained by the excitation due to the particle plasmons along the main axes of the rotated metal disks. The same is true for TE polarized waves propagating in $\pm y$ direction as well as for TM polarized waves propagating in $\pm x$ direction, when $\varphi = 90°$ and $\alpha = -90°$ (see Fig. 5.29 (b)).
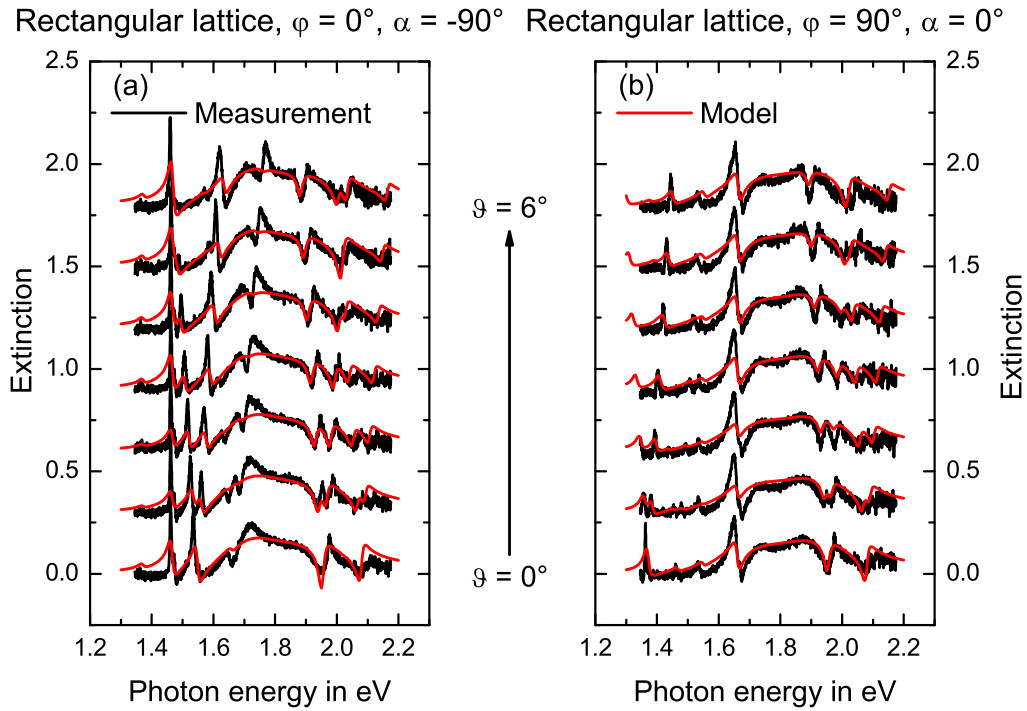

Figure 5.30: Measured (black) and modeled (red) extinction spectra of a rectangular lattice in s-polarization for (a) $\varphi = 0°$ as well as for (b) $\varphi = 90°$. The angle of incidence is changed between $\vartheta = 0°$ (bottom) and $\vartheta = 6°$ (top) in steps of 1°. The spectra are shifted upward for clarity.

This behavior can especially be seen by looking at the spectra of a rectangular lattice. Due to the fact that the periodicity in x and y direction is different, also the TE (TM) polarized waveguide modes appear at different energies in the spectrum. The measured (black) and modeled (red) curves are shown in Figs. 5.30 and 5.31 for s- and p-polarization, respectively. The angle of incidence is changed between $\vartheta = 0°$ (bottom) and $\vartheta = 6°$ in steps of 1°. In panel (a) the azimuthal angle is $\varphi = 0°$ and in panel (b) $\varphi = 90°$. The fitting parameters for the modeled curves are given by $t_{plu} = 0.0784$, $t_{plv} = 0.1169$, and $A = 0.0022$. As can be seen in Figs. 5.30 and 5.31, the agreement between the measured and the modeled curves is also here quite good.

The resonances at about $1.37\,\text{eV}$, $1.47\,\text{eV}$, $1.55\,\text{eV}$, and $1.66\,\text{eV}$ are due to TE and
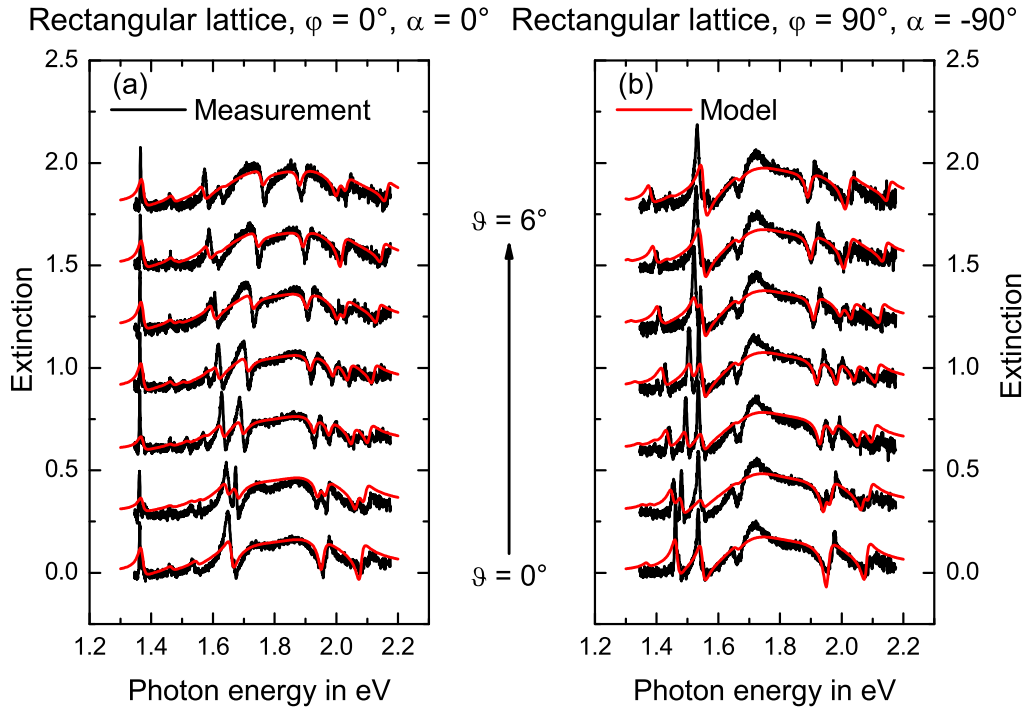
Figure 5.31: Measured (black) and modeled (red) extinction spectra of a rectangular lattice in p-polarization for (a) $\varphi = 0°$ as well as for (b) $\varphi = 90°$. The angle of incidence is changed between $\vartheta = 0°$ (bottom) and $\vartheta = 6°$ (top) in steps of 1°. The spectra are shifted upward for clarity.

TM waves propagating in $\pm y$ direction as well as to TE and TM waves propagating in $\pm x$ direction. For $\varphi = 0°$ and s-polarization (Fig. 5.30 (a)), the TE polarized wave in $\pm y$ direction as well as the TM polarized wave in $\pm x$ direction can only be explained by the rotated metal particles. These resonances are present in both the measured as well as the modeled spectra. It can be clearly seen that the waves propagating in $\pm y$ direction stay at constant energies, whereas the waves propagating in $\pm x$ direction split up into two modes. This behavior is very well described by the modeled curves. For $\varphi = 90°$ and s-polarization (Fig. 5.30 (b)), the TE polarized wave in $\pm y$ direction and the TM polarized wave in $\pm x$ direction are more pronounced when compared to the TM polarized wave in $\pm y$ direction and the TE polarized wave in $\pm x$ direction. This time, the waves propagating in $\pm y$ direction split up into two modes, whereas the waves propagating in $\pm x$ direction stay approximately constant. Also this behavior is modeled quite well. As already mentioned above, the two different azimuthal angles in s-polarization show a splitting of the more pronounced TE wave, whereas the more pronounced TM wave stays at approximately constant energies.

For $\varphi = 0°$ and p-polarization (Fig. 5.31 (a)), the waves propagating in $\pm y$ direction stay at constant energies and the waves in $\pm x$ split up into two modes as for $\varphi = 0°$ and s-polarization. However, the more pronounced waves for p-polarization are the TE wave in $\pm y$ direction and the TM wave in $\pm x$ direction. As already explained above, the minor resonances can only be explained by the rotated metal disks. The waves propagating in $\pm y$ direction for $\varphi = 90°$ and p-polarization (Fig. 5.31 (b)) split into two modes and the waves in $\pm x$ direction stay approximately constant. This is different in comparison to the p-polarized spectra with $\varphi = 0°$. It is also different that the TM polarized wave in $\pm y$ direction and the TE polarized wave in x direction are the more pronounced resonances. However, the more pronounced TE wave stays at constant energies, whereas the more pronounced TM wave splits into two modes. The behavior of these spectra is verified by our model meaning that the excitation of the minor resonances can be explained by the model presented above.

Figure 5.32: Measured (black) and modeled (red) extinction spectra of a Penrose tiling in s-polarization for (a) $\varphi = 0°$ as well as for (b) $\varphi = 90°$. The angle of incidence is changed between $\vartheta = 0°$ (bottom) and $\vartheta = 6°$ (top) in steps of $1°$. The spectra are shifted upward for clarity.

Finally, the angle-dependent spectra of the Penrose tiling of sample 2 were calculated with the model described above. The s- and p-polarized spectra are depicted in
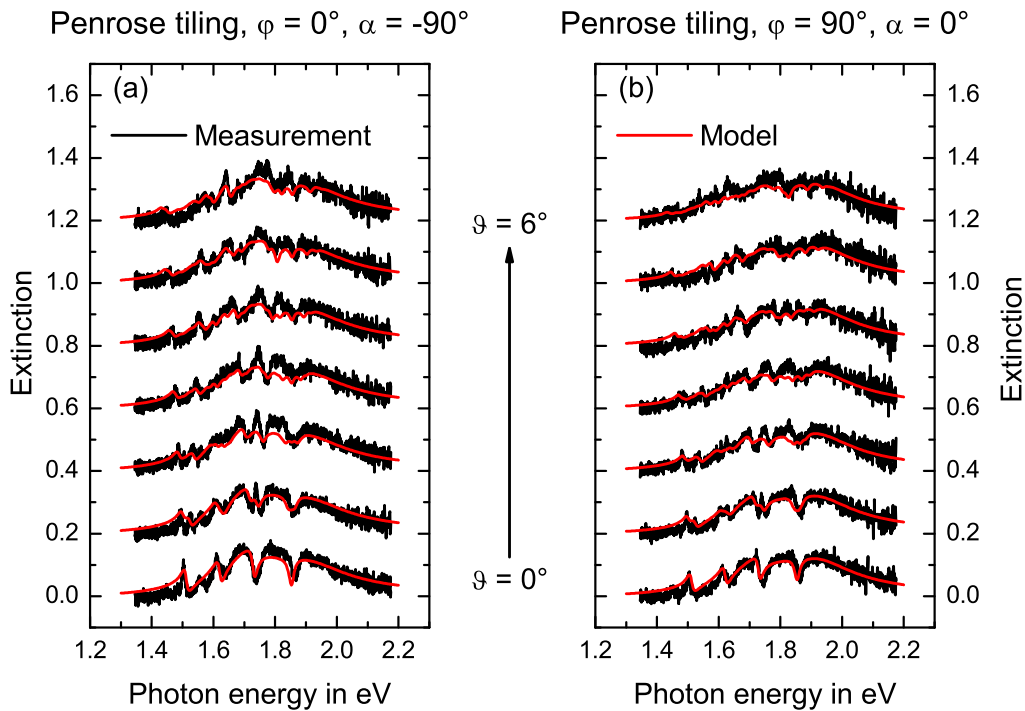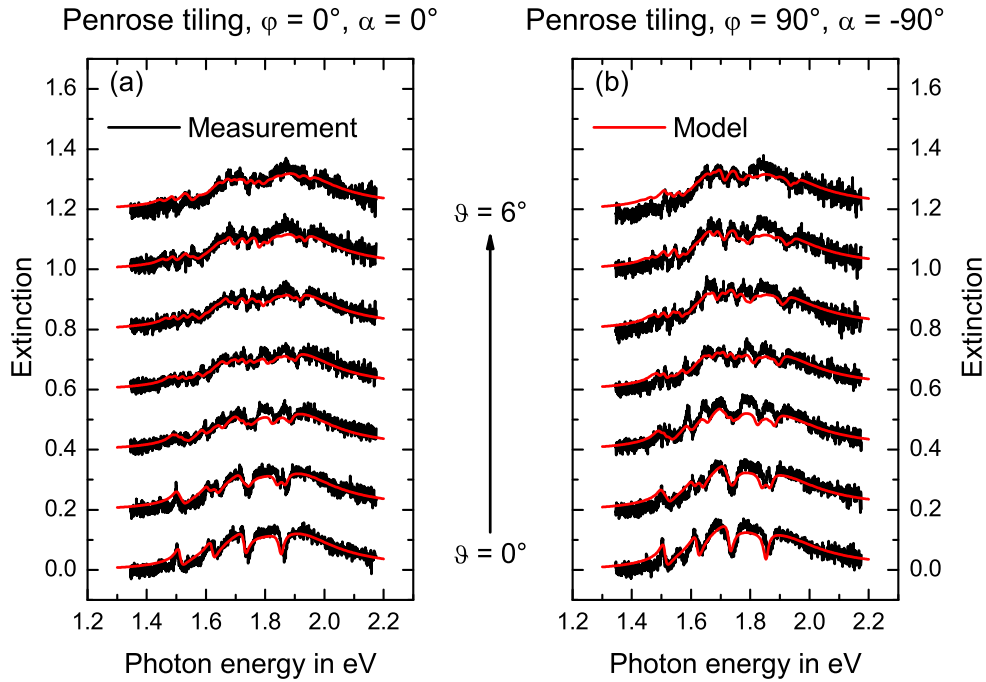
Figure 5.33: Measured (black) and modeled (red) extinction spectra of a Penrose tiling in p-polarization for (a) $\varphi = 0°$ as well as for (b) $\varphi = 90°$. The angle of incidence is changed between $\vartheta = 0°$ (bottom) and $\vartheta = 6°$ (top) in steps of $1°$. The spectra are shifted upward for clarity.

Figs. 5.32 and 5.33, respectively. The spectra with an azimuthal angle of $\varphi = 0°$ are shown in panel (a) and those with $\varphi = 90°$ are plotted in panel (b). The angle of incidence is varied in steps of $1°$ between $\vartheta = 0°$ and $\vartheta = 6°$. The modeled curves (red) are calculated with the fitting parameters $t_{plu} = 0.0685$, $t_{plv} = 0.0896$, and $A = 0.001$ for all spectra. Since the Penrose tiling possesses ten-fold symmetry in reciprocal space, the behavior is more difficult to explain when compared to the square and the rectangular lattice. However, this has been done above in section 5.5. We can observe a splitting into five or six modes of each of the normal incidence waveguide modes. These resonances are more or less pronounced depending on the incident azimuthal angle as well as the incident polarization. Some minor resonances due to the elliptical particles are also present. However, due to the fact that one resonance for normal incidence splits into several modes for oblique light incidence, these additional waveguide modes are hardly visible in the spectra. Mostly, they are even located at the same energy positions of the already present modes leading to a higher resonance peak. However, the modeled curves (red) calculated with the above presented model are compared to the measured spectra (black) for both

s- and p-polarization. The agreement between the measured and the calculated spectra is very good, which verifies our model. Therefore, quasiperiodic spectra can be modeled by using this approach.
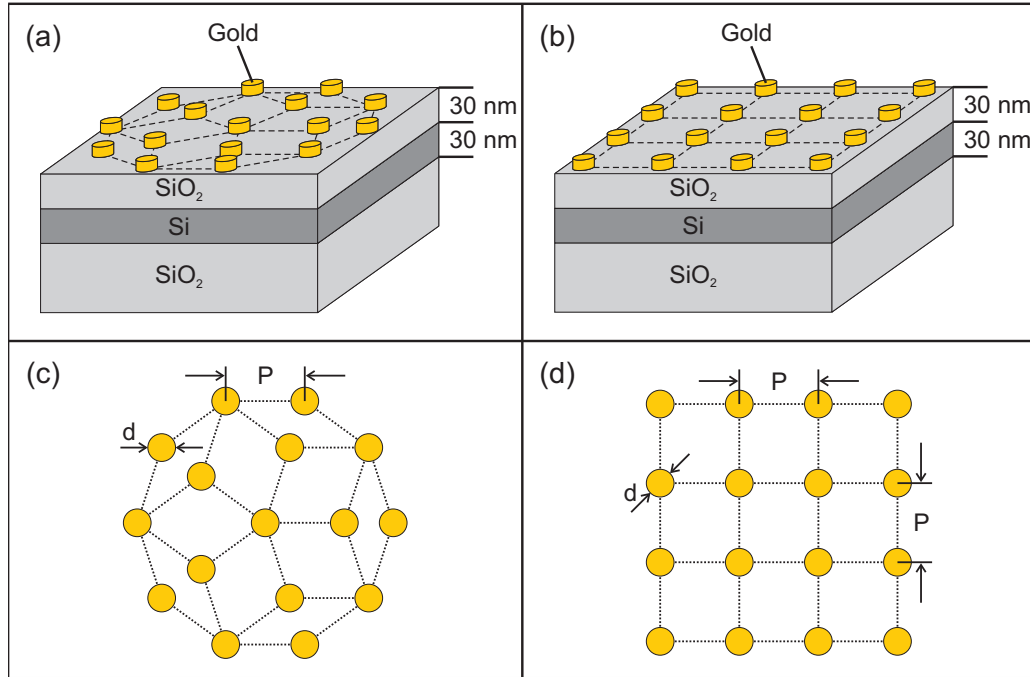
5.7   Plasmonic solar cells

Figure 5.34: Solar cell design with (a) a 2D quasiperiodic arrangement and (b) a 2D periodic arrangement of gold disks on top of a 30 nm thick SiO_2 spacer layer, a 30 nm thick Si waveguide layer, and a SiO_2 substrate. The gold disks with diameter d are arranged (c) on the vertices of a Penrose tiling with an edge length P and (d) in a periodic fashion with a periodicity P.

Possible applications of such metallic photonic crystals are light emitting diodes (LEDs) or solar cells. In either case, the waveguide layer consists of a semiconductor having a relative high index of refraction. For LEDs, a forward biased voltage is applied so that light of a specific energy is emitted. However, the working principle of solar cells is reversed meaning that light incident on the semiconductor generates a current. The efficiency of such devices can be enhanced when light is coupled into or out of the waveguide layer. This can be achieved by using a grating structure. Since all measurements in this thesis are based on light that is incident on the metallic photonic crystal, we will present here a method for enhancing the efficiency of solar cells. However, similar structure designs can be used to increase the efficiency of LEDs.

The sample in this case consists of a silicon dioxide (SiO_2) substrate with a $30\,nm$ thick crystalline silicon (Si) waveguide layer on top and is shown in Fig. 5.34. The arrangement of the circular gold disks with a diameter d of $100\,nm$ and a height of $50\,nm$ is either quasiperiodic or periodic. Since the particle plasmon resonance is strongly damped when a metal is directly placed on an absorbing semiconductor [145], a passivation layer between the Si layer and the gold disks is introduced. This passivation layer consists of a $30\,nm$ thick SiO_2. Another effect of this additional SiO_2 layer is that the sample structure is more symmetric leading to a lower cutoff energy of the waves that can be guided in the Si layer [104]. In the quasiperiodic tiling the metal particles are placed on the vertices of a Penrose tiling with an edge length $P = 425\,nm$ (see Fig. 5.34 (c)). The period of the square lattice is also $P = 425\,nm$ (see Fig. 5.34 (d)).
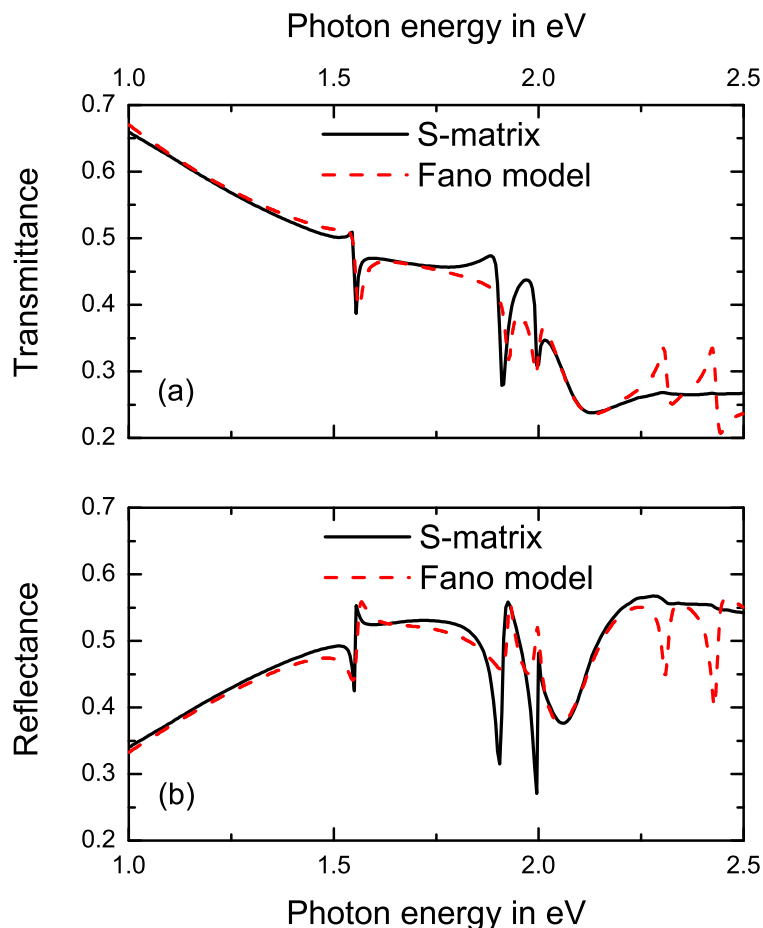

Figure 5.35: S-matrix calculated (a) transmittance and (b) reflectance spectra (black solid lines) as well as the corresponding Fano modeled spectra (red dashed lines) for a periodic gold disk arrangement.

In order to predict the absorption enhancement of such a plasmonic solar cell, the normal incidence transmittance and reflectance spectra of the periodic structure is calculated by using S-matrix simulations. This is necessary since reasonable fitting parameters are needed for the model presented in section 5.6. These S-matrix calculated transmittance and reflectance spectra are shown as black solid lines in Fig. 5.35 (a) and (b), respectively. The transmittance ($T = |t|^2$) and reflectance ($R = |r|^2$) curves of our Fano model fitted by using the transmission and reflection amplitudes t and r of Eqs. (5.17) and (5.18) are plotted as red dashed curves in Fig. 5.35 (a) and (b). The direct transmission and reflection coefficients t_d and r_d are fitted to the transmittance and reflectance spectra of the structure without the plasmonic disks and are given by

$$t_d = 1.3370 - 0.8147E + 0.3420E^2 - 0.0575E^3, \tag{5.38}$$

$$r_d = 0.0325 + 0.7545E - 0.2046E^2 + 0.0053E^3. \tag{5.39}$$

The phases of the directly transmitted and reflected waves are set to be $\phi_t = 0.269\,\pi$ and $\phi_r = 0.864\,\pi$, respectively. As already mentioned in section 5.3, the two particle plasmon terms of Eqs. (5.17) and (5.18) combine to only one term given by $\frac{t_{pl}\,\Gamma_{pl}\,e^{i\phi_{pl}}}{E-E_{pl}+i\,\Gamma_{pl}}$ and $\frac{r_{pl}\,\Gamma_{pl}\,e^{i\phi_{pl}}}{E-E_{pl}+i\,\Gamma_{pl}}$, respectively. For the energy, the phase, and the spectral width of this particle plasmon resonance, the values $E_{pl} = 2.0722\,\text{eV}$, $\phi_{pl} = \pi/2$, and $\Gamma_{pl} = 0.1081\,\text{eV}$ are used. The different waveguide modes in the energy range E possess the spectral widths $\Gamma_k = 0.01\,\text{eV}$. Their amplitudes A_k are calculated with the approach presented in section 5.6 and the corresponding energies E_k are obtained by using the waveguide mode dispersion relations of the structure. The phases of the waveguide modes ϕ_k are calculated with Eq. (5.19) as well as with the phases of the undisturbed reflected and transmitted waveguide modes $\phi_{t,\infty} = 0.4104\,\pi$ and $\phi_{r,\infty} = 0.7096\,\pi$, respectively. The fitting parameters for the correct ratio between the particle plasmon and the waveguide modes are given by $t_{pl} = 0.1512$, $r_{pl} = 0.1668$, and $A = 0.01025$. It can be seen in Fig. 5.35 (a) and (b) that the agreement between the S-matrix spectra (black solid) and the Fano model (red dashed) is good. Only above an energy value of about 2.2 eV, the waveguide modes in the Fano model are much more pronounced when compared to the S-matrix calculations. This is due to an increased absorption coefficient of the Si layer above this value, which is neglected in the Fano model. Due to the strong damping, the waveguide modes above 2.2 eV cannot be excited. Therefore, only the energy region below this value is considered. Since an electron-hole pair can only be excited above the band gap energy $E_g = 1.12\,\text{eV}$ [146], only higher energy values are used. In the following, all spectra are restricted to the energy region between 1.12 eV and 2.2 eV.

For solar cells, it is important to know how much light can be absorbed. Therefore, the absorbance A is calculated with $A = 1 - T - R$. The transmittance T and the reflectance R are calculated for the square lattice as well as for the Penrose tiling by using the above mentioned parameters. It is assumed that an electron-hole pair is created for each absorbed photon in the Si layer [147]. However, part of the light is also absorbed by the metal particles, which reduces the amount of absorbed light in the semiconductor. Thus, the calculated absorbance is higher than the part that is only absorbed by the Si layer, which is in the energy region of the excited particle plasmon. However, it is expected that the amount of light absorbed in the gold disks is independent of the structural arrangement leading to the same absorbed fraction for the Penrose tiling and the square lattice. Furthermore, the light that is coupled into the waveguide slab is only absorbed by the material in this layer.

Figure 5.36: Polarization dependent absorbance spectra for p-polarized light of (a) a Penrose tiling and (b) a square lattice as well as for s-polarized light of (c) a Penrose tiling and (d) a square lattice. The angle of incidence is $\vartheta = 6°$ and the azimuthal angle φ is changed between $0°$ and $90°$.

The azimuthal angle as well as the polar angle incident on the solar cell are different for various local times and days. Therefore, it is important to have a look at the p- and s-polarized absorbance spectra with changing azimuthal angles for a specific

angle of incidence. The p-polarized absorbance spectra of a Penrose tiling and a square lattice are plotted as color-coded images for $\vartheta = 6°$ in Fig. 5.36 (a) and (b), respectively. The azimuthal angle is changed in these plots between $\varphi = 0°$ and $\varphi = 90°$. The s-polarized quasiperiodic and periodic spectra are shown in Fig. 5.36 (c) and (d). By comparing the color-coded spectra of the Penrose tiling to the corresponding ones of the square lattice, one notices that the absorbance maxima of the quasiperiodic lattice stay almost at the same energy position, whereas the maxima of the periodic lattice are very sensitive to the incident azimuthal angle. This means that the quasiperiodic structure is much less polarization dependent due to the higher rotational symmetry. Thus, it is expected that only in the quasicrystalline case the absorbance is almost identical for any incident azimuthal angle, which is desirable.
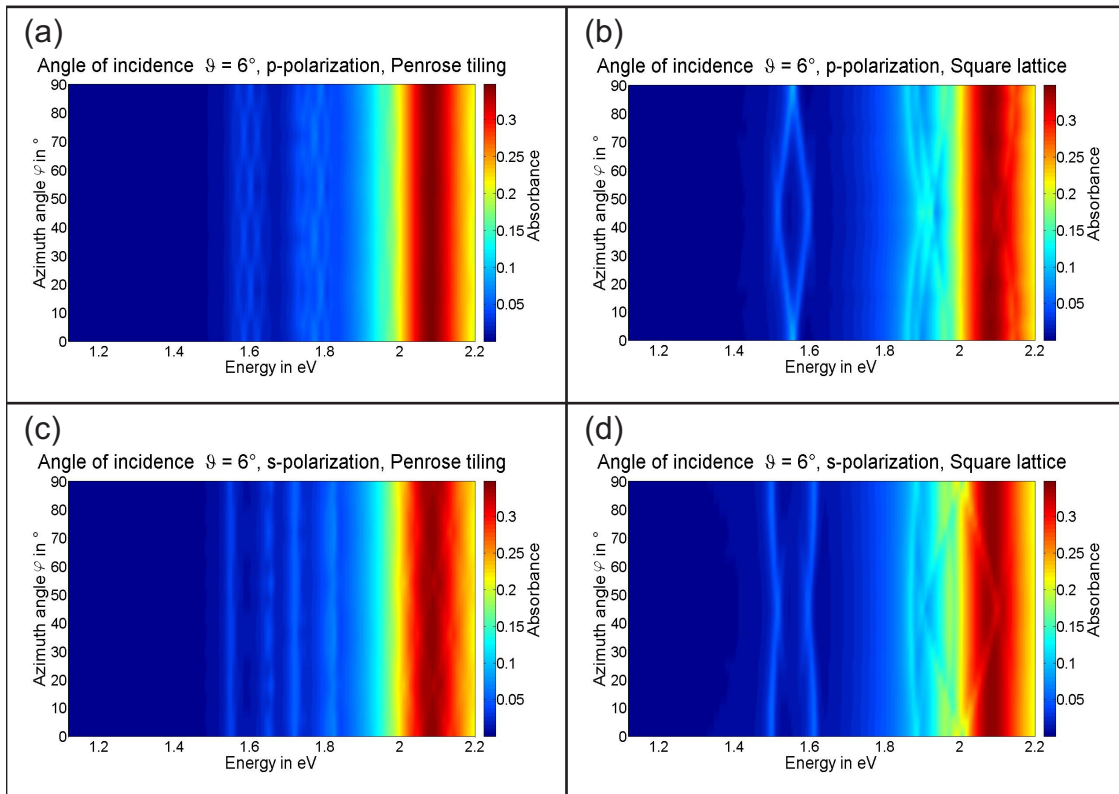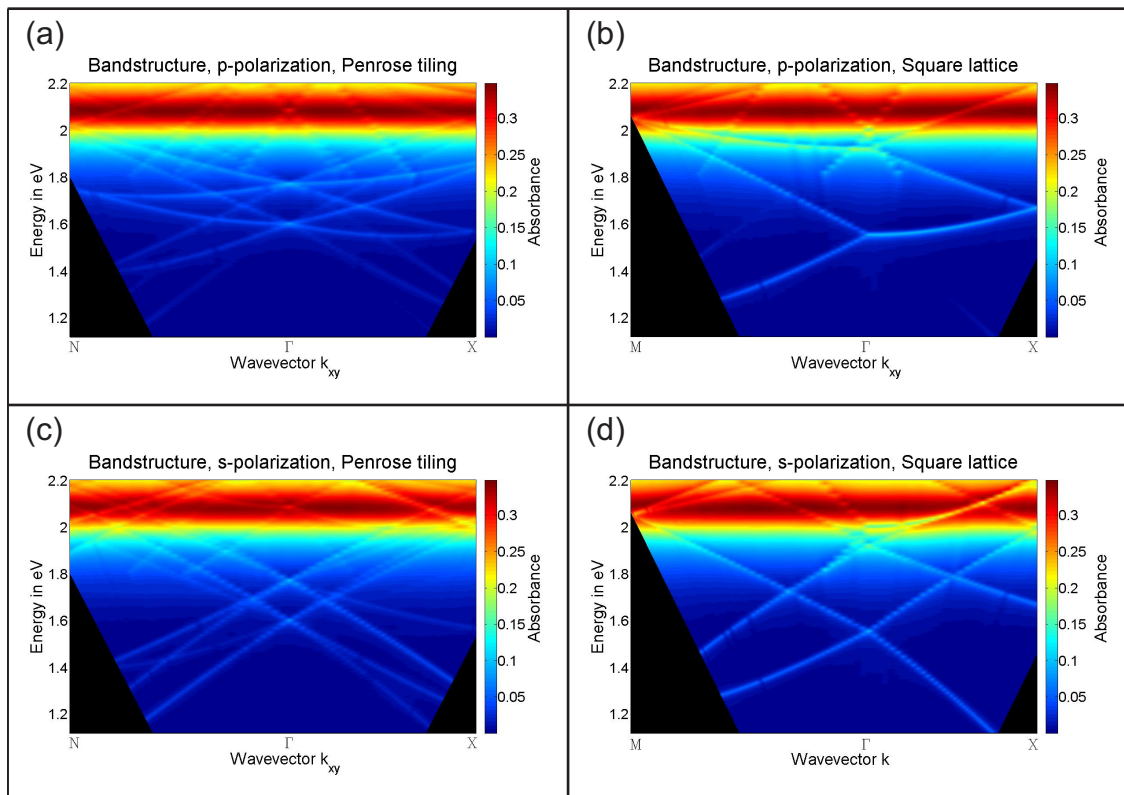

Figure 5.37: Angle dependent absorbance spectra for p-polarized light of (a) a Penrose tiling and (b) a square lattice as well as for s-polarized light of (c) a Penrose tiling and (d) a square lattice. The part from Γ to N belongs to an azimuthal angle of 18° and the part from Γ to M belongs to $\varphi = 45°$. The part from Γ to X belongs to an azimuthal angle of 0°.

Next, the angle dependent spectra are observed. The color code images for the quasiperiodic as well as the periodic arrangement in p-polarization are shown in

Fig. 5.37 (a) and (b), those in s-polarization are plotted in Fig. 5.37 (c) and (d). The right hand side in each panel belongs to an angle of incidence variation for $\varphi = 0°$, whereas the left hand side stems from an angle of incidence variation for $\varphi = 18°$ in the qausicrystalline case and for $\varphi = 45°$ in the periodic case. Normal incidence is indicated by Γ and the (pseudo-)Brillouin zone edge for $\varphi = 0°$ is given by X. N and M describe the pseudo-Brillouin zone edge for the Penrose tiling with $\varphi = 18°$ as well as the Brillouin zone edge for the square lattice with $\varphi = 45°$. For the quasicrystalline arrangement much more waveguide modes can be observed in comparison to the periodic lattice meaning that more different energies of the incident photons can be absorbed. Furthermore, the left part in each panel resembles the right part much better in the quasiperiodic case.

Due to the fact that the polar and azimuthal angles incident on the solar cell change significantly, the efficiency should be almost constant for different ϑ and φ. Therefore, it is crucial to calculate the average absorption A_{avg}, which is given by [148]

$$A_{avg} = \int_{\lambda_{min}}^{\lambda_g} A_{tot}(\lambda) \, S(\lambda) \, d\lambda. \tag{5.40}$$

The wavelengths λ_{min} and λ_g in this equation are defined by $\lambda_{min} = 1240/E_{max}$ and $\lambda_g = 1240/E_g$ with the above mentioned energy values $E_{max} = 2.2\,\text{eV}$ and $E_g = 1.12\,\text{eV}$. The total absorption A_{tot} is the arithmetic mean of the p- and the s-polarized absorbance spectra A_{p-pol} and A_{s-pol}

$$A_{tot}(\lambda) = \frac{A_{p-pol}(\lambda) + A_{s-pol}(\lambda)}{2}. \tag{5.41}$$

$S(\lambda)$ in Eq. (5.40) is the direct solar and circumsolar spectrum. It is dependent on the air mass the sunlight is propagating through. Therefore, $S(\lambda)$ changes for different zenith angles meaning that it also varies for different incident angles ϑ in combination with different azimuthal angles φ. In order to calculate the different air mass irradiance spectra, the *Simple Model for the Atmospheric Radiative Transfer of Sunshine* (SMARTS2) [149] is used. The average absorption of the enhanced structure $A_{avg, enh}$ can be normalized to that of the bare structure $A_{avg, Bare}$, which gives the enhancement factor EF [150]

$$EF = \frac{A_{avg, enh}}{A_{avg, Bare}}. \tag{5.42}$$

In the enhanced structure, the metal particles are either arranged in a quasiperiodic ($A_{avg, Penrose}$) or in a periodic fashion ($A_{avg, Square}$).

In order to see how the enhancement factor changes during the day as well as over the year, EF is plotted versus these two parameters in Fig. 5.38 (a) for the Penrose
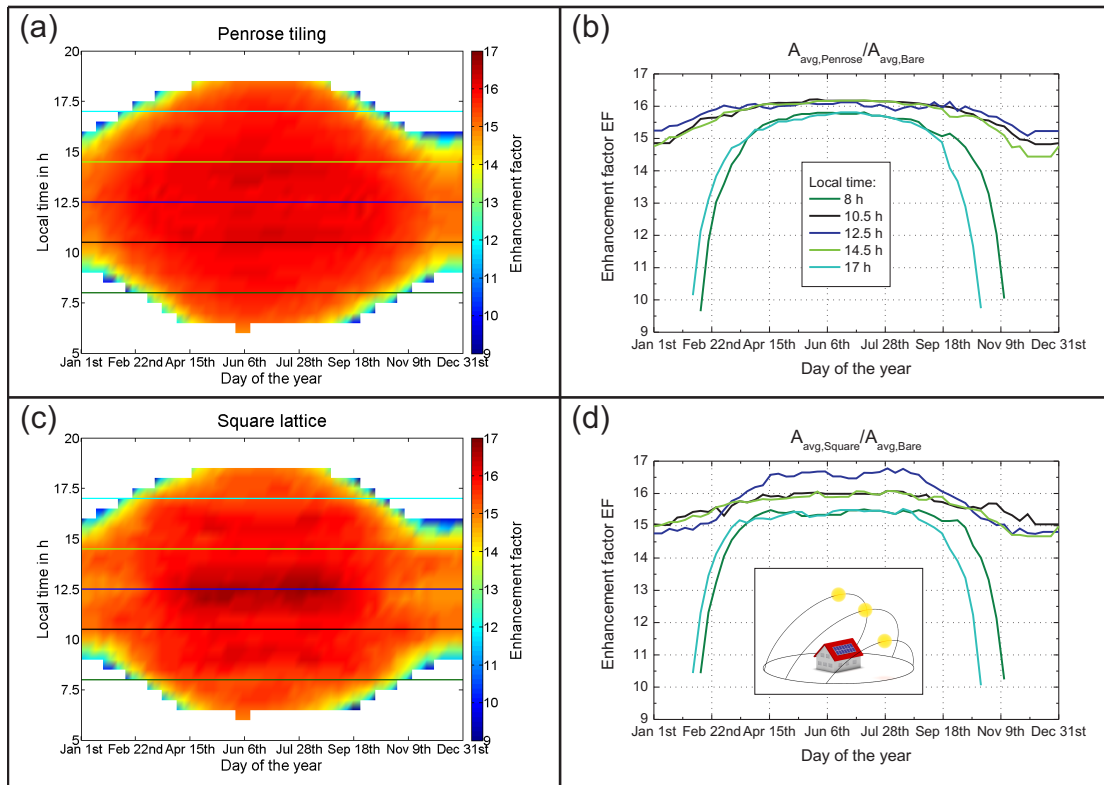
Figure 5.38: Enhancement factor of (a) a Penrose tiling for different days of the year and local times. The colored lines indicate different local times. For these local times, the enhancement factor is plotted in (b) versus the day of the year in the corresponding colors. The same plots are shown in panels (c) and (d) for the square lattice. The course of the sun for three different days of the year is shown in the inset of panel (d).

tiling and in Fig. 5.38 (c) for the square lattice. For these color-coded plots, an average latitude and longitude of Germany (51° N, 9° E [151]), an average roof pitch of 35° [152], and a solar cell directing to the south are assumed. In order to visualize how the polar and azimuthal angles change for different local times and days of the year, the course of the sun is shown for three different days in the inset of Fig. 5.38 (d). The sun rises always in the back of this figure and it sets in the front. The highest course of the sun belongs to a summer day, the middle one to a spring/fall day, and the lowest one to a winter day. The sun is always shown for noon.

It can be seen in Fig. 5.38 (a) and (c) that the enhancement factor for the quasiperiodic arrangement is more constant when compared to the periodic arrangement. Especially for noon the enhancement factor of the Penrose tiling stays almost constant throughout the whole year. In contrast, the enhancement factor of the structure with the square lattice is lower during wintertime and higher during summertime.

In order to analyze this behavior better, the enhancement factors for 8:00 a.m., 10:30 a.m., 12:30 p.m., 2:30 p.m., and 5:00 p.m. are plotted versus the day of the year in Fig. 5.38 (b) and (d) for the quasiperiodic and the periodic tiling, respectively. The cross sections with the corresponding colors in dark green, black, blue, light green, and cyan are also indicated in Fig. 5.38 (a) and (c).

For local times at 10:30 a.m. and 2:30 p.m. both the Penrose tiling and the square lattice show enhancement factors of about 15 in winter and around 16 in summer. However, the structure with the quasiperiodic gold disk arrangement reaches almost constant values between 15.8 and 16.2 between the beginning of March and the mid of October, whereas the structure with the periodic lattice achieves the same values only between the beginning of April and the mid of September. A similar behavior can be obtained by looking at the curve for a local time around noon in the quasicrystalline case. However, the enhancement factor is slightly bigger during wintertime and the constant values between 15.8 and 16.2 are even reached between the mid of February and the end of October. In contrast, for a local time around noon in the periodic case, the enhancement factor is reduced in winter to a value of about 14.7 and increased in summer to a value of about 16.6. Between the mid of April and the end of August, the enhancement factor has values of above 16.4. However, from the end of October until the beginning of March, values of only about 15 are reached. Enhancement factors between 15.8 and 16.2 are only achieved from the mid of March until the beginning of April as well as from the mid of September until the beginning of October. Thus, the enhancement factor in the quasicrystalline case stays a quite long period of the year at almost constant values between 15.8 and 16.2 for local times between 10:30 a.m. and 2:30 p.m., whereas the enhancement factor deviates from these values for several weeks in the periodic case.

Since it is desirable to reach quite high values in the morning and evening hours due to a higher energy consumption for these times, the enhancement factors for 8:00 a.m. and 5:00 p.m. are also regarded. Although the enhancement factors are reduced in both structural arrangements, the maximum values in the quasicrystalline case are about 15.8, whereas the maximum values for the square lattice are approximately 15.5. In the morning and evening hours during wintertime, the enhancement factor of both structural arrangements is much lower than 15 since the zenith angle is quite high then.

All in all, a variation of the enhancement factors in summertime are obtained between 15.8 and 16.2 for the Penrose tiling as well as between 15.5 and 16.6 for the square lattice. Except for the morning hours and the late afternoons, almost constant values between 15.8 and 16.2 are reached for at least 7.5 months in the

quasicrystalline case, whereas these values are only met for 5.5 months at the most in the periodic case. Even in the early morning and the late afternoon a maximum enhancement factor of about 15.8 is reached during summertime for the Penrose tiling, whereas a maximum value of only 15.5 is obtained for the square lattice. In comparison to the square lattice where the enhancement factor around noon varies between 14.7 and 16.6, the enhancement factor around noon of the Penrose tiling only changes between 15.1 and 16.1. This means that more constant values are reached throughout the day as well as the year for the Penrose tiling.

A total enhancement factor EF_{tot} can be calculated by integrating the average absorption of the enhanced structure over the local time t_{local} as well as over the day of the year t_{day} and by normalizing that to the same integration of the bare structure, which is given by

$$EF_{tot} = \frac{\int_1^{365} \int_0^{24} A_{avg,\,enh} \; \mathrm{d}t_{local} \; \mathrm{d}t_{day}}{\int_1^{365} \int_0^{24} A_{avg,\,Bare} \; \mathrm{d}t_{local} \; \mathrm{d}t_{day}}. \tag{5.43}$$

This calculation leads to a value $EF_{tot} = 15.573$ for the quasiperiodic as well as to a value $EF_{tot} = 15.515$ for the periodic structure. This means that, although the enhancement factor reaches higher values for the square lattice, the total enhancement factor is slightly higher for the Penrose tiling. This is due to the more constant values throughout the day and the year in the quasicrystalline case.

These findings indicate that the performance of a solar cell with a quasiperiodic metal disk arrangement is more stable during the day as well as over the year. Especially in the morning and the evening hours, when more electricity is needed, the enhancement factor of the Penrose tiling is higher. Additionally, the enhancement factor stays longer at constant values over the year. This is particularly of interest since also more electricity is needed during wintertime. For thicker silicon layers, more waveguide modes can be excited leading to a even higher absorbance for both structural arrangements. Thus, also the enhancement factor will be increased for both lattices. However, the enhancement factor should be still more constant for the Penrose tiling. Additionally, a higher difference of the total enhancement factor is expected.

Chapter 6

Conclusion and outlook

The work presented in this thesis deals with aperiodic metal gratings on top of a waveguide material. These metallic photonic crystals possess either a 1D grating or a 2D grating. The aperiodic gratings in one dimension are either disordered or arranged on the coordinates of Fibonacci-like sequences or Cantor sequences. For the aperiodic gratings in two dimensions, the gold disks are placed on the vertices of a Penrose tiling. All the aperiodic structures are compared to periodic ones. The samples are fabricated by using electron-beam lithography that allows a precise positioning of the metal particles at the desired coordinates.

The metallic photonic crystals in this thesis can excite a waveguide mode and also a particle plasmon. For the structures with a 1D grating, the particle plasmon can only be excited for a polarization perpendicular to the gold wires. When these resonances are in the same energy range, they are coupled to each other leading to a waveguide-plasmon polariton as presented in former work [31, 32].

First, the optical properties of the 1D disordered structures are analyzed. Two different disorder models are used (frozen-phonon disorder and long-range disorder) combined with two different kinds of distributions (uniform distribution and Gaussian distribution). For all disorder structures, the average grating period as well as the disorder amount was varied. It was found that the amplitude of the excited waveguide mode decreases for an increased frozen-phonon disorder amount. This is due to a less efficient excitation of the waveguide mode. When the particle plasmon is additionally excited, the smaller amplitude can also be obtained. However, this reduced amplitude might be visible as a reduced contrast between the two peaks and the dip in between. Varying the grating period just shifts the waveguide mode resonance to different energy positions. The amplitude decreases faster in the case of Gaussian distribution when compared to uniform distribution. For long-range

disorder, the amplitude for a larger disorder amount also decreases. However, also additional waveguide modes can be excited. All the excited waveguide modes possess slightly different energies leading to a broadened resonance. Due to this large number of additional waveguide modes, the amplitude reduction is faster when compared to the samples with frozen-phonon disorder. Again, the waveguide mode amplitudes decrease faster for Gaussian distribution. All these findings are consistent with the results of D. Nau [101].

These disordered samples were fabricated in order to confirm the behavior of the coupling strength V_2, which is reduced for an increased disorder amount. For this purpose, the energy positions of the extinction maxima were plotted versus the grating period for the different frozen-phonon disorder amounts. A Hamiltonian (see Eq. (2.33)) was fitted to each of the plots in order to identify the corresponding coupling strength. This was done for both uniform and Gaussian distribution. By comparing the experimentally obtained coupling strengths to the calculated ones of Ref. [101], a good agreement is achieved. Therefore, the simple model used to calculate the coupling strengths is confirmed. However, due to the large amount of waveguide modes for long-range disorder, the coupling strengths cannot be experimentally obtained. Therefore, the Urbach energy, as it is known for disordered structures, is determined for the samples. This was done for the frozen-phonon samples first in order to see if it is possible that the Urbach energy is related to the coupling strength. It is found that the Urbach energy is strongly dependent on the grating period and, thus, also on the polaritonic system. Whereas the coupling strength decreases for a larger disorder amount, the Urbach energy increases. However, the coupling strength might be inversely related to the Urbach energy. By plotting both the coupling energy and the Urbach slope versus the disorder amount into the same diagram, it is found that the behavior is quite similar. The exact relation is not known yet since the Urbach slope is different for all grating periods. However, the ratio between the coupling energy and the inverse Urbach energy is kept constant for the same grating period. The agreement for both distributions is quite good. Therefore, the Urbach energies of the long-range disorder samples were also determined and compared to the calculated coupling energies. The ratio between the coupling energy and the Urbach slope is kept constant for the same grating period. It is found that, also for this disorder model, the coupling energy shows a similar behavior for increasing disorder amounts than the inverse Urbach energy. This means that the inverse Urbach energy is somehow related to the coupling strength. However, the correct relation still has to be found. It also means that the model for calculating the coupling strengths is valid.

In the next part of this thesis, the optical properties of the 1D quasiperiodic structures were analyzed. The gold wires in these structures were placed on the coordinates of Fibonacci-like sequences. It was found that the main waveguide mode resonance is excited at an energy position corresponding to the average wire distance. The amplitude of the waveguide mode resonance is dependent on the difference between the long and the short wire distance. All Fourier peaks can be explained by using the *cut formalism*, which is a method to construct the Fibonacci-like sequences. By using this approach and by varying the construction parameters, the Fourier peaks can be tuned to the desired energy position with the desired amplitude. It is also possible to change the ratio between different Fourier peaks.

For the last part of the 1D structures, the Cantor and Cantor-6 samples were fabricated and measured. In contrast to the Cantor samples, much more waveguide mode can be excited for the Cantor-6 samples. However, all excited resonances are located around the average wire distance for the Cantor as well as for the Cantor-6 samples. Additionally, one of the excited resonances always corresponds to the short wire distance. For an increased difference between the long wire distance and the short wire distance, all the peaks are spread over a larger energy range. However, a detailed analysis of the Fourier transform could not be found.

Next, the optical properties of the 2D structures were analyzed for normally incident light on the sample. The gold disks of these samples were elliptically shaped and rotated by the angle γ around the sample x axis. The eccentricity and γ were different for the three samples. In comparison to the 1D structures, there are some important differences. First, a particle plasmon can be excited for a polarization along one of the main axes. For a polarization angle between the directions of the two main axes, both particle plasmons can be excited, however with a reduced amplitude of both particle plasmon resonances. Second, waveguide modes can be excited in all directions of the x-y-plane provided that a Fourier component exists in that direction. In each of these directions, a TE as well as a TM polarized wave can be excited depending on the incident polarization. For linearly polarized light along the sample x axis, it is expected that only a TM wave can propagate in x direction and only a TE wave in y direction. However, for elliptically shaped particles rotated by the angle γ around the sample x axis, also a TE wave propagating in x direction and a TM wave propagating in y direction are present. This can only be explained by the assumption that the excited particle plasmons along the main axes are able to excite waveguide modes by themselves.

Based on these findings, a theoretical model was developed in order to be able to model the optical properties of such 2D metallic photonic crystals. The directions

in which the waveguide modes propagate are given by the 2D Fourier transform of the structure coordinates. Not only those waveguide modes are considered that are directly excited by the incident light, but also those waveguide modes that are due to the particle plasmons along the main axes of the particles. These *plasmon waveguide modes* are dependent on the material as well as on the shape and the size of the particle. The summation of the different components determines the weighting factor for a TE or a TM wave propagating in a specific direction. The waveguide dispersion relations for a TE as well as a TM wave assign the corresponding energies to the k values of the Fourier peaks. The amplitudes of the resonances are dependent on the amplitudes of the Fourier peaks as well as on the weighting factor. A Fano model is used to calculate the spectra including all amplitudes and energies of the resonances present in the specific energy range. Since the waveguide mode and the particle plasmon are coupled to each other when they are in the same energy range, the phase of a waveguide mode changes when it is shifted through the particle plasmon. If the waveguide mode has the same energy as the particle plasmon, its phase is shifted by π when compared to an undisturbed waveguide mode. Therefore, the phase of the waveguide mode changes for all waves propagating in the waveguide layer depending on its energy. With all these considerations, it is possible to model the optical properties of such 2D systems. This was done for all samples and a good agreement was achieved between the measured and the modeled spectra.

The 2D structures were also measured for oblique light incidence. Depending on the polarization as well as on the azimuthal and polar angle of the incident light, the waveguide modes split into several modes. Due to the higher rotational symmetry of the quasiperiodic structures, the splitting results in more modes when compared to the periodic structures. In the normal incidence spectra of the square lattice sample, it cannot be seen that waveguide modes can be excited by the electric field vectors of the particle plasmons. However, three resonances are visible for oblique light incidence while it was expected to only see one or two resonances. This is again proof that the plasmon waveguide modes are present in the system.

The theoretical model presented for normally incident light was then expanded for oblique light incidence. The basic concepts were the same, however, some parts had to be adjusted. The propagation vectors of the waveguide modes are now dependent on the vector addition of the wave vector parallel to the sample surface $\mathbf{k}_{xy}$ and the reciprocal lattice vectors of the structure [32, 80]. One has to keep in mind that each Fourier component as well as each $\mathbf{k}_{xy}$ component is dependent on the energy of the incident wave leading to a different $\mathbf{k}_{xy}$ value for each Fourier component. Additionally, the propagation direction of a TE wave differs from that of

a TM wave for the same Fourier component. Due to the oblique incidence of light, also the weighting factors of the specific waveguide modes have to be modified. However, after the amplitudes of the waves and their corresponding energies have been identified, the optical properties can be modeled using the same Fano model as for normal incidence. The comparison between the measured and the modeled spectra again provides a good agreement.

In the last part of this thesis, the above presented model was used to predict the absorption enhancement of plasmonic solar cells. A silicon solar cell was assumed with either a quasicrystalline or a periodic arrangement of gold disks on top. In order to provide reasonable results, the transmittance and reflectance spectra of the periodic structure was first calculated for normal incidence by using an S-matrix approach. The Fano modeled spectra were then fit to the corresponding S-matrix spectra in order to obtain reasonable fitting parameters. Due to the more isotropic band structure of the solar cell with the quasiperiodic tiling, it was found that the absorption enhancement is more constant throughout the day as well as over the year when compared to the periodic tiling. Also the total enhancement factor was slightly higher in the quasiperiodic case.

Based on the results of this thesis, interesting future tasks can be studied. The investigations of the 1D disordered samples showed a connection between the Urbach energy and the coupling constant. It was found that the Urbach energy is strongly dependent on the grating period of the metallic photonic crystal. However, the correct relation between the two parameters is not known up to now.

It was predicted in this thesis that plasmonic solar cells possessing a quasiperiodic arrangement of the metal disks provide a more constant absorption enhancement throughout the day and over the year when compared to periodic structures. However, such solar cells have to be fabricated in order to verify the predictions. Furthermore, this solar cell design has not been optimized so far. Changing the solar cell parameters could lead to an improved absorption of the incident light. It might be also advantageous to place the metal disks underneath the silicon layer. An anti-reflection layer on top was also not considered in the presented solar cell design. The efficiency of these solar cells should also be compared to the efficiency of a solar cell with a totally disordered metal disk arrangement. For this purpose it would be also interesting to understand the behavior of 2D frozen-phonon disordered metallic photonic crystals. A detailed study of different disorder amounts should be made. The disorder should not only be changed in x direction as it has been done in Ref. [80], it should be allowed to vary in all directions.

Another research area related to the plasmonic solar cells are LEDs. It is also possible to use a quasicrystalline arrangement to improve the light extraction efficiency. These structures can be studied in future research as well.

Bibliography

[1] I. Freestone, N. Meeks, M. Sax, and C. Higgitt, *The Lycurgus Cup – A Roman Nanotechnology*, Gold Bull. **40**, 270 (2007).

[2] *The Lycurgus Cup*, http://www.britishmuseum.org/explore/highlights/highlight_objects/pe_mla/t/the_lycurgus_cup.aspx (accessed on 01/28/2013).

[3] M. Faraday, *The Bakerian Lecture: Experimental Relations of Gold (and Other Metals) to Light*, Phil. Trans. R. Soc. Lond. **147**, 145 (1857).

[4] G. Mie, *Beiträge zur Optik trüber Medien, speziell kolloidaler Metallösungen*, Ann. d. Phys. **330**, 377 (1908).

[5] G. G. Stokes, *On a remarkable Phenomenon of Crystalline Reflection*, Proc. R. Soc. Lond. **38**, 174 (1885).

[6] Lord Rayleigh, *On the Maintenance of Vibrations by Forces of Double Frequency, and on the Propagation of Waves through a Medium endowed with a Periodic Structure*, Philos. Mag. S. 5 **24**, 145 (1887).

[7] Lord Rayleigh, *On a remarkable Phenomenon of Crystalline Reflection described by Prof. Stokes*, Philos. Mag. S. 5 **26**, 256 (1888).

[8] E. Yablonovitch, *Inhibited Spontaneous Emission in Solid-State Physics and Electronics*, Phys. Rev. Lett. **58**, 2059 (1987).

[9] S. John, *Strong Localization of Photons in Certain Disordered Dielectric Superlattices*, Phys. Rev. Lett. **58**, 2486 (1987).

[10] E. Yablonovitch and T. J. Gmitter, *Photonic Band Structure: The Face-Centered-Cubic Case*, Phys. Rev. Lett. **63**, 1950 (1989).

[11] A. Mekis, J. C. Chen, I. Kurland, S. Fan, P. R. Villeneuve, and J. D. Joannopoulos, *High Transmission through Sharp Bends in Photonic Crystal Waveguides*, Phys. Rev. Lett. **77**, 3787 (1996).

[12]   S. Fan, S. G. Johnson, J. D. Joannopoulos, C. Manolatou, and H. A. Haus, *Waveguide branches in photonic crystals*, J. Opt. Soc. Am. B **18**, 162 (2001).

[13]   T. A. Birks, J. C. Knight, and P. S. J. Russell, *Endlessly single-mode photonic crystal fiber*, Opt. Lett. **22**, 961 (1997).

[14]   R. F. Cregan, B. J. Mangan, J. C. Knight, T. A. Birks, P. S. J. Russell, P. J. Roberts, and D. C. Allan, *Single-Mode Photonic Band Gap Guidance of Light in Air*, Science **285**, 1537 (1999).

[15]   J. H. Holtz and S. A. Asher, *Polymerized colloidal crystal hydrogel films as intelligent chemical sensing materials*, Nature **389**, 829 (1997).

[16]   S. A. Asher, A. C. Sharma, A. V. Goponenko, and M. M. Ward, *Photonic Crystal Aqueous Metal Cation Sensing Materials*, Anal. Chem. **75**, 1676 (2003).

[17]   W. Zhang, N. Ganesh, I. D. Block, and B. T. Cunningham, *High sensitivity photonic crystal biosensor incorporating nanorod structures for enhanced surface area*, Sensor Actuat. B **131**, 279 (2008).

[18]   T. Sünner, T. Stichel, S.-H. Kwon, T. W. Schlereth, M. K. S. Höfling, and A. Forchel, *Photonic crystal cavity based gas sensor*, Appl. Phys. Lett. **92**, 261112 (2008).

[19]   Y. Nishijima, K. Ueno, S. Juodkazis, V. Mizeikis, H. Misawa, T. Tanimura, and K. Maeda, *Inverse silica opal photonic crystals for optical sensing applications*, Opt. Express **15**, 12979 (2007).

[20]   E. Matioli and C. Weisbuch, *Impact of photonic crystals on LED light extraction efficiency: approaches and limits to vertical structure designs*, J. Phys. D: Appl. Phys **43**, 354005 (2010).

[21]   X.-H. Li, R. Song, Y.-K. Ee, P. Kumnorkaew, J. F. Gilchrist, and N. Tansu, *Light Extraction Efficiency and Radiation Patterns of III-Nitride Light-Emitting Diodes With Colloidal Microlens Arrays With Various Aspect Ratios*, IEEE Photon. J. **3**, 489–499 (2011).

[22]   W. H. Koo, W. Youn, P. Zhu, X.-H. Li, N. Tansu, and F. So, *Light Extraction of Organic Light Emitting Diodes by Defective Hexagonal-Close-Packed Array*, Adv. Funct. Mater. **22**, 3454–3459 (2012).

[23]   S. Guldin, S. Hüttner, M. Kolle, M. E. Welland, P. Müller-Buschbaum, R. H. Friend, U. Steiner, and N. Tétreault, *Dye-Sensitized Solar Cell Based on a Three-Dimensional Photonic Crystal*, Nano Lett. **10**, 2303 (2010).

[24] M. Florescu, H. Lee, I. Puscasu, M. Pralle, L. Florescu, D. Z. Ting, and J. P. Dowling, *Improving solar cell efficiency using photonic band-gap materials*, Sol. Energ. Mat. Sol. C. **91**, 1599 (2007).

[25] G. Gomard, X. Meng, E. Drouard, K. E. Hajjam, E. Gerelli, R. Peretti, A. Fave, R. Orobtchouk, M. Lemiti, and C. Seassal, *Light harvesting by planar photonic crystals in solar cells: the case of amorphous silicon*, J. Opt. **14**, 024011 (2012).

[26] E. R. Brown and O. B. McMahon, *Large electromagnetic stop bands in metallodielectric photonic crystals*, Appl. Phys. Lett. **67**, 2138 (1995).

[27] B. Lamprecht, A. Leitner, and F. R. Aussenegg, *Femtosecond decay-time measurement of electron-plasma oscillation in nanolithographically designed silver particles*, Appl. Phys. B **64**, 269 (1996).

[28] B. Lamprecht, G. Schider, R. T. Lechner, H. Ditlbacher, J. Krenn, A. Leitner, and F. R. Aussenegg, *Metal Nanoparticle Gratings: Influence of Dipolar Particle Interaction on the Plasmon Resonance*, Phys. Rev. Lett. **84**, 4721 (2000).

[29] N. Félidj, J. Aubard, G. Lévi, J. R. Krenn, M. Salerno, G. Schider, B. Lamprecht, A. Leitner, and F. R. Aussenegg, *Controlling the optical response of regular arrays of gold particles for surface-enhanced Raman scattering*, Phys. Rev. B **65**, 075419 (2002).

[30] N. Vasilantonakis, K. Terzaki, I. Sakellari, V. Purlys, D. Gray, C. M. Soukoulis, M. Vamvakaki, M. Kafesaki, and M. Farsari, *Three-Dimensional Metallic Photonic Crystals with Optical Bandgaps*, Adv. Mater. **24**, 1101 (2012).

[31] A. Christ, S. Tikhodeev, N. A. Gippius, J. Kuhl, and H. Giessen, *Waveguide-Plasmon Polaritons: Strong Coupling of Photonic and Electronic Resonances in a Metallic Photonic Crystal Slab*, Phys. Rev. Lett. **91**, 183901 (2003).

[32] S. Linden, J. Kuhl, and H. Giessen, *Controlling the Interaction between Light and Gold Nanoparticles: Selective Suppression of Extinction*, Phys. Rev. Lett. **86**, 4688 (2001).

[33] S. Linden, A. Christ, J. Kuhl, and H. Giessen, *Selective suppression of extinction within the plasmon resonance of gold nanoparticles*, Appl. Phys. B **73**, 311 (2001).

[34] T. Zentgraf, A. Christ, J. Kuhl, and H. Giessen, *Tailoring the Ultrafast Dephasing of Quasiparticles in Metallic Photonic Crystals*, Phys. Rev. Lett. **93**, 243901 (2004).

[35] M. W. Klein, *Nonlinear Optics of Metallic Photonic Crystal Slabs and Planar Metamaterials*, PhD thesis, Universität Karlsruhe (2007).

[36] T. Utikal, T. Zentgraf, T. Paul, C. Rockstuhl, F. Lederer, M. Lippitz, and H. Giessen, *Towards the Origin of the Nonlinear Response in Hybrid Plasmonic Systems*, Phys. Rev. Lett. **106**, 133901 (2011).

[37] M. Geiselmann, T. Utikal, M. Lippitz, and H. Giessen, *Tailoring the ultrafast dynamics of the magnetic mode in magnetic photonic crystals*, Phys. Rev. B **81**, 235101 (2010).

[38] T. Utikal, M. I. Stockman, A. P. Heberle, M. Lippitz, and H. Giessen, *All-Optical Control of the Ultrafast Dynamics of a Hybrid Plasmonic System*, Phys. Rev. Lett. **104**, 113903 (2010).

[39] S. Feng, Z.-Y. Li, Z.-F. Feng, B.-Y. Cheng, and D.-Z. Zhang, *Engineering the imaging properties of a metallic photonic-crystal slab lens*, Appl. Phys. Lett. **88**, 031104 (2006).

[40] D. Nau, R. P. Bertram, K. Buse, T. Zentgraf, J. Kuhl, S. G. Tikhodeev, N. A. Gippius, and H. Giessen, *Optical switching in metallic photonic crystal slabs with photoaddressable polymers*, Appl. Phys. B **82**, 543 (2006).

[41] D. Nau, A. Seidel, R. B. Orzekowsky, S.-H. Lee, S. Deb, and H. Giessen, *Hydrogen sensor based on metallic photonic crystal slabs*, Opt. Lett. **35**, 3150 (2010).

[42] X. Zhang, X. Ma, F. Dou, P. Zhao, and H. Liu, *A Biosensor Based on Metallic Photonic Crystals for the Detection of Specific Bioreactions*, Adv. Funct. Mater. **21**, 4219 (2011).

[43] X. Zhang, S. Feng, J. Zhang, T. Zhai, H. Liu, and Z. Pang, *Sensors Based on Plasmonic-Photonic Coupling in Metallic Photonic Crystals*, Sensors **12**, 12082 (2012).

[44] D. Shechtman, I. Blech, D. Gratias, and J. W. Cahn, *Metallic Phase with Long-Range Orientational Order and No Translational Symmetry*, Phys. Rev. Lett. **53**, 1951 (1984).

[45] D. Levine and P. J. Steinhardt, *Quasicrystals: A New Class of Ordered Structures*, Phys. Rev. Lett. **53**, 2477 (1984).

[46] A. L. Mackay, *Crystallography and the Penrose Pattern*, Physica A **114**, 609 (1982).

[47] R. Penrose, *The role of Aesthetics in Pure and Applied Mathematical Research*, Bull. Inst. Maths. Its Appl. **10**, 266 (1974).

[48] M. Gardner, *Mathematical Games: Extraordinary nonperiodic tiling that enriches the theory of tiles*, Sci. Am. **236**, 110 (1977).

[49] T. Ishimasa, H. U. Nissen, and Y. Fukano, *New Ordered State Between Crystalline and Amorphous in Ni-Cr Particles*, Phys. Rev. Lett. **55**, 511 (1985).

[50] S. J. Poon, A. J. Drehman, and K. R. Lawless, *Glassy to Icosahedral Phase Transformation in Pd-U-Si Alloys*, Phys. Rev. Lett. **55**, 2324 (1985).

[51] B. Dubost, J.-M. Lang, M. Tanaka, P. Sainfort, and M. Audier, *Large Al-CuLi single quasicrystals with triacontahedral solidification morphology*, Nature **324**, 48 (1986).

[52] N. Wang, K. K. Fung, and K. H. Kuo, *Symmetry study of the MnSiAl octagonal quasicrystal by convergent beam electron diffraction*, Appl. Phys. Lett. **52**, 2120 (1988).

[53] J.-M. Dubois, *Useful Quasicrystals* (World Scientific, Danvers, MA, USA, 2005).

[54] A. Tsai and M. Yoshimura, *Highly active quasicrystalline Al-Cu-Fe catalyst for steam reforming of methanol*, Appl. Catal. A - Gen. **214**, 237 (2001).

[55] T. Eisenhammer, *Quasicrystal films: numerical optimization as a solar selective absorber*, Thin Solid Films **270**, 1 (1995).

[56] T. Eisenhammer, A. Haugeneder, and A. Mahr, *High-temperature optical properties and stability of selective absorbers based on quasicrystalline Al-CuFe*, Sol. Energ. Mat. Sol. C. **54**, 379 (1998).

[57] *The Nobel Prize in Chemistry 2011*, http://www.nobelprize.org/nobel_prizes/chemistry/laureates/2011/ (accessed on 10/26/2012).

[58] J. Mikhael, J. Roth, L. Helden, and C. Bechinger, *Archimedean-like tiling on decagonal quasicrystalline surfaces*, Nature **454**, 501 (2008).

[59] J. Mikhael, M. Schmiedeberg, S. Rausch, J. Roth, H. Stark, and C. Bechinger, *Proliferation of anomalous symmetries in colloidal monolayers subjected to quasiperiodic light fields*, P. Natl. Acad. Sci. USA **107**, 7214 (2010).

[60] S. Fischer, A. Exner, K. Zielske, J. Perlich, S. Deloudi, W. Steurer, P. Lindner, and S. Förster, *Colloidal quasicrystals with 12-fold and 18-fold diffraction symmetry*, P. Natl. Acad. Sci. USA **108**, 1810 (2011).

[61] W. Steurer and D. Sutter-Widmer, *Photonic and phononic quasicrystals*, J. Phys. D: Appl. Phys. **40**, R229 (2007).

[62] D. Sutter-Widmer, S. Deloudi, and W. Steurer, *Periodic average structures in phononic quasicrystals*, Philos. Mag. **87**, 3095 (2007).

[63] A. Chatzopoulos and H.-R. Trebin, *Hydrodynamic structure factor of quasicrystals*, Phys. Rev. B **81**, 064205 (2010).

[64] M. Engel, M. Umezaki, H.-R. Trebin, and T. Odagaki, *Dynamics of particle flips in two-dimensional quasicrystals*, Phys. Rev. B **82**, 134206 (2010).

[65] J. A. Kromer, M. Schmiedeberg, J. Roth, and H. Stark, *What Phasons Look Like: Particle Trajectories in a Quasicrystalline Potential*, Phys. Rev. Lett. **108**, 218301 (2012).

[66] M. Schmiedeberg and H. Stark, *Comparing light-induced colloidal quasicrystals with different rotational symmetries*, J. Phys.: Condens. Matter **24**, 284101 (2012).

[67] V. Passias, N. V. Valappil, Z. Shi, L. Deych, A. A. Lisyansky, and V. M. Menon, *Luminescence properties of a Fibonacci photonic quasicrystal*, Opt. Express **17**, 6636 (2009).

[68] B. Freedman, G. Bartal, M. Segev, R. Lifshitz, D. N. Christodoulides, and J. W. Fleischer, *Wave and defect dynamics in nonlinear photonic quasicrystals*, Nature **440**, 1166 (2006).

[69] M. C. Rechtsman, H.-C. Jeong, P. M. Chaikin, S. Torquato, and P. J. Steinhardt, *Optimized Structures for Photonic Quasicrystals*, Phys. Rev. Lett. **101**, 073902 (2008).

[70] P. N. Dyachenko, V. S. Pavelyev, and V. A. Soifer, *Graded photonic quasicrystals*, Opt. Lett. **37**, 2178 (2012).

[71] W. Man, M. Megens, P. J. Steinhardt, and P. M. Chaikin, *Experimental measurement of the photonic properties of icosahedral quasicrystals*, Nature **436**, 993 (2005).

[72] A. Ledermann, L. Cademartiri, M. Hermatschweiler, C. Toninelli, G. A. Ozin, D. S. Wiersma, M. Wegener, and G. von Freymann, *Three-dimensional silicon inverse photonic quasicrystals for infrared wavelengths*, Nature Mater. **5**, 942 (2006).

[73] A. Ledermann, M. Wegener, and G. von Freymann, *Rhombicuboctahedral Three-Dimensional Photonic Quasicrystals*, Adv. Mater. **22**, 2363 (2010).

[74] T. Matsui, A. Agrawal, A. Nahata, and Z. V. Vardeny, *Transmission resonances through aperiodic arrays of subwavelength apertures*, Nature **446**, 517–521 (2007).

[75] C. Rockstuhl, F. Lederer, T. Zentgraf, and H. Giessen, *Enhanced transmission of periodic, quasiperiodic, and random nanoaperture arrays*, Appl. Phys. Lett. **91**, 151109 (2007).

[76] F. M. Huang, N. Zheludev, Y. Chen, and F. J. García de Abajo, *Focusing of light by a nanohole array*, Appl. Phys. Lett. **90**, 091119 (2007).

[77] D. Nau, A. Schönhardt, C. Bauer, A. Christ, T. Zentgraf, J. Kuhl, and H. Giessen, *Disorder issues in metallic photonic crystals*, phys. stat. sol. (b) **243**, 2331 (2006).

[78] D. Nau, A. Schönhardt, C. Bauer, A. Christ, T. Zentgraf, J. Kuhl, M. Klein, and H. Giessen, *Correlation Effects in Disordered Metallic Photonic Crystal Slabs*, Phys. Rev. Lett. **98**, 133902 (2007).

[79] D. Nau, A. Schönhardt, D. N. Chigrin, H. Kroha, A. Christ, and H. Giessen, *Polariton bandstructure of disordered metallic photonic crystal slabs*, phys. stat. sol. (b) **244**, 1262 (2007).

[80] S. Linden, *Kontrolle der Wechselwirkung zwischen Licht und Partikelplasmonen durch selektive Unterdrückung der Extinktion*, PhD thesis, Philipps-Universität Marburg (2001).

[81] M. Florescu, S. Torquato, and P. J. Steinhardt, *Complete band gaps in two-dimensional photonic quasicrystals*, Phys. Rev. B **80**, 155112 (2009).

[82] J. D. Joannopoulos, P. R. Villeneuve, and S. Fan, *Photonic crystals: putting a new twist on light*, Nature **386** (1997).

[83] J. D. Joannopoulos, S. G. Johnson, J. N. Winn, and R. D. Meade, *Photonic Crystals: Molding the Flow of Light (Second Edition)* (Princeton University Press, Princeton, NJ, 2008).

[84] P. Vukusic and J. R. Sambles, *Photonic structures in biology*, Nature **424**, 852 (2003).

[85] S. Kinoshita and S. Yoshioka, *Structural Colors in Nature: The Role of Regularity and Irregularity in the Structure*, ChemPhysChem **6**, 1443 (2005).

[86] J. V. Sanders, *Coulour of Precious Opal*, Nature **204**, 1151 (1964).

[87] R. Anselmann and H. Winkler, *Ordered Structures from Nanoparticles*, Adv. Eng. Mater. **5**, 560 (2003).

[88] V. R. Almeida, C. A. Barrios, R. R. Panepucci, and M. Lipson, *All-optical control of light on a silicon chip*, Nature **431**, 1081 (2004).

[89] M. Koshiba, *Wavelength Division Multiplexing and Demultiplexing With Photonic Crystal Waveguide Couplers*, J. Lightwave Technol. **19**, 1970 (2001).

[90] B. Temelkuran, E.Ozbay, M. Sigalas, G. Tuttle, C. M. Soukoulis, and K. M. Ho, *Reflection properties of metallic photonic crystals*, Appl. Phys. A **66**, 363 (1998).

[91] T. D. Drysdale, R. J. Blaikie, and D. R. S. Cumming, *Calculated and measured transmittance of a tunable metallic photonic crystal filter for terahertz frequencies*, Appl. Phys. Lett. **83**, 5362 (2003).

[92] C. Kittel, *Introduction to Solid State Physics* (John Wiley & Sons, 1996).

[93] U. Kreibig and M. Vollmer, *Optical Properties of Metal Clusters* (Springer, Berlin, 1995).

[94] C. F. Bohren and D. R. Huffman, *Absorption and Scattering of Light by Small Particles* (Wiley-VCH, 2004).

[95] P. B. Johnson and R. W. Christy, *Optical Constants of the Noble Metals*, Phys. Rev. B **6**, 4370 (1972).

[96] C. Sönnichsen, *Plasmons in metal nanostructures*, PhD thesis, Ludwig-Maximilians-Universität München (2001).

[97] S. A. Maier, *Plasmonics: Fundamentals and Applications* (Springer, New York, NY, 2007).

[98] L. Novotny and B. Hecht, *Principles of Nano-Optics* (Cambridge University Press, Cambridge, UK, 2006).

[99] E. David, *Deutung der Anomalien der optischen Konstanten dünner Metallschichten*, Z. Physik **114**, 389 (1939).

[100] K. Okamoto, *Fundamentals of Optical Waveguides* (Academic Press, San Diego, CA, 2006).

[101] D. Nau, *The influence of disorder in metallic photonic crystals*, PhD thesis, Rheinische Friedrich-Wilhelms-Universität Bonn (2006).

[102] P. K. Tien, *Light Waves in Thin Films and Integrated Optics*, Appl. Opt. **10**, 2395 (1971).

[103] M. K. Barnoski, *Introduction to Integrated Optics* (Plenum Press, New York, NY, 1974).

[104] A. Christ, *Optical properties of metallic photonic crystal structures*, PhD thesis, Philipps-Universität Marburg (2005).

[105] S. G. Tikhodeev, A. L. Yablonskii, E. A. Muljarov, N. A. Gippius, and T. Ishihara, *Quasiguided modes and optical properties of photonic crystal slabs*, Phys. Rev. B **66**, 045102 (2002).

[106] U. Fano, *Effects of Configuration Interaction on Intensities and Phase Shifts*, Phys. Rev. **124**, 1866 (1961).

[107] P. Vincent and M. Nevière, *Corrugated Dielectric Waveguides: A Numerical Study of the Second-Order Stop Bands*, Appl. Phys. **20**, 345 (1979).

[108] M. W. Klein, T. Tritschler, M. Wegener, and S. Linden, *Lineshape of harmonic generation by metallic nanoparticles and metallic photonic crystal slabs*, Phys. Rev. B **72**, 115113 (2005).

[109] A. Christ, S. Linden, T. Zentgraf, K. Schubert, D. Nau, S. G. Tikhodeev, N. A. Gippius, J. Kuhl, F. Schindler, A. W. Holleitner, J. Stehr, J. Crewett, J. Lupton, T. Klar, U. Scherf, J. Feldmann, C. Dahmen, G. von Plessen, and H. Giessen, *Optical properties of planar metallo–dielectric photonic crystals*, in Photonic Crystals: Advances in Design, Fabrication, and Characterization, edited by K. Busch, S. Lölkes, R. B. Wehrspohn, and H. Föll (Wiley-VCH, 2004).

[110] P. Y. Yu and M. Cardona, *Fundamentals of Semiconductors: Physics and Materials Properties* (Springer, Berlin, 2005).

[111] R. Zallen, *The Physics of Amorphous Solids* (John Wiley & Sons, New York, NY, 1983).

[112] J.-F. Gouyet, *Physics and Fractal Structures* (Springer, Berlin, 1996).

[113] X. Sun and D. L. Jaggard, *Wave interactions with generalized Cantor bar fractal multilayers*, J. Appl. Phys. **70**, 2500 (1991).

[114] S. V. Zhukovsky, A. V. Lavrinenko, and S. V. Gaponenko, *Spectral scalability as a result of geometrical self-similarity in fractal multilayers*, Europhys. Lett. **66**, 455 (2004).

[115] A. V. Lavrinenko, S. V. Zhukovsky, K. S. Sandomirski, and S. V. Gaponenko, *Propagation of classical waves in nonperiodic media: Scaling properties of an optical Cantor filter*, Phys. Rev. E **65**, 036621 (2002).

[116] *Crystals of golden proportions*, Technical Report, The Royal Swedish Academy of Sciences (2011).

[117] D. Levine and P. J. Steinhardt, *Quasicrystals. I. Definition and structure*, Phys. Rev. B **34**, 596 (1986).

[118]   *Report of the Executive Committee for 1991*, Acta Cryst. A **48**, 922 (1992).

[119]   J. E. S. Socolar and P. J. Steinhardt, *Quasicrystals. II. Unit-cell configurations*, Phys. Rev. B **34**, 617 (1986).

[120]   R. K. P. Zia and W. J. Dallas, *A simple derivation of quasi-crystalline spectra*, J. Phys. A: Math. Gen. **18**, L341 (1985).

[121]   V. Elser, *The Diffraction Pattern of Projected Structures*, Acta Cryst. A **42**, 36 (1986).

[122]   J. Q. You and T. B. Hu, *A Global Cut-and-Project Method to Construct Generalized Fibonacci Lattices and Quasilattices*, phys. stat. sol. (b) **147**, 471 (1988).

[123]   A. I. Goldman and R. F. Kelton, *Quasicrystals and crystalline approximants*, Rev. Mod. Phys. **65**, 213 (1993).

[124]   J. C. López, G. Naumis, and J. L. Aragón, *Renormalization group of random Fibonacci chains*, Phys. Rev. B **48**, 12459 (1993).

[125]   N. G. de Bruijn, *Algebraic theory of Penrose's non-periodic tilings of the plane I*, Indagat. Math. (Proc.) **84**, 39 (1981).

[126]   N. G. de Bruijn, *Algebraic theory of Penrose's non-periodic tilings of the plane II*, Indagat. Math. (Proc.) **84**, 53 (1981).

[127]   J. E. S. Socolar, P. J. Steinhardt, and D. Levine, *Quasicrystals with arbitrary orientational symmetry*, Phys. Rev. B **32**, 5547 (1985).

[128]   M. C. P. Brunelli, *Crack Propagation in Quasicrystals at Different Temperatures*, PhD thesis, Universität Stuttgart (2000).

[129]   A. Subramaniam and K. Ramakrishnan, *Rational approximants to 5, 8 and 7-fold two-dimensional tilings*, Z. Kristallogr. **218**, 590 (2003).

[130]   A. Christ, T. Zentgraf, J. Kuhl, S. G. Tikhodeev, N. A. Gippius, and H. Giessen, *Optical properties of planar metallic photonic crystal structures: Experiment and theory*, Phys. Rev. B **70**, 125113 (2004).

[131]   F. Urbach, *The Long-Wavelength Edge of Photographic Sensitivity and of the Electronic Absorption of Solids*, Phys. Rev. **92**, 1324 (1953).

[132]   M. V. Kurik, *Urbach Rule*, phys. stat. sol. (a) **8**, 9 (1971).

[133]   G. D. Cody, T. Tiedje, B. Abeles, B. Brooks, and Y. Goldstein, *Disorder and the Optical-Absorption Edge of Hydrogenated Amorphous Silicon*, Phys. Rev. Lett. **47**, 1480 (1981).

[134] J. Szczyrbowski, *The Exponential Shape of the Optical Absorption Edge Tail*, phys. stat. sol. (b) **105**, 515 (1981).

[135] J. Wolny, *The reference lattice concept and its application to the analysis of diffraction patterns*, Philos. Mag. A **77**, 295 (1998).

[136] U. Shmueli, *International Tables for Crystallography, Reciprocal Space*, Vol. B (Springer, Dordrecht, NL, 2008).

[137] G. Kobiela, *Manufacturing and Spectroscopy of Nano- and Meta-Structures*, Diploma thesis, Universität Stuttgart (2009).

[138] A. C. Kak and M. Slaney, *Principles of Computerized Tomographic Imaging* (IEEE Press, New York, NY, 1988).

[139] R. M. Mersereau and A. V. Oppenheim, *Digital Reconstruction of Multidimensional Signals from Their Projections*, Proc. IEEE **62**, 1319 (1974).

[140] W. Demtröder, *Experimentalphysik 2: Elektrizität und Optik* (Springer, Berlin, 2009).

[141] C. Bauer, G. Kobiela, and H. Giessen, *Optical properties of two-dimensional quasicrystalline plasmonic arrays*, Phys. Rev. B **84**, 193104 (2011).

[142] S. Fan and J. D. Joannopoulos, *Analysis of guided resonances in photonic crystal slabs*, Phys. Rev. B **65**, 235112 (2002).

[143] A. Christ, Y. Ekinci, H. H. Solak, N. A. Gippius, S. G. Tikhodeev, and O. J. F. Martin, *Controlling the Fano interference in a plasmonic lattice*, Phys. Rev. B **76**, 201405(R) (2007).

[144] C. Bauer, G. Kobiela, and H. Giessen, *2D quasicrystalline plasmonic crystals*, Sci. Rep. **2**, 681 (2012).

[145] R. A. Pala, J. White, E. Barnard, J. Liu, and M. L. Brongersma, *Design of Plasmonic Thin-Film Solar Cells with Broadband Absorption Enhancements*, Adv. Mater. **21**, 3504 (2009).

[146] M. J. Weber, *Handbook of Optical Materials* (CRC Press, Boca Raton, FL, 2003).

[147] J. N. Munday and H. A. Atwater, *Large Integrated Absorption Enhancement in Plasmonic Solar Cells by Combining Metallic Gratings and Antireflection Coatings*, Nano Lett. **11**, 2195 (2011).

[148] D. Zhou and R. Biswas, *Photonic crystal enhanced light-trapping in thin film solar cells*, J. Appl. Phys. **103**, 093102 (2008).

[149] C. Gueymard, *SMARTS2, Simple Model for the Atmospheric Radiative Transfer of Sunshine: Algorithms and performance assessment*, Technical Report FSEC-PF-270-95, Florida Solar Energy Center, Cocoa, FL (1995).

[150] J. G. Mutitu, S. Shi, C. Chen, T. Creazzo, A. Barnett, C. Honsberg, and D. W. Prather, *Thin film silicon solar cell design based on photonic crystal and diffractive grating structures*, Opt. Express **16**, 15238 (2008).

[151] *The latitude and longitude of Germany*, http://www.travelmath.com/country/Germany (accessed on 12/13/2012).

[152] H. Schwarz and S. Ying, *Urban photovoltaic potential*, in 2010 9th International Conference on Environment and Electrical Engineering (EEEIC) (2010), p. 26.

ACKNOWLEDGMENTS

I want to thank all the people who supported me during the last years. Many thanks go to ...